AGH UNIVERSITY OF KRAKOW

FIELD OF SCIENCE: Engineering and Technical Sciences

SCIENTIFIC DISCIPLINE: Materials Engineering

DOCTORAL THESIS

Application of multicomponent pentlandites as cathodic materials in the electrocatalytic water splitting process

Author: MSc Eng. Maciej Ryszard Kubowicz

First supervisor: DSc Eng. Andrzej Mikuła

Completed in: AGH University of Krakow
Faculty of Material Science and Ceramics
Department of Inorganic Chemistry

Krakow, 2025

Podziękowania

Na samym początku chciałbym serdecznie podziękować swojemu promotorowi: **Panu dr hab. inż. Andrzejowi Mikule**, tak właściwie za wszystko. Za cierpliwość, wsparcie naukowe, pokazanie nowego spojrzenia na świat, ogrom pozytywnej energii i wszystko inne. Dziękuję, że mogłem tu być.

Serdecznie dziękuję również **Pani prof. dr hab. inż. Marcie Radeckiej**, za wzięcie mnie pod swoje skrzydła oraz całe merytoryczne wsparcie, które od niej uzyskałem.

Dziękuję **Pani dr hab. inż. Magdalenie Król**, za rozwinięcie mej raczkującej kariery naukowej oraz zarażenie mnie pasją do zadawania pytań i szukania na nie odpowiedzi.

Dziękuję Paniom **dr Annie Kusior**, **Kindze Michalec** oraz **Julii Mazurków**, które pomogły mi na początku tej drogi, gdy byłem jeszcze zagubiony, oraz za wsparcie i odpowiedzi uzyskane w dalszej części tej przygody.

Dziękuję kolegom z zespołu, którzy wraz ze mną szli przez przygodę zwaną doktoratem, służąc mi radą i pomocą, gdy tylko jej potrzebowałem. **Miłosz Kożusznik, Tomasz Kurek, Jakub Dechnik**, powodzenia, chłopaki.

Dziękuję **dr Jakubowi Czerskiemu** oraz **Katarzynie Płachecie**, bez was te lata nie byłyby takie same.

Dziękuję rodzinie, **mamie Teresie** oraz **bratu Michałowi**, **mojej Ani** oraz **wszystkim znajomym i przyjaciołom**, którzy zawsze we mnie wierzyli i od których zawsze mogłem liczyć na motywacje we wszelakich formach.

Niniejsza praca była częściowo finansowana przez Narodowe Centrum Nauki w ramach grantu nr 2022/45/B/ST8/03336

Acknowledgements

First and foremost, I would like to sincerely thank my supervisor, **Andrzej Mikuła, DSc, PhD, Eng.**, truly for everything – for his patience, scientific guidance, showing me a new perspective on the world, his boundless positive energy, and so much more. Thank you for allowing me to be here.

I am also deeply grateful to **Prof. Marta Radecka, DSc, Eng.,** for taking me under her wing and for all the valuable scientific support I have received from her.

My thanks go as well to **Magdalena Król, DSc, PhD, Eng.,** for helping me develop my emerging scientific career and for inspiring me with her passion for asking questions and seeking answers.

I would also like to thank **Anna Kusior, PhD, Kinga Michalec, PhD, and Julia Mazurek, PhD**, who supported me at the very beginning of this path, when I was still lost, as well as for their help and answers later on during this journey.

I am grateful to my colleagues from the research group, who shared the doctoral adventure with me, always ready to offer advice and assistance whenever I needed it. **Miłosz Kożusznik, Tomasz Kurek, Jakub Dechnik** – good luck, guys.

Special thanks also go to **Jakub Czerski, PhD, and Katarzyna Płacheta** – without you these years would not have been the same.

Finally, I would like to thank my family – **my mother Teresa and my brother Michał** – as well as **my Ania, all my friends and companions**, who always believed in me and from whom I could always count on motivation in all its forms.

This work was partially supported by the National Science Centre, Poland, under grant no. 2022/45/B/ST8/03336.

First of all, I would like to point out that the results presented in this doctoral thesis have been published, in whole or in part,in the following publications:

Mikuła Andrzej, Dąbrowa Juliusz, Kusior Anna, Mars Krzysztof, Lach Radosław and Kubowicz Maciej - "Search for mid- And high-entropy transition-metal chalcogenides - investigating the pentlandite structure". *Dalt. Trans.* **50**, 9560–9573 (2021).

Mikuła Andrzej, Kubowicz Maciej, Mazurków Julia, Mars Krzysztof, Smialkowski Mathias, Apfel Ulf-Peter and Radecka Marta – "Tailoring the electrocatalytic activity of multicomponent $(Co,Fe,Ni)_9S_{8-x}Se_x$ pentlandite solid electrodes." *J. Mater. Chem. A* 7526–7538 (2023) doi:10.1039/d2ta08893b.

Mikuła Andrzej, Kubowicz Maciej, Smialkowski Mathias., Sanden Sebastian and Apfel Ulf-Peter – "Tuning the Electrocatalytic Properties of Trimetallic Pentlandites: Stability and Catalytic Activity as a Function of Material Form and Selenium Concentration." *ACS Mater. Lett.* **6**, 1581–1592 (2024).

Kubowicz Maciej, Kożusznik Miłosz, Kurek Tomasz, Mars Krzysztof and Mikuła Andrzej – "Role of Foreign Phases, Synergistic Effects, and Morphology in the HER Performance of Trimetallic Pentlandites with Non-Equimolar Co:Fe:Ni Ratio." *Energies* **17**, (2024).

Kubowicz Maciej, Kożusznik Miłosz, Rusiniak Piotr, Smialkowski Mathias, Apfel Ulf-Peter and Mikuła Andrzej - "Multicomponent Pentlandites with High Selenium Content: Unveiling New HER Mechanisms with Reduced Cation Influence" – under review

Table of content

I. Nomenclature

I.1. Abbreviations

AUX – auxiliary/counter electrode

CCUS – carbon capture, utilization and storage

CORR/CO_2RR – Carbon monoxide or dioxide reduction reaction

CV – cyclic voltammetry

d.n.a. – did not achieve

DFT – density functional theory

DLS – dynamic light scattering

ECSA – electrochemical active surface area

EIS – impedance spectroscopy in solutions

EOR – ethanol electrooxidation reaction

E_{RHE} – electrical potential of the reversible hydrogen electrode

FAOR – formic acid oxidation reaction

GHG - greenhouse gas

GoF – goodness of fit

HBE – hydrogen binding energy

HEA – high entropy alloys

HER – hydrogen evolution reaction

HOR – hydrogen oxidation reaction

H_{UPD} – underpotential of hydrogen, on which the local maxima can be observe

IHP – Inductive hot pressing

LPCE – low Pt content electrocatalyst

LSV – linear sweep voltammogram

Me – metal

MOR – methanol electrooxidation reaction

n.d. – no data

NRR – Nitrogen reduction reaction

OER – oxygen evolution reaction

ORR – oxygen reduction reaction

PEM – proton exchange membranes

pH – hydrogen ion exponent

PVD – physical vapor deposition

REF – reference electrode

RF – roughness factor

RHE – reversible hydrogen electrode

RI – reaction intermediate

SPE – solid polymer electrolyte

TMCh – transition metal chalcogenide

TMSO – oxygen doped transition-metal sulfide

VASP – Vienna Ab initio Simulation Package

VDOS – vibrational density of states

WE – working electrode

wRp – weighted R profile

WtE – waste-to-energy

WtH – waste-to-hydrogen

I.2. Symbols

m_a – mass of the sample in air [g]

m_w – mass of the sample in water [g]

ρ_{H_2O} – density of the water [g/cm^3]

ρ_A – density of the sample [g/cm^3]

ρ_C – theoretical crystallographic density calculated using Rietveld analysis [g/cm^3].

ρ_R – relative density of the sample [%]

A – geometric surface area [m^2]

a – Tafel slope, the slope of the Tafel curve [mV/dec]

A^* – active site

a_O – activity coefficient of the reactant in oxidized state

a_R - activity coefficient of the reactant in reduced state.

C_{dl} – charging current density, double layer capacitance

C_i – electrode surface concentration [–]

C_i^* – bulk concentration [–]

C_s – specific capacitance [mF/cm²]

E^0 – standard potential of the electrode [V]

E_r – potential of the electrode in the equilibrium state [V]

F – Faraday constant ($9.5 \cdot 10^4$ [C/mol]) [1]

I – current [A]

j – current density [A/cm^2]

j_0 – exchange current density [A/cm^2]

n – number of electrons exchanged during reaction [–]

η – overpotential [V]

η_{HER} – overpotential in HER measurements [V]

η_{OER} – overpotential in OER measurements [V]

R – ideal gas constant (8.3143 [kJ/kmol·K]) [2]

T – temperature [°C]

v_r – rate of reaction

α – charge transfer coefficient [–]

β – symmetry factor [–]

ΔG_{H^*} - Gibbs free energy of hydrogen adsorption [eV]

1. State-of-the-art

1.1. Introduction

Modern science and technology are placing increasing demands on the performance and durability of materials utilized in chemical processes. A key area of research is the development of new catalysts that accelerate chemical reactions without consuming the catalyst itself. The performance of catalysts has a direct impact on the energy and economic efficiency of many industrial processes, including the production of chemicals, fuels, and other critical substances. Research into new catalytic materials focuses on optimizing their chemical and physical properties to meet growing market demands. A significant challenge is finding alternatives to the expensive and rare metals that currently dominate the industry [3–6].

Hydrogen, obtained through electrochemical water splitting, is considered one of the most promising energy carriers for a future low-carbon economy. However, the large-scale deployment of this technology is limited by the high cost and scarcity of state-of-the-art catalysts based on platinum group metals (PGMs), such as Pt, Ir, and Ru, which dominate the hydrogen evolution reaction (HER) and oxygen evolution reaction (OER). As a result, recent research has focused on developing alternative catalysts composed of earth-abundant transition metals. Among these, transition-metal chalcogenides (sulfides and selenides) have attracted significant attention due to their favorable electronic structure, high catalytic activity, and tunable composition. In particular, pentlandites with a general formula TM_9Ch_8 (where TM = Fe, Ni, Co, or their combinations; Ch = S, Se, or their combinations) offer a unique combination of metallic conductivity, structural stability, and catalytic activity toward HER.

Most existing work has concentrated on binary systems, leaving the role of multicomponent approach or compositionally complex pentlandites largely unexplored. Moreover, the correlation between composition, crystal structure, and catalytic performance in water splitting is still poorly understood. This doctoral research addresses these challenges by investigating the application of multicomponent pentlandites as cathodic materials in electrocatalytic water splitting. The study focuses on designing and synthesizing novel pentlandite-based compositions, evaluating their catalytic activity and stability, and establishing structure–property–activity relationships that may guide the development of next-generation non-noble catalysts for sustainable hydrogen production.

1.1.1. Hydrogen

One of the most promising solutions to the energy crisis is the use of hydrogen as an energy source. Its high demand stems from several advantageous properties. In particular, the reaction between hydrogen and oxygen produces a significant amount of energy (143.1 MJ/kg) with pure water as the only by-product, resulting in no environmental pollution during this process [5,7]. Additionally, hydrogen has an excellent storage capacity; 1 kg of hydrogen contains approximately 120 MJ of energy, which is more than double that of commonly used fuels, such as natural gas (47 MJ/kg), diesel (43 MJ/kg), and methanol (20 MJ/kg) [7]. Furthermore, hydrogen is a sustainable and non-toxic energy source [7,8].

Hydrogen is widely used in fuel cells due to its ability to directly convert energy from hydrogen-oxygen reactions into electricity. If an effective and economically viable technology for hydrogen production were developed, Earth's water resources could serve as an inexhaustible source of hydrogen, as it is the most abundant element in the universe, constituting more than 90% of atoms [7]. However, current hydrogen production relies on high-energy processes such as the steam reforming of hydrocarbon fuels, including propane, gasoline, methane (from natural gas), ethane, and diesel [3,5,9,10], which contributes to significant environmental pollution and costs.

Initially, synthetic hydrogen was classified as either gray or green based on its production method. The former is produced from processes like steam reforming (using fossil fuels), whereas the latter is obtained through water electrolysis. Over the years, new production methods and potential technologies for hydrogen generation have been researched and developed, leading to an expansion of the “color” classification [9,11,12,I4]. Various publications refer to hydrogen produced from the electrical grid as "yellow hydrogen" [11,I1], while hydrogen derived from nuclear power-derived is also referred to as "purple/pink hydrogen" [13,14]. Some other classifications include e.g. "orange hydrogen" [15] and others [9,10,12,16,I2-I6]. In this work, I adopted the color classification system outlined in Table 1.

The hydrogen types associated with the highest CO_2 emissions are black and brown hydrogen, both produced through the gasification of bituminous (black) or lignite (brown) coal. Interestingly, hydrogen can also be produced from the gasification of biomass, which is not classified as black or brown hydrogen. However, the overall process – referred to as waste-to-energy (WtE) or waste-to-hydrogen (WtH) – results in a level of environmental pollution similar to that of black and brown hydrogen production [9,11].

Gray hydrogen is now considered the most common method of hydrogen production, specifically through steam reforming without carbon capture, utilization, and storage (CCUS) technologies. In the steam reforming process, high-temperature steam reacts with hydrocarbon fuels to produce syngas, a mixture of hydrogen and carbon monoxide. Although a variety of hydrocarbon-based gases can be used in this process, methane is one of the most commonly used fuels for hydrogen production [11,17,18].

Table 1. The summary of the hydrogen colors [9–11,13,15,16,II-7]

Electricity source	Color	Source of hydrogen	Technology	CO_2 emission
Non-renewable energy, fossil fuels	Black Hydrogen	Black coal	Gasification	High
	Brown Hydrogen	Brown coal, biomass		
	Grey Hydrogen	Natural gas	Natural gas reforming	High/Medium
	Turquoise Hydrogen	Natural gas	Pyrolysis	By-product, no direct CO_2 emission
	Blue Hydrogen	Natural gas, biomass, coal	Natural gas reforming, gasification + CCUS	Low
Solar	Red Hydrogen	Water	Thermolysis, thermochemical process	Minimum, no direct CO_2 emission
	Orange Hydrogen			Minimum, no direct CO_2 emission
A mix of electricity grid	Yellow Hydrogen		Electrolysis	Medium depends on the electricity mix
Nuclear	Purple/Pink Hydrogen			Minimum, no direct CO_2 emission
Renewable energy	Green Hydrogen			Minimum, no direct CO_2 emission

Turquoise hydrogen is produced through the pyrolysis of methane, where the primary products are hydrogen and solid carbon. The absence of oxygen in this process prevents the formation of carbon oxides. Solid carbon can be stored in forms such as carbon nanotubes or carbon nanofibers [19,20]. However, this approach presents challenges due to the high temperatures (above 1000°C) required for the thermal decomposition of methane [21–23]. To mitigate this, metal catalysts such as iron, nickel, cobalt, or carbon-based catalysts can be used to lower the required temperature [24].

To reduce CO_2 emissions in gasification and natural gas reforming processes, CCUS technologies are applied to hydrogen production, resulting in what is referred to as blue hydrogen. These methods aim to capture CO_2 from large production sources or directly from the atmosphere [11].

Red hydrogen is a rare term for hydrogen produced through thermal and thermochemical water splitting [25]. This process involves the direct decomposition of water molecules into hydrogen and oxygen [26]. The two main challenges associated with this approach are preventing the recombination of H_2O and the high cost of the required equipment. Red hydrogen is sometimes associated with white hydrogen, which refers to hydrogen stored in natural deposits [11,25].

Purple or pink hydrogen is produced using nuclear power, depending on whether it serves as a thermal or electrical energy source, respectively. The primary method involves electrical energy, which can come from processes such as thermochemical water splitting, low- and high-temperature water electrolysis, and steam methane reforming [9,11,16,27].

Yellow hydrogen is produced through the process of water electrolysis powered by electricity from the grid. Although the electrolysis process itself does not generate environmental pollution, the sources of that electricity can, such as coal-fired power plants or other methods that produce greenhouse gas (GHG) emissions. According to the European Environment Agency, Poland was the second-highest country in Europe (after Estonia) in terms of the intensity of greenhouse gas emissions in electricity generation in 2020 [9,11,16,I6].

Orange hydrogen is produced using solar power. While it appears to be a promising "color" of hydrogen, this method requires a substantial energy supply chain and large areas for solar farms. Furthermore, it is statistically one of the most expensive forms of hydrogen production [15].

Green hydrogen is highly desired because it is produced from renewable sources other than biomass and achieves a 70% reduction in GHG emissions compared to fossil fuels. Generally, it is obtained through water electrolysis powered by renewable energy sources such as photovoltaics or wind turbines [11,15,28–32]. It seems to be the most promising aspect of hydrogen technologies, and in my work, I have focused on aspects related to the production of efficient and cost-effective electrodes for the water electrolysis process.

1.1.2. Water electrolysis

Water electrolysis is a process in which electrical current powers the decomposition of H_2O molecules. The electrolysis phenomenon was discovered by Troostwijk and Diemann in 1789 [4], while the electrolytic decomposition of water was discovered by Nicholson and Carlisle in 1800 [33]. Since then, research on this phenomenon has led to significant advancements, including the establishment of the first large water electrolysis plant in 1939, with a capacity of 10,000 Nm^3 H_2/h. In 1948, Zdansky and Lonza invented the first pressurized industrial electrolyzer. Then, in 1966, General Electric built the first solid polymer electrolyte (SPE) system, followed by the invention of the first solid oxide water electrolysis system in 1972 [34].

Nowadays, three main subtypes of water electrolysis are being tested, depending on the operational conditions [35,36]:

- PEM (Proton-Exchange Membrane) electrolysis, which operates mainly in acidic environments. It offers highly compact and flexible technology but relies heavily on expensive platinum-based or other PGM catalysts.
- AEM (Anion Exchange Electrolysis), which avoids the use of PGMs, but is significantly less efficient and less flexible than PEM.
- HT-WSE (High-Temperature Water-Splitting Electrolysis), which provides the highest efficiency due to its elevated operating temperatures. However, it requires the most expensive construction materials and electrocatalysts capable of withstanding aggressive conditions.

It is worth mentioning that the materials described in this thesis show the greatest potential for use in PEM electrolysis, due to their stability in acidic environments. With further research, these materials may also be suitable for AWE applications, as Ni-rich pentlandites are known from the literature to perform well in alkaline electrolysis [37].

During basic reaction of water electrolysis, a water molecules can be split into gaseous hydrogen and oxygen, as shown in the equation (1.1) [4,34,38–40]:

$$H_2O \rightarrow H_{2(g)} + \frac{1}{2}O_{2(g)} \qquad (1.1)$$

This process occurs on electrodes surface (or catalysts anchored to electrodes) made of noble metals and, depending on electrolyte and pH, can occur via different pathways. In acidic media the mechanism is described by equations (1.2) and (1.3) [34,40]:

Anode (+) $$H_2O \rightarrow 2H^+ + \frac{1}{2}O_2 + 2e^- \qquad (1.2)$$

Cathode (–) $$2H^+_{(aq)} + 2e^- \rightarrow H_{2(g)} \qquad (1.3)$$

And in alkaline or neutral solution as in the following equations (1.4) and (1.5) [40]:

Anode (+) $$2OH^- \rightarrow H_2O + \frac{1}{2}O_2 + 2e^- \qquad (1.4)$$

Cathode (–) $2H_2O + 2e^- \rightarrow H_2 + 2OH^-$ (1.5)

what leads to the summary equation (1.6) (which leads to the general equation (1.1)) [34]:

$$2H_2O \rightarrow (4e^-) \rightarrow 2H_2 + O_2 \quad (1.6)$$

1.2. Electrocatalytic activity

The basis of electrochemical reactions lies in redox reactions, during which electron transfers occur. Oxidation always occurs at the anode, and reduction at the cathode. However, the electrode polarity differs depending on the type of electrochemical cell. In a galvanic cell, the anode is negative, and the cathode is positive, as the cell generates electrical current through spontaneous chemical reactions. In contrast, in an electrolytic cell, the anode is positive and the cathode is negative, since the reactions are driven by an external power source. In both systems, electrons flow from the anode to the cathode. The working electrode either supplies or absorbs charge, enabling two possible processes: generating electricity from a reaction, as seen in galvanic cells, or supplying current to induce a reaction, as in the process of electrolysis [41–43]. .

For a chemical reaction to occur, the energy barrier must be overcome. To lower this barrier, catalysts are used – substances that accelerate the reaction by lowering its activation energy without being permanently altered. This means the catalyst is not consumed or changed during the reaction and can be reused once the reaction is complete. Catalysts work by forming a transient complex with the reactants, which facilitates the conversion of reactants into products more easily. While they do not participate in the overall energy balance of the reaction, they help reduce the amount of energy required for the reaction to proceed. In summary, a catalyst lowers the "energy threshold" of a reaction, making it faster or enabling it to occur under conditions that would otherwise be impossible. Catalysts play a crucial role in many industrial processes, such as chemical production and the reduction of nitrogen (N_2) to ammonia (NH_3). A summary of electrocatalytic processes is presented in Table 2 [44–46].

Table 2. Summary of the electrocatalysts processes.

Short name	Full name	Main reaction	Reference
HER	Hydrogen evolution reaction	$2H^+ + 2e^- \rightarrow H_2$	47
HOR	Hydrogen oxidation reaction	$H_2 \rightarrow 2H^+ + 2e^-$	47–49
OER	Oxygen evolution reaction	$4OH^- \rightarrow O_2 + 2H_2O + 2e^-$	3,34,40,50
ORR	Oxygen reduction reaction	$O_2 + 2H_2O + 4e^- \rightarrow 4OH^-$	47,48,51,52
MOR	Methanol electrooxidation reaction	$2CH_3OH + 3O_2 \rightarrow 2CO_2 + 4H_2O$	47,48,53,54
EOR	Ethanol electrooxidation reaction	$CH_3CH_2OH + 3O_2 \rightarrow 2CO_2 + 3H_2O$	13,47,48,54
NRR	Nitrogen reduction reaction	$N_2 + 3H_2 \rightarrow 2NH_3$	47,55
FAOR	Formic acid oxidation reaction	$HCOOH \rightarrow HCOOH^* \rightarrow CO_2 + 2H^+ + 2e^-$	48,56
ECH	Electrochemical hydrogenation	Various reactions, see Ref.	57–59
CORR/CO_2RR	Carbon monoxide or dioxide reduction reaction	Various reactions, see Ref.	48,60,61

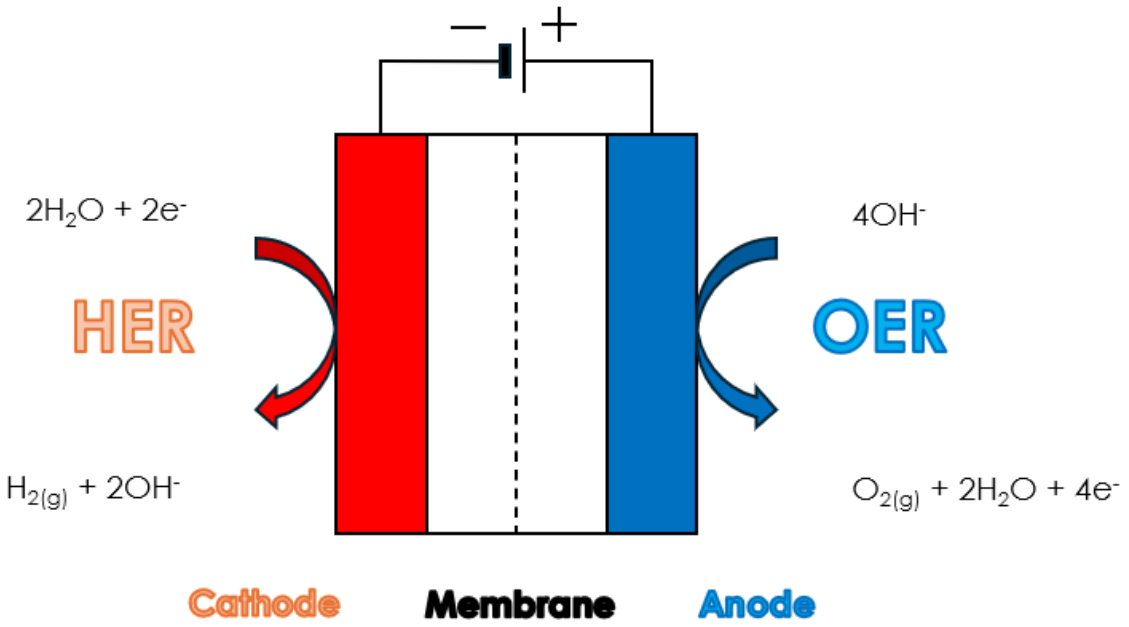

Figure 1. Schematic representation of HER/OER reaction in electrolyzer (alkaline conditions).

1.2.1. Hydrogen and oxygen evolution reactions

Water electrolysis can be represented by two half reactions: the hydrogen evolution reaction (HER, equations 1.3 and 1.5) and oxygen evolution reaction (OER, equations 1.2 and 1.4). HER is a reaction occurring at the cathode, during which a water molecule is reduced to H_2, and OER is a reaction occurring at the anode, in which a water molecule is oxidized to form an O_2 molecule. To induce the desired reaction, a potential difference must be applied at the electrodes, with a negative potential favoring HER and a positive driving OER [3,34,40]. The general scheme of the HER and OER reactions is shown in Figure 1.

The main mechanism of the hydrogen evolution reaction, regardless of the solution's pH during electrolysis, consists of three steps. The first step, known as the Volmer step, involves the adsorption of hydrogen onto the electrode surface by discharged protons. In the second step, hydrogen desorbs from the cathode. This process can occur via two routes: the electrochemical pathway, referred to as the Heyrovsky step (an adsorbed hydrogen atom reacts with a proton and an electron to form H_2), or the chemical pathway, known as the Tafel step (two adsorbed hydrogen atoms combine without electron transfer). The overall HER mechanism is illustrated in Figure 2 [38,62] and shown in details in equations (1.7-1.14) depending on the pH of the electrolyte. The HER response can involve both mechanisms, but which one dominates depends on the specific electrochemical conditions. The Heyrovsky step tends to dominate at lower overpotentials, under conditions of lower hydrogen ion concentration and lower pressure, whereas the Tafel step becomes dominant at higher overpotentials, higher hydrogen concentrations (or pressure), and elevated temperatures, where it is easier for hydrogen atoms to combine into an H_2 molecule. From an efficiency standpoint, the Tafel step is more advantageous, as it allows for faster and more efficient hydrogen production, minimizes dependence on electron supply from an external source, and facilitates the rapid removal of hydrogen molecules from the electrode surface [33,51,63–67].

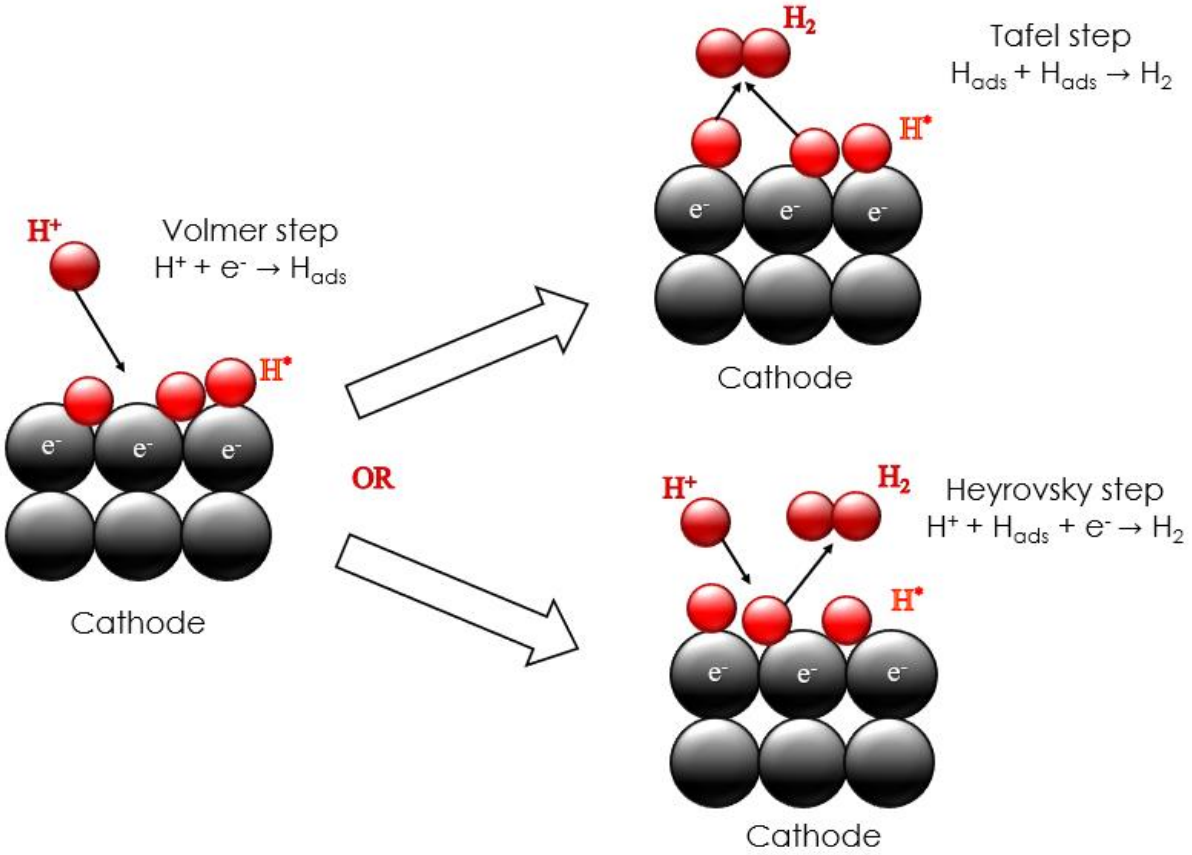

Figure 2. Schematic illustration of a potential HER mechanism on a cathode. Based on [38].

In acidic media the whole HER process and individual steps follow (1.7-1.10):

Overall	$2H_{(aq)}^{+} + 2e^{-} \rightarrow H_{2(g)}$	(1.7)
Volmer	$H^{+} + e^{-} + A^{*} \rightarrow H_{ads}$	(1.8)
Heyrovsky	$H^{+} + e^{-} + H^{*} \rightarrow H_{2(g)}$	(1.9)
Tafel	$2H^{*} \rightarrow H_{2(g)}$	(1.10)

In alkaline and neutral media (1.11-1.14):

Overall	$2H_2O + 2e^{-} \rightarrow H_{2(g)} + 2OH_{aq}$	(1.11)
Volmer	$H_2O + e^{-} + A^{*} \rightarrow H^{*} + OH^{-}$	(1.12)
Heyrovsky	$H_2O + e^{-} \rightarrow H_{2(g)} + OH^{-}$	(1.13)
Tafel	$2H^{*} \rightarrow H_{2(g)}$	(1.14)

A^{*} – active site
H^{*} – adsorbed hydrogen

In both cases, during the Volmer step, the active site (A^{*}) is required to start the reaction. This site is a location on the electrode (or catalyst) surface where the hydrogen atom can be adsorbed as H^{*} [3,38,68–74].

Due to the more complex nature of the OER process, there are several different mechanisms involved, which are related to the higher number of electron transfers required for the reaction to proceed. Although the reactions in the system are similar to those in HER, they follow different pathways and involve a significantly greater number of possible intermediates. In acidic conditions, the reactions proceed as follows: (1.15-1.18) [3,75–78]:

$$2H_2O_{(l)} \rightarrow O_{2(g)} + 4H^+ + 4e^- \quad (1.15)$$

$$H_2O + A^* \rightarrow H_{ads} + AOH + e^- \quad (1.16)$$

$$AOH + OH^- \rightarrow AO + H_2O + e^- \quad (1.17)$$

$$2AO \rightarrow 2A + O_{2(g)} \quad (1.18)$$

And in alkaline media (1.19-1.22):

$$2H_2O_{(l)} \rightarrow O_{2(g)} + 4H^+ + 4e^- \quad (1.19)$$

$$A^* + OH^- \rightarrow AOH \quad (1.20)$$

$$AOH + OH^- \rightarrow AO + H_2O_{(l)} \quad (1.21)$$

$$2AO \rightarrow 2A + O_{2(g)} \quad (1.22)$$

1.3. Electrolyzers

The design of electrodes and electrolyzers is a key factor influencing the efficiency and scalability of electrochemical processes. Currently, water electrolysis is primarily carried out using two main system configurations [79–82]:

- H-type cells (Figure 3a), consisting of a simple single-cell design in which the electrodes are separated by an ion-exchange membrane, immersed in an aqueous solution of a suitable electrolyte (typically 0.5 M H_2SO_4 under acidic conditions or 1 M KOH under alkaline conditions).
- Flow cells, suitable for electrolysis in both the gas and liquid phases, require a continuous flow of electrolyte through designated compartments of the electrochemical system. Unlike H-type cells, they are not limited by diffusion-based mass transport. A notable subclass of flow cells is represented by zero-gap electrolyzers (Figure 3b), where the electrodes are pressed directly against the membrane. This design eliminates the internal gap between the electrode and the membrane, significantly enhancing charge transport.

The advantages and limitations of both types of electrolyzers are summarized in Table 3.

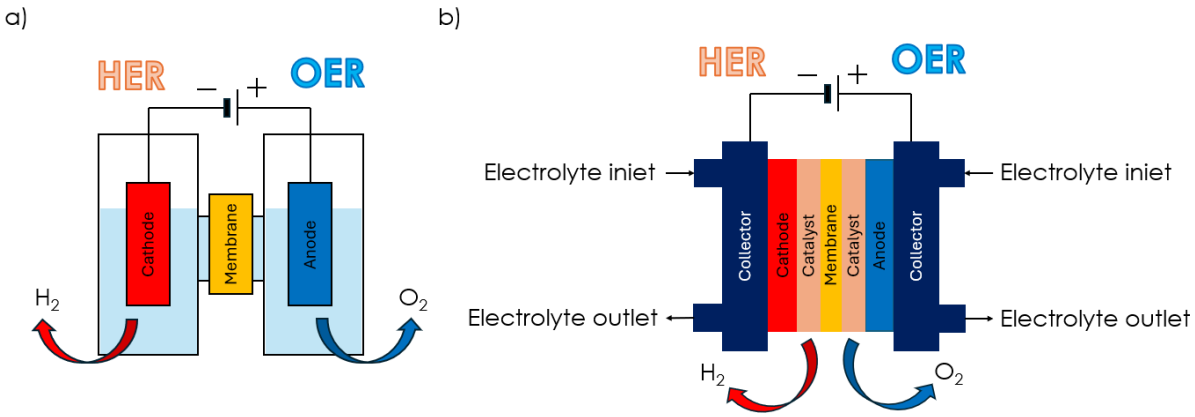

Figure 3. Schematic representation of electrochemical cells: a) H-type cell; b) zero-gap cell.

Table 3. Summary of advantages, disadvantages, key requirements of H-type, flow cells and zero gap electrolyzers.

	H-type	**Flow cell**	**Zero-gap electrolyzer**
Advantages	- Simple construction - Minimal cross-contamination of products between anodic and cathodic compartments - Precise control over reaction mechanisms, facilitating the investigation of electrodes and electrocatalyst materials under well-defined conditions - Straightforward electrode preparation: platinum wire, foil, or suitable pellets; metal foils coated with catalyst layers; or screen-printed electrodes (SPEs)	- High current densities - Suitable for large-scale applications, including energy storage and conversion - Enables investigation of large-surface electrodes, as the system accommodates thick or additively manufactured electrodes - Highly modular and tunable, allowing adaptation for fundamental research - Enhanced control over mass transport and improved stability of reaction conditions	- Improved charge transport through minimization of ohmic losses and enhanced ionic conductivity - Reduced material requirements compared to conventional flow cells - Compact form factor, enabling efficient scalability
Limitations	- Mass transport limitations due to diffusion-controlled processes, resulting in low current densities and restricted scalability - Primarily suitable for fundamental research applications only	- Requires continuous electrolyte flow - Lower current densities compared to zero-gap electrolyzers - Ohmic resistance may occur due to limited contact pressure between the membrane and electrode	- Require thin, conductive, and well-integrated catalytic layers - Not suitable for bulky or non-planar electrodes

Due to the scope of this work and the focus on so-called solid electrodes (i.e., bulk materials simultaneously serving as both electrode and catalyst), both types of electrolyzers (classical H-type and flow-cells) are of great importance. On the one hand, experiments were carried out in standard single-compartment setups. On the other hand, the use of solid electrodes also offers potential relevance for flow-cell configurations, where large electrode surfaces are exposed to the electrolyte, although not necessarily in zero-gap systems.

1.4. Electrochemical methods

Electrochemical methods offer a variety of techniques that can be used to study electrochemical cells, including the electrocatalyst properties. Insight is gained by analyzing the response of the system, which is different, depending on the excitation method (Table 4).

Table 4. General classification of electrochemical techniques [83–85].

Type of method		**The principle**
Amperometry		Current is measured as a function of:
	Chronoamperometry	Time
	Voltammetry	Electrode potential
	Polarography	-
Potentiometry		The potential of a solution is measured between two electrodes
Coulometry		Change in the oxidation state of the analyte by application of current or potential

Due to the nature of this work, amperometry techniques, especially voltammetry, require a more detailed discussion. However, the basic principles of electrochemical methods should be introduced first.

In electrochemical systems, current density (*j)* is a crucial measurement parameter. It represents the current (*I*) flowing between the electrode and the electrolyte interface, which is directly related to the reaction rate (v_r). However, discrepancies can arise due to variations in catalyst geometry or nature of the electrode-solution interface. To address these issues, current is normalized to the electrode surface area (resulting in current density), providing a more accurate representation of the system's performance and enabling comparisons between different electrocatalytic materials. The reaction rate can be described by equation (1.18):

$$v_r = \frac{I}{n \cdot F \cdot A} = \frac{j}{n \cdot F'} \tag{1.18}$$

where*:*
n – number of electrons exchanged during the reaction [-];
A – geometric surface area [cm^2].

The simplest way to increase the current, which is a primary goal in electrochemical methods, is by enhancing the electrode surface area. However, this may not always be feasible, especially when using fixed-size electrode holders. Alternatively, the current can be increased by enhancing the reaction rate (v_r). This method is more complex, requiring careful design and optimization of the catalyst's chemical composition, geometry, and electronic structure. Consequently, electrocatalysis is defined as the dependence of the electrochemical reaction rate on the electrode material [86].

In addition to the parameters mentioned above, that affect reaction kinetics and reaction rate – such as temperature, pressure, and reactant concentration – there are methods to adjust the electrode potential (E). To fully grasp this concept, it is essential to illustrate the redox reaction occurring at the electrode, as shown in equation (1.19):

$$O + n \cdot e^{-} = R \tag{1.19}$$

where:
O – species in its oxidized state;
R – species in its reduced state.

Voltammetry methods are based on creating an electric potential difference between two electrodes, typically within a two- or three-electrode system, over a predetermined range within a specified time frame. Current-voltage characteristics are measured for the working electrode, which is the electrode where these changes occur. When the potential of the working electrode is altered, the energy level of the electrons, represented by the Fermi level, is also affected. This energy change can lead to either reduction or oxidation reactions (Figure 4). Reduction occurs (as shown in Figure 4b) when a more negative potential is applied to the working electrode, raising the Fermi level toward higher energies. If there are a species in the electrolyte with higher-energy empty orbitals, electrons can transfer from the electrode to these species, facilitating a reduction reaction. Conversely, oxidation occurs (illustrated in Figure 4c) when a more positive potential is applied, allowing electrons of the species in the electrolyte, which occupy orbitals of higher energy than the Fermi level, to be transferred to the electrode.

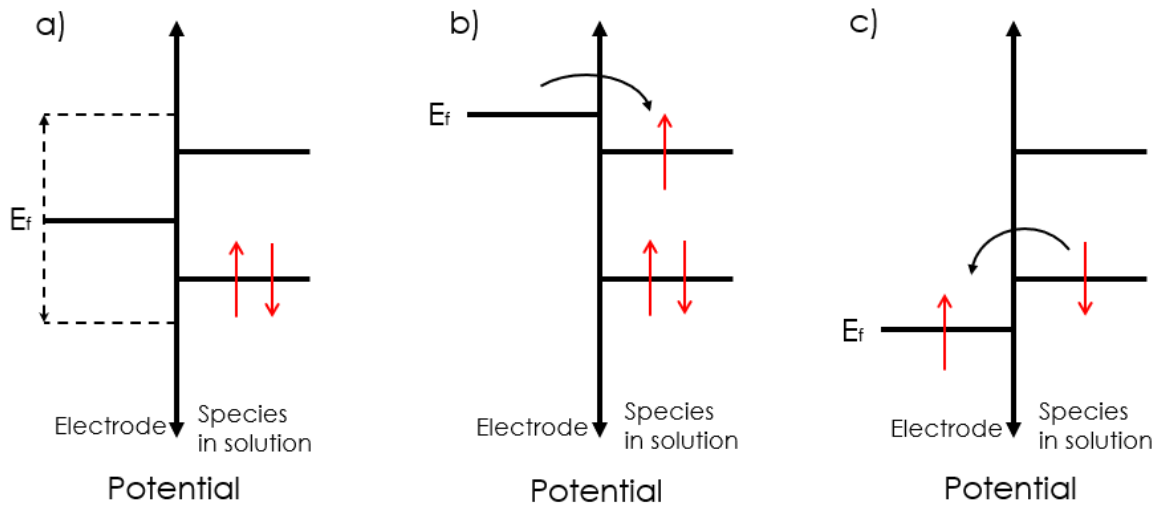

Figure 4. Schematic diagrams illustrating how changing the potential of the electrode affects the system: a) initial state; b) reduction process; c) oxidation process. E_f – Fermi energy. Based on [87].

In general, two types of situations can occur at the electrode/electrolyte interface: the equilibrium state and the non-equilibrium state. In the equilibrium state, no current flows through the interface, and the potential (E_r) is described by the Nernst equation (1.20). In contrast, the non-equilibrium state features a flowing current, which leads to electrode polarization. In this state, the potential

of the electrode depends on the current density and is defined by an overpotential (eq. 1.21). The overpotential represents the additional energy needed to increase the voltage between the two electrodes, allowing the reaction to occur at a given rate, which is determined by the corresponding current density.

$$E_r = E^0 + \frac{RT}{nF} + ln\frac{a_O}{a_R} \tag{1.20}$$

$$\eta = E - E_r \tag{1.21}$$

where:
E^0 – standard potential of the electrode [V];
T – temperature [K];
a_O – activity coefficient of the reactant in oxidized state [-];
a_R - activity coefficient of the reactant in reduced state [-].

This leads to the Tafel equation (1.22), which is fundamental in electrochemical kinetics, since it quantitatively describes the relationship between overpotential and measured current density. To compare the electrochemical performance of different materials, I focus on the Tafel slope (more specifically: the slope of the Tafel curve, (a)), often expressed in mV/dec. A specific value "x" for this parameter indicates that when the overpotential increases by "x", the current density will increase by one order of magnitude. One key difference between chemical and electrochemical systems is that, in electrochemistry, the reaction rate can be adjusted by controlling the potential of one electrode relative to the other. This is achieved by generating an appropriate voltage between them.

$$\eta = a \cdot \log j + b \tag{1.22}$$

Benchmarking parameters are crucial for evaluating electrochemical performance of catalysts, with the Tafel slope and overpotential being two key indicators of performance. When comparing two materials with identical Tafel slope values, the one with the lowest overpotential is considered superior. Conversely, if both materials exhibit the same overpotential, the one with the smaller Tafel slope is preferred. Furthermore, a specific tool, the Butler-Volmer equation (1.23), a generalization of which is the Tafel relationship, provides further insight into these processes. This equation was initially developed by the German scientist Volmer in the 20th century, and its validity was later confirmed by Butler and Erdey-Gruz. It consists of two main terms: a positive term associated with the oxidation reaction and a negative term related to the reduction reaction. For sufficiently high or low overpotential values, this equation can be simplified to the Tafel equation. The graphical representation of the Butler-Volmer equation (1.23) is shown in Figure 5:

$$j = j_0 \cdot \left\{\frac{C_R}{C_R^*}\exp\left[\frac{\beta nF\eta}{RT}\right] - \frac{C_0}{C_0^*}\exp\left[-\frac{(1-\beta)nF\eta}{RT}\right]\right\} \tag{1.23}$$

where:
C_i (electrode surface concentration) – concentration of electroactive species (depolarizers) in reduced and oxidized states on the electrode surface [-];
C_i^* (bulk concentration) – concentration of electroactive species (depolarizers) in the electrolyte volume (bulk) [-];
R – Gas constant, which relates to the energy of the system (8.3143 [kJ/kmol·K]);
β (symmetry factor) – a parameter that describes the symmetry of the energy barrier for the electrochemical reaction [-].

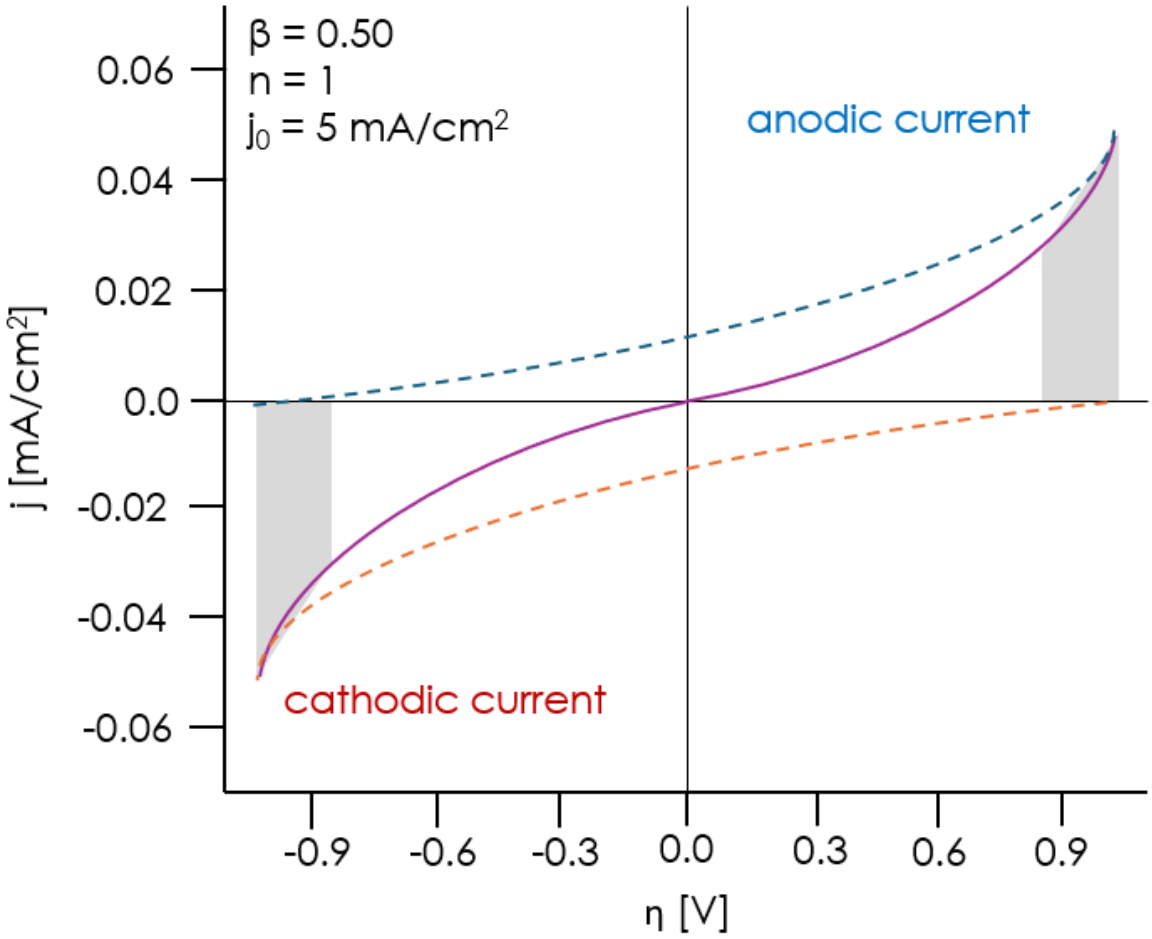

Figure 5.Graphical representation of the Butler-Volmer equation for a one-electron reaction.

The symmetry factor describes the contributions of both cathodic and anodic currents, which, like the exchange current density, depend on the specific reaction occurring on the electrode/catalyst surface. When comparing two electrode materials, the one with higher j_0 values is considered superior in terms of catalytic performance. While equation (1.23) can determine many crucial parameters for simple electrode reactions, real systems often exhibit more complex behavior. This complexity is one of the reasons why the Tafel equation remains the most popular method for extracting information about electrochemical systems.

1.4.1. Benchmarking materials using electrochemical methods

Several electrochemical methods can be classified based on the voltammetric techniques or the apparatus used, such as stripping voltammetry and polarography. The differences between these techniques arise from the measurement setups, accuracy, and the mathematical models employed to interpret electrochemical data. In cyclic voltammetry (CV), the technique predominantly used in this work, the way the electrode potential is applied is a defining characteristic. In linear sweep voltammetry (LSV), the electrode potential is varied linearly from a lower potential (E_1) to a higher potential (E_2), or vice versa. When the potential is increased to more positive values ($E_1 \rightarrow E_2$), oxidation

reactions dominate, and this is referred to as an anodic scan. Conversely, when the potential is decreased ($E_2 \rightarrow E_1$), reduction reactions take place, which is called a cathodic scan. A cyclic voltammogram, which involves both anodic and cathodic scans, can provide valuable information about the reversibility of the electrochemical reaction. This reversibility is closely related to the charge-transfer kinetics, which, in turn, depend on the nature of the electrode/catalyst material.

Figure 6a shows typical voltammograms (also called cyclic voltammograms). The x-axis in the cyclic voltammetry plot represents the electrode potential (E), while the y-axis corresponds to the current response, usually shown as current density. Two standard conventions are commonly used to present CV data, as illustrated in Figure 6b and Figure 6c. In this study, all measurements follow the IUPAC convention. As depicted in Figure 6, a four key points are marked: the starting potential (E_1), the maximum potential (E_2), and two points corresponding to the maximum ("A") and minimum ("B") current. Beginning from E_1, the current density increases as the potential becomes more positive, reaching point A. This rise is caused by the rapid migration of anions toward the electrode surface, which initially outpaces the diffusion of oxidized species back into the bulk solution. Point A marks the maximum current, representing a dynamic equilibrium between the oxidized and reduced species near the electrode interface. Beyond point A, as the potential continues to increase, the current density begins to decline. This decrease occurs because a diffusion layer enriched in oxidized species builds up near the surface, which slows further anion migration. In this region, the current becomes diffusion-limited, governed by how fast the oxidized species can move away from the electrode. At the upper potential limit (E_2), the scan direction is reversed, initiating the cathodic (reverse) scan. During this phase, the current from reduction reactions grows as species at the electrode surface are reduced. The resulting cathodic curve from E_2 back to E_1 generally mirrors the anodic path, though now the limiting processes involve the migration and diffusion of cations. The maximum reduction current occurs at point B [88].

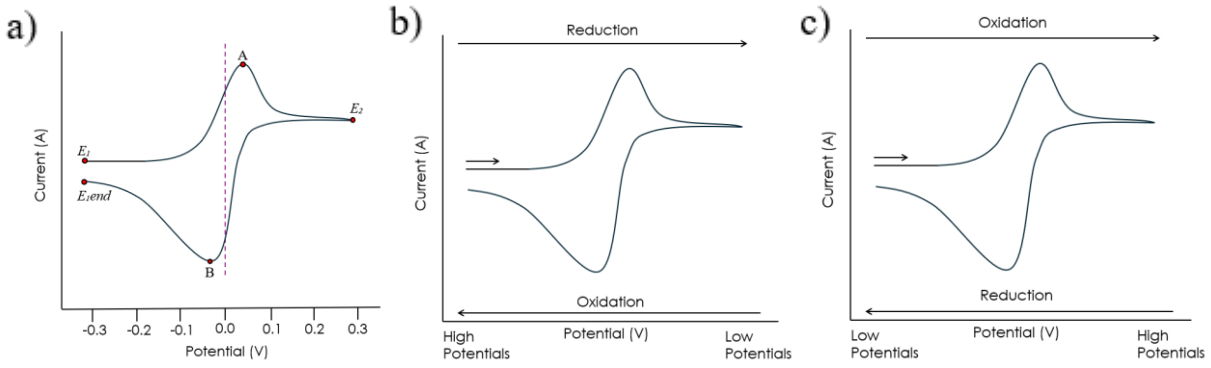

Figure 6. a) An example of typical voltammogram with key points; b) US convention; c) IUPAC convention [88].

There are several key parameters in cyclic voltammetry, one of which is the scan rate – the rate at which the electrode potential changes. The scan rate directly influences the size of the diffusion layer. As the scan rate increases, the time available for electroactive molecules to form a sufficiently large diffusion layer decreases, leading to higher current densities in the recorded voltammogram. This leads

to another important parameter, the electrochemically active surface area (ECSA), which is crucial when comparing the electrochemical performance of different electrode materials. The current can be normalized in two main ways: one is based on the geometric surface area, often referred to as the geometric current density (j_{GEO}) or to electrochemical area ECSA (j_{ECSA}). The former is the simpler approach, as it only considers the macroscopic surface area of the electrode. However, this method has limitations because it does not account for key surface features such as the material's microstructure, roughness, or the presence of impurities, contaminants, pores, pits, or channels. These factors can create additional active sites [89,90] on the electrode surface, which are crucial in electrochemical reactions. In general chemistry, an active site can also refer to the specific part of a molecule involved in acid-base interactions. According to Brønsted-Lowry theory, an acid is a substance that donates a proton (H^+), and a base is a substance that accepts a proton. In this context, the 'active site' refers to the specific part of the molecule that directly participates in donating or accepting protons during the reaction [91].

To better understand the influence of surface features on electrochemical measurements, the concept of electrochemically active surface area was introduced. Determining the ECSA requires more effort than simple surface area measurements and typically involves techniques such as stripping methods, voltammetry or electrochemical impedance spectroscopy (EIS) [92–94]. The first method involves measuring the deposition of atoms or molecules (e.g., Cu, O_2, or H_2) on the electrode surface. However, the results from this technique can vary significantly, with differences of up to 200 [%] [95]. The second method, based on voltammetry, involves analyzing the current-potential ($j - E$) curve in the region where non-Faradic currents are observed (i.e., currents not associated with redox reactions). Specifically, the double-layer capacitance (C_{dl}) is analyzed (eq. 1.24), which is related to the ECSA through the equation (1.25). In practice, ECSA is determined by performing cyclic voltammetry measurements at progressively increasing scan rates within an experimentally defined potential range. This yields the double-layer capacitance values, which are then divided by the specific capacitance (C_s), a value determined experimentally and taken from literature. The typical range for C_s is 0.015 to 0.110 mF/cm^2 in H_2SO_4 and 0.022 to 0.130 mF/cm^2 in KOH for transition metal-based compounds [96,97].

$$C_{dl} = I\left(\frac{dE}{dt}\right)^{-1} \tag{1.24}$$

$$ECSA = \frac{C_{dl}}{C_s} \tag{1.25}$$

where:
dE/dT – scan rate.

This method, despite its frequent use in literature, is not without flaws. One of the main issues is the lack of standardized value for the C_s used in literature. The most accepted value, 0.035 mF/cm^2 [96–101], was calculated by McCrory et al. [97] from the average specific capacitance of various materials in different concentrations of H_2SO_4. However, this value is not universally normalized, which can lead to discrepancies in ECSA measurements across different studies, depending on the choice of C_s values.

Beyond the specific capacitance value, several other factors can affect the accuracy of ECSA calculations. These include the grain size distribution, catalyst loading, the method of applying the catalytic layer (especially in the case of thin film-based electrodes), the degree of amorphization, and the nature of the material (mono- vs. polycrystalline form) [54,66,102,103]. For example, varying the platinum catalyst loading on a rotating disk electrode from 13 ng/cm^2 to 197 ng/cm^2 (illustrated by the blue lines in Figure 7) can lead to a nearly threefold increase in overpotential. Further increases in catalyst loading (as shown by the red lines in Figure 7 for commercial electrodes) result in additional decreases in overpotential [104]. As demonstrated, ECSA measurements can be difficult to compare across different studies, due to numerous variables. However, efforts are underway to develop a more uniform and reliable methodology for determining ECSA in electrochemical measurements [96,97,105,106]. An additional tool to normalize the ECSA value with respect to the geometric area of the measured material is the roughness factor (RF), shown in equation 1.26 [96,107–109]:

$$RF = \frac{ECSA}{A} \tag{1.26}$$

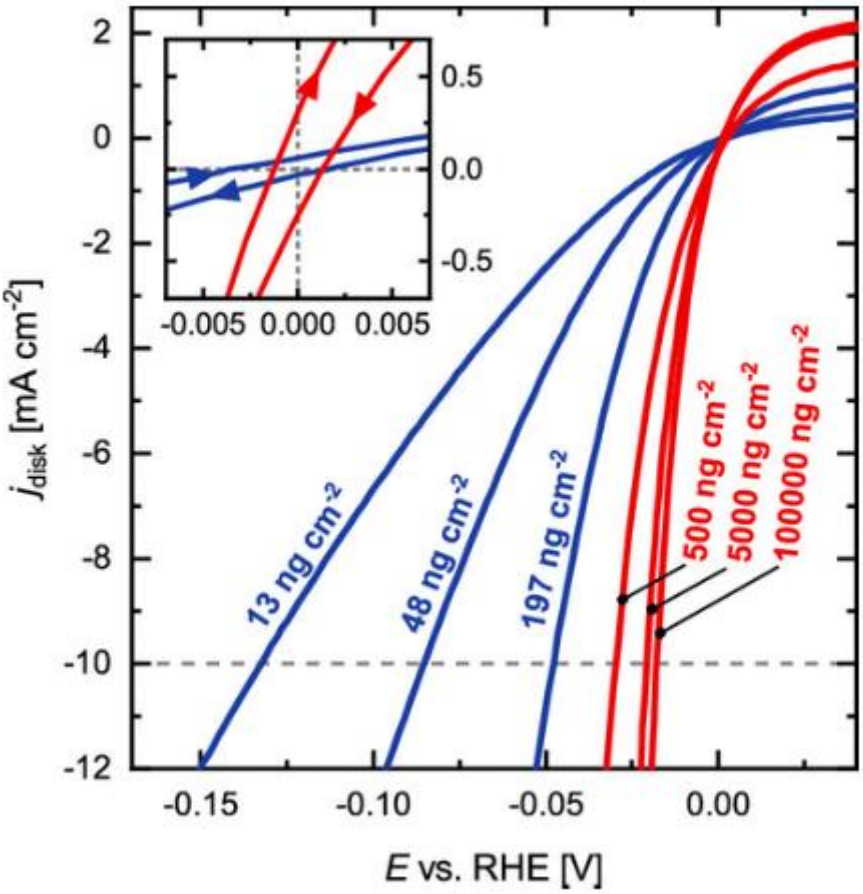

Figure 7. Differences between cathodic sweeps of HER cyclic voltammograms for a different set of Pt loading [104].

Typically, cyclic voltammetry is performed in the three-electrode system in acidic (PEM) or alkaline (AEM) media, for example 0.5 M H_2SO_4 and 1.0 M KOH solutions, respectively, as shown in Figure 8a. This system consists of three electrodes:

- WE (Working Electrode): The working electrode is made of the material being measured. To minimize the influence of electronic components (e.g. leads) on the current-potential (I-E) response, the material of interest can be mounted in a dedicated holder. A key requirement is that only one surface of the material is exposed to the electrolyte, while the remaining surfaces and connecting wire are properly insulated.
- REF (Reference Electrode): The reference electrode provides a stable reference potential that should remain constant during the experiment. Commonly employed reference electrodes in CV are the silver/silver chloride (Ag/AgCl) electrode and the saturated calomel electrode (SCE).
- AUX (Auxiliary or Counter Electrode): The auxiliary electrode completes the circuit and allows the current to flow between the WE and itself, providing a constant current to maintain potential difference between WE and REF. The auxiliary electrode is typically made from catalytically active inert material, such as Pt or Pt-black. Additionally, the surface area of AUX should be made large enough with respect to WE to make sure that AUX is not the current-limiting factor.

The equivalent circuit of the three-electrode system for CV measurements is shown in Figure 8b. All electrodes are connected to a potentiostat, which in turn is connected to a computer or other signal recording device. Current flows only between the WE and AUX, while the potential is measured relative to the REF, whose potential remains fixed. The result of this setup is the current-voltage (I-V) characteristic of the working electrode.

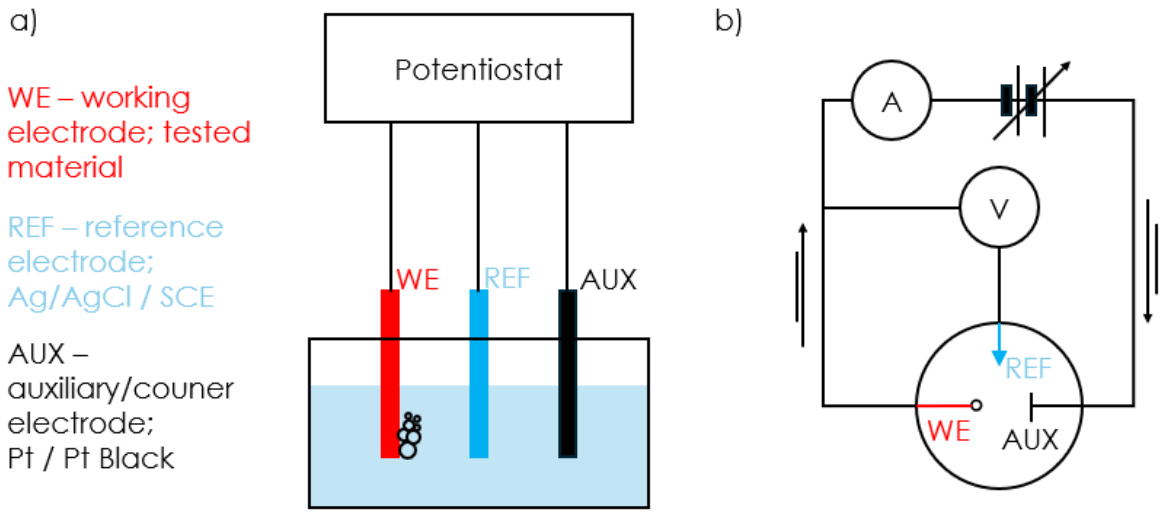

Figure 8. a) Schematic diagram of the test cell for electrochemical measurements; b) equivalent circuit of three-electrode measurement cell.

To summarize electrocatalytic measurements, there are a few key points to consider. First, the tests are usually conducted in a three-electrode system in the electrolyte solution, where the current flowing through the WE is measured. Second, several benchmark parameters are used to describe the obtained results. These include: η_j (mV) – the overpotential at a specific current density; j_η (mA/cm^2) – the current density at a specific overpotential; and a (mV/dec) – the Tafel slope. By comparing these three parameters and normalizing them to either the electrochemical active surface area (j_{ECSA}) or the geometric area (j_{geo}), valuable information about the electrocatalytic efficiency of the material can be obtained. However, as noted earlier, there are some challenges with this testing approach. A standardized and fully reproducible method to obtain these results, particularly when normalizing to j_{ECSA}, is lacking. Therefore, a more insightful interpretation by the investigator is often needed to properly compare the obtained values, for example by utilizing methods such as Electrochemical Impedance Spectroscopy (EIS).

EIS is a technique widely used in electrochemistry to understand how various chemical systems function and how they respond to alternating electric currents. The more complex a material is (e.g., having multiple layers or changing over time), the more resistance can vary depending on the frequency of the current passing through it, allowing for deconvolution of the overall material response into time-scale-dependent phenomena. In practice, EIS involves applying an alternating current signal at different frequencies to a material and measuring how the material responds. From this data, conclusions can be drawn about how the material behaves, such as its efficiency in storing energy, its electrochemical properties, or how quickly chemical processes occur within it.

To conduct EIS, a time-varying current signal is applied to the material under test. This current is modulated in a sinusoidal (wave-like) manner. Impedance testing then involves measuring the material's resistance in response to this current at various frequencies. The material may react differently depending on the frequency of the signal. By analyzing the changing impedance, insights into the material's structure and properties can be gained.

In electrochemical systems, EIS allows for quantitative separation of various resistive and capacitive components of the electrode–electrolyte interface. The resulting impedance spectrum is typically presented as a Nyquist plot or a Bode plot and analyzed by fitting an equivalent electrical circuit model composed of discrete elements. A typical equivalent circuit includes the uncompensated solution resistance R_u, which reflects the ionic resistance of the electrolyte and wiring; the charge transfer resistance R_{CT}, associated with electron transfer across the electrode–electrolyte interface; and the double-layer capacitance C_{dl}, representing the non-Faradaic charge accumulation at the interface. In porous or inhomogeneous electrodes, a constant phase element (CPE) is often used instead of a pure capacitor to model non-ideal capacitive behavior [110,111]

The high-frequency region (typically above 10^4 Hz) is dominated by R_u, while the mid-frequency region (10–10^4 Hz) provides information about R_{CT} and C_{dl}. The low-frequency region (0.01–10 Hz)

can indicate diffusion-limited processes, often modeled using a Warburg impedance element (W). From EIS fitting, one can extract precise values of R_{CT}, which correlate inversely with the electrocatalytic activity: a lower R_{CT} typically indicates more efficient charge transfer at the electrode surface. Moreover, C_{dl}, obtained in the non-Faradaic potential range, can be used to estimate the ECSA, as described earlier. In electrochemistry, EIS can also be used to obtain the ECSA (from C_{dl}) values of the tested material [112–114].

1.5. HER kinetics

Going forward, my work will primarily focus on HER, as hydrogen production is my main area of interest. However, OER will be briefly addressed where relevant. To fully understand the mechanisms and performance of the hydrogen evolution reaction process, a few main factors have to be discussed.

Kinetics of the reaction strongly depend on the catalyst material, which manifests in the overpotential needed for a reaction to begin [115]. For hydrogen evolution, the reversible thermodynamic potential is 0 V, while for the OER, it is 1.23 V [116]. The overpotential is measured at a desired current density and does not account for any iR drop correction (which refers to the adjustment of the measured electrode potential to account for the voltage drop caused by the solution resistance (R) and the current (I), ensuring an accurate representation of the actual electrode potential.). This relationship can be described by the following equations: (1.15 and 1.16) [38,117]:

(HER) $$\eta_{HER} = E_{RHE} - 0 \text{ [V]} \quad (1.15)$$

(OER) $$\eta_{OER} = E_{RHE} - 1.23 \text{ [V]} \quad (1.16)$$

E_{RHE} - the electrochemical potential of the reversible hydrogen electrode [118,119].

In the literature, a reference overpotential value is often used to evaluate the performance of HER and OER electrode materials at a current density of 10 mA/cm^2. This current density corresponds to the expected performance of a solar-to-fuel conversion device equivalent to illumination of 1 sun [97,120]. However, this is merely a convention; in practice, the reaction can be evaluated at any current density, especially since, from an application perspective, the relevant current densities are significantly higher. While comparing materials based on this parameter is valuable, it is essential to approach it with caution. The overpotential is indeed a critical metric, but other factors, such as pH, exchange current densities, and the ECSA or geometric area of the sample, significantly influence overpotential values.

Two important catalytic benchmarks parameters in HER also include the Tafel slope and the exchange current density. The slope of the linear portion of the Tafel plot reflects the relationship between η and the current density (j) and can be described by a specific equation (1.17) [115,121]:

$$\frac{dlog(j)}{d\eta} = \frac{2.3 \cdot RT}{\alpha z F} \quad (1.17)$$

where:
j – current density [mA/cm^2];
η – overpotential [V]
α – transfer coefficient [-]
z – number of transferred electrons [-] – 4 for OER and 2 for HER

The lowest Tafel slope values indicate that a given increase in current density requires a smaller overpotential, suggesting a faster reaction rate. Typically, LSVs obtained at low scan rates yield Tafel slopes with minimal experimental inaccuracies. The j_0 is derived from the extrapolation of the linear fit, intersecting at the point where the equilibrium potential (zero potential) of the electrocatalytic process meets the corresponding current density on a logarithmic scale. This means that the exchange current

density is directly correlated with the onset overpotential in the HER. It is crucial not to compare Tafel slopes and exchange current densities separately among samples, as different materials can exhibit similar Tafel slope values but significantly different j_0 values [38,115,121].

The stability of materials used for HER electrodes is a crucial feature for commercial applications [38]. There are two primary methods for assessing the stability of a material in electrochemical applications: chronoamperometry (constant exposure to a fixed potential) and chronopotentiometry (constant exposure to a fixed current density). It is widely accepted that a material is considered stable if its properties remain intact (i.e., it does not degrade) over a period of 12 hours at a stable potential or through more than 5,000 cyclic voltammetry cycles [121–125].

The environment in which electrochemical measurements are performed significantly affects the properties of the electrocatalysts. In acidic conditions, the kinetics of the HER increase due to the increased concentration of H^+ ions, which facilitates easier adsorption on the catalyst's active sites. For platinum (Pt) [122], the benchmark electrocatalyst, the current densities during the HER decrease by up to three orders of magnitude as the pH of the electrolyte solutions increases from 0 to 13 [33,45,76,126,127].

In addition to the features discussed above, the microstructure of the electrode/catalyst materials plays a crucial role in electrochemical tests, impacting the kinetics of the reactions. Factors such as the amorphization of materials, their form (monocrystalline or polycrystalline), and the alignment and exposure of individual crystallographic planes significantly affect current densities during voltammetric techniques [128]. Figure 9a illustrates the cyclic voltammogram of a polycrystalline platinum electrode, highlighting the underpotential hydrogen phenomenon (H_{UPD}), where adsorption occurs before the hydrogen evolution reaction. The voltammogram displays three local maxima in current densities corresponding to specific crystallographic facets: adsorption on the (111) surface occurs at the highest potentials, followed by the (100) plane, and finally the (110) plane [66]. Figure 9b presents the Arrhenius dependence of exchange current densities for platinum monocrystals with individual facets exposed on the surface. The linear relationship of the recorded current densities aligns with the results obtained for the polycrystalline material. From the slopes of the respective lines, the activation energy can be determined, showing the trend: Pt(110) < Pt(100) < Pt(111) [103].

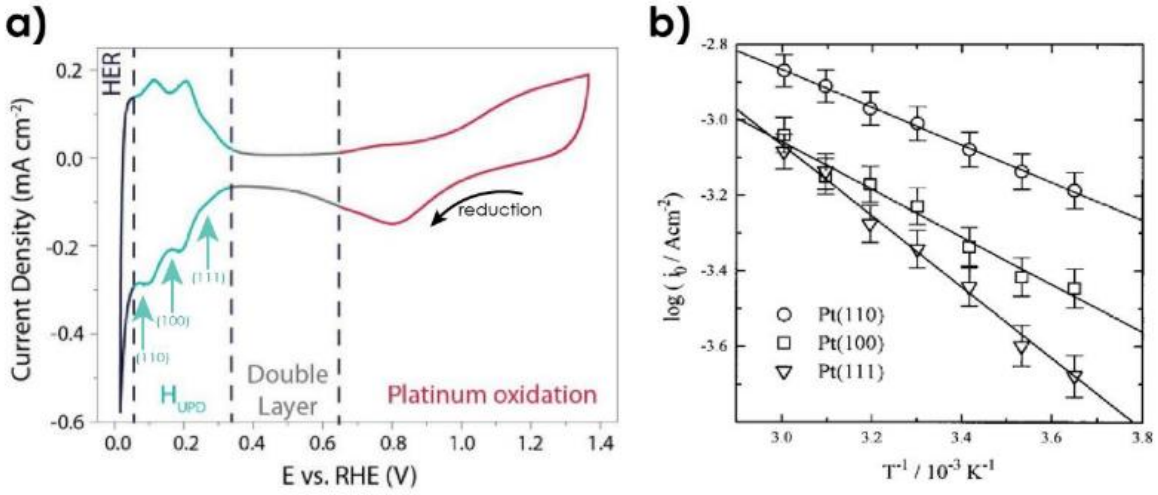

Figure 9. a) Cyclic voltammogram for polycrystalline Pt recorded at 50 [mV/s] in 0.5 M H_2SO_4 [66]; b) Arrhenius plots of exchange current densities j_0 as a function of temperature for Pt monocrystals [103].

1.6. HER catalysts

In this chapter, state-of-the-art materials based on platinum and other noble metals will be discussed, as well as those based on non-noble metals. Additionally, the concept of "volcano plots" and other catalytic activity descriptors, and how they can be used to identify the most promising materials for HER will be described.

1.6.1. Platinum-based materials

The ideal material for electrocatalytic applications should exhibit the following key characteristics: high current densities during operation, high activity at possibly low overpotentials (the point at which the reaction begins), low Tafel slope values (which indicate the kinetic speed of the reaction, particularly for the H_2/O_2 evolution), and good stability under operating conditions. Based on these criteria, Pt is considered the optimal material for HER, while RuO_2 and IrO_2 are preferred for OER. Pt, for example, shows a Tafel slope around 29–30 mV/dec, a near-zero overpotential for hydrogen production, and high current densities in acidic electrolytes [65,67,104,122,129–135]. Due to the high cost, limited availability, challenges with recycling, and dependence on geopolitical factors, extensive research is being conducted to reduce or completely replace platinum in electrocatalytic processes with alternative materials. Several approaches have been explored to achieve this goal. These include, notably, the nanostructuring of platinum [50,53,133–140], attempts to synthesize platinum-based composite materials [65,129,135,140–142], the development of heterostructures containing platinum [134,139], and the creation of platinum alloys with both precious and non-precious metals, or its compounds [53,137]. These efforts have led to the emergence of low-platinum-content electrocatalysts (LPCEs). Additionally, attempts have been made to modify platinum electrodes themselves by depositing thin platinum layers onto conductive surfaces in various shapes [50,52,122,133,136,138,140], tailoring the platinum active sites by controlling defect concentrations [52,141,143], or modifying the platinum surface with a layer of other metals, active carbon, or graphene oxide [141,144]. A general summary of platinum-based materials is shown in Table 5, but samples presented are only selected examples. More materials and summaries can be found in references: [50,53,145].

While platinum is highly advantageous in hydrogen evolution reactions, there are several notable disadvantages. The most significant is its limited availability, which makes it expensive. Another issue is the tendency of platinum nanoparticles to agglomerate into larger clusters. This agglomeration reduces the number of active sites on the electrode, thereby compromising both the efficiency and stability of the catalyst [146].

Table 5. A summary of chosen electrode materials for platinum-based HER applications [50,53,145].

Catalyst	Overpotential [mV]	Current density [mA/cm^2]	Tafel slope [mV/dec]	Electrolyte	Ref
Pt/C	32	10	30	0.5 M H_2SO_4	65,147
Pt@DNA	26 (45)	10 (20)	30	0.5 M H_2SO_4	122
Pt-SnS_2	117	10	69	0.5 M H_2SO_4	125
[7%Pt-3%Ni]/[C-Si (1:1)]	161	10	136	0.5 M H_2SO_4	129
Pt nanopowder	~50*	10	~29	0.5 M H_2SO_4	130
Pt	30	10	n.d.	1 M KOH	131
Pt	10-90*	10	29	1 M HCl	132
Pt/5% TiO_2/C	~50	20	n.d.	0.5 M H_2SO_4	133
Pt/10% TiO_2/C	~50	20	n.d.	0.5 M H_2SO_4	
Pt/20% TiO_2/C	~45	20	n.d.	0.5 M H_2SO_4	
Pt/Mo-90	10	10	41	0.5 M H_2SO_4	135
0.5Pt/Ni-SP	250	10	115	1 M NaOH	136
0.75Pt/Ni-SP	125	10	32	1 M NaOH	
1Pt/Ni-SP	76	10	28.3	1 M NaOH	
2Pt/Ni-SP	42	10	28.5	1 M NaOH	
5Pt/Ni-SP	32	10	29.1	1 M NaOH	
Pt(73%)/Pd/Co	"Negligible" ~50*	10	<30	0.5 M H_2SO_4	53
Pt-Ni NTAs	23	10	38	1 M KOH	137
Pt-Ni NWAs	43	10	40	1 M KOH	
SSMPF/Pt	70	10	76.8	1 M KOH	50
Pt@NOMC-700	91	10	88	0.5 M H_2SO_4	138
Pt@NOMC-A	7	10	43	0.5 M H_2SO_4	
PtC_{60}	24.3	10	41.9	1 M KOH	139
P/TC'(HR)	44	10	118	0.5 M H_2SO_4	140
PyPOP-Pt@G	~175*	100	37	1 M H_2SO_4	141
Pt/Rh_2O_3-CN_x	26.7	10	35	1 M KOH	142
PtW_6O_{24}/C	22	10	29.8	0.5 M H_2SO_4	143
Au-Pt	n.d.	n.d.	33	0.5 M H_2SO_4	144
Pt disc	125	4.4-1.8	36-68	0.5 M H_2SO_4	148
Mo_2C@C@Pt	27	10	28	0.5 M H_2SO_4	149
PtCoFe@Cn	45	40	46	0.5 M H_2SO_4	150
Pt/GNs	25	10	33	0.5 M H_2SO_4	151
Pt/Mo_2C	144	50	35	0.5 M H_2SO_4	152
PtO_x/TiO_2	-	-	40	0.5 M H_2SO_4	153
Pd/Cu-Pt	23	10	25	0.5 M H_2SO_4	154
Pt/WO_3/CC	42	10	101	0.5 M H_2SO_4	155

n.d. – no data
** - value taken from figure*

1.6.2. Non-noble-metal-based materials

In response to the disadvantages of platinum and the need for more cost-effective, widely available, and highly efficient materials for hydrogen evolution applications, efforts have been made to develop suitable alternatives (the same remains true for alternatives to Ru- and Ir-based materials for OER). In 2018, Peng Yo et al. briefly described the history of new, non-noble materials for HER uses, the scheme of which is shown in Figure 10 [156]. Various research groups have focused on materials such as alloys, chalcogenides (described in more detail in chapters 1.6 and 1.7), carbides, nitrides, borides, phosphides, metal-free catalysts, and composites in general. Another approach to addressing this challenge is the use of structured materials with a large surface area. Examples of non-noble elements used in HER and materials from both approaches are presented in Figure 11 and Table 6.

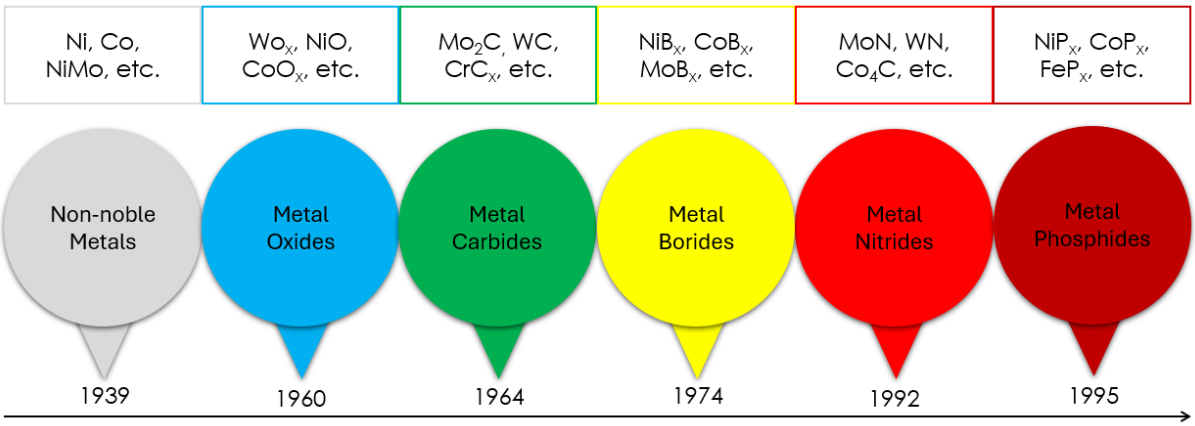

Figure 10. Timeline of development of the first reported non-noble metal-based HER electrocatalysts [156].

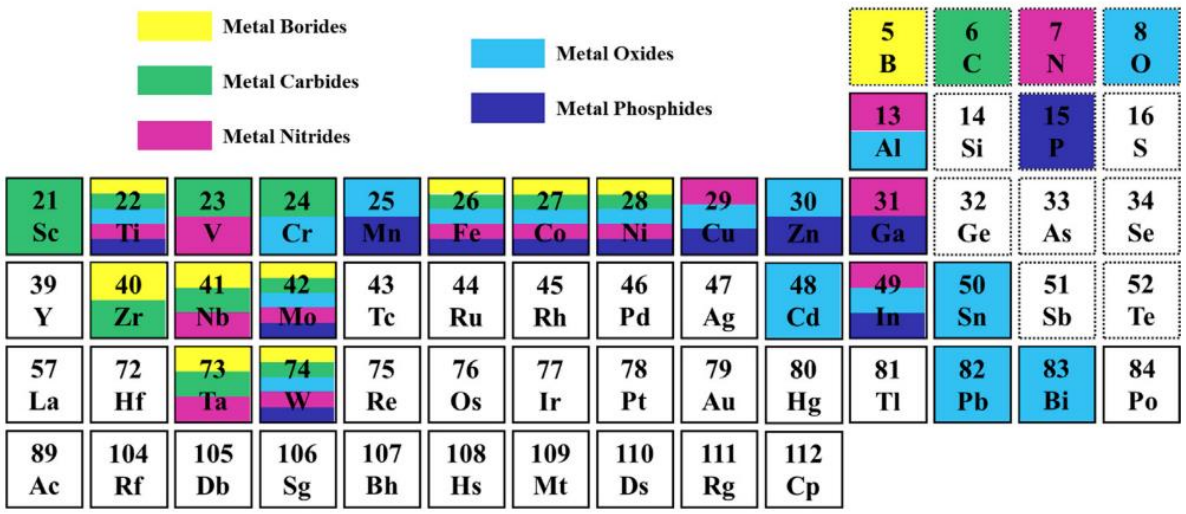

Figure 11. The elements involved in preparing non-noble-metal based HER electrocatalysts in the periodic table [156].

Table 6. Summary of the chosen materials for HER application. Platinum-based and chalcogenide materials are not included [33,40,156,157].

Catalyst	Overpotential [mV]	Current density [mA/cm^2]	Tafel slope [mV/dec]	Electrolyte	Ref
Alloys					
Mo_2C on carbon nanotubes	152	10	n.d.	H_2-saturated 0.1 M $HClO_4$	[158]
SCEINs on SWNTs[A]	77	10	40	0.5 M H_2SO_4	[159]
Ni-Mo electrodeposided on steel foil	185	300	112	6 M KOH, 80 °C	[160]
CoNi/ultrathin graphene layer	142	10	105	0.1 M H_2SO_4	[161]
Carbides					
WC nanoparticles	125	10	84	0.5 M H_2SO_4	[162]
Mo_2C/graphene hybrid	~175	10		0.5 M H_2SO_4	[163]
β-Mo_2C nanoparticles on carbon black	~150	33.5	58	0.5 M H_2SO_4	[158]
Nanoporous Mo_2C nanowires	125	10	53	0.5 M H_2SO_4	[164]
Nitrides					
$NiMoN_x$/C	~225	5	35.9	0.1 M $HClO_4$	[165]
MoN nanosheets	300	38.5	90	0.5 M H_2SO_4	[166]
γ-Mo_2N	381	10	108	0.5 M H_2SO_4	[167]
Fe-WCN	220	10	47	0.1 M H_2SO_4	[168]
Borides					
MoB	210	10	59	0.1 M KOH	[169]
MoB_2	193	10	n.d.	0.5 M H_2SO_4	[147]
$Cr_{0.4}Mo_{0.6}B_2$	225	10	60	0.5 M H_2SO_4	[147]
MoAlB	301	10	68	0.5 M H_2SO_4	[170]

Catalyst	Overpotential [mV]	Current density [mA/cm^2]	Tafel slope [mV/dec]	Electrolyte	Ref
Phosphides					
Ni_2P	130 (180)	20 (100)	n.d.	0.5 M H_2SO_4	[171]
FeP	~250*	10	67	0.5 M H_2SO_4	[172]
CoP nanoparticles	85	20	50	0.5 M H_2SO_4	[173]
WP/Ti	120	20	n.d.	0.5 M H_2SO_4	[174]
Metal free catalysts					
C_3N_4@NG		10	240	0.5 M H_2SO_4	[175]
C_3N_4 nanorods on FTO		0.8	300		[176]
N and P co-doped graphene		10	420	0.5 M H_2SO_4	[177]
Oxidized carbon nanotubes		10	220	0.5 M H_2SO_4	[178]
Composites					
Ni/NiO/$CoSe_2$ nanocomposite	120	20	39	0.5 M H_2SO_4	[179]
Other					
Ni-Mo nanopowder	80	20		0.5 M H_2SO_4	[180]
MoCat	96	10	37	0.5 M H_2SO_4	[181]

*value read from the graph.

d.n.a. – does not achieved

n.d. – no data

[A] – single-shell carbon-encapsulated iron nanoparticles decorated on single-walled carbon nanotubes

As shown in Table 6, there are many different approaches to developing high-performance materials for HER applications. This is a positive trend, as it opens up numerous avenues for discovering materials that could potentially replace platinum-based catalysts in this field. However, several issues need to be addressed. First, there is a lack of a standardized testing protocol between studies. This inconsistency can complicate the comparison of materials because factors such as different current densities or the choice of electrolyte often vary across publications. Second, the widespread use of nanostructuring in materials is common. While nanostructuring can improve HER performance by increasing the active surface area and number of active sites, the process itself can be expensive and challenging to perform. Moreover, nanomaterials must be anchored to a conductive substrate, which requires additional procedure steps and may influence the electrochemical properties of the materials being tested. Finally, there is significant variability in the reported values for overpotentials and current densities, even within the same series of materials. While most of the materials tested show promising potential, none are without drawbacks. Issues such as high material cost, limited stability, or suboptimal electrochemical performance remain. These challenges create significant obstacles in the development and testing of new materials for electrochemical applications.

1.6.3. Binding energy approach – volcano plots

In 1977, Trasatti developed a clear relationship between $\log(j_o)$ data and the hydrogen chemisorption energies, which takes the form of "volcano plots". A schematic example of this plot can be seen in Figure 12a. These volcano plots represent the hydrogen binding energy (HBE), which describes the strength of the metal-hydrogen bond (Me-H). According to Sabatier's law, the ideal catalyst should bind hydrogen strongly enough to absorb protons from the solution (in the HER, this corresponds to the Volmer step), but not too strongly, as excessive binding negatively impacts the desorption kinetics, which are crucial for hydrogen gas formation during the Heyrovsky and Tafel steps [182]. It is important to note that volcano plots for HER in acidic media are better established than in alkaline media for several reasons. First, there are fewer comparative data available for alkaline media, and the existing data tend to be less reliable and older [67]. Another key point, described by Petrii and Tserlina [183], is the difference in the rate-controlling step for HER in acidic versus alkaline solutions, which is related to the different identities of the proton source: H^+ in acidic media and H_2O in alkaline media. A good example of this is Ni, where the rate-controlling step differs between acidic and alkaline solutions, with the j_0 values in acidic solutions typically being an order of magnitude or higher [184,185].

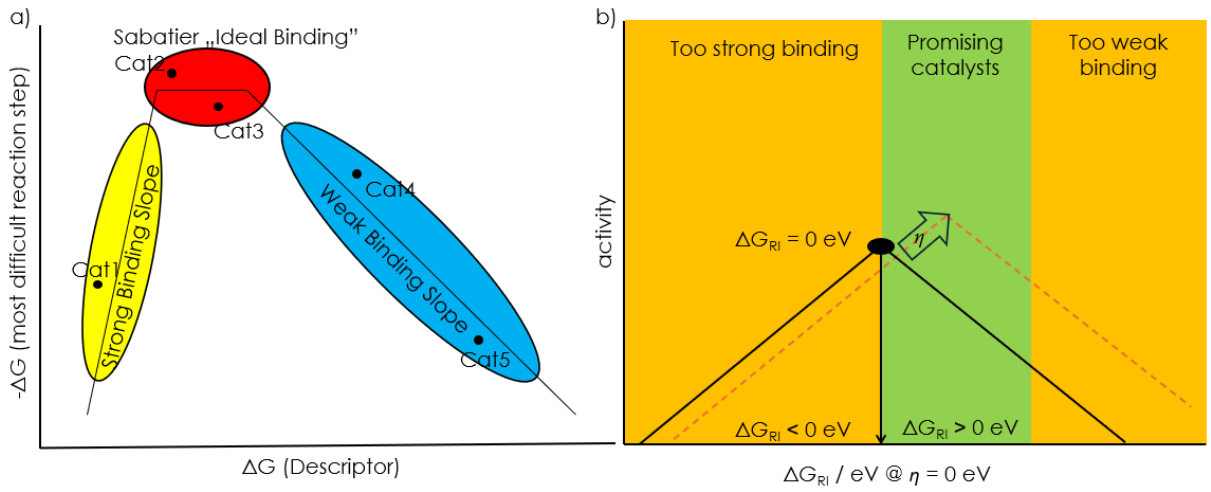

Figure 12. a) Schematic volcano plot[186]*; b) a prototypical volcano diagram* [187].

In Figure 12a, the schematic volcano plot is shown. The descriptor value is plotted along the x-axis, while the y-axis represents the negative of the free energy change of the most difficult reaction step in the catalytic cycle (or another measure of catalytic activity). Catalysts with the best thermodynamic/kinetic profiles (Cat2 and Cat3) are located near the volcano plateau (or peak) in the Sabatier ideal binding region (red). Catalysts with overly strong catalyst−substrate interactions (Cat1) appear along the left "strong-binding" slope (yellow), while catalysts with overly weak catalyst−substrate interactions (Cat4 and Cat5) are found along the right "weak-binding" slope (blue) [186]. In Figure 12b, a prototypical volcano diagram is shown, where activity is plotted as a function of the free-binding energy of the reaction intermediate at zero overpotential. While the common assumption, based on thermodynamic considerations, is that the apex of the volcano occurs at thermoneutral bonding (equation), the inclusion of the applied overpotential and kinetics shifts the volcano's peak toward weak bonding (equation) with increasing driving force [187].

Figure 13 shows HBE values for the HER activity for pure metals. Platinum is the state-of-the-art material for these applications, with rhodium and iridium showing slightly lower activity. However, both Rh and Ir are expensive and rare materials. Although volcano plots are commonly used to evaluate electrocatalysis performance, they are not a perfect or definitive solution in this context. Various factors, such as different approaches, measurement techniques, or even the experience level of those who perform electrochemical measurements, can lead to discrepancies in the obtained results [188].

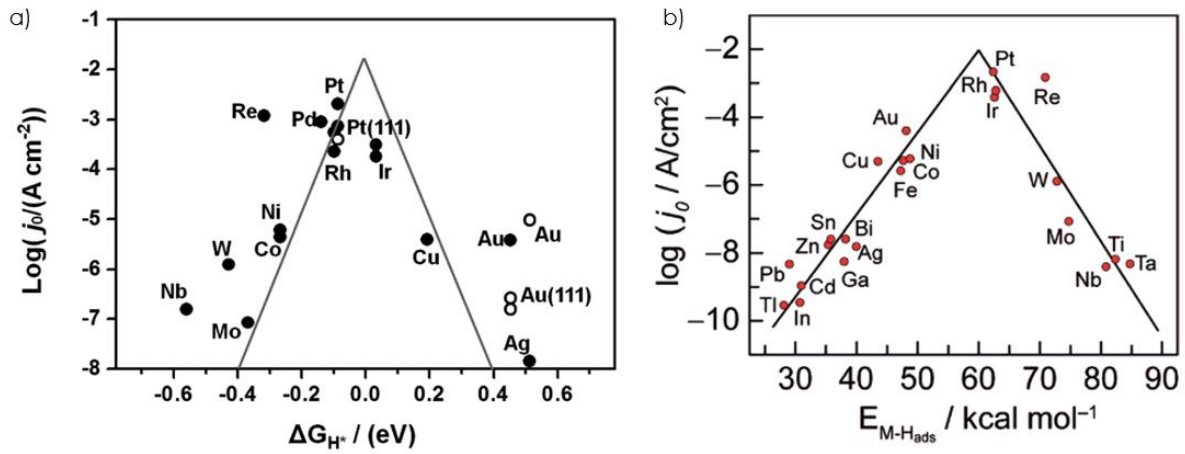

Figure 13. Examples of „volcano" plots: a) as a function of DFT-calculated Gibbs free energy (ΔG_H) of absorbed atomic hydrogen on pure metals [33]; b) for HER on metal electrodes in acidic media [40].*

A clear example of the limitations of volcano plots is molybdenum disulfide (MoS_2), which demonstrates excellent HER activity despite having low HBE values. This discrepancy is due to MoS_2's role in the pure hydrogen oxidation reaction. The high electrocatalytic efficiency of these materials is due to their active centers, which are formed at sulfur vacancies [189]. As a result, volcano plots should not be taken as an absolute determinant of HER activity. Instead, they should be considered as a useful starting point for simple HER scenarios or for *ab initio* calculations in more complex systems.

1.6.4. Other descriptors of catalytic activity

In addition to the previously discussed factors that influence HER electrocatalytic activity – such as electronic conductivity, surface morphology, and the overpotential at a given current density – other catalytic activity descriptors can also be considered. Although these were not the primary focus of my work, they supported the interpretation of the results. The corresponding calculations were carried out by other members of the research team, namely Associate Professor, DSc Andrzej Mikuła and PhD candidate Miłosz Kożusznik. These additional descriptors include:

- The Gibbs free energy of hydrogen adsorption (ΔG_{H^*}), which represents the change in free energy upon adsorption of hydrogen atoms on the catalyst surface. This parameter is closely related to the d-band center (d_{bc})or p-band (p_{bc}) center, defined as the average energy of the d- or p-electron states relative to the Fermi level. The position of the d_{bc} center influences the binding strength between the metal surface and adsorbed species, and therefore directly affects ΔG_{H^*} [72].
- The electronic density of states (DOS) at the Fermi level, which directly determines the availability of electrons for participation in the hydrogen evolution reaction [72,190].

Most of these descriptors are directly related to the electronic structure of the catalyst and should therefore be regarded as complementary tools to the volcano plot approach and the Sabatier principle, rather than as independent evaluation criteria. It is important to note that for each material, whether differing in structure or elemental composition within one or both sublattices, the relationship between a given descriptor, the material, and its HER activity must be re-evaluated individually. This makes the process inherently complex and time-consuming.

1.7. Transition metal chalcogenides

Transition metal chalcogenides (TMChs, TM – transition metal, Ch – chalcogenide) are among the most promising materials to replace state-of-the-art catalysts in electrocatalytic water splitting processes [191]. They contain chalcogen elements (sulfides, selenides, and tellurides) as anions [192], combined with transition metals (d-block elements) as cations [193]. TMChs have been intensively investigated for hydrogen technologies due to their affordability and unique properties. One notable feature of these compounds is their wide variety of chemical compositions and crystal structures, allowing doping and forming solid solutions over the wide range of elemental solubility, and thus tunable electronic properties. A popular structure of TMChs is $TMCh_2$, which is characterized by the presence of edge and surface defect sites, disulfide linkages [194], and excellent electroconductivity (allowing fast charge-transfer capabilities). Within this structure, several well-performing examples can be found, such as MoS_2 exhibiting high HER activity with an η_{10} of 175 mV and a Tafel slope of 42 mV/dec [195], or FeS_2, which achieves an η_{10} of 96 mV and a Tafel slope of 78 mV/dec [196].

Other examples include $CuFeS_2$ (chalcopyrite) structure in nanosheet (NS) form, which achieves an η_{10} of 88.7 mV and a Tafel slope of 22.3 mV/dec [197]; or nickel sulfides (NiS, Ni_3S_2), which, anchored to graphene or gold surfaces, exhibit promising properties (Table 7) [64,198]. Other noteworthy TMCh structures include pentlandite (described in detail in 1.6.1. and 1.7) and spinel-like (TM_3Ch_4) structures, which are tested as bifunctional catalysts (HER and OER).

TMCh structures can also be synthesized using a variety of methods, including epitaxial growth, wet-chemical synthesis, and solid-state synthesis. Different techniques can influence material properties such as nanostructurization, defects, amorphization, and phase changes [199]. Furthermore, TMChs are highly susceptible to morphological changes, as demonstrated in Co_3Se_4 and $CoNi_2Se_4$ [200,201], exhibiting good stability in both acidic and alkaline media [200]. Numerous studies have also shown that combinations of oxides and transition-metal chalcogenides (e.g. heterostructures, composites, and layers) can further enhance catalytical activity [75]. A good example of improvement of HER performance could be the MoS_2 material, which achieves η_{10} of 485 mV and Tafel slope equal to 203 mV/dec [202], whereas MoS_2 nanoparticles and MoS_2/RGO (MoS_2 nanoparticles grown on reduced glassy carbon) show η_{10} of 406 mV and ~175 mV and Tafel slopes of 95 and 41 mV/dec, respectively [203,204]. Doping MoS_2 by transition metals also affects the HER activity, yielding η_{10} of 490 mV, 350 mV and 302 mV and Tafel slopes of 94 mV/dec, 69 mV/dec and 66 mV/dec for Fe-, Co- and Ni-doped MoS_2, respectively [204].

However, despite their satisfactory electrochemical activity, TMChs often exhibit electrical conductivity significantly lower than that of noble metal-based catalysts. This limitation necessitates additional surface engineering. Furthermore, the long-term stability of TMChs remains a challenge in HER- and OER-oriented applications. A summary of various TMCh electrocatalysts for OER and HER applications is presented in Table 7.

Table 7. The examples of transition metal chalcogenides investigated as HER/OER catalysts.

Catalyst	Overpotential [mV]	Current density [mA/cm^2]	Tafel slope [mV/dec]	Electrolyte	Ref
$TMCh_2$					
$CoSe_2$ nanobelts	140	20	48	0.5 M H_2SO_4	179
MoS_2/Mo foil	175	10	41	0.5 M H_2SO_4	195
MoS_2/RGO	150	10	41	0.5 M H_2SO_4	203
MoS_2 NP (nano-particles)	d.n.a.	10	94	0.5 M H_2SO_4	203
FeS_2/NF	96	10	78	0.1 M KOH	196
NiS_2/GCE	219	10	157	1.0 M KOH	205
TM_6Ch_8					
Mo_6S_8	321	10	74	0.5 M H_2SO_4	194
Mo_6Se_8	432	10	81	0.5 M H_2SO_4	
Mo_6Te_8	634	10	77	0.5 M H_2SO_4	
TM_3Ch_4					
Co_3Se_4/CF	1880	10	n.d.	1 M KOH	200
$(Co,Fe,Ni)_3Se_4$(*)	180	50	150	0.5 M H_2SO_4	206
$CoNi_2Se_4$/CP	220	10	72	1 M KOH	201
$CuCo_2S_4$/CP	69	10	55	1 M KOH	207
$NiCo_2S_4$/NF	80	10	59	1 M KOH	208
$(Ni_{0.62}Co_{0.35}Fe_{0.03})_3Se_4$/CC	87	10	123	1 M KOH	209
TM_9Ch_8(**)					
Co_9S_8	364	50	148	0.5 M H_2SO_4	68
$Ni_{4.5}Co_{4.5}S_8$	336	10	101	0.5 M H_2SO_4	73
$Fe_{4.5}Co_{4.5}S_8$	327	10	155	0.5 M H_2SO_4	73
$Fe_{4.5}Ni_{4.5}S_8$ (rock)(*)	630	10	n.d.	0.5 M H_2SO_4	130
$Fe_{4.5}Ni_{4.5}S_8$(*)	280	10	72	0.5 M H_2SO_4	130
$Fe_2Co_4Ni_3S_8$	378	50	108	0.5 M H_2SO_4	68
$Fe_{4.5}Ni_{4.5}S_4Se_4$(*)	300	10	120	0.5 M H_2SO_4	210
Other					
$CuFeS_2$ NSs	88.7	10	22.3	0.5 M H_2SO_4	197
CuS NSs	375	10	74	0.5 M H_2SO_4	197

(*) – bulk material
(**) – described in more detail in chapter 1.7.1
n.d. – no data
d.n.a. – do not achived

Analyzing Table 7, several key observations can be made. First, TMCh structures are highly susceptible to changes in their composition and structure, which significantly impact their electrochemical properties. Currently, the primary methods for creating TMCh electrodes involve nanostructurization and anchoring a thin layer onto a conductive substrate. However, these processes are costly, complicated, and can alter the material's properties. Konkena *et al*. demonstrated that nature itself offers potential solutions to bypass these processes and yield materials with electrochemical properties comparable to platinum and other noble metals [130]. For instance, hydrogenases, natural enzymes, are capable of efficiently reducing protons to H_2 molecules due to the presence of bimetallic Ni-S and Fe-S active sites [211]. A catalyst that incorporates these properties – and more – is pentlandite.

1.7.1. Pentlandite

Pentlandite naturally occurs as an orthomagmatic ore in various locations on Earth. The $(Fe,Ni)_9S_8$ form of pentlandite was first reported in Sudbury in 1960, while a cobalt-rich variant, approaching Co_9S_8 in composition, was first identified in Finland in 1959. Pentlandite was first synthesized in 1929 by Newhous as a Fe-Ni-S material with the TM_9S_8 structure. In 1936, Lindqvist et al. characterized it as a face-centered cubic $(Fe,Ni)_9S_8$ system, which is isostructural with synthetic Co_9S_8. In 1961, Knop and Ibrahim conducted experimental studies on the pentlandite solid solution in the Fe-Ni-Co-S system (Fe_9S_8-Ni_9S_8-Co_9S_8) [212]. Later, in 1976, Kojonen investigated the complete solid solution series between the two "end members": $(Fe,Ni)_9S_8$ and Co_9S_8, showing that the production of trimetallic pentlandite is possible, although further research is required – opening the door to future studies, such as this thesis (but it's worth mention that in monometallic form only pure Co_9S_8 can exist) [213]. In pentlandite cubic $Fm\bar{3}m$ structure, the transition metal cations occupy both tetrahedral and octahedral positions (Figure 14)., which contributes to the mineral's unique properties, including electrochemical applications, such as HER and OER.

The presence of two or more cations in the structure contributes to its close-to-metallic properties, e.g., metallic conductivity, a high concentration of charge carriers, and fast charge-transfer abilities [73,130,210,214–217]. Additionally, pentlandite shows intriguing metal-metal bonding [214,218], as well as active sites formed by Fe-, Ni-, or Co-S hydrogenase-like bridges [130,210,211,216]. The elemental composition of pentlandites is highly flexible, and targeted synthesis with precise stoichiometric control can be achieved through various methods, such as hydrothermal, mechanochemical, or solid state approaches [68,219–224]. These synthetic methods allow for the creation of materials with diverse multi-element structures, including $(Fe,Ni)_9S_8$, $(Co,Fe)_9S_8$, $(Co,Ni)_9S_8$, $(Fe,Ni)_9S_{8-x}Se_x$ (x = 1-6), and even three-metal compositions like $Co_{9-x-y}Fe_xNi_yS_8$ (x,y = 1-7) [68,73,77,210,225]. Such flexibility in the elemental composition enables tailoring either the cationic or anionic sublattice, thereby enhancing the electrochemical properties. None of the above methods, however, allow obtaining this material in the form of nanopowder.

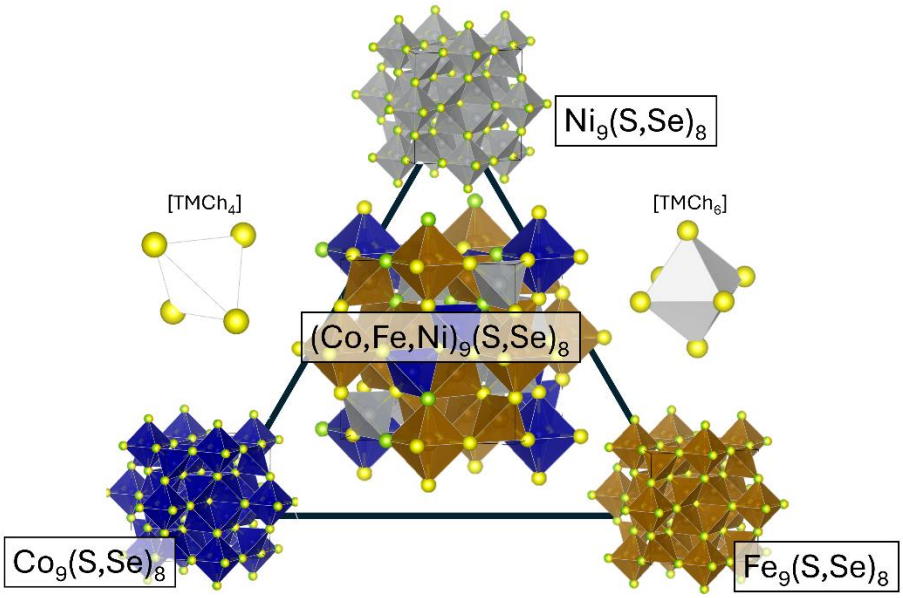

Figure 14. Pentlandite structure with Gibbs triangle depicting possible cation occupancies with Co, Fe, and Ni polyhedra depicted in blue, brown and gray, respectively[226].

Both natural pentlandite ore and synthesized pentlandite materials exhibit high long-term durability under corrosive conditions. Additionally, these materials undergo an "activation process", which involves the creation of additional active sites at sulfur vacancies on the surface, a phenomenon known as "*sulfur depletion"* mechanism (Figure 15a/b) [217]. This effect has been confirmed in subsequent studies using in situ techniques under operando HER conditions, such as nuclear resonant inelastic X-ray scattering. By analyzing the obtained vibrational density of states (VDOS) spectra and comparing them with theoretical spectra calculated via density functional theory (DFT), Zegkinoglou *et al.* pinpointed sulfur vacancies as the primary cause of the activation process. They calculated the energy required to replace a sulfur vacancy with a hydrogen atom or to add hydrogen at an interstitial position in both the presence and absence of sulfur vacancy. Their calculations clearly demonstrated that, in the case of preexisting sulfur vacancies, the hydrogen atom prefers to occupy a sulfur site at Wyckoff position 8c rather than an interstitial position, leading to a substitutional configuration [74]. Theoretical insights into the activation process were also provided by Lu *et al.*, who concluded that, during electrolysis, three main crystallographic planes are exposed. These planes differ in their catalytic properties, primarily due to a varying number of active sites (Figure 15c) [72]. It is worth mentioning that Smialkowski *et al.* observed that during the activation process the pentlandite material (in this case: $Fe_xCo_{9-x}S_8$ and $Ni_yCo_{9-y}S_8$ (x = y = 0–4.5) systems) may decompose into foreign phases such as troilite (FeS), linnaeite (Co_3S_4), or heazlewoodite (Ni_3S_2) [73].

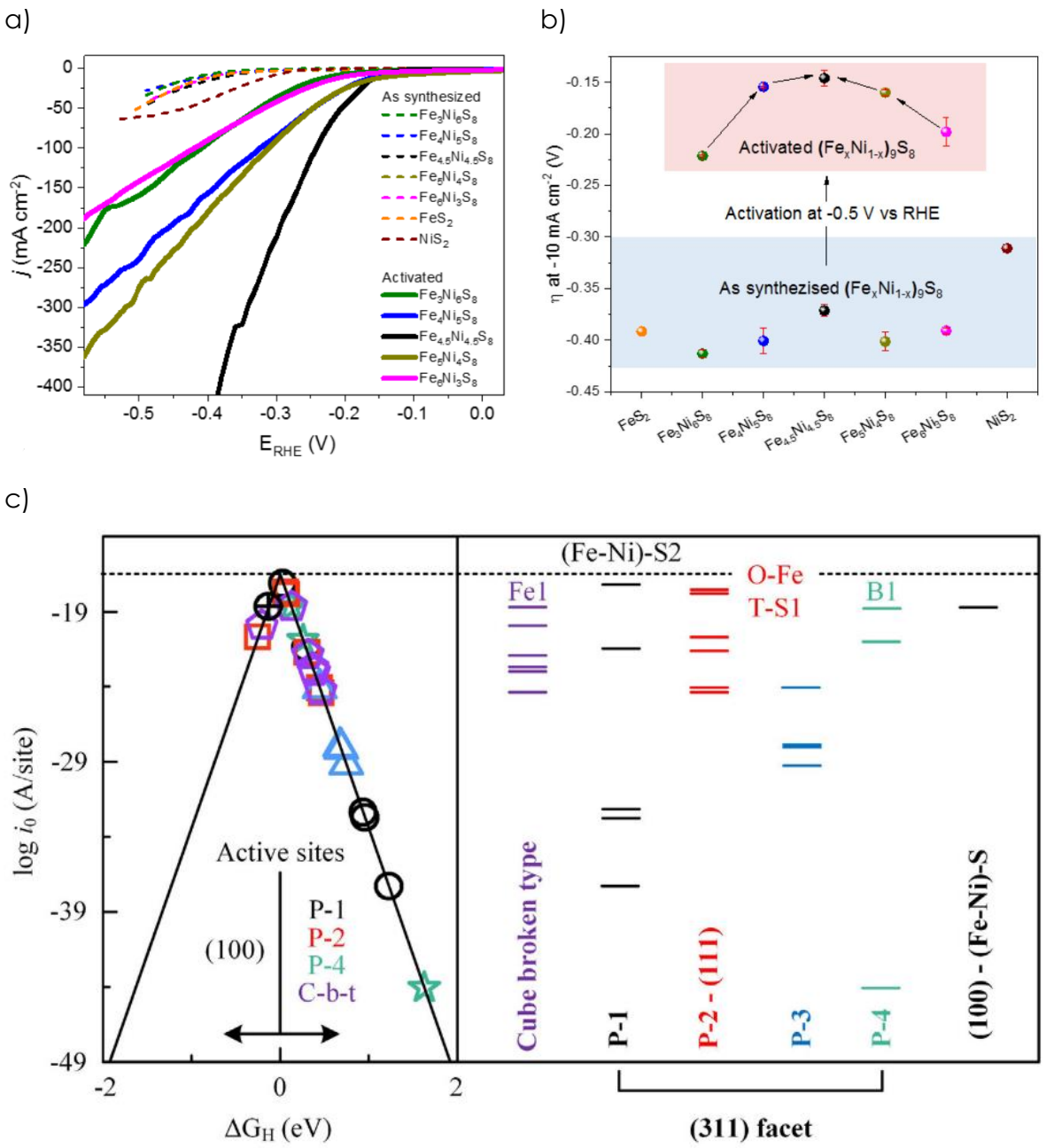

Figure 15. a) LSV curves of "as-synthesized" and activated pentlandite material in the example of $(Fe,Ni)_9S_8$ system; b) catalytic activity of pentlandite-structured materials described as overpotential to achieve current density of -10 mA/cm^2 [217]; c) volcano plot for different planes exposed at the surface of pentlandites during the electrolysis process [72].

Additionally, Konkena et al. showed that both natural pentlandite ("rock") and as-synthesized *rock-like* materials exhibit outstanding electrochemical properties even as a bulk materials with significantly reduced surface area compared to typically applied nanopowders. Specifically, the synthesized bulk $Fe_{4.5}Ni_{4.5}S_8$ material demonstrated HER activity with an overpotential of η_{10} = 280 mV (normalized to the geometric area) and a Tafel slope of 72 mV (Figure 16) [130]. This finding is significant for several reasons. First, the material in solid form can serve as both an electrode and a catalyst simultaneously, avoiding the expensive and complex processes typically used for nanostructuring and anchoring a catalysts to conductive substrates, thus simplifying surface shaping. Moreover, pentlandites in bulk form can be successfully synthesized through relatively simple and scalable methods, such as direct

reactions between the constituent elements. This makes them an attractive electrocatalytic solution from both technological and commercial perspectives [130,217].

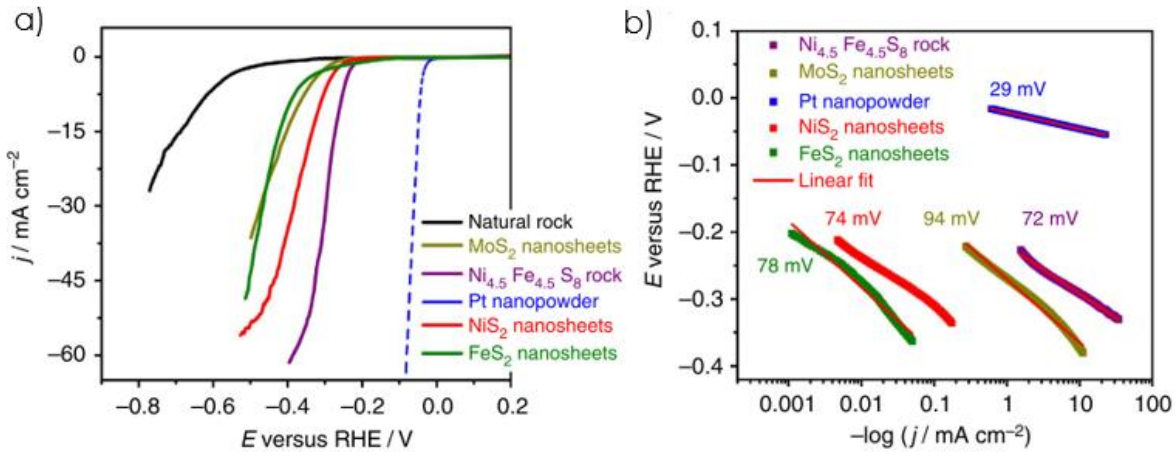

Figure 16. a) LSV curves of the catalysts recorded at a sweep rate of 5 [mV/s] in 0.5 M H_2SO_4 (normalized to geometric area); b) Tafel plots derived from voltammograms at a sweep rate of 1 mV/s [130].

1.8. Methods of materials modification

Electrocatalytic performance of the materials can be improved in a few ways: by modifying chemical composition, microstructure, and experimental setup. These strategies are well-founded and could lead to significant improvements in the electrocatalytic performance of pentlandites. It is important to consider that these modifications could interact with each other, and therefore a systematic optimization approach is necessary. Understanding the effects of element doping, composition variations, morphology changes, and electrolyte conditions on the material's electrochemical properties can guide the design of more efficient pentlandite-based electrocatalysts for various energy conversion applications. These include:

- changing the form of the material;
- multicomponent approach, adding new elements to material, creating a four- or even five-elements structures;
- modification of the chemical and phase compositions of the material;
- modification of surface morphology;
- temperature dependence;
- change in the pH of the electrolyte.

1.8.1. Form of the material

As mentioned earlier, most research on the electrochemical activity of materials in the field of HER involves anchoring nano- or micro-sized powders onto conductive substrates. The fabrication of electrodes from powder materials is inherently associated with one of two main challenges, depending on the method used. The first approach involves depositing powders onto a conductive substrate — for example, using the drop-casting technique. In this method, the powder is first dispersed into an ink, which is then applied onto the electrode surface. However, this often results in an uneven distribution of the material, leading to inconsistencies in the ECSA and an increased contribution from the underlying substrate to the overall electrochemical response [227,228]. The second approach involves physical vapor deposition (PVD) techniques, such as magnetron sputtering. While these methods offer better control over film uniformity and adhesion, not all materials can be deposited using sputtering, especially those with complex compositions, low thermal stability, or generating highly corrosive plasma environment (like S-rich compounds). Furthermore, the process requires the fabrication of a sputtering target, which adds further complexity and cost to the overall electrode preparation [229,230].

However, Konkena *et al.* (2016) demonstrated that natural pentlandite, extracted directly from rock, exhibits significant electrocatalytic properties. They synthesized the $Fe_{4.5}Ni_{4.5}S_8$ material in bulk form (by milling the obtained material and compacting it by free compression) and tested its HER activity, showing that the material does not need to be obtained as nanometric powder to exhibit notable electrochemical performance [130]. This approach simplifies the electrode fabrication process and ensures that the electrochemical response originates solely from the investigated material, rather than

from the underlying substrate. Since then, only a few studies have investigated the electrochemical activity of bulk pentlandites. Table 8 summarizes the HER activity of pentlandites in bulk forms, along with various compositions.

As shown in Figure 16, the bulk-synthesized $Fe_{4.5}Ni_{4.5}S_8$ achieves better overpotential values (η_{10} = ~280 mV) compared to MoS_2, NiS_2, or FeS_2 nanosheets, which have overpotentials of approximately 400 mV, 350 mV, and 420 mV, respectively. This discovery marks a significant shift in the study of electrochemistry for hydrogen generation reactions, highlighting the potential of bulk materials over their nano counterparts. Puring et al. also provided a brief tutorial on how to synthesize and prepare bulk non-noble electrodes for electrocatalytic applications [231].

Of course, the synthesized pentlandite material exhibits electrochemical properties significantly more favorable than those of the natural rock, because of impurities and undesirable compounds on the surface of the latter. Additionally, later studies have shown that, for bulk materials, the ratios of coexisting metal particles play a more critical role in determining electrochemical properties than factors such as topology or electrical conductivity [130,217]. This led to a new wave of research focused on multi-component approaches and tailoring the composition of pentlandites.

1.8.2. Multicomponent approach

Increasing the number of components in a material system can lead to behaviors that follow the mixing rule, where the resultant properties of the final material reflect a weighted average of the properties of the end-member compounds. However, it may also trigger a "cocktail effect," where unexpected properties emerge, sometimes contradicting the behavior of the individual elements (synergistic effect). Examples of such effects include: progressive microstructure refinement, which can enhance strain-hardening capacity, making the material more resistant to deformation under stress; improved tensile ductility without a loss of high strength, leading to a material that is both strong and more stretchable; interstitial strengthening, which alters dislocation behavior and can result in increased material strength [232]. In addition, such deviations from the mixing rule can significantly affect local atomic ordering and electronic structure, which in turn may strongly influence the catalytic performance of the material.

High-entropy compounds were originally defined in the context of High Entropy Alloys (HEAs) by Yeh and coworkers in 2004 [233], and later expanded to include other material classes such as carbides, oxides, nitrides, and chalcogenides. HEAs are composed of five or more elements, with each element typically making up between 5% and 35% of the alloy, although proportions lower than 5% are also possible. These materials are of significant interest because they tend to form far fewer phases than the Gibbs phase rule would predict. HEAs are characterized by four main features: a) high entropy effect: This effect increases the potential for solid solution formation at high temperatures; b) slow reaction kinetics: HEAs exhibit lower diffusion coefficients compared to conventional alloys, resulting in slower transformation rates; c) severe distortion of the crystal lattice: The large differences in atomic sizes among the alloy components cause significant lattice distortion, influencing the energy and behavior

of defects; d) synergy effect: This refers to the enhancement of properties due to the interactions between the different components of the alloy [233–235]. While the high-entropy concept does not fully apply to the systems investigated in this thesis, it can help explain some of the observed behaviors in multicomponent pentlandites.

In the pentlandite structure, examples of this approach up to beginning of my PhD (2021) include two methods: pentlandite with three metal elements on cationic sublattice [226], or two metal pentlandites with sulfur and selenium on anionic sublattice [210]. The first study [226], published in early 2021 by the research group in which I carried out my PhD, was initially not focused on catalytic properties, although I was directly involved in these investigations. These examples will be described in more detail in chapter 1.8.3, but it is worth mentioning now that this approach does not involve doping, but the formation of solid solutions. There are examples of other structures modified by this doping approach, for example spinel-like material in HER/OER ($(Co_{0.35}Fe_{0.03}Ni_{0.62})_3Se_4$/CC [209]).

1.8.3. Tailoring chemical composition of the materials

This approach involves altering the stoichiometry or the ratio of elements within materials. By optimizing the composition, it is possible to enhance the intrinsic properties, such as electrical conductivity, electronic structure, and catalytic activity. Senthamaraikannan *et al.* described the influence of various amounts of transition metal elements in the TMS and TMSO (oxygen doped transition-metal sulfides) structures on the HER activity, as shown in the volcano plots (Figure 17). Based on these studies, they deduced that the single-metal structures (like FeS, NiS) have the highest stability, but the two-metal materials show a higher HER performance due to preferred Gibbs free energy of proton adsorption (ΔG_{H^*}) in relation to exchange current densities, with the best exhibited by $Ni_{0.25}Fe_{0.75}S$ material [236].

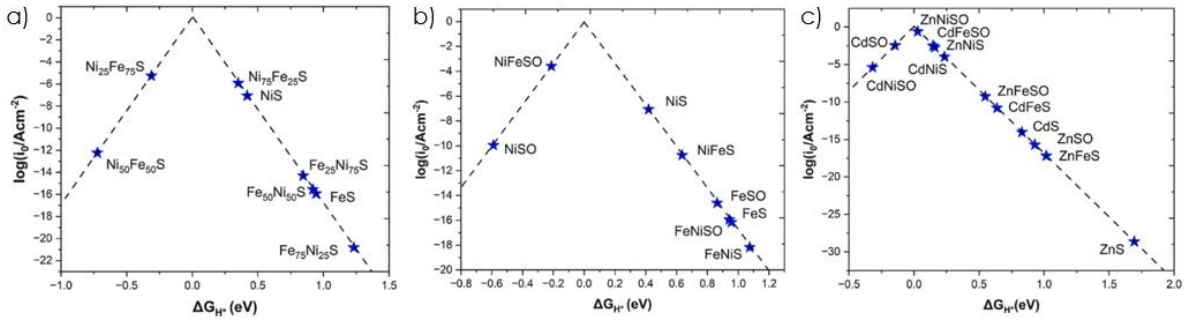

Figure 17. The volcano plots of exchange current density as a function of the adsorption Gibbs free energy for a) TMS materials from the scope of FeS-NiS; b) oxygen doping FeS-NiS system; c) various TMS materials including oxygen doped ones [236].

In the case of pentlandite, three main approaches are commonly used to modify the material's composition: adjusting the Co:Fe, Co:Ni, or Fe:Ni ratios in binary sulfur pentlandites [73,217,222,225]; altering the Co:Fe:Ni ratio in ternary sulfur pentlandites [68,213]; or substituting sulfur with selenium [210].

While Co_9S_8 pentlandite is relatively easy to synthesize, multi-metallic materials are not always stable within the Fe_9S_8-Ni_9S_8 system. Amin *et al.* described that phase-pure $(Fe,Ni)_9S_8$ pentlandite can be obtained only within a limited range of stoichiometries ($2 < Fe < 7$). For higher Fe or Ni content, foreign phases, such as NiS, Ni_3S_2, or FeS, are observed [225].

In the case of mixed metal sulfides $(Fe_xNi_{1-x})_9S_8$ (x = 0–1), the 1:1 Fe:Ni ratio exhibits the highest number of active sites. As the amount of Fe or Ni increases, the number of active sites and HER performance decreases (Figure 18). This behavior is attributed to specific metal-metal interactions (Fe-Ni), which are important for superior electrocatalytic HER activity, akin to hydrogenases. Furthermore, an activation process is notably effective at the equimolar Fe:Ni ratio (Figure 18a; b), due to the highest number of Fe-S-Ni bridges, which are particularly susceptible to activation [217].

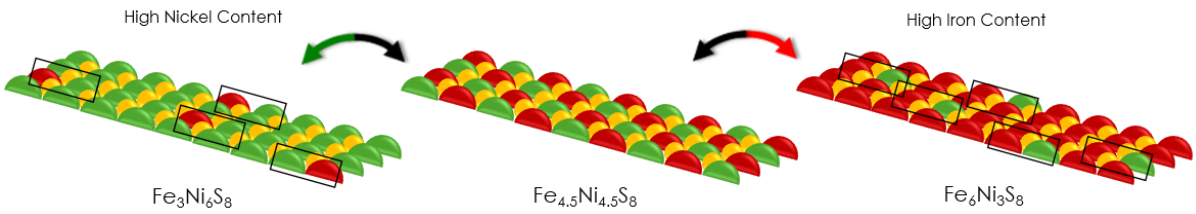

Figure 18. Schematic surface area of $(Fe_xNi_{1-x})_9S_8$ with enriched nickel surface (left) and enriched iron content (right). The pentlandite (middle) serves as an idealized system with a recurring pattern sequence and active centers. Inspired by [217].

Doping monometallic Co_9S_8 pentlandite with Fe or Ni significantly influences HER performance. The formation of bimetallic bridges on sulfur enhances the susceptibility of these materials to *sulfur depletion*, which in turn leads to an increase in ECSA and improved overall electrochemical properties. Fe-rich pentlandites, such as $(Fe,Co)_9S_8$, show a marked increase in ECSA, while simultaneously benefiting from significant activation during electrolysis [73,217]. In contrast, materials with a higher Co content (e.g. $NiCo_8S_8$ or $Ni_3Co_6S_8$) are more prone to deactivation.

Interesting observations arise from the substitution of sulfur by selenium in bimetallic pentlandites $Fe_{4.5}Ni_{4.5}S_8$. This material remains single-phase up to high selenium contents ($Fe_{4.5}Ni_{4.5}S_3Se_5$), decomposing into multiple phases only beyond this point. Additionally, the material with selenium content Se_7 exhibits a reduced overpotential of 172 mV at a current density of 10 mA/cm^2, outperforming even the pure sulfide material (190 mV). This demonstrates the potential for further enhancement of pentlandite-based catalyst performance through modification of the anionic sublattice composition. The incorporation of selenium induces significant changes in interatomic distances and electronic properties at sulfur-deficient sites, which serve as hydrogen adsorption sites in pentlandites. Consequently, modifications of the adsorption properties of pentlandite ultimately govern its HER performance, as reflected in the decreased activity of pentlandites with high selenium content [210].

When modifying the composition of any material structure, it is essential to maintain single-phase purity, as this ensures reliable interpretation and meaningful comparison with other materials. In multiphase systems or those containing, for example, surface precipitates, it is unclear which phase or component

is primarily responsible for the catalytic activity. Moreover, the catalytic effects of different phases may either enhance or suppress each other, making such systems difficult to interpret.

1.8.4. Temperature dependence

Although most scientific research is conducted at room temperature, industrial electrolyzers typically operate at temperatures between 60°C and 90°C. It is well known that elevated temperatures can reduce charge-transfer resistance, facilitate H_2 bubble removal, decrease overpotentials, and generally increase double-layer capacitance [237–240]. Several studies have investigated the influence of temperature on the electrochemical properties of pentlandite materials (Figure 19 and Table 8).

The temperature dependence of the equimolar $(Fe,Ni)_9S_8$ pentlandite clearly shows that increasing the temperature gradually improves the electrochemical performance of the material, as evidenced by reduced overpotentials (Figure 19a) and Tafel slopes (Figure 19b). Piontek *et al.* observed that while electrical conductivity decreases with increasing temperature, the core mechanism of the hydrogen evolution reaction (Volmer-Heyrovsky) remains unchanged (Figure 19b), which is consistent with previous reports [130,217].

Smialkowski *et al.* combined temperature dependence studies with the tailoring of the metal composition on the cationic sublattice of S-based pentlandite. They found that although all materials exhibited decreased overpotential values at higher temperatures, the material tested at room temperature showed significantly greater changes in catalytic activity during testing (Figure 19c). They also observed that the trend of higher activity for Co-deficient compounds persisted, with Ni/Co compounds demonstrating significantly higher activity than Fe/Co compounds (Table 8, 1.7.) [73].

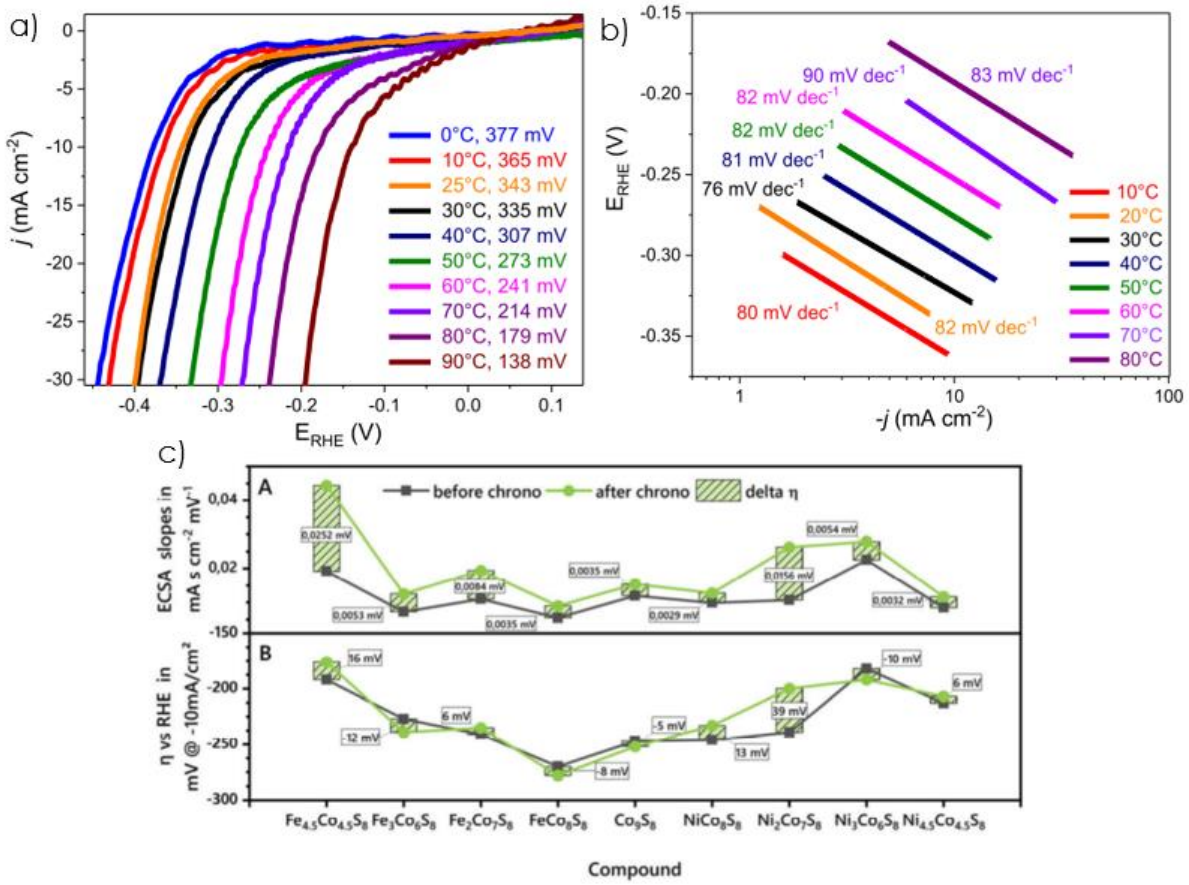

Figure 19. a) LSV of $Fe_{4.5}Ni_{4.5}S_8$ at sweep rate of 5 mV/s in 0.5 M H_2SO_4 at different temperatures; b) Tafel plot derived from linear sweep experiments at sweep rates of 1 mV/s [217]; c) ECSA slopes before (grey) and after (green) chronoamperometry at −400 mV vs. RHE (A) and recorded overpotentials before (grey) and after (green) chronoamperometry (B) with green bar graphs indicating the difference between the respective data points. All values obtained at 75 °C cell temperature [73].

1.8.5. pH dependence

pH significantly influences electrochemical performance. As mentioned above, various materials exhibit electrocatalytic properties across a wide pH range, such as $(NH_4)_2MoS_4$, which functions effectively between pH 0 and 13 [33], and nanometric Mn_3O_4, which operates in neutral pH (7) [241]. However, for platinum (Pt), the resulting current densities during the hydrogen evolution reaction decrease by up to three orders of magnitude when the pH of the electrolyte solution increases from 0 to 13 [127].

Research on the HER performance of pentlandites in different pH ranges is limited. Sanden *et al.* investigated the electrochemical performance of trimetallic pentlandites in a 1 M KOH electrolyte. Each tested material generated a substantial amount of H_2. However, after chronopotentiometry stability testing in alkaline conditions, the *sulfur depletion* process was still observed, highlighting the fact that the sulfur depletion mechanism is also pH independent. While this study was conducted at 75°C, the direct comparison with materials tested in acidic media is limited, the overpotentials and Tafel slopes were less favorable in alkaline media. For example, Co_9S_8 had overpotentials of 302 in acidic and 329 mV in alkaline solution, and Tafel slopes of 145 and 200 mV/dec, respectively. Similarly, $Co_3Fe_3Ni_3S_8$ showed overpotentials of 298 (acidic) and 344 mV (alkaline), and Tafel slopes of 88 and 159 mV/dec, respectively. The hypotheses were proposed in the paper : in an alkaline environment, the increased Tafel slope values are due to the expected contribution of water dissociation at high pH, and the alkaline electrolyte has a corrosive effect on the surface of the working electrode, reducing its efficiency [242].

1.9. Summary of recent pentlandite research

To summarize the discussion from the previous chapters, it can be observed that materials with a pentlandite-type structure for HER applications are typically studied in either powder or as solid-state material forms. However, powders deposited on conductive substrates are used much more frequently. As mentioned earlier, this approach introduces several challenges, such as the complexity of substrate preparation, significant substrate effects, and the fact that the electrode coverage is never exactly the same. Solid-state materials, on the other hand, bypass these issues. Moreover, since they act as both the electrode and the catalyst (solid electrodes), they provide valuable insight into the intrinsic properties of the material. For this reason, Table 8 compiles data specifically for these solid-state materials.

The analysis of the collected results can be divided into two main trends and two additional observations. The first trend concerns the difference between using natural and laboratory-synthesized materials (*First bulk material* section). While natural pentlandite does exhibit electrocatalytic properties, the lab-synthesized material shows significantly more favorable catalytic behavior.

The first major comparative group involves modifications to the cationic sublattice, in both bimetallic and trimetallic systems. For bimetallic systems based on iron and nickel, it is clearly observable that the best catalytic performance is achieved by materials whose structure closely resembles that of naturally occurring pentlandite – specifically $Fe_{4.5}Ni_{4.5}S_8$ (*Fe:Ni ratio* section). A similar trend is seen in systems where cobalt replaces either iron or nickel: materials with near-equimolar compositions again show the most promising activity toward HER (*Co:Ni/Co:Fe content and temperature dependence* section).

In the case of trimetallic pentlandites, mixing and adjusting the metal ratios does not lead to unexpected results. The best electrocatalytic properties are still observed in compositions that are equimolar or close to equimolar, as well as those with slightly increased cobalt content. Nevertheless, their overall performance remains noticeably lower compared to the optimal bimetallic systems (*Trimetallic approach and Co:Fe:Ni ratio in alkaline media* sections). It is worth noting, however, that although the addition of cobalt does not significantly improve HER activity compared to the bimetallic $Fe_{4.5}Ni_{4.5}S_8$ system, it provides enhanced long-term stability. This effect can be attributed to a more homogeneous distribution of cations and the associated charge-compensation mechanism, which reduces local lattice strain and mitigates structural degradation under operating conditions. These results were obtained during the course of my PhD work, and their confirmation will also be presented among my own findings.

The second major comparative group focuses on changes within the anionic sublattice in bimetallic systems, specifically the substitution of sulfur with selenium (*Doping sulfur by selenium* section). The data clearly show that while selenium generally reduces the electrocatalytic activity of these materials, a small amount of selenium substitution (up to a composition of $Fe_{4.5}Ni_{4.5}S_7Se$) can enhance

the performance in solid-state samples. An explanation of this phenomenon can be found in the experimental section dedicated to trimetallic systems.

The final comparative aspect involves testing under elevated temperatures, which overall has a positive effect on the catalytic performance of the materials.

Chapters 1.7 and 1.8 and Table 8 discuss recent research on the electrochemical catalytic performance of various pentlandite materials and approaches to obtain effective HER catalysts. These sections highlight how different methods influence the properties of pentlandite. One key conclusion is that the pentlandite can be used as an HER electrode in bulk form, obtained by free compaction, which simplifies the material preparation process. In addition, bulk materials are the best form for comparing properties because they eliminate the degree of catalyst loading and the number of defects, focusing instead on the intrinsic properties of the materials. Another important finding is that $Fe_{4.5}Co_{4.5}S_8$ demonstrates the best catalytic performance, but multicomponent materials tend to be more stable. The effect is explained by the key role of cobalt, which stabilizes the electronic structure, ensures a uniform distribution of cations, and provides an almost ideal binding strength of hydrogen to Co-Co and Co-Fe active centers. The latter, however, reduces the number of active centers (by blocking the *sulfur depletion* mechanism), which is why the overall properties remain comparable to $Fe_{4.5}Ni_{4.5}S_8$.

The next two conclusions are related to the testing conditions rather than the materials themselves. First, increasing the temperature significantly enhances the HER performance of pentlandites. Second, lower pH values are associated with better electrocatalytic properties in the tested materials. This is due to the expected contribution of water dissociation at high pH and the corrosive effects of the alkaline environment on the electrode surface. Therefore, these two parameters were not systematically investigated in the present work.

Table 8. A summary of past research on pentlandites (in solid form) in case of HER performance.

Catalyst	Overpotential [mV]	Current density [mA/cm^2]	Tafel slope [mV/dec]	Form of electrode	Electrolyte	Temperature [°C]	Ref.
First bulk material							
$Fe_{4.5}Ni_{4.5}S_8$ natural rock	~500	10	n.d.	Rock	0.5 M H_2SO_4	25	[130]
$Fe_{4.5}Ni_{4.5}S_8$ rock	~280		72	Pellet			
Fe:Ni ratio							
$Fe_3Ni_6S_8$	~350[1]	50	n.d.	Pellet	0.5 M H_2SO_4	25	[217]
$Fe_4Ni_5S_8$	~250[1]						
$Fe_{4.5}Ni_{4.5}S_8$	~200[1]						
$Fe_5Ni_4S_8$	~250[1]						
$Fe_6Ni_3S_8$	~350[1]						
Temperature dependence							
$Fe_{4.5}Ni_{4.5}S_8$	377	10	n.d.	Pellet	0.5 M H_2SO_4	0	[217]
$Fe_{4.5}Ni_{4.5}S_8$	365		80			10	
$Fe_{4.5}Ni_{4.5}S_8$	343		82			25	
$Fe_{4.5}Ni_{4.5}S_8$	335		76			30	
$Fe_{4.5}Ni_{4.5}S_8$	307		81			40	

$Fe_{4.5}Ni_{4.5}S_8$	273		82		50	
$Fe_{4.5}Ni_{4.5}S_8$	241		82		60	
$Fe_{4.5}Ni_{4.5}S_8$	214		90		70	
$Fe_{4.5}Ni_{4.5}S_8$	179		83		80	
$Fe_{4.5}Ni_{4.5}S_8$	138		n.d.		90	
Doping sulfur by selenium						
$Fe_{4.5}Ni_{4.5}S_8$	280	10	76	Pellet	0.5 M H_2SO_4 25	210
$Fe_{4.5}Ni_{4.5}S_7Se$	273		120			
$Fe_{4.5}Ni_{4.5}S_6Se_2$	336		130			
$Fe_{4.5}Ni_{4.5}S_5Se_3$	306		143			
$Fe_{4.5}Ni_{4.5}S_4Se_4$	300		120			
$Fe_{4.5}Ni_{4.5}S_3Se_5$	296		150			
Co:Ni/Co:Fe content and temperature dependence						
$Ni_{4.5}Co_{4.5}S_8$	336	10	n.d.	Pellet	0.5 H_2SO_4 ?? 25	73
$Ni_{4.5}Co_{4.5}S_8$	213				75	
$Ni_3Co_6S_8$	256				25	
$Ni_3Co_6S_8$	182				75	
$Ni_2Co_7S_8$	334				25	
$Ni_2Co_7S_8$	239				75	
$NiCo_8S_8$	345				25	

$NiCo_8S_8$	246				75	
Co_9S_8	333				25	
Co_9S_8	247				75	
$FeCo_8S_8$	334				25	
$FeCo_8S_8$	270				75	
$Fe_2Co_7S_8$	357				25	
$Fe_2Co_7S_8$	241				75	
$Fe_3Co_6S_8$	354				25	
$Fe_3Co_6S_8$	227				75	
$Fe_{4.5}Co_{4.5}S_8$	327				25	
$Fe_{4.5}Co_{4.5}S_8$	192				75	
Trimetallic approach						
Co_9S_8	364		148		25	
Co_9S_8	302		145		75	
$Ni_3Co_6S_8$[2]	405		118		25	
$Fe_{4.5}Ni_{4.5}S_8$	385		78		25	
$Fe_3Co_3Ni_3S_8$	376	50	114	Pellet	0.5 H_2SO_4 25	[68]
$Fe_3Co_3Ni_3S_8$	298		88		75	
$Fe_3Co_2Ni_4S_8$	394		102		25	
$Fe_3CoNi_5S_8$	383		92		25	
$Fe_4Co_3Ni_2S_8$[2]	412		111		25	

$FeCo_5Ni_3S_8$	406		113			25	
$Fe_2Co_4Ni_3S_8$	378		108			25	
$Fe_{1.6}Co_{5.6}Ni_{1.8}S_8$	399		108			25	
Co:Fe:Ni ratio in alkalic media							
$Fe_{1.6}Co_{5.6}Ni_{1.8}S_8$	201		158				
$FeCo_5Ni_3S_8$	210		156				
$Fe_2Co_4Ni_3S_8$	287		170				
$Fe_3CoNi_5S_8$	336		186				
$Fe_4Co_3Ni_2S_8$	224		157				
$Fe_3Co_3Ni_3S_8$	344	10	159	Pellet	1 M KOH	75	[242]
$Fe_{4.5}Ni_{4.5}S_8$	250		182				
$Fe_3Co_2Ni_4S_8$	343		163				
$Co_6Ni_3S_8$	322		165				
$Co_{4.5}Ni_{4.5}S_8$	118		148				
Co_9S_8	329		200				

[1] – values taken from Figure

[2] – composite compounds [68]

2. Objectives and Scope of the Thesis

The overarching aim of this study was to establish structure–composition–property relationships in multicomponent transition metal chalcogenides by correlating their crystal structure, microstructure, chemical composition, and electronic configuration with electrocatalytic performance in the hydrogen evolution reaction.

This research focused on trimetallic pentlandite-type materials based on Co, Fe, and Ni, synthesized in various molar ratios. In addition to sulfur-rich systems, selenium-rich pentlandites were also investigated. Particular attention was given to evaluating how the chemical composition and the physical form of the material – powders, pellets, and bulk ingots – influence their electrocatalytic properties toward HER (Figure 20).

A systematic screening of multiple chemical compositions, combined with the evaluation of materials in different physical forms, enabled the assessment of the individual effects of cationic elements and selenium content on the electrochemical behavior of each form. As a result, this work identifies the most promising materials for potential integration into electrolyzers of different designs and operational requirements.

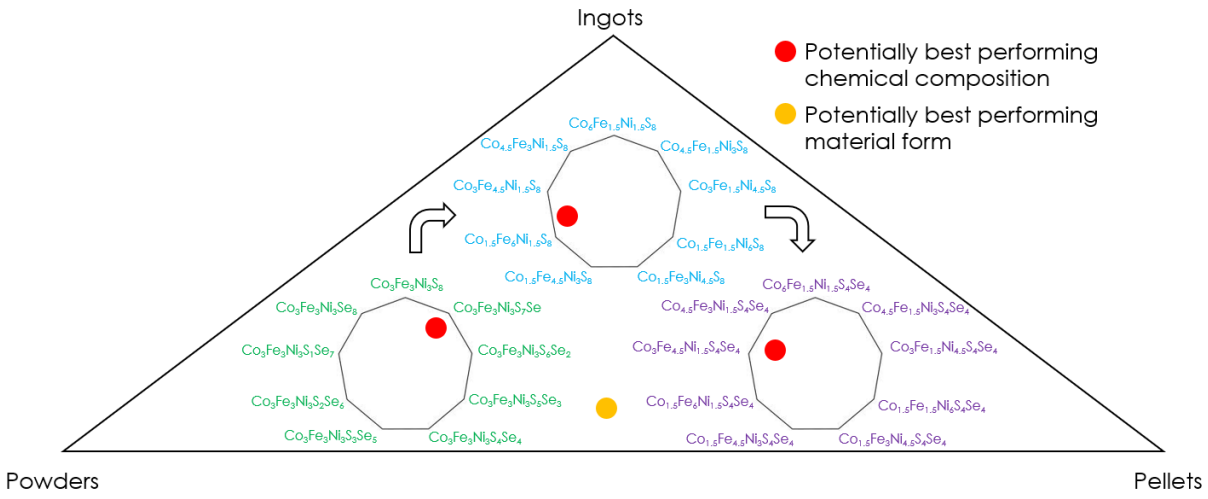

Figure 20. Schematic representation of the objectives and scope of the presented thesis, illustrating the focus on three material series in three distinct physical forms.

Based on these investigations, the study established the following objectives:

- To synthesize single-phase four- and five-component materials with the pentlandite (TM_9Ch_8) structure.
- To determine the solubility limits of individual components (Co, Fe, Ni, S, Se) within the pentlandite structure across different compositions.
- To fabricate materials in three distinct forms: pellets, ingots, and powders deposited on conductive substrates.
- To identify sustainable and stable material compositions and forms.
- To evaluate the electrochemical performance of all synthesized materials and determine the optimal composition and form for HER applications.

3. Materials and methods

3.1. Motivation

In this doctoral thesis, I concentrated on trimetallic systems, as comprehensive studies on such compositions are still lacking, which makes this a novel direction. The idea of exploring five-component pentlandite-type materials for hydrogen evolution reaction originated from preliminary investigations carried out in my research group under the supervision of my advisor [226]. These initeial studies revealed several intriguing properties of multicomponent systems, which provided additional motivation for my work.

The first significant achievement was the successful synthesis of single-phase, trimetallic pentlandites in both quaternary ($Co_3Fe_3Ni_3S_8$) and quinary ($Co_3Fe_3Ni_3S_4Se_4$) compositions. Furthermore, incorporating multiple metal elements enabled a substantial reduction in thermal conductivity – from around 40 W/mK in pure-phase Co_9S_8 to just 2–3 W/mK in the multicomponent materials – while simultaneously maintaining high electrical conductivity of 10^5 S/m, with a near-to-metallic temperature dependence.

Additionally, theoretical calculations such as DFT indicated that these materials possess an electronic structure favorable for HER catalysis. Key features include the presence of multiple redox pairs, enhanced electrochemical properties arising from synergistic effects between cations, their influence on the DOS near the Fermi level, and high charge carrier concentrations.

Moreover, according to parallel studies conducted by the group of Professor Apfel (Ruhr University, Bochum, Germany), carried out independently but overlapping in time with our own work, later formed the basis for collaboration between out groups. These studies shown that cobalt, when introduced as a third component into iron-nickel-based pentlandites, does not improve catalytic performance but does significantly enhance the structural stability of the material [68]. It is also worth noting that Se-rich trimetallic pentlandites represent an unexplored approach globally, with no prior studies available in literature to date.

Ultimately, the concept of solid electrodes – further advanced by our group through the development of sintering conditions enabling their consolidation into bulk form using IHP – established an entirely new research direction, previously unexplored in the field of catalysis.

3.2. Materials

This study investigates a range of trimetallic materials within the pentlandite (TM_9Ch_8) structure, composed of cobalt, iron, and nickel in the cationic sublattice, and sulfur, optionally selenium in the anionic sublattice. The materials were divided into three series, as summarized in Table 9:

1. Trimetallic pentlandites with equimolar amounts of transition metals and varying amounts of sulfur and selenium, ranging from S_8 to Se_8 – **$TM_9S_{8-x}Se_x$** series. This series was designed to evaluate the influence of selenium content on the electrochemical properties of the trimetallic pentlandites.

2. Materials with only sulfur in the anionic sublattice and varying amounts of transition metals in the cationic sublattice. This series is assigned as **$Co_{9-x-y}Fe_xNi_yS_8$**, where x and y can be 1.5, 3, 4.5, or 6, with the smallest amount of a given element being 1.5. This series was used to assess the effect of different cationic ratios on the HER activity in sulfur-based pentlandites.

3. This series is similar to the second one, but with an equimolar amount of sulfur and selenium on the anionic sublattice, represented as **$Co_{9-x-y}Fe_xNi_yS_4Se_4$**. This allowed to investigate whether the catalytic behavior of various cationic combinations remains consistent in Se-rich compositions.

All three series represent an unexplored field of materials (with the exception of a partially overlapping scope of the second series with the work of Apfel's group [68]), particularly in view of the adopted convention of using bulk material form.

Table 9. Chemical composition of the pentlandite materials tested in this thesis together with individual sample abbreviations.

$TM_9S_{8-x}Se_x$ series		**$Co_{9-x-y}Fe_xNi_yS_8$ series**		**$Co_{9-x-y}Fe_xNi_yS_4Se_4$ series**	
Chemical composition	Symbol	Chemical composition	Symbol	Chemical composition	Symbol
$Co_3Fe_3Ni_3$	X.S8	$Co_3Fe_{1.5}Ni_{4.5}S_8$	X.314.S8	$Co_3Fe_{1.5}Ni_{4.5}S_4Se_4$	X.314.S4
$Co_3Fe_3Ni_3S_7Se$	X.S7	$Co_{1.5}Fe_{1.5}Ni_6S_8$	X.116.S8	$Co_{1.5}Fe_{1.5}Ni_6S_4Se_4$	X.116.S4
$Co_3Fe_3Ni_3S_6Se_2$	X.S6	$Co_{1.5}Fe_3Ni_{4.5}S_8$	X.134.S8	$Co_{1.5}Fe_3Ni_{4.5}S_4Se_4$	X.134.S4
$Co_3Fe_3Ni_3S_5Se_3$	X.S5	$Co_{4.5}Fe_{1.5}Ni_3S_8$	X.413.S8	$Co_{4.5}Fe_{1.5}Ni_3S_4Se_4$	X.413.S4
$Co_3Fe_3Ni_3S_4Se_4$	X.S4	$Co_6Fe_{1.5}Ni_{1.5}S_8$	X.611.S8	$Co_6Fe_{1.5}Ni_{1.5}S_4Se_4$	X.611.S4
$Co_3Fe_3Ni_3S_3Se_5$	X.S3	$Co_{4.5}Fe_3Ni_{1.5}S_8$	X.431.S8	$Co_{4.5}Fe_3Ni_{1.5}S_4Se_4$	X.431.S4
$Co_3Fe_3Ni_3S_2Se_6$	X.S2	$Co_3Fe_{4.5}Ni_{1.5}S_8$	X.341.S8	$Co_3Fe_{4.5}Ni_{1.5}S_4Se_4$	X.341.S4
$Co_3Fe_3Ni_3SSe_7$	X.S1	$Co_{1.5}Fe_6Ni_{1.5}S_8$	X.161.S8	$Co_{1.5}Fe_6Ni_{1.5}S_4Se_4$	X.161.S4
$Co_3Fe_3Ni_3Se_8$	X.S0	$Co_{1.5}Fe_{4.5}Ni_3S_8$	X.143.S8	$Co_{1.5}Fe_{4.5}Ni_3S_4Se_4$	X.143.S4

The procedure of sample syntheses and electrode preparations involved several steps, as illustrated in Figure 21. Each of the series mentioned earlier was tested in three different forms: ingots directly after synthesis, powders deposited on a conductive substrates, and sintered pellets. This approach allowed to assess not only the impact of material composition on electrochemical performance, but also the influence of material form, intrinsic properties, density, and other factors. For that reason, in Table 9, the prefix "X." before the sample name indicates the material form, where "P" stands for powder, "I" for ingot, and "S" for sinter. For example, S.S8 refers to the $Co_3Fe_3Ni_3S_8$ powder sample, I.314.S8 denotes the $Co_3Fe_{1.5}Ni_{4.5}S_8$ ingot sample, and S.116.S4 indicates the sintered form of sample $Co_{1.5}Fe_{1.5}Ni_6S_4Se_4$.

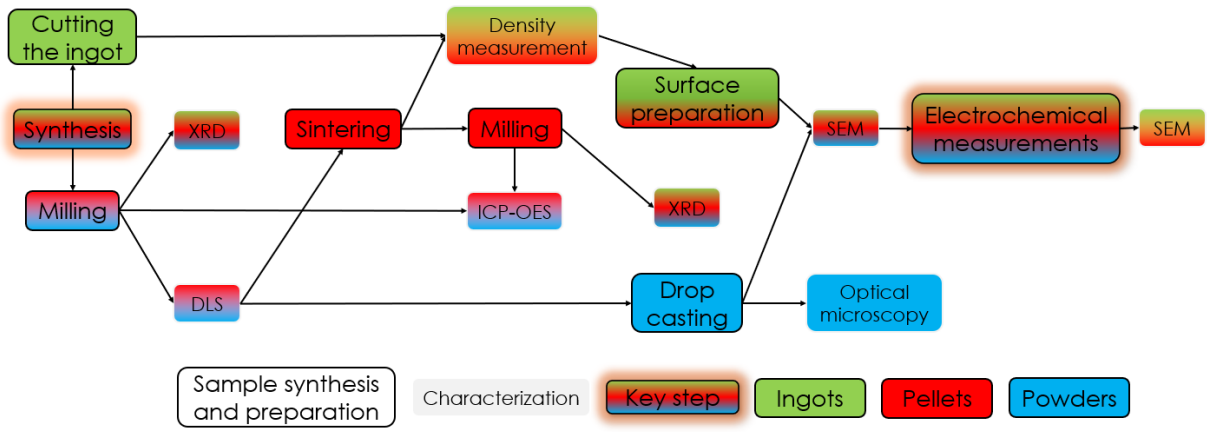

Figure 21. Schematic workflow of sample synthesis and testing procedures.

3.2. Synthesis of materials

Figure 22 shows a schematic illustration of the material synthesis process. All materials were synthesized from pure elements (Co, 99.8% Alfa Aesar powder, Fe, 99.98% Alfa Aesar granules, Ni, 99.8% Alfa Aesar powder, S, 99.999% Alfa Aesar pieces, Se, 99.999% Alfa Aesar shot), which were weighed and transported into self-made quartz ampoules inside the *MBRAUN LABstar* Glovebox under an argon atmosphere. The ampules were then sealed under vacuum (10^{-3} atm) to ensure an oxygen-free environment. Subsequently, the ampules were placed in a tube furnace and subjected to a two-step temperature treatment, which was empirically optimized in our group: first, they were heated to 1050 °C (1°C/min) and annealed for 24 hours; then, the temperature was decreased to 500 °C (2°C/min), and the materials were annealed for 72 hours. Finally, the ampules were quenched in tap water at room temperature to ensure the formation of the desired cubic phase structure ($Fm\bar{3}m$ space group). The temperature profile is graphically presented in Figure 22b.

Attempts to obtain phase-pure pentlandite-type multi-component compounds by alternative synthesis routes were unsuccessful, which is likely related to thermodynamic constraints and the requirement of high-temperature formation of the pentlandite phase. Only more recently, such materials have also been synthesized using mechanical alloying (mechanosynthesis) [243].

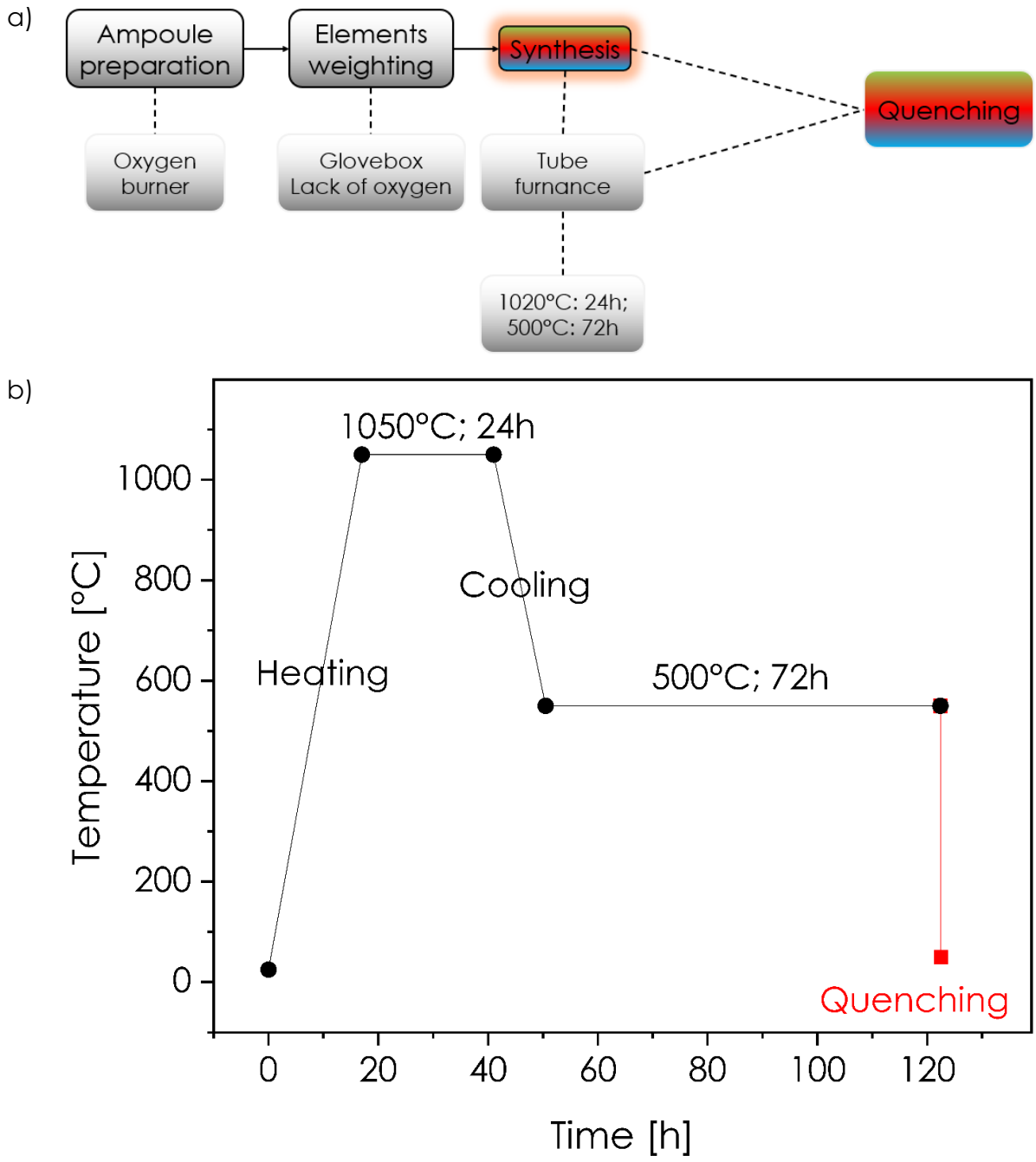

Figure 22. a) Schematic presentation of synthesis process; b) thermal annealing profile used during the synthesis.

3.3. Preparation of materials

After synthesis, the obtained materials were subjected to mechanical treatment, which varied depending on the final form of the electrode. The pure ingot, shown in Figure 23, was cut into several pieces, each intended for different purposes. These included obtaining material in the form of powder or sintered electrodes or conducting structural analyses like XRD (X-ray diffraction), ICP-OES (Inductively Coupled Plasma Optical Emission Spectroscopy), SEM+EDS (Scanning Electron Microscopy with Energy Dispersive X-ray Spectroscopy), and subsequent electrochemical studies.

Figure 23. The photograph of synthesized ingot sample prior to mechanical treatment.

3.3.1. Powders

The procedure of obtaining powder electrodes is shown in Figure 24. To obtain powders from synthesized ingots for XRD and ICP-OES analysis, as well as to create a powder electrode for electrochemical testing, the pentlandites were milled using a *Retsch RM 200* planetary mill with agate mortar and pestle, following manual pre-milling in an agate mortar. The milling procedure was standardized to 5 minutes [189,244]. Milled pentlandite can be seen in Figure 25a. The prepared powders were then examined using Dynamic Light Scattering (DLS) with a *Malvern Zetasizer Pro ZSU5800* analyzer to determine the particle size.

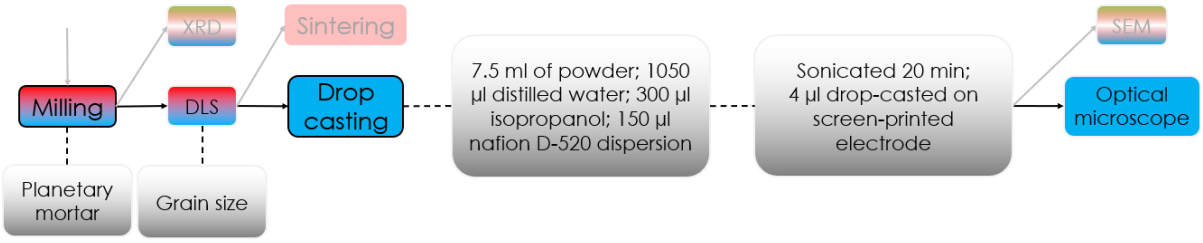

Figure 24. Schematic illustration of the powder electrode preparation process.

To prepare an electrode, a powder suspension (ink) was made. The ink was composed of 7.5 mg of powder, 1050 µl of distilled water, 300 µl of isopropanol, and 150 µl of Nafion *D-520* dispersion. The entire mixture was homogenized for 20 minutes. After sonication, 4 µl of the ink was drop-casted onto a screen-printed electrode (*DRP-110 nLab*) and left to dry for 24 h in air. An example of a prepared

electrode is shown on Figure 25b. Each powder electrode prepared in this manner was photographed using an *Olympus SZX7* optical microscope.

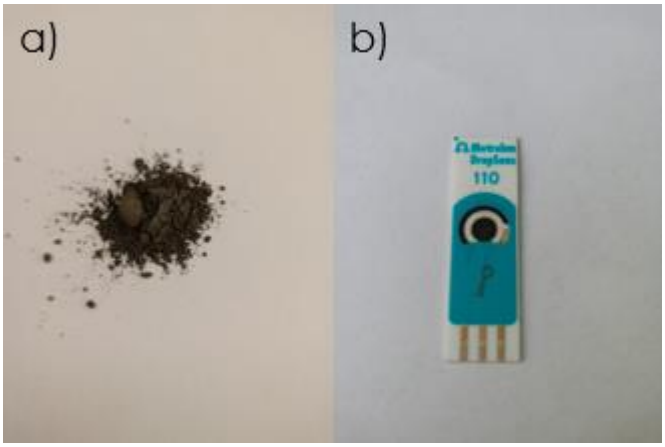

Figure 25. a) Example of milled pentlandite powder; b) Pentlandite drop-casted onto DRP-110 nLab *screen-printed electrode.*

3.3.2. Ingots

To prepare the ingot samples (Figure 26), the material was cut into flat pieces directly after synthesis. These bulk pieces required further treatment before electrode preparation. The flat surface of each ingot was polished manually using a *KLINGSPOR* abrasive paper set with gradations of P600, P2000, and P3000 to achieve a smoother surface. During this process, the ingots were washed with acetone to prevent excessive heating of the samples. The ingots were then transferred to a pre-soaked suede cloth with a suspension of Al_2O_3-based 3 μm polishing paste and polished manually. Finally, each sample was washed with tap water and left to dry completely. An example of the ingot material is shown in Figure 27.

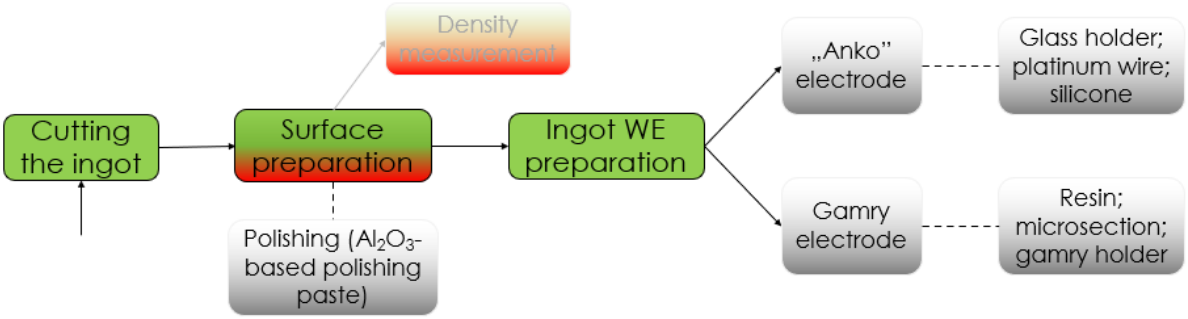

Figure 26. Graphical presentation of the ingot samples and working electrode preparation.

Two methods were used to prepare the working electrode from the ingots. The first method involves mounting the material in a glass holder by wrapping a platinum wire around the sample. Silicone was then applied with a spatula between the holder and the sample to ensure that the electrode does ot penetrate the glass holder or react with the platinum wire. The WE prepared this way was ready for use after 24 hours and was used with the *MTM Anko M161* potentiostat, as shown in Figure 27.

The second method involved embedding the sample in resin and grinding it into the shape of a microsection. This type of WEs were used with the *GAMRY Interface 1010E* apparatus in a special *Gamry* holder, as shown in Figure 27. The TM_9S_8-S_3 and $Co_{9-x-y}Fe_xNi_yS_8$ series were prepared using the "Anko" method, while the $Co_{9-x-y}Fe_xNi_yS_4Se_4$ series was prepared using the *Gamry* method.

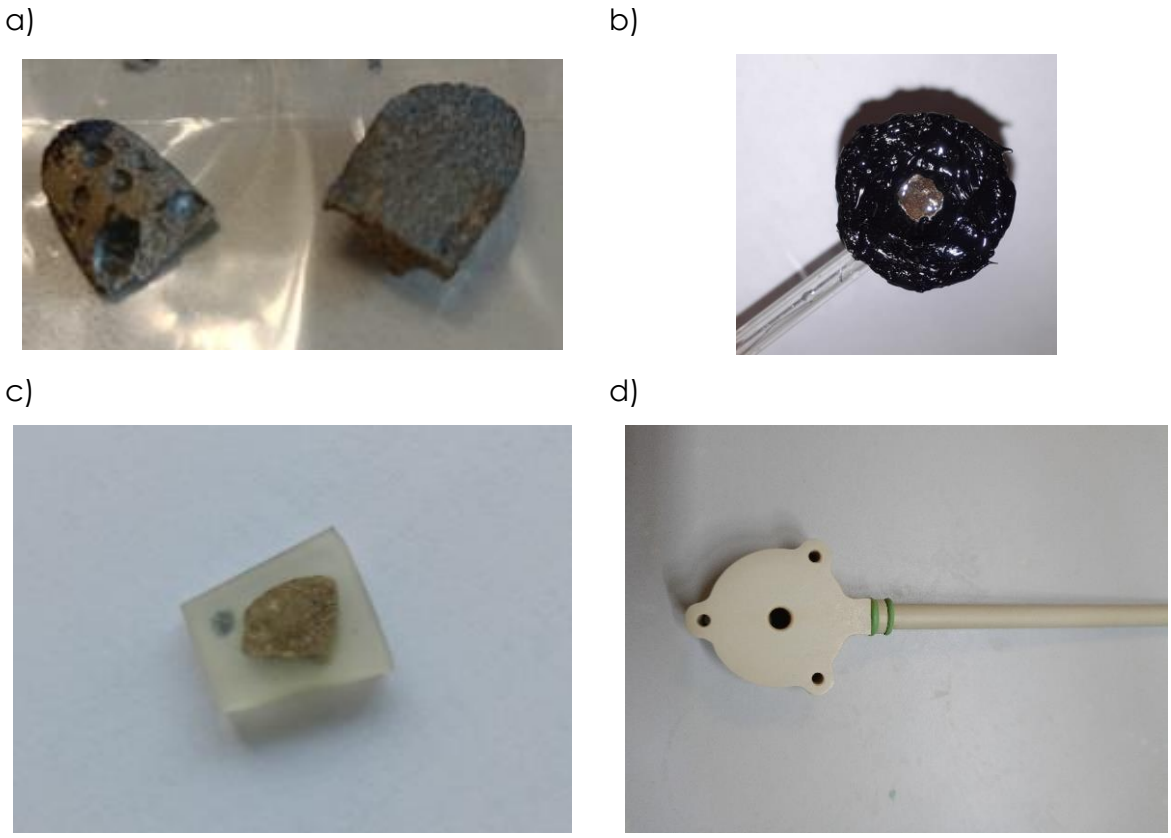

Figure 27. Photographs of a) cut ingot; b) Anko holder; c) polish of ingot; d) Gamry holder.

3.3.3. Pellets

Before the "pellet samples" could be tested electrochemically, several preparatory steps were necessary. The milled powders, initially characterized by DLS, were sintered into bulk pellet form. After sintering, the obtained pellets were subjected to surface preparation and subsesquently used for mounting working electrodes(Figure 28).

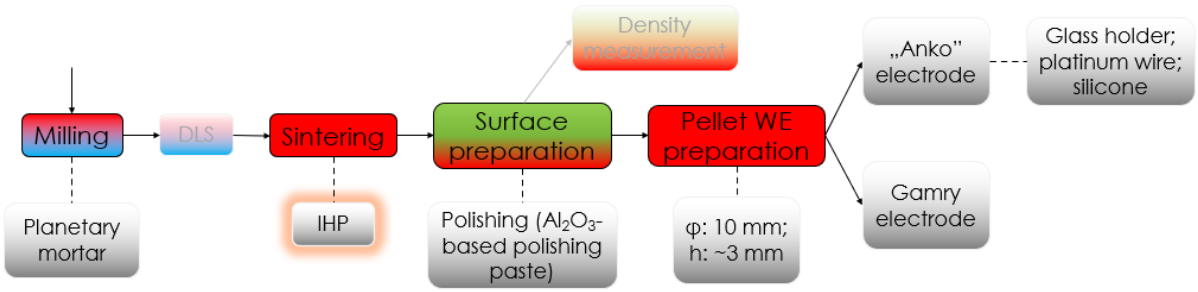

Figure 28. Schematic representation of pellet samples preparation.

The samples were sintered to produce solid materials that could serve as WEs in the electrochemical HER, avoiding the need for the more complex process of powder milling.This approach also ensured

that only the working material was tested, minimizing the signal interference coming from the substrate. It is important to note that during the sintering process, undesirable phenomena may occur, such as the evaporation of sulfur or selenium from the surface of the samples or the precipitation of other phases. To verify that the material maintained its integrity, the sintered pellets were subjected to SEM+EDS and XRD analysis.

Another critical factor in the sintering process is its effect on the density of the samples. Lower density can lead to greater surface area development and higher porosity, which allows the electrolyte to penetrate through various types of microchannels, thus facilitating HER within the material's volume, not just on the electrode surface. In contrast, higher density enhances electrical conductivity and promotes a higher concentration of defects and active sites, which can increase the ECSA and RF. Therefore, the density, porosity, defects, and roughness factor of the material are crucial when designing electrocatalysts in the form of solid electrodes, making the sintering temperature a critical parameter.

When comparing the tested samples, it is essential that all samples have the same density. This ensures that their electrochemical properties can be accurately compared, without discrepancies arising from factors such as those described above.

To obtain the pellet samples, the powder was sintered using the Inductive Hot Pressing (IHP) process (Figure 29). The standard procedure included flushing the working chamber twice with argon at a pressure of 0.5 atm at room temperature, followed by the main sintering process. The sample was then heated to 200 °C at a rate of 100 °C/min and annealed for 5 minutes. Afterward, the temperature was increased to the target temperature, which in the standard procedure was 400 °C. The sample was then annealed for 14 minutes under an applied pressure of 50 MPa. Following this, the pressure was released to relieve stress in the material, and the material was annealed for an additional minute. Finally, the entire apparatus and sample were cooled down to room temperature.

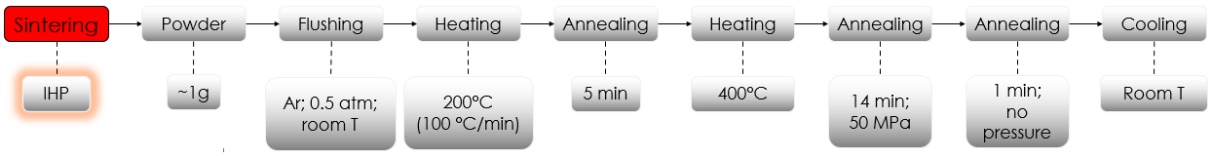

Figure 29. Schematic illustration of the IHP process.

The pellets were sintered to achieve a high-density bulk sample. The temperature of 400 °C was determined in previous experiments to be sufficient to ensure a dense and durable material. The 15-minute duration of the process was also established experimentally. Although the majority of pellet samples were sintered at 400 °C for 15 minutes, additional tests were conducted at higher temperatures (450, 500, 550, 600, and 650 °C) and longer durations (20 and 25 minutes), as shown in Table 10, in order to assess the effect of these factors on the density and phase purity of the samples after sintering, as well as for additional studies on surface precipitates and electrochemical properties.

Before sintering, the pellets were wrapped in graphite, which was subsequently removed after the process. Initial layers of graphite were removed mechanically using a wallpaper cutter, and the pellets were then placed in a grinding machine, where the residual graphite was removed with abrasive paper. After the graphite was completely removed, the surface preparation process followed the same procedure applied to the ingot samples. It should be emphasized that the sintering of multicomponent pentlandites by IHP represents an entirely novel approach. The relatively low temperature required to obtain dense pellets results from the combined effect of the applied pressure and the IHP method itself, which generates so-called eddy currents. In the case of our materials, rich in delocalized electrons, these currents further facilitate the sintering process. Importantly, sintering at relatively low temperature not only reduces processing costs but also limits grain growth (which is particularly beneficial for maintaining the desired microstructure). Additionally, the graphite matrix provides locally reducing conditions, effectively preventing oxidation during the treatment.

3.4. Material characterization

Due to the multi-component, multi-form, and multi-stage nature of the testing process, it is crucial to monitor the chemical composition, phase structure, and homogeneity of all materials at various stages of their processing. To gain a comprehensive understanding of the samples behavior throughout the entire process, the following techniques were employed: XRD, SEM+EDS, ICP-OES, XPS, and DLS.

3.4.1. X-ray diffraction (XRD)

To determine the phase composition of the samples, XRD was employed. Measurements were conducted using a *PANalytical X'Pert Pro* apparatus (Cu $K\alpha_1$ = 1.54 Å radiation) and analyzed using the *X'Pert High Score Software*.

The XRD tests were performed twice (Figure 30). The first test was conducted immediately after synthesis, where the samples were manually milled, to verify that the synthesized material was a single-phase pentlandite. The second test involved analyzing sintered pellets to assess the phase stability of the material after IHP sintering.

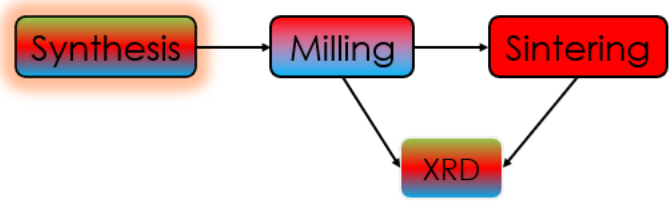

Figure 30. Schematic procedure involving XRD measurements and analyses.

3.4.2. Scanning electron microscopy with energy-dispersive X-ray spectroscopy (SEM+EDS)

To determine the microstructure and elemental composition of all samples, the SEM+EDS method was employed. SEM imaging and EDS analysis were conducted using *Fischer Phenom XL* equipped with an EDS analyzer.

The SEM+EDS tests were performed on all sample forms – pellets, ingots, and powders – prior to electrochemical measurements. Additional tests were conducted on the pellets and ingots after the HER processing to verify the phase composition and stability of the materials during the electrochemical operation (Figure 31).

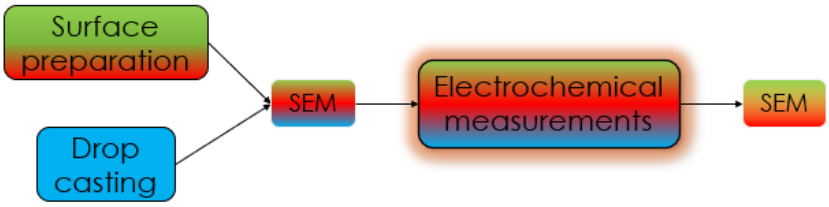

Figure 31. Schematic procedure involving SEM measurements and analyses.

3.4.3. Inductively coupled plasma optical emission spectroscopy (ICP-OES)

As an alternative method for verifying elemental composition, the ICP-OES technique was employed. These tests were performed at the accredited Hydrogeochemical Laboratory of the AHG-UST Department of Hydrogeology and Engineering Geology, using a *PerkinElmer Optima 7300DV* spectrometer. Samples were mineralized in concentrated HNO_3 at a temperature of 523 K and a pressure of 8.1×10^6 Pa.

ICP-OES analysis was conducted on the powders directly after synthesis and on the milled pellets after sintering, to verify the stability of the elemental composition (Figure 32).

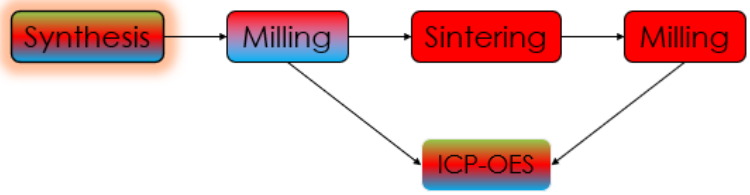

Figure 32. Schematic procedure involving ICP-OES measurements and analyses.

3.4.4. X-ray photoelectron spectroscopy (XPS)

To investigate the surface changes during electrochemical testing of the $Co_{1.5}Fe_6Ni_{1.5}S_4Se_4$ (S.161.S4) pellet sample, XPS measurements were conducted. Additionally, XPS tests were performed on the $Co_3Fe_3Ni_3S_4Se_4$ (S.S4) pellet for comparison with the S.161.S4 reference. For both pellets, XPS measurements were taken before and after the electrochemical tests (Figure 33).

The XPS analysis was carried out using a *PHI5000 VersaProbe II Scanning XPS Microprobe*, equipped with a monochromatic Al Kα X-ray source. The X-ray power settings were 4 mA and 15 kV, and the analysis was performed on an area of 400 µm × 400 µm. The base pressure in the chamber was maintained at $< 2.0 \cdot 10^{-9}$ mbar. The analyzer used was of the SCA type, with a pass energy of -46.95 eV for XPS measurements. Charge neutralization was achieved through a dual-beam system, consisting of an electron flood gun (1 eV) and an Ar^+ ion gun (7 eV). The instrumental resolution was determined to be ≤ 0.5 eV at a 23.50 eV pass energy, using the Ag $3d_{5/2}$ line from a sputter-cleaned metallic silver sample at room temperature.

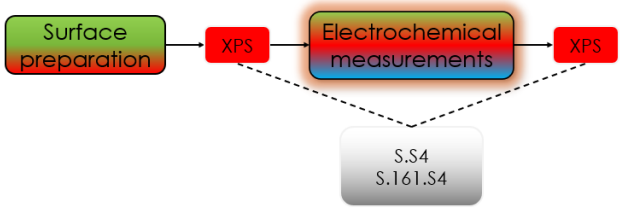

Figure 33. Schematic procedure involving XPS measurements and analyses.

3.4.5. Dynamic Light Scattering (DLS)

In order to determine the particle size of the powders before creating a pellet and powder electrodes, the DLS method has been employed. The DLS test was performed with a *Malvern Zetasizer Pro ZSU5800* analyzer and Figure 34 shows the schematic DLS process.

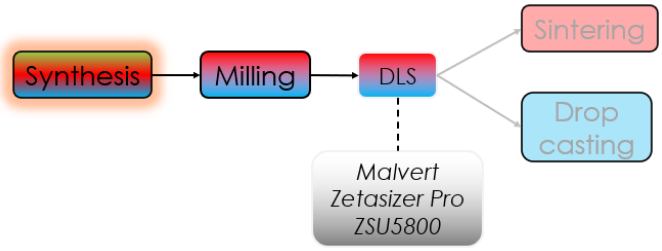

Figure 34. Schematic procedure involving DLS measurements and analyses.

3.4.6. Density measurement

The density of the obtained ingots and pellets was measured using the hydrostatic (Archimedes) method (equation 3.1).

$$\rho_A = \frac{m_a}{m_a - m_w} \cdot \rho_{H_2O}(T) \tag{3.1}$$

ρ_A – density of the sample [g/m^3] ;
m_a – mass of the sample in air [g];
m_w – mass of the sample in water [g];
ρ_{H_2O} – density of the water [g/m^3].

Then the relative density of the sinter was determined using equation (3.2)

$$\rho_R = \frac{\rho_A}{\rho_C} \tag{3.2}$$

ρ_R – relative density of the sample [g/m^3];
ρ_C – theoretical crystallographic density calculated using Rietveld analysis [g/m^3].

3.4.7. Electrochemical Impedance Spectroscopy (EIS)

EIS was employed to evaluate the uncompensated resistance (R_u) and charge-transfer resistance (also known as polarization resistance – R_{CT}). The measurements were performed over a frequency range from 1 Hz to 50 kHz using a *Gamry Interface 1010E* potentiostat. The equivalent circuit model

applied in this analysis consisted of R_u, R_{CT}, a constant phase element (CPE), and a Warburg diffusion element, as illustrated in Figure 35.

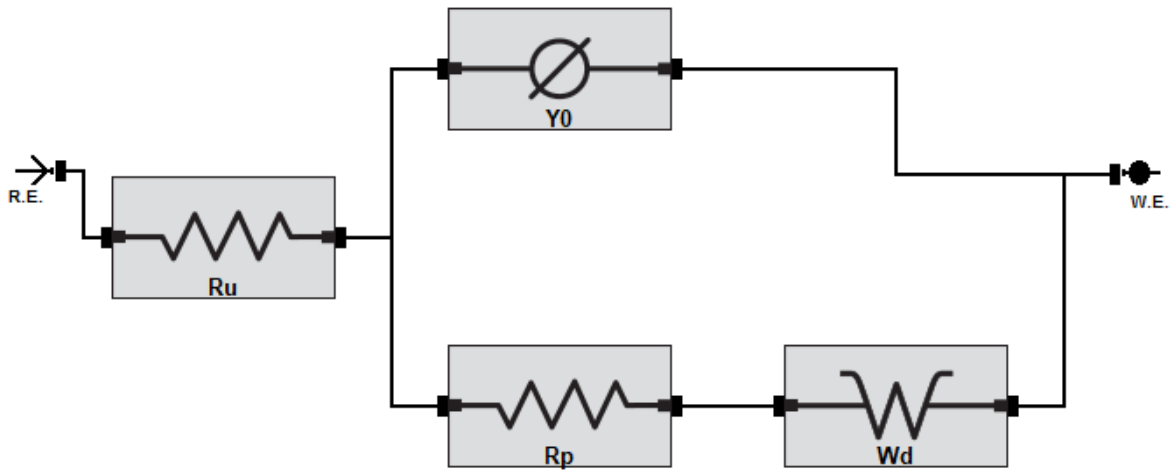

Figure 35. Equivalent circuit used for EIS analysis, consisting of: Ru – uncompensated resistance; R_{CT} – polarization resistance; Y_0 – constant phase element (CPE); W_d – Warburg diffusion element.

3.5. Electrochemical measurement methodology

The electrochemical performance tests were conducted using two different measurement systems. The former, used for testing the $TM_9S_{8-x}Se_x$ and $Co_{9-x-y}Fe_xN_yS_8$ samples, was based on the *MTM-ANKO M161* potentiostat, with subsequent analysis performed using the *MTM-Anko EaLAB* software. The second system, used for the $Co_{9-x-y}Fe_xN_yS_4Se_4$ series, involved the *GAMRY Interface 1010E* potentiostat, with the samples placed in a specialized *RedoxMe* holder with an electrode area of 0.196 cm^2.

All measurements were conducted in a 0.5 M H_2SO_4 electrolyte. For ingots and pellets, an Ag/AgCl reference electrode was used during testing, and a Pt/Pt black electrode served as the counter electrode during tests in the *ANKO* system, while a Pt spiral wire served as the counter electrode in the *Gamry* system. Screen-printed electrodes, which were used as conductive substrates for powders, have built-in Pt counter electrode and Ag reference electrode. The electrochemical performance tests were carried out in seven distinct steps (Figure 36). All potential values are given with reference to E_{RHE} (electrical potential of the reversible hydrogen electrode).

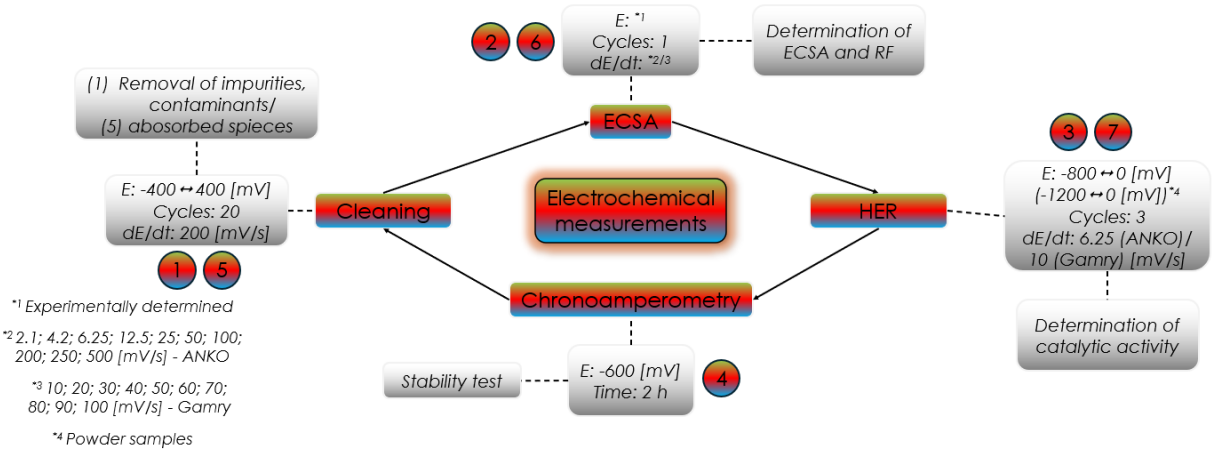

Figure 36. Schematic procedure involving electrochemical tests. Numbers denote the order of the steps to be performed.

The first step involved fast CV electrochemical scanning consisting of 20 cycles, to remove impurities and contaminants from the surface of the sample. However, if the signal remained unstable after this step, the number of cycles can be increased.

The second step involves the evaluation of the ECSA, which is determined by recording CV plots at different scan rates. In the *ANKO* apparatus, the scan rates were systematically set to values marked as "*2" in Figure 36, while in the *Gamry* system, the scan rates were manually adjusted based on literature values (e.g., ref. [130]). The ECSA calculation involves determining the double-layer capacitance (C_{dl}) by plotting the differences between the cathodic and anodic current values at the midpoint of the potential range, referenced to Ag/AgCl, and then plotting this against the scan rate (Figure 37a/b). Linear regression is used to approximate C_{dl} as the slope of the curve, as shown in Figure 37c. The ECSA and the RF values were calculated using equations (1.25 and 1.26), with C_s (specific capacitance) set

to an average value of 0.035 mF/cm^2 [96–101]. The CV curves related to these measurements are included in the Supplementary Materials.

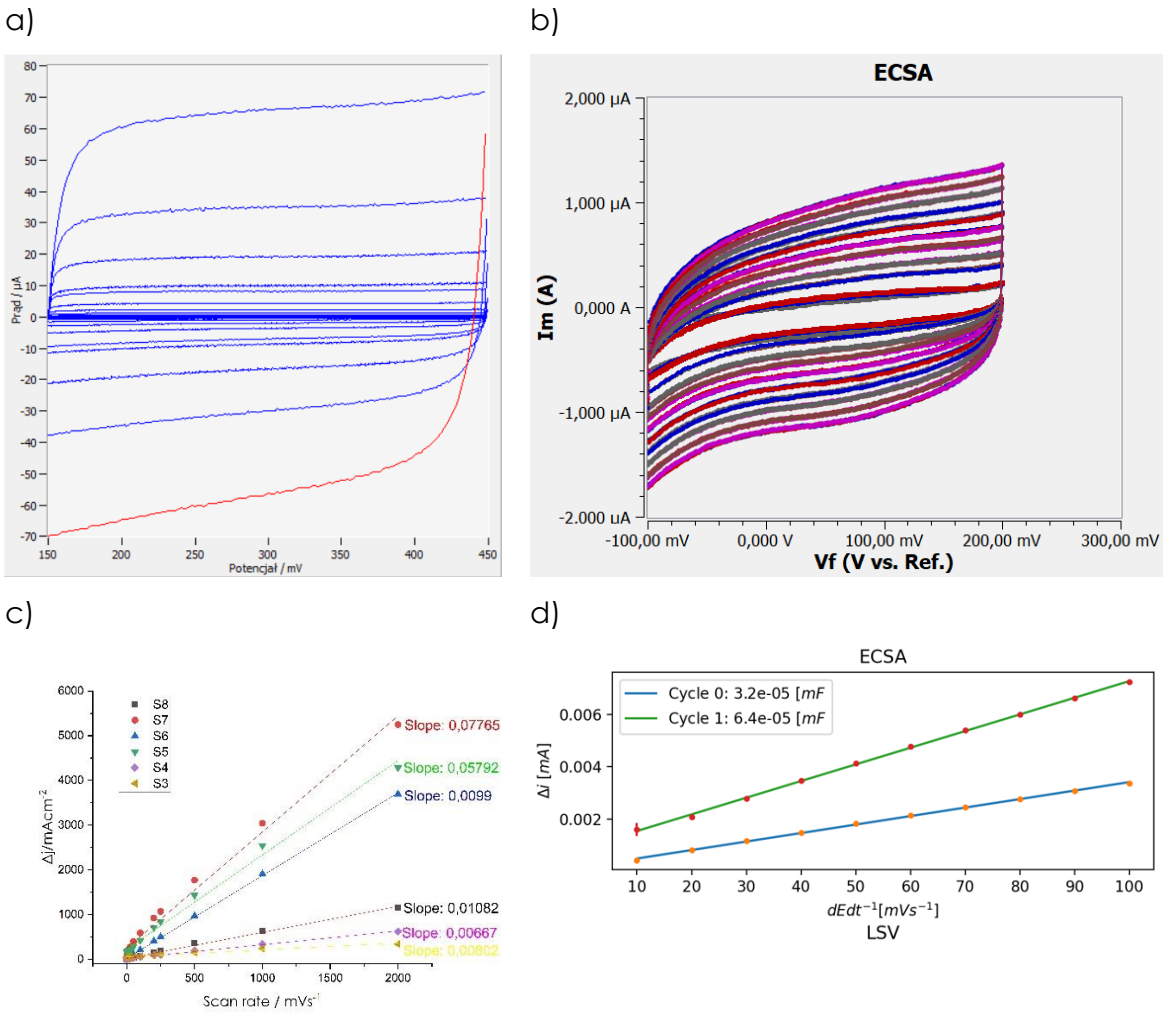

Figure 37. Examples of a) CV curves obtained by ANKO apparatus; b) CV curves obtained by GAMRY apparatus; c) C_{dl} obtained by ANKO apparatus; d) C_{dl} obtained by GAMRY apparatus.

The third step was the most critical and assessed the material's activity toward HER. For ingots and pellets, the testing range was from -800 mV to 0 mV and reversed, while for powder samples, the measurement range extended from -1200 mV to 0 mV and reversed, due to different potentials of reference electrodes. The HER test included three scans, and the average value of these was used for analysis.

A short-term – lasting two hours – stability test (chronoamperometry) was then performed to assess the material's stability and examine its properties after extended operation. This test helped to identify phenomena such as *sulfur depletion* or material decomposition. After the stability test, cleaning, ECSA, and HER steps were repeated to evaluate the potential changes in the material's performance. Long-term (12 h) stability tests were not conducted due to the large number of investigated samples and limited availability of the electrochemical measurement equipment.

The overpotential and current densities reached by the materials during the LSV tests are among the most important benchmarks for HER measurements, alongside ECSA, RF, and other parameters.

However, due to the varying approaches in HER research, the 10 mV/cm^2 criterion is not always ideal. In some cases, materials may fail to reach this current, particularly when normalized to ECSA, or a non-zero current might be observed due to factors such as highly defective surfaces, electrochemically active precipitates, or agglomeration of residual charge on the catalyst surface. Therefore, in my research, I will use alternative current densities values to describe the electrochemical performance of the materials: 0.2 mA/cm^2 for ECSA: $\eta_{0.2ECSA}$; and standard 10 mA/cm^2 for geometric area: η_{10geo}.

3.6. Preparation of powder working electrodes

To determine the particle size distribution of all obtained materials in the form of powders (which were also later used for pellet preparation and thus determined the potential amount of grain boundaries), DLS tests were performed. In the $Co_3Fe_3Ni_3S_{8-x}Se_x$ series (Figure 38), the P.S7 sample exhibits the most uniform and unimodal particle size distribution of around 350-400 nm. In contrast, the other powder samples show at least two populations; however, the second population is typically negligible (Figure 38b). P.S7 has an average particle size of approximately 400 nm, while the other samples exhibit larger particle sizes, nearly 1 µm, which could affect their electrochemical performance, for example, by exhibiting the higher ECSA and, consequently, the best HER performance – not necessarily due to its chemical composition or intrinsic properties, but rather due to the average linear grain size.

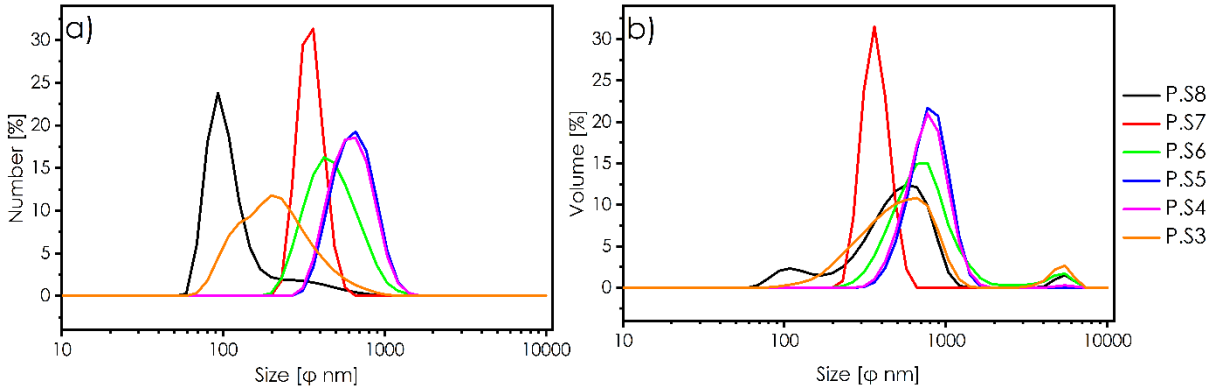

Figure 38. DLS results of the particle size for $Co_3Fe_3Ni_3S_{8-x}Se_x$ series as a function of a) number and b) volume distribution.

After the preparation of the powder working electrodes, as described in Section 3.3.1, optical microscopy was performed to examine the distribution of powder grains on the surface of the conductive substrate. A significant issue was immediately apparent: the distribution and size of the powder grains vary considerably from one electrode to another. This inconsistency can cause serious problems during electrochemical testing, primarily due to variations in the geometric working area. Additionally, several concerns arise in relation to the ECSA. The measured ECSA values may be influenced not only by the powder itself, but also by the conductive substrate and the Nafion binder used in the powder suspension. Therefore, the geometric area has been fixed at 0.187 cm^2, corresponding to the defined working area of the substrate.

For the $Co_3Fe_3Ni_3S_{8-x}Se_x$ series (Figure 39) specifically, electrochemical measurements show a visible layer of Nafion solution on the conductive substrate (Figure 39g), further complicating interpretation of the results. Additionally, in this Figure – as well as in the corresponding ones for the other two series (Figure 41 and Figure 43) – it is clearly visible that the material is not uniformly dispersed across all samples, which may affect its electrochemical properties, especially R_u and R_{CT} values. To address these challenges, an alternative system for evaluating the electrochemical performance of powders on conductive substrates is proposed in Chapter 4.4.4.

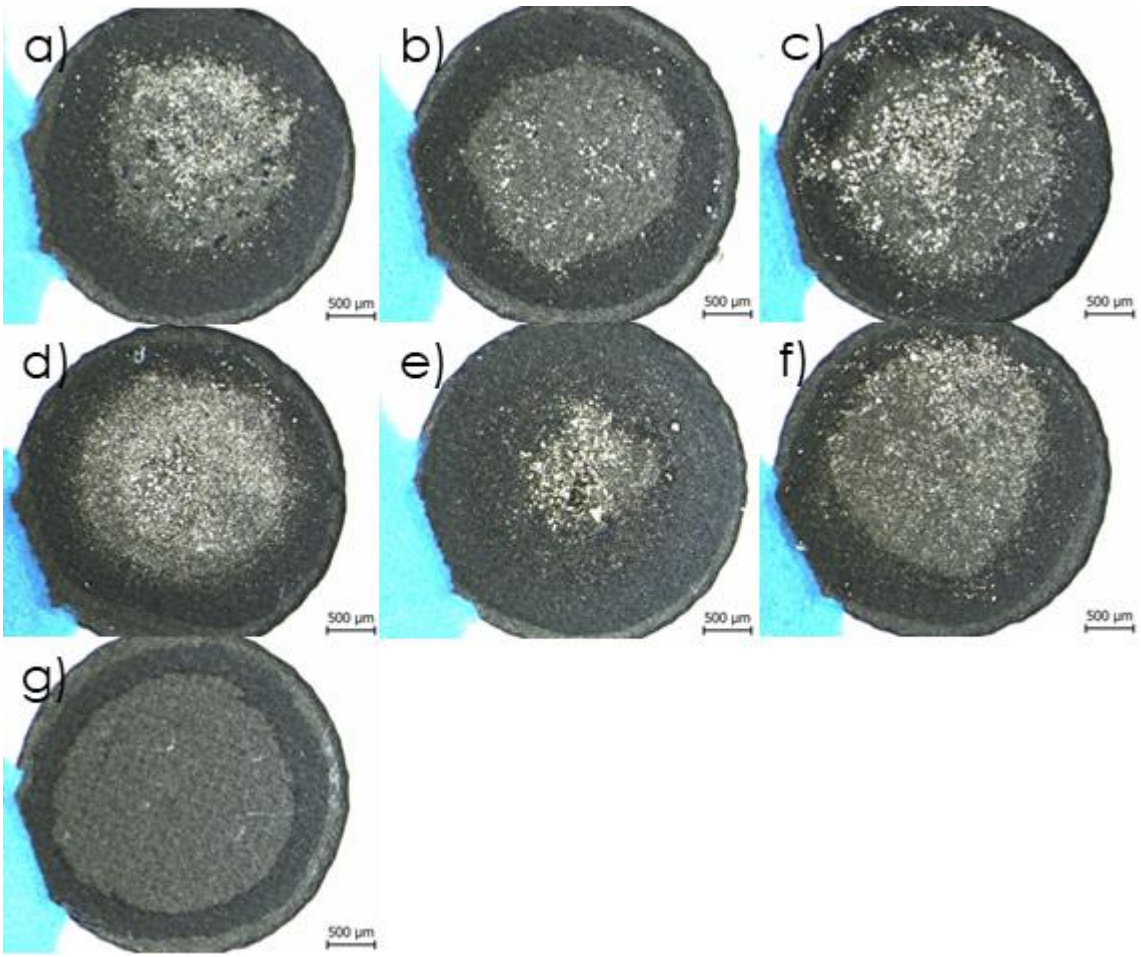

Figure 39. Photos of powders applied to screen-printed electrodes a) P.S8; b) P.S7; c) P.S6; d) P.S5; e) P.S4; f) P.S3; g) nafion solution.

Among the $Co_{9-x-y}Fe_xN_yS_8$ series (Figure 40), the samples demonstrate a broader size distribution, ranging from approximately 0.6 to 2.5 µm. Among them, only P.431.S8, P.341.S8, and P.161.S8 display unimodal particle size distributions, although their average sizes are still exceed 1 µm.

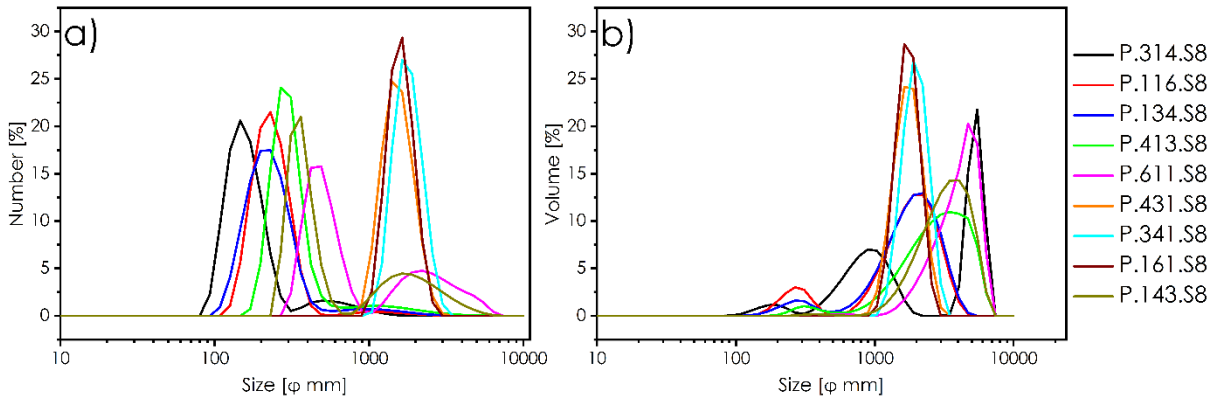

Figure 40. DLS results of the particles size for $Co_{9-x-y}Fe_xN_yS_8$ series as a function of a) number and b) volume distribution.

Figure 41 shows the microscope images of powder grain distribution on the surface of the conductive substrate.

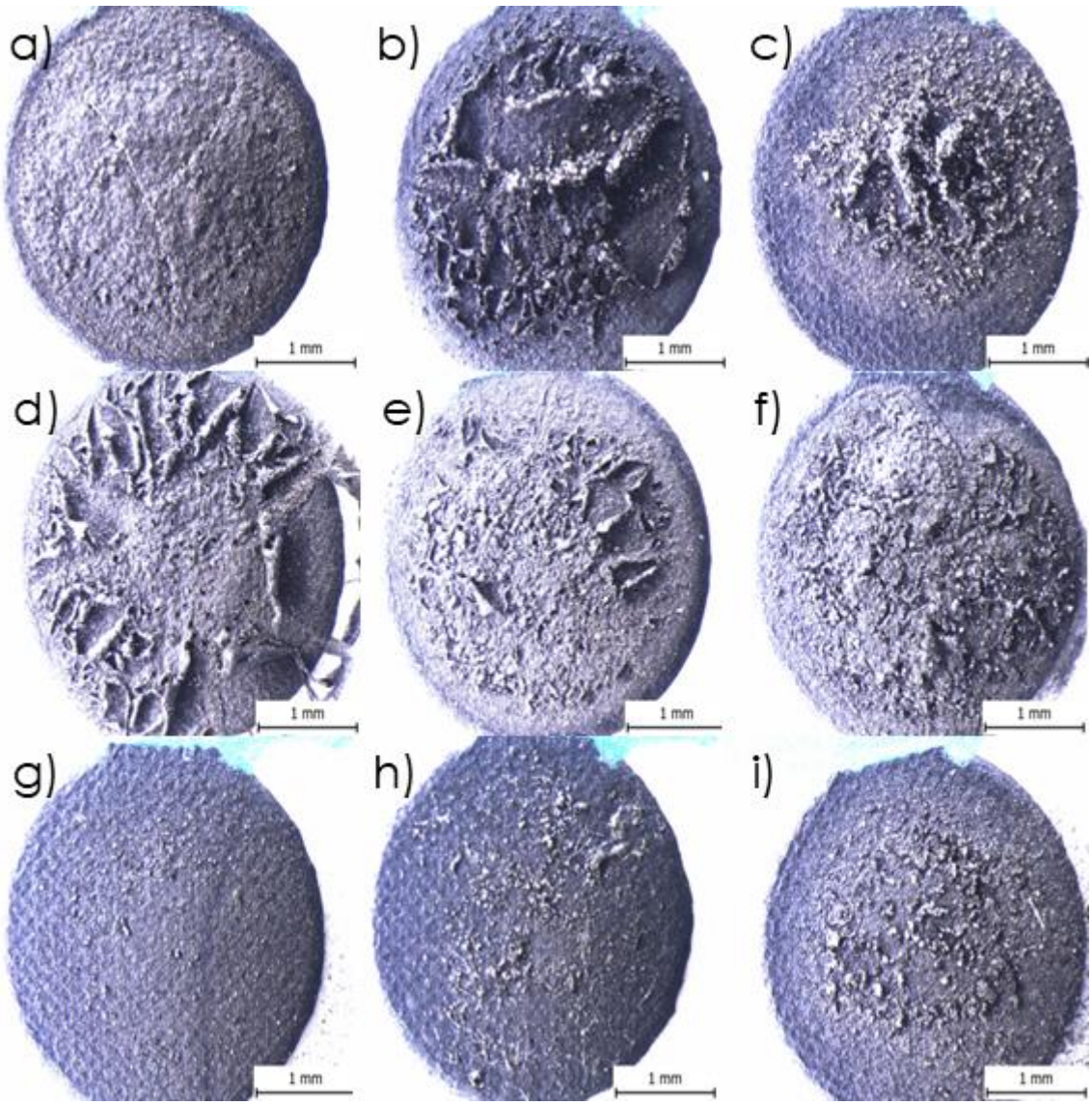

Figure 41. Photos of powders applied to screen-printable electrodes: a) P.314.S8; b) P.116.S8; c) P.134.S8; d) P.413.S8; e) P.611.S8; f) P.431.S8; g) P.341.S8; h) P.161.S8; i) P.143.S8.

The $Co_{9-x-y}Fe_xN_yS_4Se_4$ series (Figure 42) shows the most scattered results. Only three samples: P.134.S4, P.431.S4, and P.161.S4 deviate from a unimodal distribution. However, for nearly all other samples in this series, the particle size distribution is too broad to allow definitive conclusions about a dominant particle size.

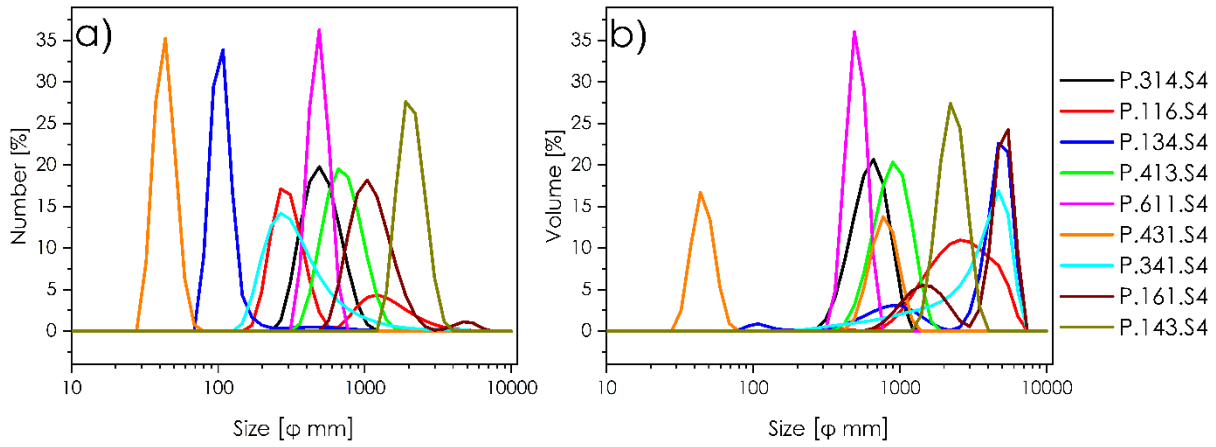

Figure 42. DLS results of the particle size for $Co_{9-x-y}Fe_xN_yS_4Se_4$ series as a function of a) number and b) volume distribution.

Distribution of powder grains on the surface of the conductive substrate for this series is shown in Figure 43.

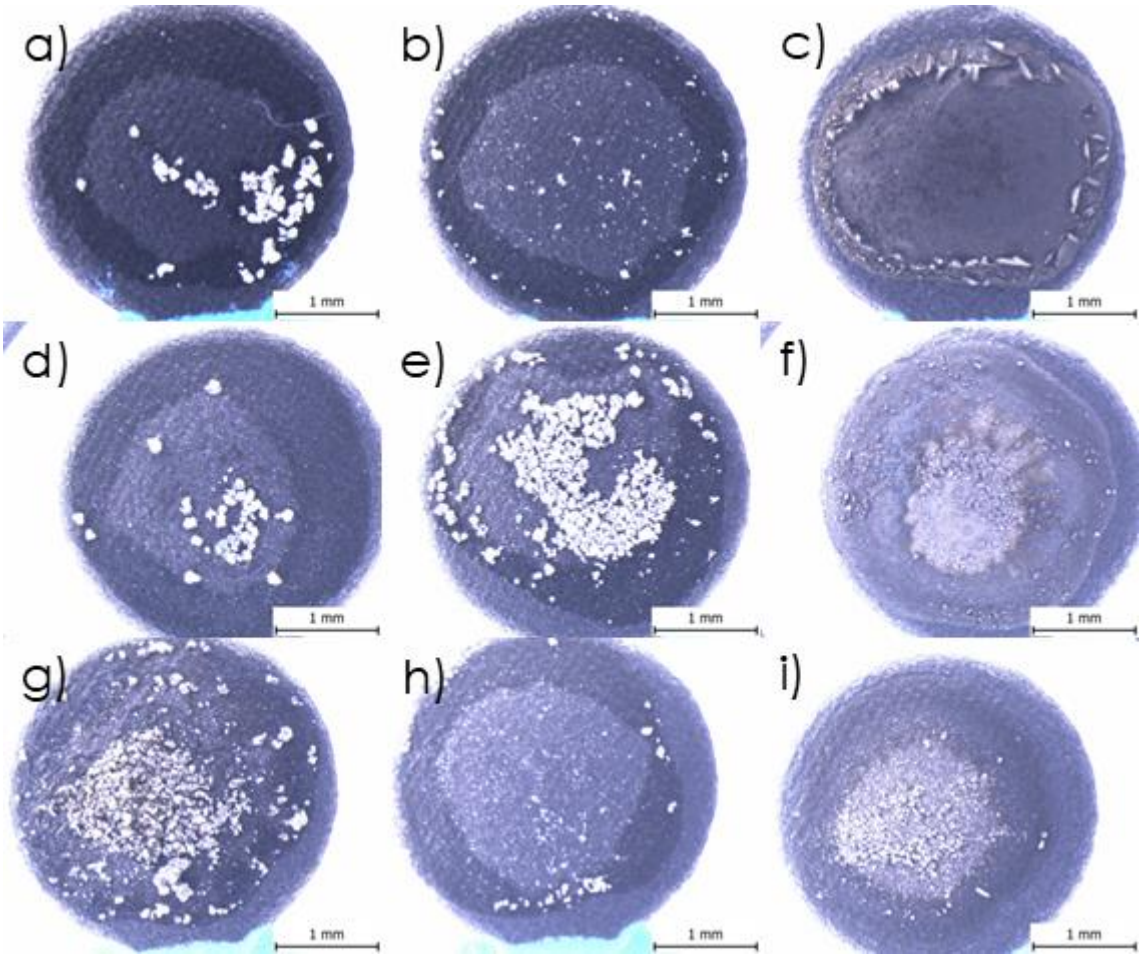

Figure 43. Photos of powders applied to screen-printable electrodes a) P.314.S4; b) P.116.S4; c) P.134.S4; d) P.413.S4; e) P.611.S4; f) P.431.S4; g) P.341.S4; h) P.161.S4; i) P.143.S4.

3.7. Supporting DFT calculations

Some of the interpretations presented later in this dissertation are based on calculations performed as part of a team effort by my supervisor, DSc Andrzej Mikuła, and PhD student Miłosz Kożusznik. These calculations were carried out using the VASP (Vienna Ab initio Simulation Package) software for DFT computations. The detailed computational parameters and results are available in the corresponding publications [245–247].

4. Results

In order to clearly present and describe the results obtained, the experimental part of the work has been divided into three main parts, each describing the results for an individual series. Within each section, a consistent convention has been applied: structural analysis, followed by electrocatalytic property evaluation, and, where applicable, additional complementary studies. Further supplementary parts are presented after these three main sections. The discussion and conclusions begin in Chapter 5.

4.1. $Co_3Fe_3Ni_3S_{8-x}Se_x$ series

4.1.1. Structural investigation

4.1.1.1. XRD analysis

The first structural technique applied to all materials immediately after synthesis, to determine its phase composition (with special emphasis placed on phase-purity), was the X-ray diffraction analysis The single-phase nature of the obtained materials is crucial for comparing their properties based on intrinsic characteristics, as the catalytic activity of multiphase systems may arise from one or both phases, or their activities may overlap or suppress each other – making such systems impossible to reliably compare with others. It is worth noting that these materials were likely the first five-component pentlandites obtained as a single phase worldwide. Figure 44 shows the XRD pattern for the $TM_9S_{8-x}Se_x$ series.

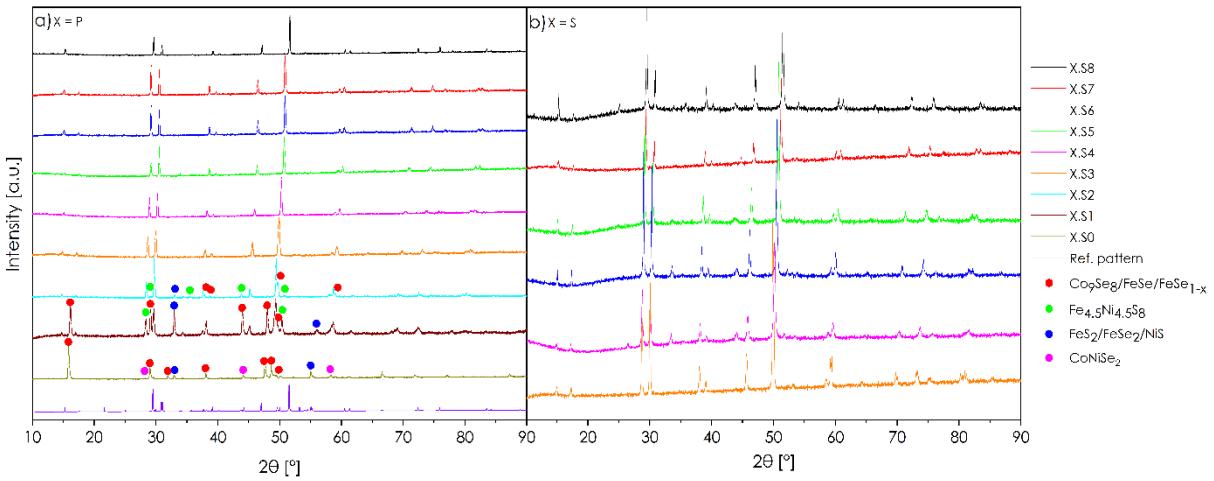

Figure 44. XRD patterns of the $TM_9S_{8-x}Se_x$ series in the form of a) powders and b) sinters.

Previous studies [210,245,247] report that selenium solubility limit in the pentlandite structure is approximately 65 mol% for bimetallic systems. The XRD patterns shown in Figure 44a support this finding, as they reveal that the trimetallic pentlandite with selenium, specifically $TM_9S_3Se_5$, remains a single-phase structure. Based on DFT calculations, the formation energy of trimetallic pentlandites as well as all experimentally observed phases in the form of mono- and bimetallic chalcogenides was determined. Although the gradual addition of selenium increases the formation energy of trimetallic

pentlandites (i.e., makes it less negative), the values remain negative across the entire S–Se composition range. Importantly, up to the critical composition (S_3Se_5), the overall formation energy of the pentlandite phase is still lower than that of Co_9Se_8, $Fe_{4.5}Ni_{4.5}S_8$, or the individual sulfides observed experimentally above this limit. Beyond this selenium content, however, the multiphase assemblage becomes thermodynamically more favorable. Therefore, the selenium solubility limit is governed not by steric effects related to the S/Se ratio, but by thermodynamic constraints. Moreover, the fact that Fe- and Ni-rich pentlandites (Fe_9S_8 and Ni_9S_8) cannot be synthesized using the method described in this thesis (and are not experimentally observed, such as Fe_9Se_8 and Ni_9Se_8) [212,213], while Co-rich monometallic pentlandites crystallize naturally (Co_9S_8) and can be easily synthesized as pure-phase materials [68,248] (even the Co_9Se_8 can be synthesized [249]) which is consistent with the DFT calculations. Based on the observations above, subsequent studies in this series exclude multi-phase materials (S2, S1, S0). XRD analysis of the pellet surfaces made from single-phase pentlandite powders (Figure 44b) shows that the multimetallic pentlandite, with equimolar amounts of metals on the catodic sublattice, remains single-phased even after sintering in 400 °C. Accordingly, this partial objective of the thesis was accomplished at an early stage, as the selenium solubility limit in trimetallic pentlandites could be clearly established [245].

4.1.1.2. Vegard's law

The detailed Rietveld analysis, including fitting parameters and unit cell data, is provided in the Supporting Information. All samples exhibit a Goodness of Fit (GoF) below 10 (with most below 3), indicating accurate structural characterization in the XRD studies. For the $Co_3Fe_3Ni_3S_{8-x}Se_x$ series, the GoF value increases due to changes in the intensity ratio of the reflection doublet around 30° 2θ as the Se content increases. A detailed Rietveld analysis (Table S1) of these reflections suggests that selenium predominantly occupies the 8c position, which causes the reflection to deviate from the ideal pattern [74]. This trend is shown in Table S1 and visually represented in Figure 45, which depicts the main diffraction peaks of each sample in the series. The unit cell size increases almost linearly with each sample in the solid solution range. This is accompanied by a clear shift of the corresponding XRD peaks toward lower angles, in accordance with Vegard's law. This analysis supports the first thesis of this dissertation, which posits that the solubility limit of selenium in trimetallic pentlandite-structured materials is reached at the $Co_3Fe_3Ni_3S_3Se_5$ composition, beyond which solid solutions no longer form.

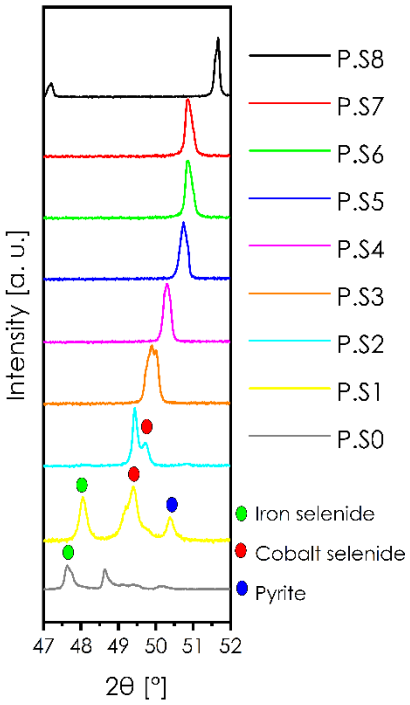

Figure 45. The influence of Se concentration on the position of the most intense reflection peak at Q_v ~ 51.8°.

4.1.1.3. SEM + EDS analysis

Figure S1–Figure S5 show the SEM-EDS images for the $TM_9S_{8-x}Se_x$ series. SEM observations, supported by XRD analysis, were performed only on the materials that remained single-phased, from the TM_9S_8 to $TM_9S_3Se_5$ compositions, as these were the only compositions subjected to electrochemical testing. Based on EDS elemental maps, almost all the samples investigated showed uniform elemental distribution. Only a few maps showed small precipitates of pure Fe (P.S4; I.S5; I.S4; S.S4; S.S3), but they were small and sparse enough not to significantly affect the overall composition of the materials. Notably, the high-temperature treatment did not affect the phase-purity and elemental homogeneity of the materials in this series.

4.1.2. Catalytic properties

As described earlier, the evaluation of electrochemical properties of materials involverd several steps: determination of the ECSA (via C_{dl}) and RF measurements, analysis of water-splitting activity from voltametric curves and Tafel slope evaluation, and finally assessment of material stability during operation.

4.1.2.1. ECSA, RF, C_{dl}

Because not all the samples were measured on the same equipment, there are several differences in the approach to various issues, such as the geometric area of the measured sample, electrochemical scanning rate, and IR-drop correction. In presenting data, it is specified whether the measurements were performed on *MTM Anko* or *Gamry* equipment.

For all pellet and ingot samples tested with the *MTM Anko* setup, the geometric area varied due to the manual sealing of the sample with silicone. To determine the geometric area of these samples, a photo of the constructed electrode – consisting of the glass holder, silicone, and bulk material – was taken, and the area was calculated using the *ImageJ* program (Figure S6). For bulk samples measured on the *Gamry* system, this process is simpler, as all samples have the same geometric area, determined by the shape of the dedicated holder. The geometric area of powder samples was determined based on the surface of the substrate: the *DRP-110 nLab* screen-printed electrode. Table S2 provides a summary of the geometric areas for all measured samples, along with a note on which measurement equipment was used during the electrochemical tests.

Due to variations in the geometric area of most samples and the significantly greater influence of ECSA on electrochemical performance, C_{dl} measurements were conducted to calculate both the ECSA and the RF. However, due to differences in their geometric area, better parameters for this are ECSA and RF, determined directly from the C_{dl}.

Table 3 summarizes the values of C_{dl}, ECSA and RF of all samples before and after stability tests. Figure S7-Figure S12 shows CV and Figure 46 show C_{dl} values for $Co_3Fe_3Ni_3S_{8-x}Se_x$ series.

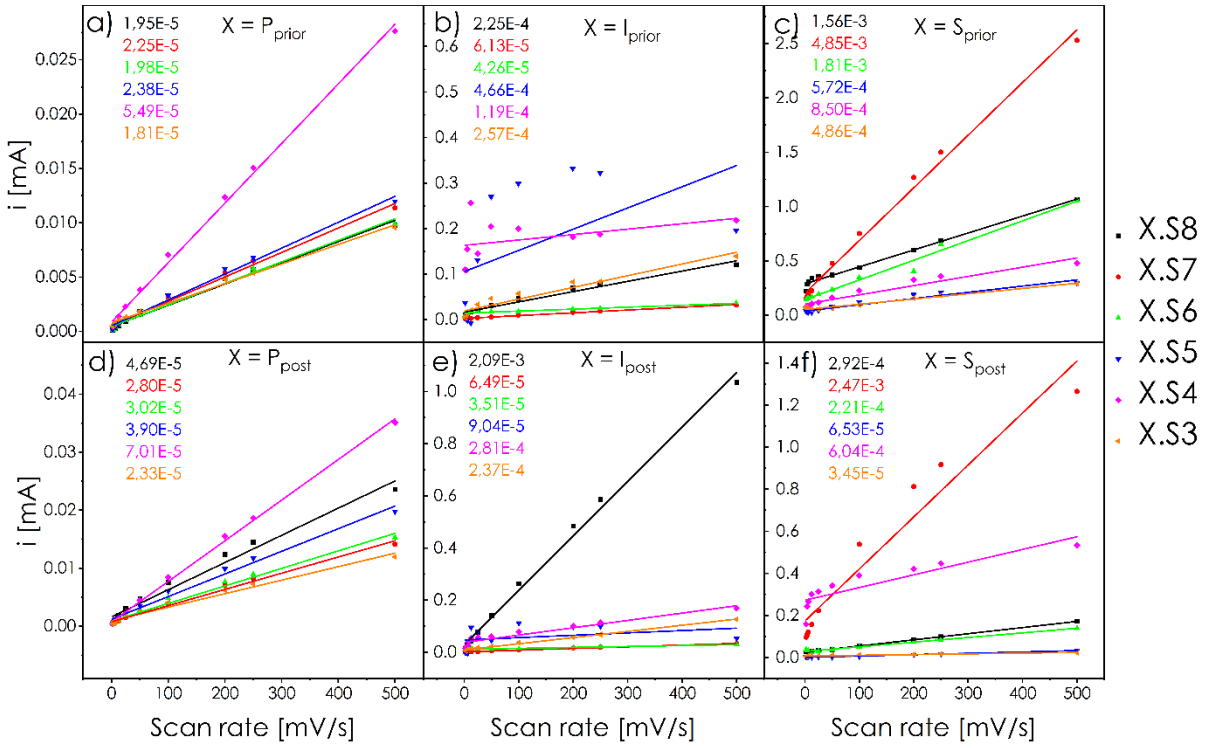

Figure 46. Charging current densities representing C_{dl} for $Co_3Fe_3Ni_3S_{8-x}Se_x$ series for a) pellets before; b) ingots before; c) powders before; d) pellets after; e) ingots after; f) powders after chronoamperometry. Numerical colored data indicates the slope – C_{dl}.

Upon examining Figure 46a and d, a clear correlation can be observed: larger surface areas correspond to higher values of ECSA for the materials, which is explained by the increased amount of active sites. However, despite higher ECSA values for the powder and ingot samples, the pellet samples in the $Co_3Fe_3Ni_3S_8$-S_3 series exhibit the highest RF values, which correlates with the highest C_{dl} observed for this form of the material, and suggests that although pellets expose less geometric area, their surface is significantly more electrochemically active per unit area, possibly due to higher surface roughness or more efficient utilization of active sites.

For samples with a high Se ratio, the formation of sulfur vacancies may be limited by low sulfur content or poor surface development (as seen in the pellet samples). In such cases, the high concentration of Se could create an alternative form of active sites in intermetallic positions, which may explain the high ECSA and RF values observed for the S.S7 sample.

The first general observation is that pellet samples exhibit significantly higher ECSA values (Figure 47a) and show greater changes during chronoamperometry tests compared to other sample forms, particularly powders. RF values follow the same trend: they are higher for pellets, intermediate for ingots, and lowest for powders. This trend is directly related to the number of active sites: the more advanced the surface preparation, the greater the tendency to generate active sites.

In comparing the cationic equimolar series, additional conclusions can be drawn. The activation process is observed mainly for powders, most likely due to their large exposed surface area. However, the magnitude of this effect is small and may partly originate from systematic or measurement errors.

A clearer correlation is seen in the RF values (Figure 47b), which decrease systematically with increasing selenium content, indicating that sulfur depletion is the dominant mechanism of active-site formation. On the other hand, the ΔECSA values for bulk samples (ingots and sinters) become less positive with higher selenium contents, suggesting that active sites on the surface are not blocked, but rather that other types of active centers are being formed. These are most likely assicoated with intermetallic positions, as the larger selenium atoms systematically elongate TM-Ch bonds [226,245,247]. The simultaneous weakening of TM–S bonds facilitates the formation of vacancies, which in turn suggests that there exists a critical selenium concentration that positively influences the mechanisms of active-site formation related to *sulfur depletion* mechanism.

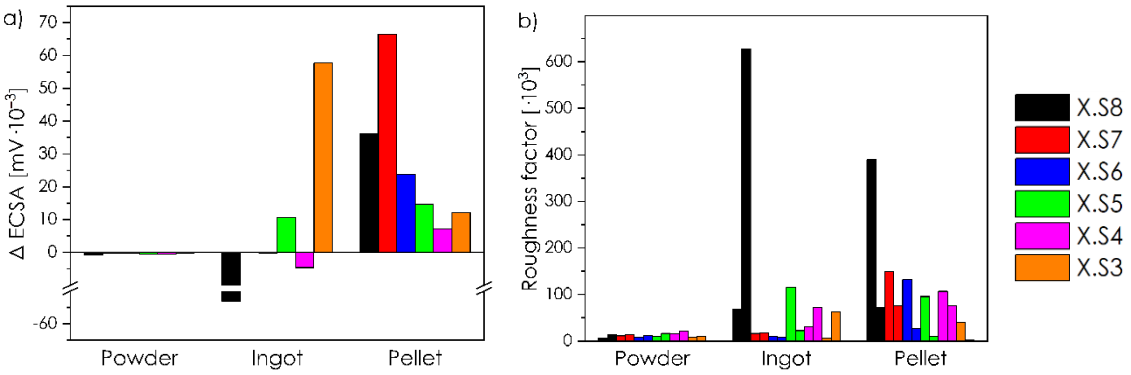

Figure 47. Graphical illustration of a) ΔECSA and b) RF for $Co_3Fe_3Ni_3S_{8-x}Se_x$ series.

4.1.2.2. Polarization resistance

Electrochemical impedance spectroscopy (EIS) measurements were carried out to determine the charge-transfer resistance (R_{CT}) and ohmic resistance (R_u), as shown in Figure 48 and in Table S4. The general trend in this series appears to be clear: the higher the density, and consequently the greater the interparticle contact, the lower the recorded values of R_u and R_{CT}, following the order of highest values for powders and significantly lower values for ingots and sinters. Within individual sample forms, no clear dependence is observed between selenium concentration and either R_{CT} or R_u, with the exception of powder electrodes, where an increase in selenium content correlates with a decrease in R_u. This can be attributed to the degree of electrode coverage (the higher the coverage, the better the contact), the increasing metallic character of Se-rich compositions, as well as the average linear grain size within this powder series. Considering the potential implications for HER efficiency, selenium content does not appear to significantly affect charge-transfer abilities. Therefore, any correlations are more likely to arise from morphological factors, or from the influence of selenium on the electronic structure and/or the limitation of *sulfur depletion* mechanisms. For future analysis, it is also worth noting that sample I.S4 exhibits a significantly higher R_{CT} compared to the rest of the series, which is most likely the result of experimental errors and may be relevant during data interpretation.

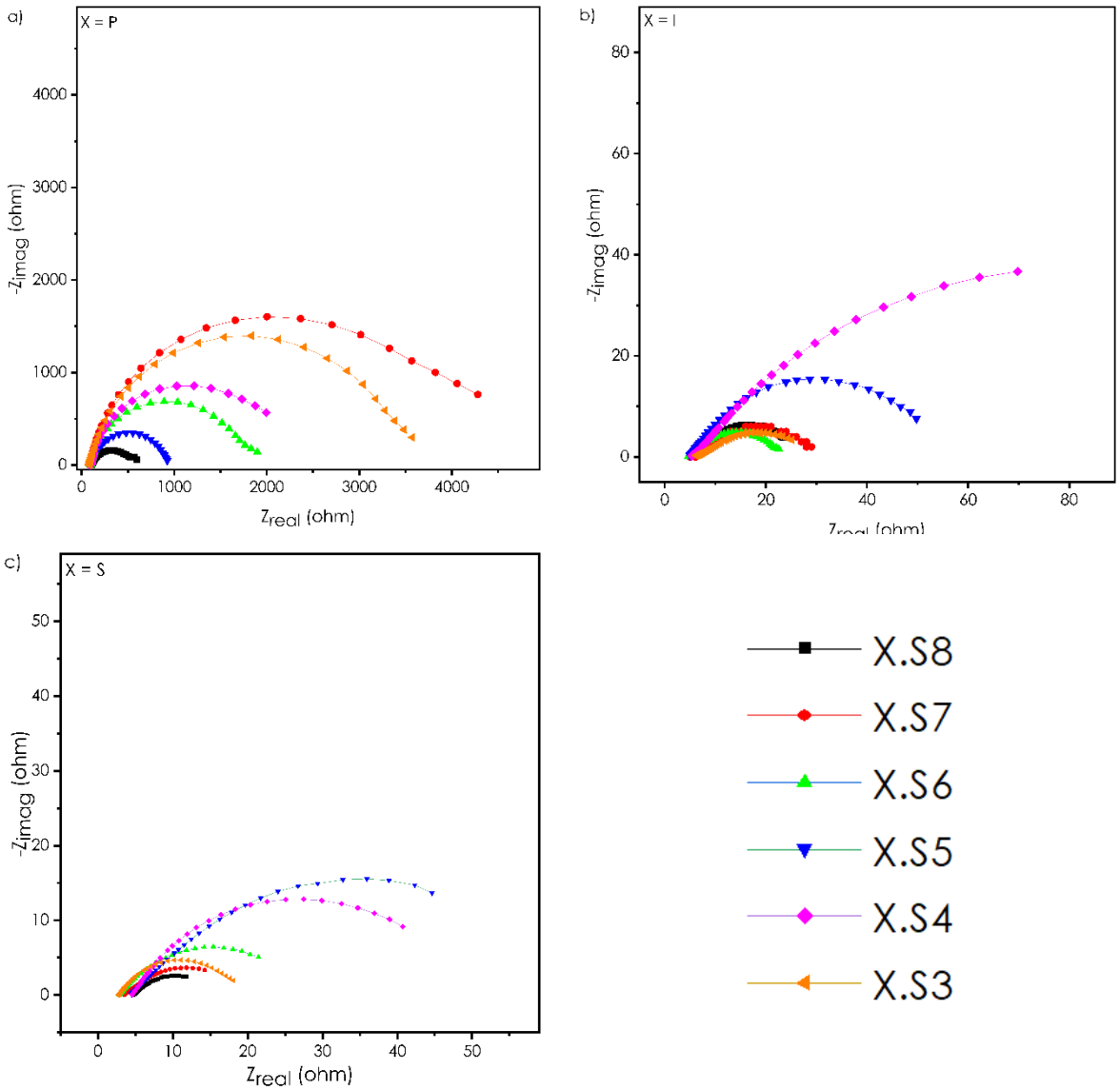

Figure 48. Nyquist plots for a) powders; b) ingots and c) pellets from the $Co_3Fe_3Ni_3S_{8-x}Se_x$ series.

4.1.2.3. HER

As shown in Figure 49a and d, which display the LSV curves for the first $Co_3Fe_3Ni_3S_{8-x}Se_x$ series in powder form, a clear trend can be observed: as the selenium content increases, the electrochemical performance decreases, which stay in contrast to the recorded R_u values. Additionally, the influence of chronoamperometry, a short stability test, is evident. Before the stability test, materials with small amounts of selenium (especially P.S7, P.S8, and P.S5) exhibit the best electrochemical performance. However, after the stability test, two materials stand out – those with a small amount of selenium (but not completely absent): P.S7 and P.S6, reaching $\eta_{0.2ECSA}$ of 481 mV and 510 mV, respectively. This behavior suggests a combination of two factors: *sulfur depletion*, which is more effective at higher surface development, and the introduction of additional active sites associated with an increased TM–Ch bond length due to the larger selenium atom.

According to the calculations carried out by our team, both Se incorporation and S vacancies shift the d_{bc} toward the Fermi level. This applies to single point defects as well as to increasing concentrations of Se

or S vacancies. These observations are consistent with the bonding trends: as the selenium content increases, the TM–Ch bonds become weaker and longer, which in theory facilitates the *sulfur depletion* mechanism and leads to the formation of new, Se-related active sites (although these are less favorable for proton adsorption). On the other hand, a high selenium content reduces the amount of sulfur available for removal, once again suggesting the existence of a critical selenium concentration that is beneficial for HER. This interpretation is also supported by the best catalytic performance observed for compositions with a small selenium addition [74,210,247]. .

As mentioned earlier, the best results are achieved by combining these effects, with vacancies located in the 24e site and Se in the 8c site [74,246]. When the surface area is large, the effects of *sulfur depletion* are not limited, which may explain why the P.S7 sample performs the best in this series. Another factor contributing to its performance could be the particle distribution on the electrode. This is the only sample where the particles have a uniform, unimodal distribution, while the other powders show bimodal distributions with the second peak being much smaller. This suggests that particles around 400 nm are the most effective for catalytic applications. Larger and smaller particles exhibit lower performance, although it remains uncertain whether this is due to particle size or chemical composition. Nonetheless, the performance of P.S7 is likely due to its intrinsic properties, with the particle size distribution further supporting its superior performance.

The powders normalized to geometric area exhibit the same trend as those normalized to ECSA, but they do not reach η_{10}. This discrepancy could be due to uncertain and random electrode surface coating, which necessitates considering the entire surface of the electrode. Nevertheless, the P.S7 sample still demonstrates the best performance, and the activation process for samples with small amounts of selenium remains clearly visible.

In the case of bulk materials, it is visible that ingots and pellets exhibit distinct performances. Among the ingot samples, I.S7 again demonstrates the best performance in terms of both ECSA and geometric area. However, the general trend differs from that seen in the powder series. Still, the S-rich compositions (I.S8 and I.S7) deliver the best results, with a noticeable increase after activation during the stability test. In contrast, I.S4 and I.S3 - ingots with the highest selenium content – show significantly better performances in comparison to powders with analogous Se content. This suggests that intrinsic properties, such as changes in the d_{bc} caused by Se addition and the associated longer TM-Ch bonds, begin to play a more significant role as the surface area decreases [245,247].

For the pellet series, there is a clear correlation between selenium content and performance: the higher the selenium content, the better the HER performance, in contrast with the powder and ingot series. In the pellet series, S.S8 has the worst HER performance, while Se-rich samples like S.S3 and S.S4 exhibit the best overpotentials and current densities. This suggests that when surface development is limited, and activation is restricted (due to smaller ECSA and higher Se content), intrinsic properties

– such as the d_{bc} offset and longer TM-Ch bonds – along with the presence of additional active centers facilitated by higher Se content, become crucial for HER performance [247].

The slight decrease after chronoamperometry in HER performance observed for sintered pellets can be attributed to their relatively small ECSA, which leads to the blocking of active sites and, potentially, partial oxidation of the surface (as indicated by high values in the C_{dl} curves). The only increase in registered overpotential during prolonged electrolysis tests among the pellets is observed for the S.S4 sample – $\eta_{0.2ECSA}$ equal to 309 mV and 307 mV before and after chronopotentiometry tests, respectively. One possible reason for this is that with an equimolar S:Se ratio, both anions adopt a specific order in the structure (for example, Se predominantly occupies 8c sites and S predominantly occupies 24e sites), which facilitates *sulfur depletion* mechanisms [74]. However, this behavior may also be influenced by the randomness associated with the preparation of the working surface.

It is important to note that bulk materials (both sinters and ingots) do not show macroscopic changes in microstructure, and their chemical composition remains mostly unchanged during the electrolysis process, as observed in the SEM+EDS micrographs. Additionally, when normalizing to ECSA, S.S3 shows better performance (almost on par with S.S4) compared to that normalized to a geometric area. This suggests that the S.S3 composition has favorable kinetics, including a high number of active sites. In addition, sintering the materials with high content of Se results in a high concentration of defects, which leads to the creation of effective percolation paths, confirmed by residual cathodic currents increasing with the content of selenium [247].

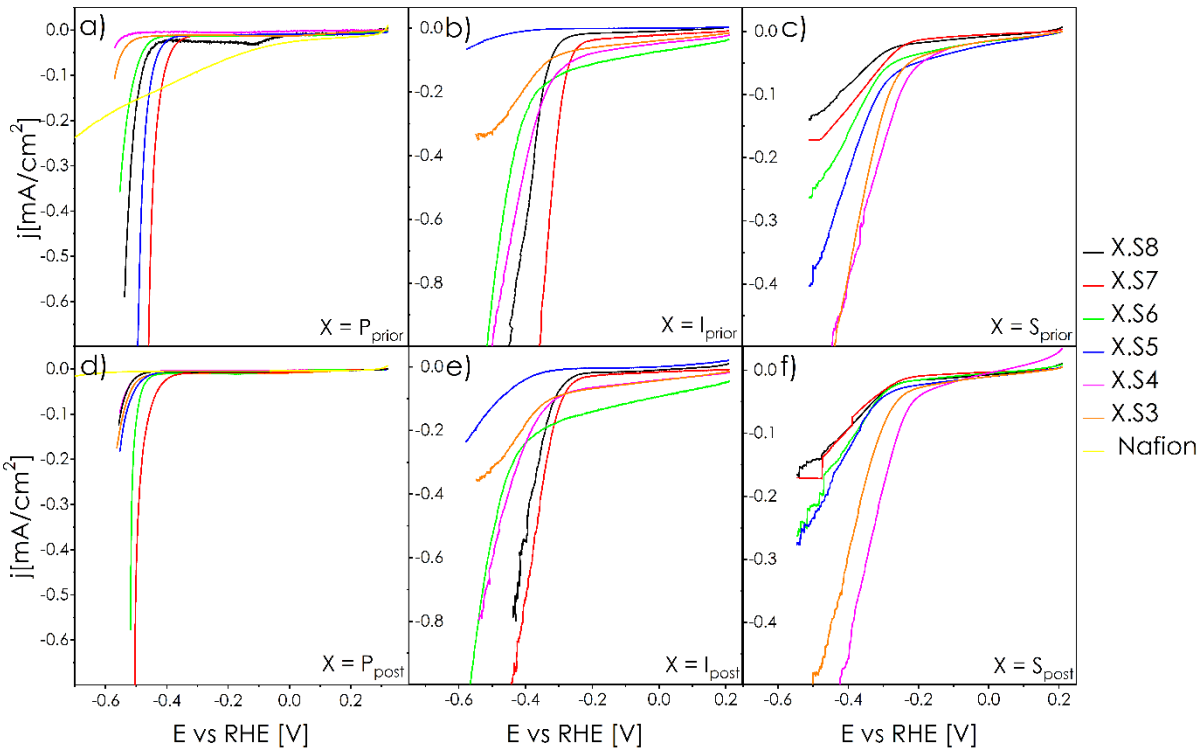

Figure 49. LSV voltammograms recorded at a sweep rate of 6.25 mV/s in 0.5 M H_2SO_4 for $Co_3Fe_3Ni_3S_{8-x}Se_x$ series normalized to ECSA for: a) powder samples before chronoamperometry; b) ingot samples before chronoamperometry; c) pellet samples before chronoamperometry; d) powder samples after chronoamperometry; e) ingot samples after chronoamperometry and f) pellet samples after chronoamperometry.

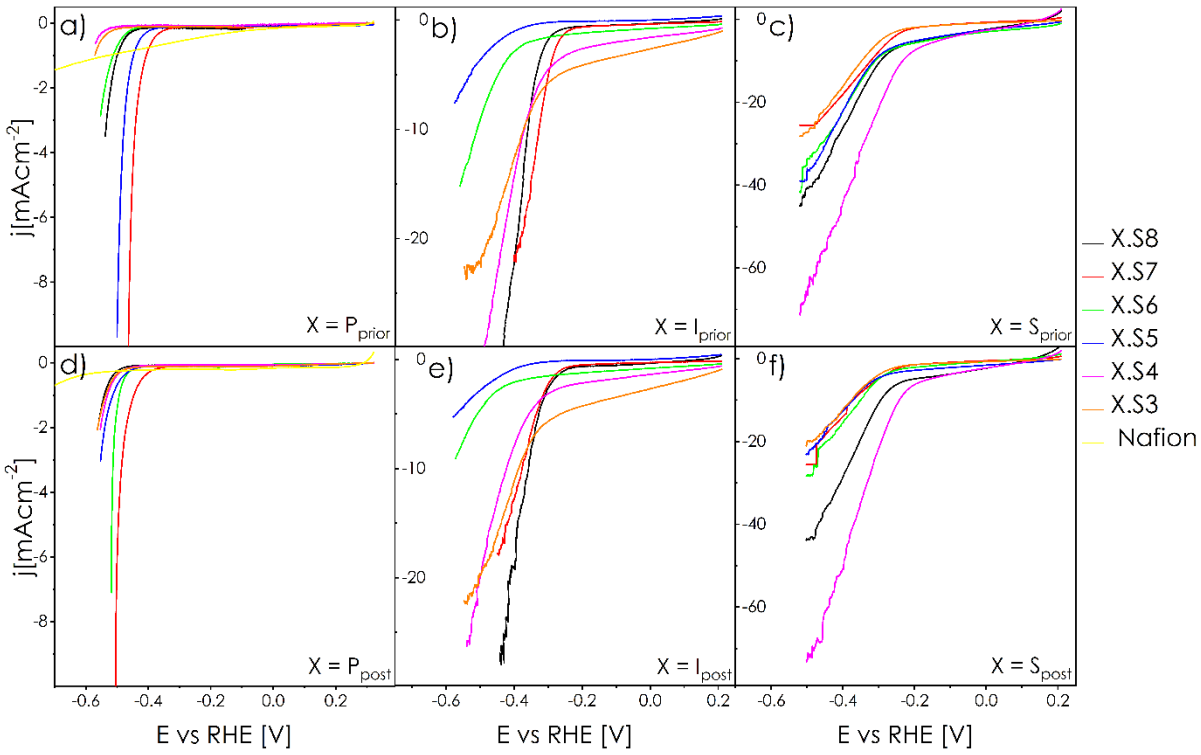

Figure 50. LSV voltammograms recorded at a sweep rate of a 6.25 mV/s in 0.5 M H_2SO_4 for $Co_3Fe_3Ni_3S_{8-x}Se_x$ series normalized to geometric area for: a) powder samples before chronoamperometry; b) ingot samples before chronoamperometry; c) pellet samples before chronoamperometry; d) powder samples after chronoamperometry; e) ingot samples after chronoamperometry and f) pellet samples after chronoamperometry.

4.1.2.4. Tafel slope

Figure 51 and Figure 52 show the Tafel slopes for the first group, the $Co_3Fe_3Ni_3S_{8-x}Se_x$ series, before and after chronoamperometry. The Tafel slopes obtained for powders (Figure 51a, d and Figure 52a, d) are favorable, with values below 90 mV/dec, suggesting a Volmer-Tafel mechanism with only a slight tendency to increase (which would decrease reaction kinetics) as the selenium content rises. This trend is in line with earlier studies (e.g., presented by Smialkowski et al. for bimetallic systems [210] which also indicates that selenium has an adverse effect on HER kinetics in pentlandite-type materials. After chronoamperometry, higher Tafel slopes are observed, which can be attributed mainly to the blocking of a fraction of the active sites, reducing the number of electrochemically accessible centers [210,247].

Interestingly, the Tafel slopes of powder electrodes do not match those of the ingot samples, which also differ significantly from the pellets, following ECSA and RF values. This discrepancy highlights the significant influence of material form on hydrogen evolution kinetics, but in this case, it is most likely caused by limited contact between the powder and the substrate, which slows down the reaction kinetics in accordance to R_u values presented in the previous sections. For ingot samples (Figure 51b; e; Figure 52b; e), the best kinetics are shown by the I.S8 and I.S7 samples, with Tafel slopes below 100 mV/dec, indicating a Volmer-Tafel mechanism. However, as the selenium concentration increases, the Tafel slopes systematically increase, with I.S3 reaching the highest value (over 200 mV/dec), suggesting an unfavorable Volmer-Heyrovsky mechanism, again suggesting unfavorable influence of selenium on HER kinetics.

Pellet samples (Figure 51c, f; Figure 52c; f) exhibit the highest Tafel slopes among all the $Co_3Fe_3Ni_3S_{8-x}Se_x$ series, indicating that the reduced surface development in this form leads to slower kinetics, regardless of the R_u and R_{CT} values. Unlike powder and ingot electrodes, pellet samples do not show a further increase in Tafel slope values after chronoamperometry, instead, the remain stable or even show a slight improvement, most likely due to the better exposure of their surfaces during operation. This behavior highlights the strong influence of material form and density on hydrogen evolution kinetics. Furthermore, It is worth noting that among all solid-state samples, the lowest Tafel slope values are observed for compositions with a small Se addition, particularly X.S7, once again suggesting the presence of an optimal, critical selenium concentration that positively affects the catalytic performance.

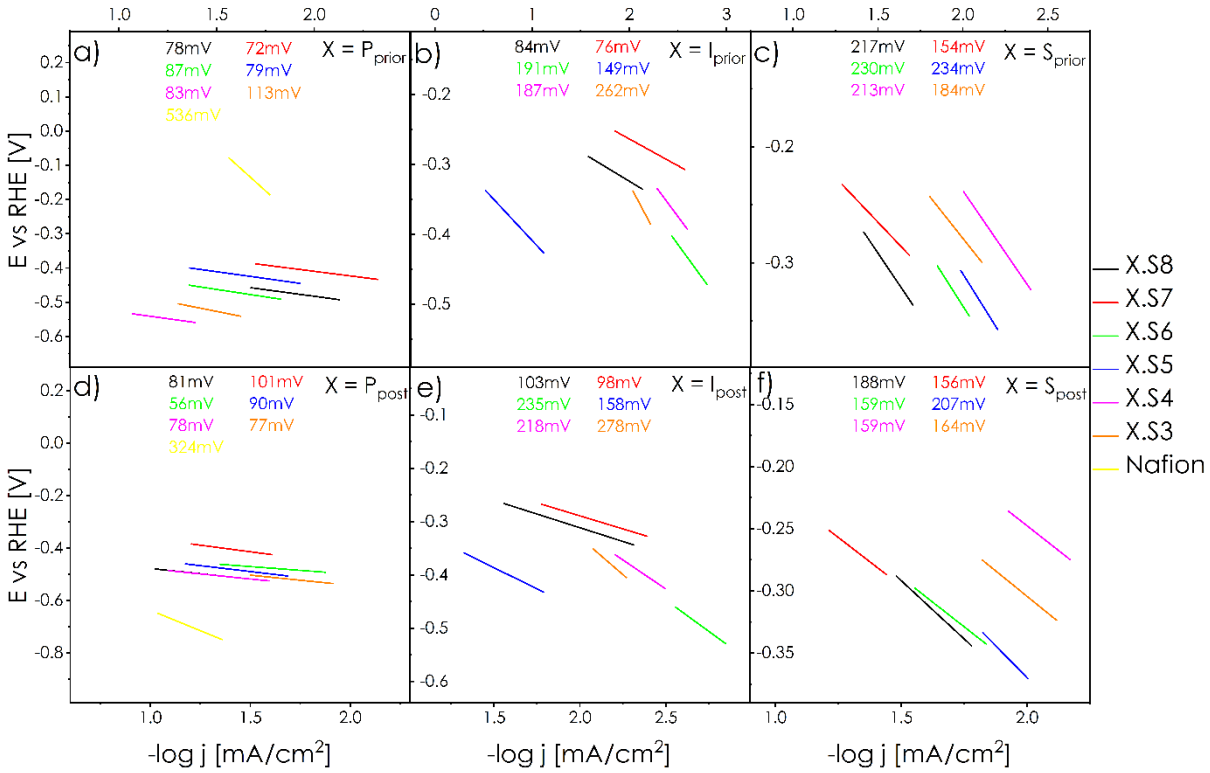

Figure 51. Tafel slope recorded in 0.5M H_2SO_4 at a 6.25 mV/s sweep rate and normalized to ECSA for $Co_3Fe_3Ni_3S_{8-x}Se_x$ series for: a) powder samples before chronoamperometry; b) ingot samples before chronoamperometry; c) pellet samples before chronoamperometry; d) powder samples after chronoamperometry; e) ingot samples after chronoamperometry; f) pellet samples after chronoamperometry.

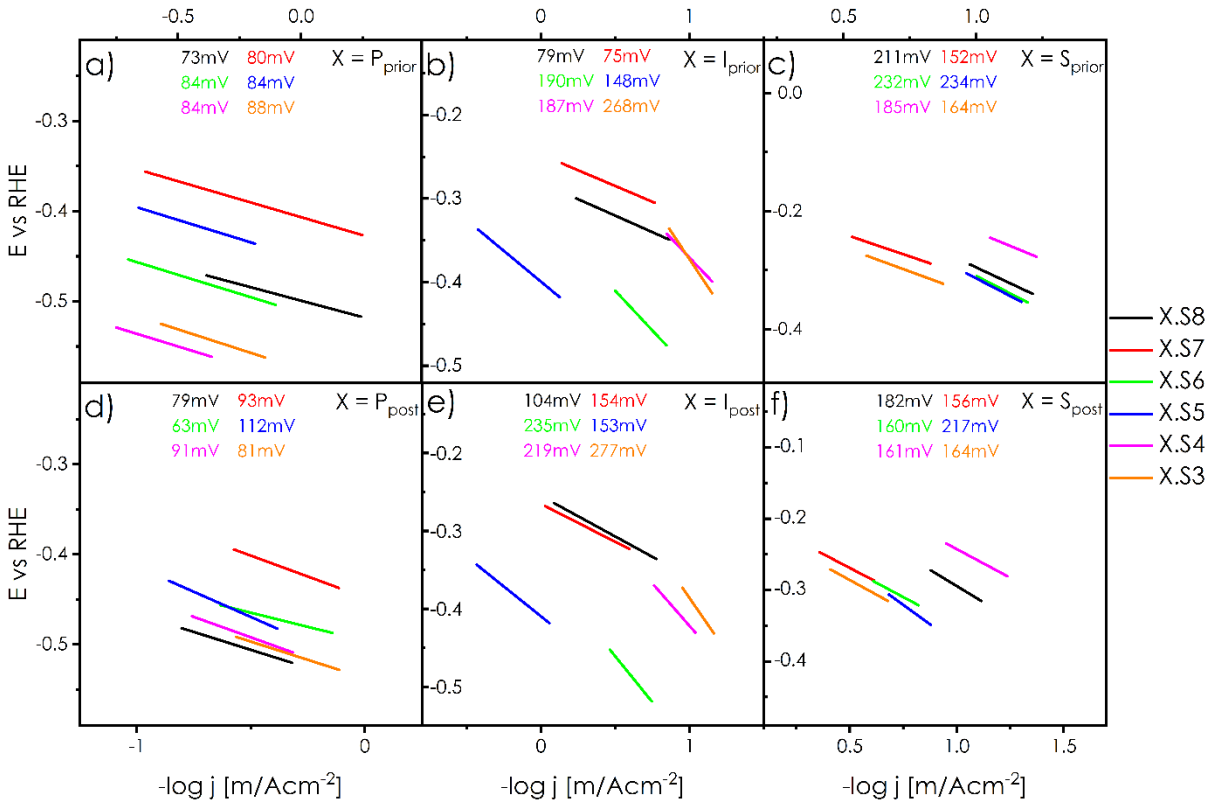

Figure 52. Tafel slope recorded in 0.5 M H_2SO_4 at a 6.25 mV/s sweep rate and normalized to geometric area for $Co_3Fe_3Ni_3S_{8-x}Se_x$ series for: a) powder samples before chronoamperometry; b) ingot samples before chronoamperometry; c) pellet samples before chronoamperometry; d) powder samples after chronoamperometry; e) ingot samples after chronoamperometry; f) pellet samples after chronoamperometry.

It thus appears that selenium deteriorates the reaction kinetics, which is consistent with literature data; however, it positively affects the electronic structure and masks the influence of the cationic composition, resulting in the highest current densities observed for bulk samples. Among all series, X.S7 deserves particular attention – as the beneficial effect of selenium seems to be most optimally expressed in this composition: it improves the metallic character and band structure, while still retaining a high sulfur content, which provides active sites preferentially interacting with protons. At higher selenium contents, this effect becomes dependent on the material form; nevertheless, it appears evident that an excess of selenium partially blocks the sulfur-rich surface.

4.2. $Co_{9-x-y}Fe_xNi_yS_8$ series

4.2.1. Structural investigation

4.2.1.1. XRD analysis

In the $Co_{9-x-y}Fe_xN_yS_8$ series, where cationic sublattice was altered, determining the chemical composition range characterized by single-phase pentlandite structure was less straightforward. As shown in Figure 53a, nearly all products remain single-phase immediately after synthesis, except for those with high amounts of Ni (P.116.S8) or Fe (P.341.S8 and P.161.S8). Almost all samples undergo phase decomposition after sintering, with reflections corresponding to phases such as Fe, NiS, and FeS. As previously discussed, monometallic composition can only be achieved for Co-rich systems, while bimetallic Fe- or Ni-rich compositions remain single-phased only when the amounts of Fe and Ni are comparable. An excess of either element drives the system beyond the stability range of the pentlandite phase. This suggests that Co-rich systems are more flexible, as cobalt tolerates a wider range of atomic configurations and preserves the structure even in excess. Cobalt also promotes greater lattice order, making the phase more resistant to local distortions. These are the first synthesized trimetallic pentlandites and, as will be shown later in this work, while cobalt does not enhance the catalytic properties compared to the bimetallic system, it significantly improves the structural stability of pentlandite-type materials (Figure 53b).

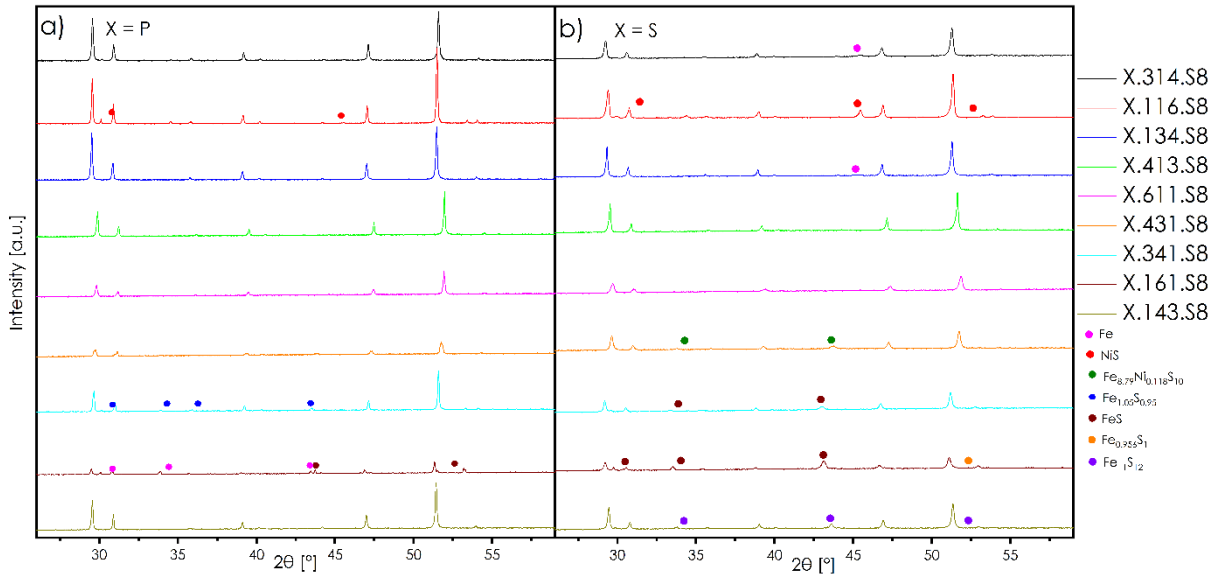

Figure 53. XRD patterns of $Co_{9-x-y}Fe_xN_yS_8$ series in the form of a) powders and b) sinters.

4.2.1.2. SEM + EDS

As shown by the XRD patterns, the synthesized materials for the $Co_{9-x-y}Fe_xN_yS_8$ series, in powder form, contain fewer secondary phases than the pellets. However, SEM+EDS imaging (Figure S13-Figure S17) indicates that, in addition to the limited solubility – particularly of iron – and the tendency toward phase decomposition under reducing and elevated temperature conditions, this series of materials also exhibits significantly lower stability. It is evident that the as-synthesized ingots (Figure S14-Figure S17) contain

considerably fewer chemically (and presumably also structurally) inhomogeneous regions compared to the powders. Only minor iron precipitates are observed in samples I.413.S8 and I.341.S8, most likely resulting from limited solubility or unreacted iron, as well as a clearly biphasic region in sample I.161.S8. This is most likely not a matter of the solubility of iron alone, but rather of the overall limited solubility in the trimetallic system. In such conditions – being the element with the lowest reduction potential among the three – segregates first, either in metallic form or iron sulfides, particularly under reducing conditions. The grinding process, which is inherently high-energy and poses a risk of phase decomposition, further promotes segregation, as seen in the powder images (Figure S13). As a result, not only iron precipitates but also iron sulfides appear almost ubiquitously. Importantly, no Co-rich segregations are observed, which once again highlights the key role of cobalt in stabilizing the pentlandite structure. This study did not investigate whether this process results from pentlandite decomposition or from slow reactions between Fe-rich precipitates and sulfur-rich surfaces.

Moreover, additional phase decomposition is evident during sintering (Figure S15) as only S.314.S8, S.413.S8, and S.611.S8 samples remain chemically homogeneous (Co-rich ones). It must therefore be concluded that, although the system with equimolar cationic composition may be stable, in ternary pentlandites the solubility of Fe (and/or Ni), as well as the stability – especially thermal stability – of these materials, remains significantly reduced, effectively disqualifying these systems from application-oriented work at this stage. This measurement series was nevertheless included, due to the fact that these materials still predominantly exhibit pentlandite as the main phase. However, any comparisons and correlations should be considered at least partially speculative.

4.2.2. Catalytic properties

4.2.2.1. ECSA, RF, C_{dl}

In this section, the ECSA, RF, and double-layer capacitance (C_{dl}) are analyzed for the $Co_{9-x-y}Fe_xN_yS_8$ series. The CV plots are provided in Figures S18–S23, while the corresponding C_{dl} values are summarized in Figure 54**.** The lowest ECSA values are observed in the powder samples (e.g., $5.16 \cdot 10^{-1}$ cm^2 for P.S3), while the highest values are found in the pellet samples (e.g., $1.37 \cdot 10^{2}$ cm^2 for S.S7), particularly when compared to the geometric working area. An increase in density leads to a higher ECSA, especially for samples with a high Fe content. Moreover, the combine presence of Fe and Co further enhances the number of accessible active sites. In contrast, increasing the Ni content appears to suppress this effect. This can be attributed to the electronic influence of Ni, which uniquely shifts d_{bc} away from the Fermi level in the opposite direction compared to Fe and Co, thereby reducing the favorability of hydrogen adsorption in HER (particularly noticeable in acidic environments).

Additional insights can be gained from interpretation after the chronoamperometry tests , which confirm the occurrence of *sulfur depletion* in all powder and most pellet samples. Materials with a high Ni content, or more specifically, those with a large number of high-nickel precipitates on the surface,

do not exhibit an activation process. This is because the Ni precipitates effectively inhibit the H^+ adsorption/desorption processes in these materials.

These results confirm that S-rich pentlandites exhibit the sulfur-depletion mechanism in practically all material forms, with the effect being more pronounced when surface development (powders) or surface exposure (pellets) is higher. The samples richest in Co and Fe provide the highest number of active centers. Taken together, these findings are consistent with the conclusions of the previous chapter, where it was postulated that selenium tends to mask the influence of cations

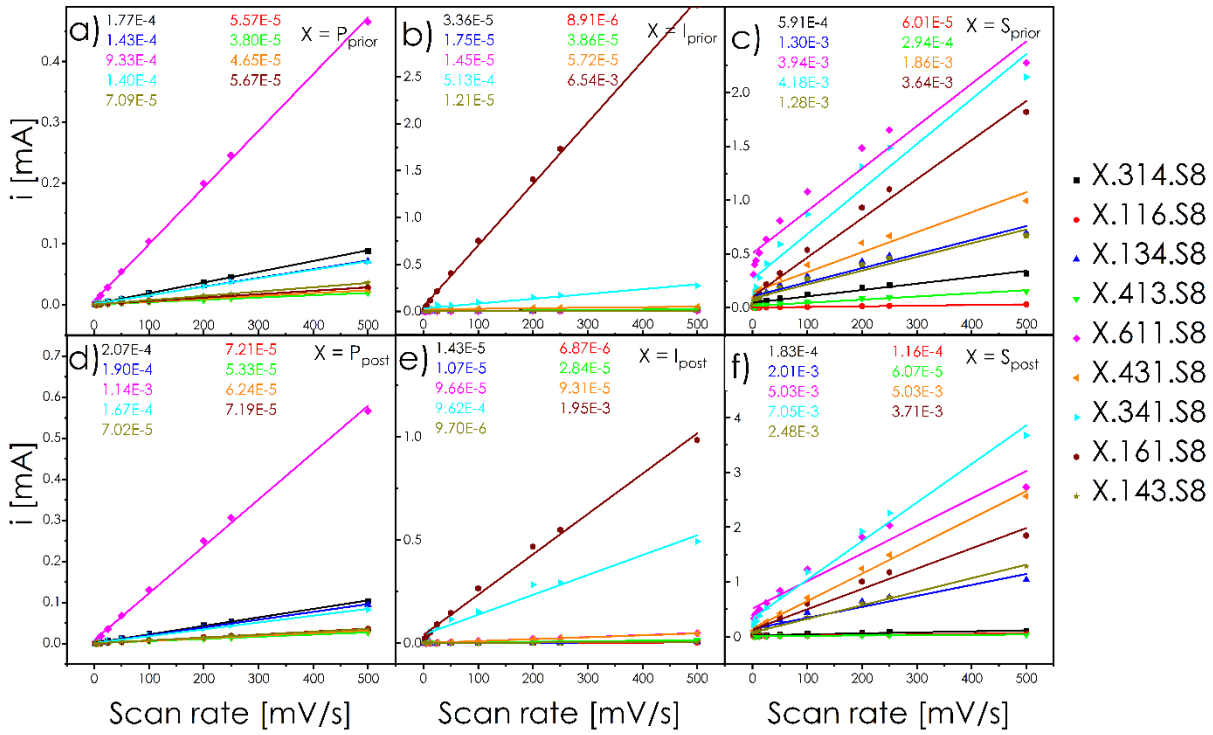

Figure 54. Charging current densities representing C_{dl} for $Co_{9-x-y}Fe_xN_yS_8$ series for a) pellets before; b) ingots before; c) powders before; d) pellets after; e) ingots after; f) powders after chronoamperometry. Numerical colored data indicates the slope – C_{dl}

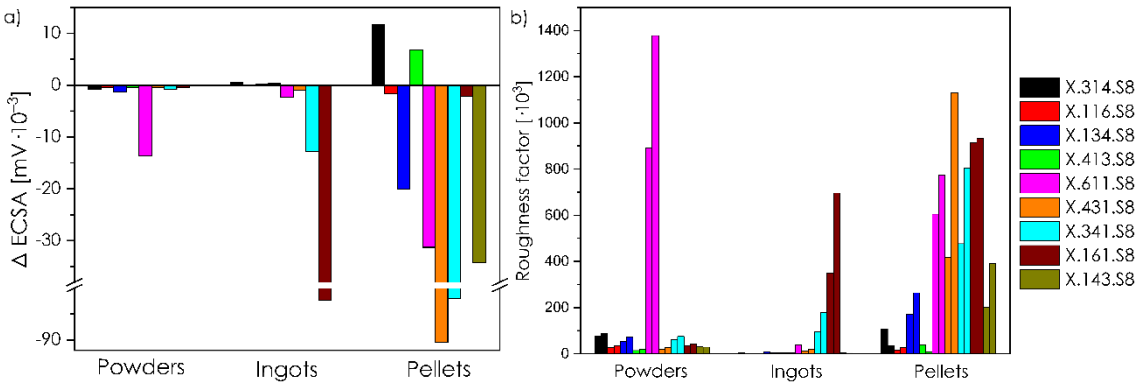

Figure 55. Graphical illustration of a) ΔECSA and b) RF for the $Co_{9-x-y}Fe_xN_yS_8$ series.

4.2.2.2. EIS analysis

A similar trend to that seen in the previous series , where the resistance of sintered pellets is approximately an order of magnitude lower than that of the as-synthesized ingots, and even lower compared to the powders, can be noticed in the $Co_{9-x-y}Fe_xNi_yS_8$ series (Figure 56 and Table S4). This behavior can be attributed to differences in contact resistance, the compactness of the materials, and, to a lesser extent, the higher charge-carrier density and cation mobility in the samples with the greatest resistance values. Sintering leads to densification of the material, thereby facilitating charge transport within the grains[250].

For powders, no clear trends are observed in either R_u or R_{CT}, with the exception of samples P.116 and P.143, which exhibit unusually low R_{CT} values; however, these deviations are most likely incidental. In ingot samples, R_u shows no correlation, while Fe-rich compositions (I.431.S8, I.341.S8, I.161.S8, I.143.S8) display the lowest R_{CT} values. A similar tendency is observed for pellets: no systematic correlation is found for R_u, but again Fe-rich samples exhibit significantly reduced R_{CT}. These results suggest that iron strongly enhances charge-transfer abilities, regardless of whether the material is phase-pure or contains iron-rich precipitates. Consequently, Fe-rich samples can be expected to exhibit the most favorable catalytic properties. At the same time, the clear manifestation of cation-related effects further supports the conclusions of the previous chapter, where selenium was shown to mask the influence of cations.

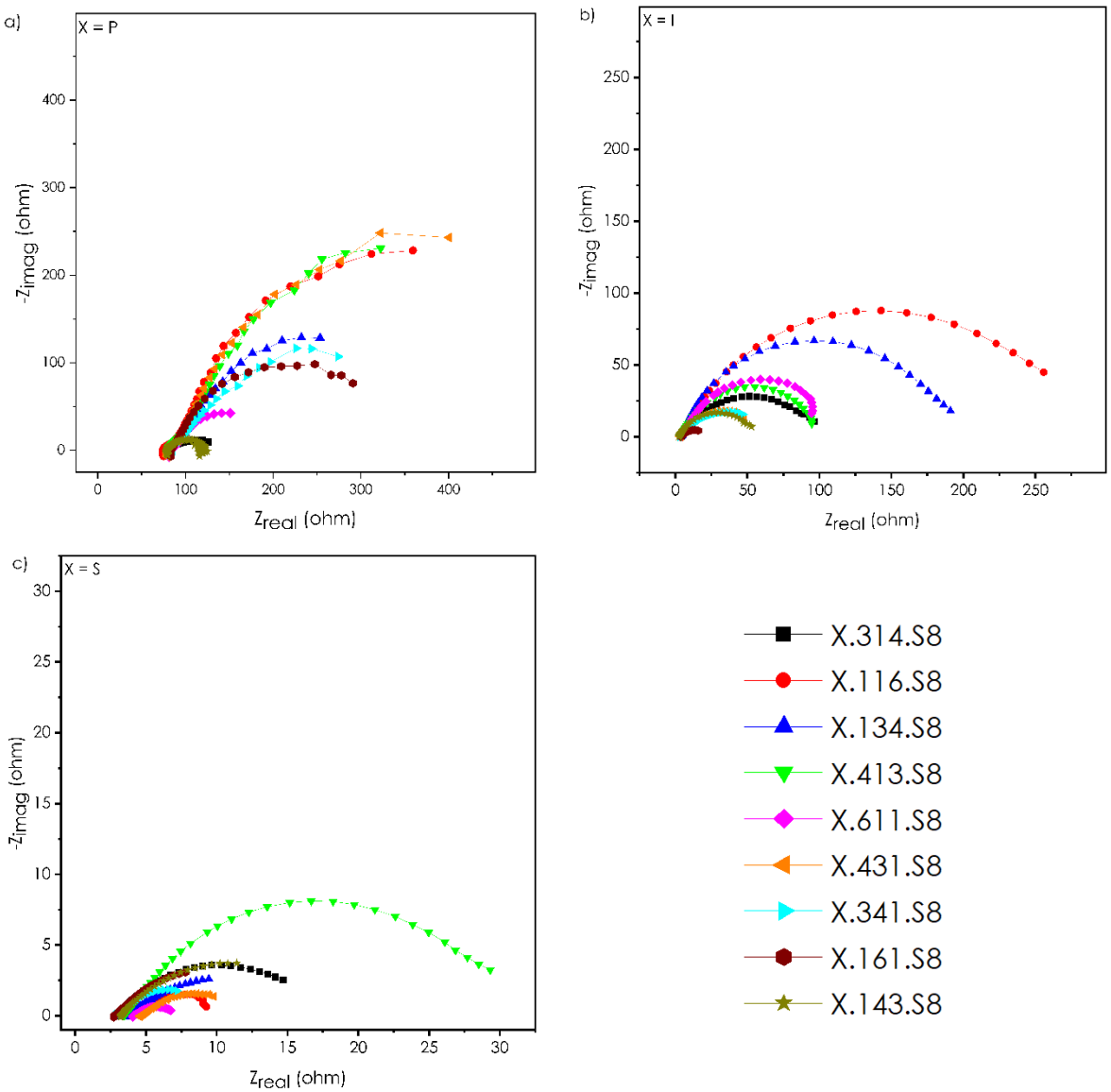

Figure 56. Nyquist plots for a) powders; b) ingots and c) pellets from the $Co_{9-x-y}Fe_xNi_yS_8$ series.

4.2.2.3. HER

Generally, it is assumed that samples exhibiting the highest C_{dl} and ECSA values demonstrate the best HER performance. However, as shown in Figure 57 and Figure 58, which present the LSV curves for the $Co_{9-x-y}Fe_xN_yS_8$ series normalized to both ECSA and geometric area, this assumption does not hold true for all samples. Regardless of the material form, the best performance, normalized to ECSA (Figure 57), appears to be the $Co_{4.5}Fe_{1.5}Ni_3S_8$ composition, which exhibits the lowest overpotential values (e.g. $\eta_{0.2ECSApost} = 465$ mV/cm^2 for powders, or $\eta_{0.2ECSAprior} = 338$ mV/cm^2 for ingots) and enhanced durability. While these values might seem surprising in the context of ECSA, they are typical for pentlandite-like behavior, which highlights the importance of phase homogeneity in the material. Notably, these values are comparable to those of the $Co_3Fe_3Ni_3S_8$ composition, which also demonstrates excellent catalytic properties and durability, where both equimolar cation ratio and the presence of cobalt itself playing a key role in this system [68].

The behavior of these materials, including both $Co_{4.5}Fe_{1.5}Ni_3S_8$ and $Co_3Fe_3Ni_3S_8$ (as well as all other combinations with near-equimolar cationic configuration and a relatively high cobalt content), cannot, however, be directly attributed to the electronic structure of pentlandites. The d_{bc} – while a successful descriptor of catalytic activity in bulk materials with variable selenium content (see previous series) – is generally assumed to correlate positively with activity when it lies closer to the Fermi level. Among the present cations, iron is the one that most significantly shifts the d_{bc}. In this case, however, cobalt appears to play a more decisive role as a structural stabilizer, promoting persistent sulfur bridging and a unimodal distribution of active sites. Moreover, Co-less systems are likely to exhibit a greater tendency toward the leaching of other cations, particularly iron, from the material surface – an effect that should ideally be verified by ICP-OES analysis of the post-electrolysis solution. Unfortunately, measurements were not included at the time when the experiments were conducted. Nonetheless, the above considerations appear well justified, as all near-equimolar systems behave in a similar manner, highlighting the crucial role of cobalt in this trimetallic system. The behavior of sample S.116.S8 deviates from the rest and will be discussed in additional analyses (4.4.2).

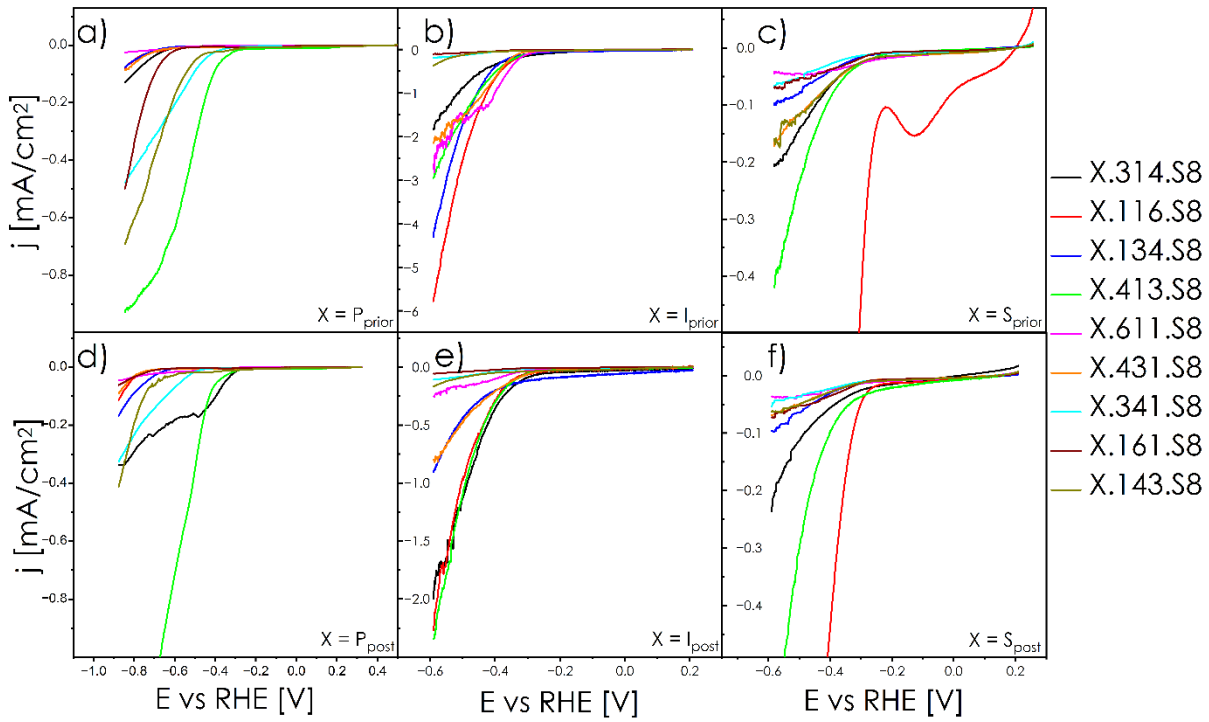

Figure 57. LSV voltammograms recorded at a sweep rate of 6.25 mV/s in 0.5 M H_2SO_4 for $Co_{9-x-y}Fe_xNi_yS_8$ series normalized to ECSA for: a) powder samples before chronoamperometry; b) ingot samples before chronoamperometry; c) pellet samples before chronoamperometry; d) powder samples after chronoamperometry; e) ingot samples after chronoamperometry and f) pellet samples after chronoamperometry.

When discussing the LSV values of the $Co_{9-x-y}Fe_xN_yS_8$ series normalized to the geometric area (Figure 58), completely different conclusions can be drawn. The best-performing samples are the iron-rich compositions, particularly those with high cobalt content (e.g., 161.S8, 431.S8, and 341.S8). There are two possible reasons why the Fe- and Co-rich samples show such high HER performance. First, this could be due to a favorable chemical composition, followed by an optimal d_{bc} position, the highest ECSA/RF values, and the lowest R_{CT}. Second, it is related to phase homogeneity or the result

of catalytically active iron sulfide precipitates on the already catalytically active and well-conductive substrate (pentlandite). The latter effect is highly probable here, as such behavior is not unique to this material, and will be discussed in detail in subsection 4.4.1. This indicates that, while bulk materials are best suited for comparative analysis, parameters determined from cyclic voltammetry – such as ECSA or RF – do not necessarily correlate with the final catalytic performance. However, when referring to the total surface area (geometric area), the influence of chemical composition becomes evident and aligns well with theoretical expectations.

In agreement with the ECSA-normalized results, the long-term stability of these materials shows that those with near-equimolar compositions (e.g., S.431.S8 and S.341.S8) show improved performance after prolonged electrolysis.

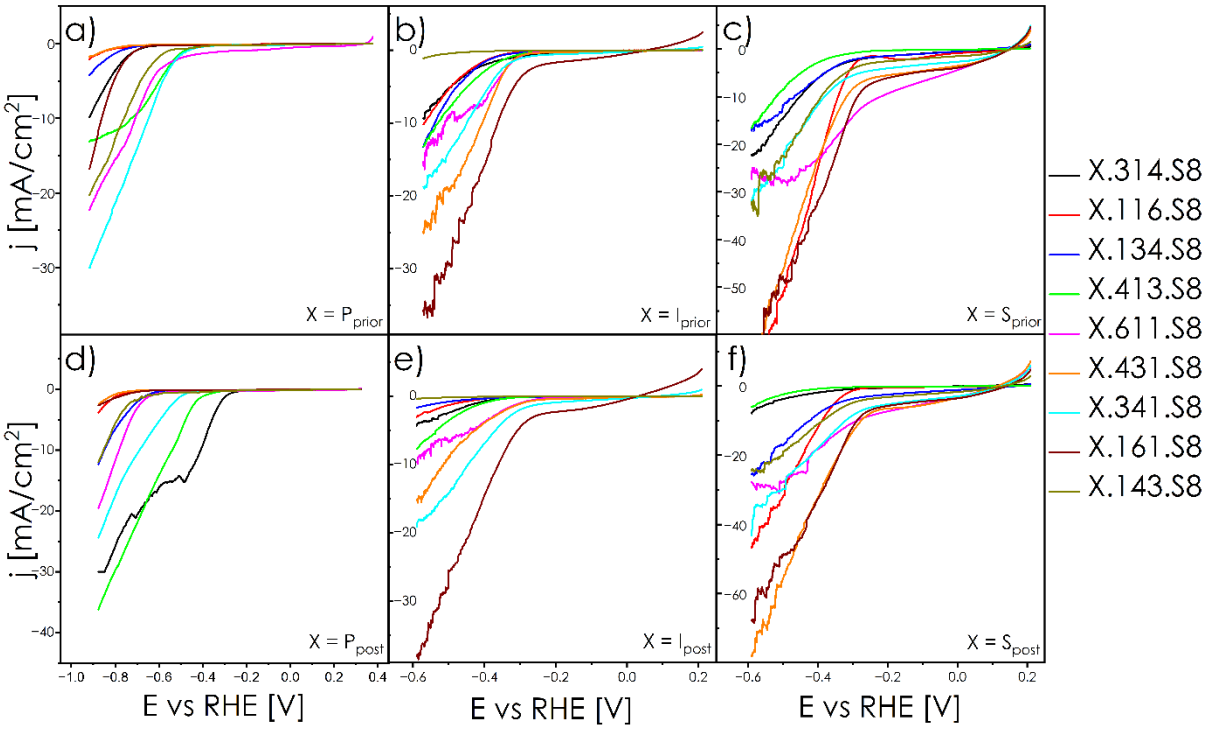

Figure 58. LSV voltammograms recorded at a sweep rate of 6.25 mV/s in 0.5 M H_2SO_4 for $Co_{9-x-y}Fe_xNi_yS_8$ series normalized to geometric area for: a) powder samples before chronoamperometry; b) ingot samples before chronoamperometry; c) pellet samples before chronoamperometry; d) powder samples after chronoamperometry; e) ingot samples after chronoamperometry and f) pellet samples after chronoamperometry.

4.2.2.4. Tafel Slope

In the case of Tafel slopes for the $Co_{9-x-y}Fe_xN_yS_8$ series normalized to ECSA (Figure 59), some general trends can be observed. The interpretation of Tafel slope values for powders is imprecise due to the non-homogeneous coverage of screen-printed electrodes, and a lack of correlation is noticeable for this sample form. Nevertheless, based on the available results, materials rich in iron or cobalt can be identified as the best-performing in terms of reaction kinetics (Figure 59a; d), with Tafel slope values of 116 mV/dec, 136 mV/dec, and 140 mV/dec for P.161.S8, P.413.S8, and P.314.S8, respectively.

In contrast to powder electrodes, the Tafel slopes of ingots (Figure 59b; e) in this series are lower than those of the powders, which may be attributed to the absence of the influence of the screen-printed

substrate - which correlates with the results obtained from EIS. For the ingot samples, the best performers are characterized by Tafel slopes below 100 mV/dec, indicating the desired Volmer-Tafel mechanism, in which proton chemisorption onto the surface occurs rapidly, followed by a limiting recombination reaction on the catalyst surface [246]. These include two samples with a high Co ratio: I.611.S8 and I.431.S8. Interestingly, these two samples remain single-phase and do not show any surface precipitation, which could otherwise block the mechanism responsible for creating active sites. Other ingot samples in this series predominantly follow the Volmer-Heyrovsky mechanism, with no clear correlation between composition and Tafel slope values.

As with the previous series, the surface of the pellet samples appears to be relatively inactive (Figure 59c, f), as evidenced by the high Tafel slope values – much higher than those for the ingots. This can be attributed to their significantly less developed surface area. The lowest Tafel slopes, indicating the highest kinetics, are seen in the iron-rich sample, P.161.S8, and the nickel-rich sample, P.116.S8 (113 mV/dec and 162 mV/dec, respectively), following the highest ECSA/RF and lowest R_{CT} values in this series. However, even these best-performing Tafel slopes suggest a non-preferred Volmer-Heyrovsky mechanism for HER, considering the chemisorption of a solvated proton followed by a reaction with another proton [246]. This may also be caused by foreign phases, such as metallic iron, present on the surface, as well as the exposure to metallic active centers, as described earlier by Smialkowski et al. [68]. . The highest Tafel slope value (466 mV/dec) is observed in the Co-rich sample, I.611.S8. This result suggests that an excessive concentration of cobalt, while positively affecting the material's durability, may bind sulfur atoms too strongly, preventing the creation of sulfur vacancies necessary for the formation of a high concentration of active sites.

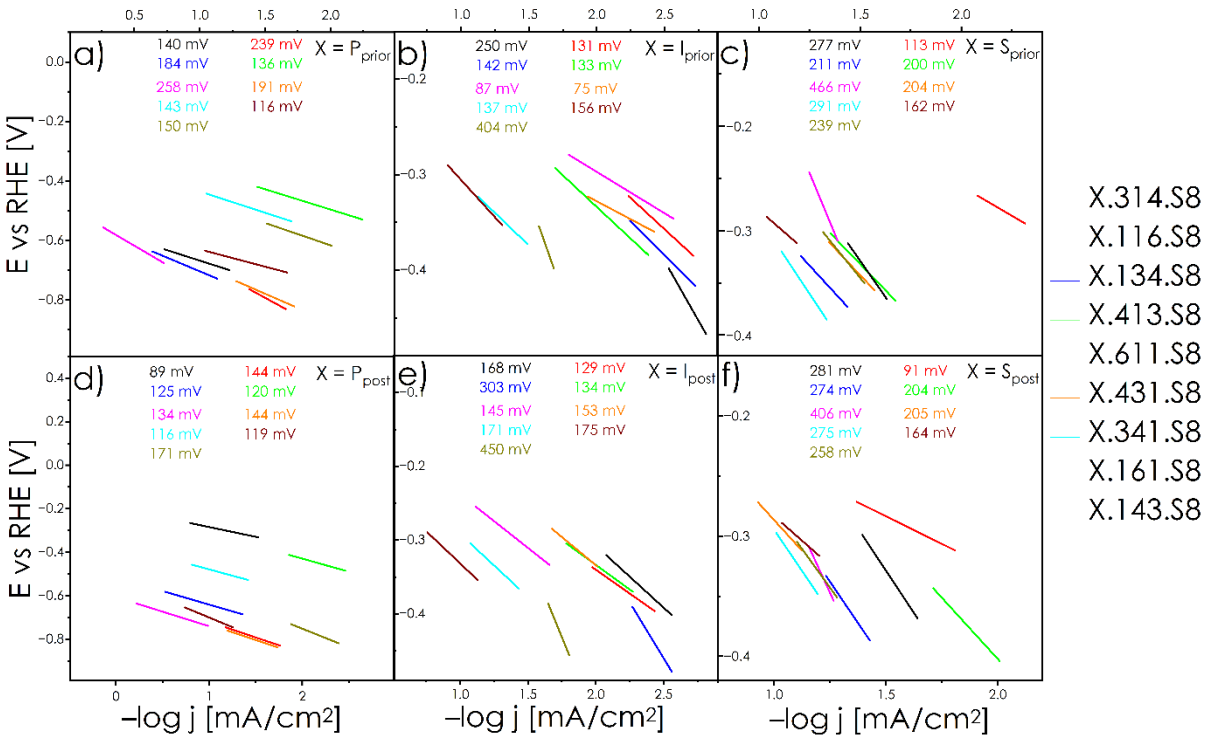

Figure 59. Tafel slope recorded in 0.5 M H_2SO_4 at 6.25 mV/s sweep rate and normalized to ECSA for $Co_{9-x-y}Fe_xN_yS_8$ series for: a) powder samples before chronoamperometry; b) ingot samples before chronoamperometry; c) pellet samples before chronoamperometry; d) powder samples after chronoamperometry; e) ingot samples after chronoamperometry and f) pellet samples after chronoamperometry.

The reaction kinetics of the $Co_{9-x-y}Fe_xN_yS_8$ series as a function of geometric area are similar to those normalized to ECSA (Figure 60). In the case of powders (Figure 60a; d), the key role of iron and cobalt is once again evident, with an emphasis on the unfavorable impact of excessive Co and Ni content. For both bulk materials – pellets and ingots (Figure 60b; c; e; f) – the best hydrogen evolution reaction kinetics are observed in materials with extreme concentrations of Co, Fe, or Ni in a single-phase system (such as the "611" or "413" series), showing a relatively large contribution from the favorable Volmer-Tafel mechanism.

For the ingots with the best kinetics, once again, the single-phase samples stand out: I.611.S8 and I.431.S8, with Tafel slopes of 84 mV/dec and 78 mV/dec, respectively. This clearly indicates that materials unaffected by further processing are the best for HER, as they allow typical pentlandite activation via *sulfur depletion*. When the material's surface is contaminated by foreign phases or subjected to treatments (such as sintering), the resulting properties tend to be more dependent on the chemical composition, which corelates with the $Co_3Fe_3N_3S_{8-x}Se_x$ series [245]. This observation supports the idea that the presence of active precipitates can alter ECSA and improve overpotentials at specific current densities, but it negatively affects the adsorption and desorption processes on the surface.

At this point, a more general remark arises: in the case of trimetallic pentlandites, Se-rich materials tend to exhibit a better correlation between intrinsic properties, electronic structure, and catalytic performance. This is an expected outcome, given the increase in metallic character with increasing

selenium content. At the same time, the presence of sulfur remains critical due to *sulfur depletion* mechanism. However, modifications within the cationic sublattice suggest that high-throughput screening may point to materials whose electronic structure only partially explains their behavior, with thermodynamic effects and structural stability playing an increasingly dominant role – particularly with regard to the stabilizing function of cobalt. The combined results of both series appear to provide a solid foundation for simultaneously analyzing both phenomena: changes in the cationic sublattice and the effect of high selenium content in the anionic framework.

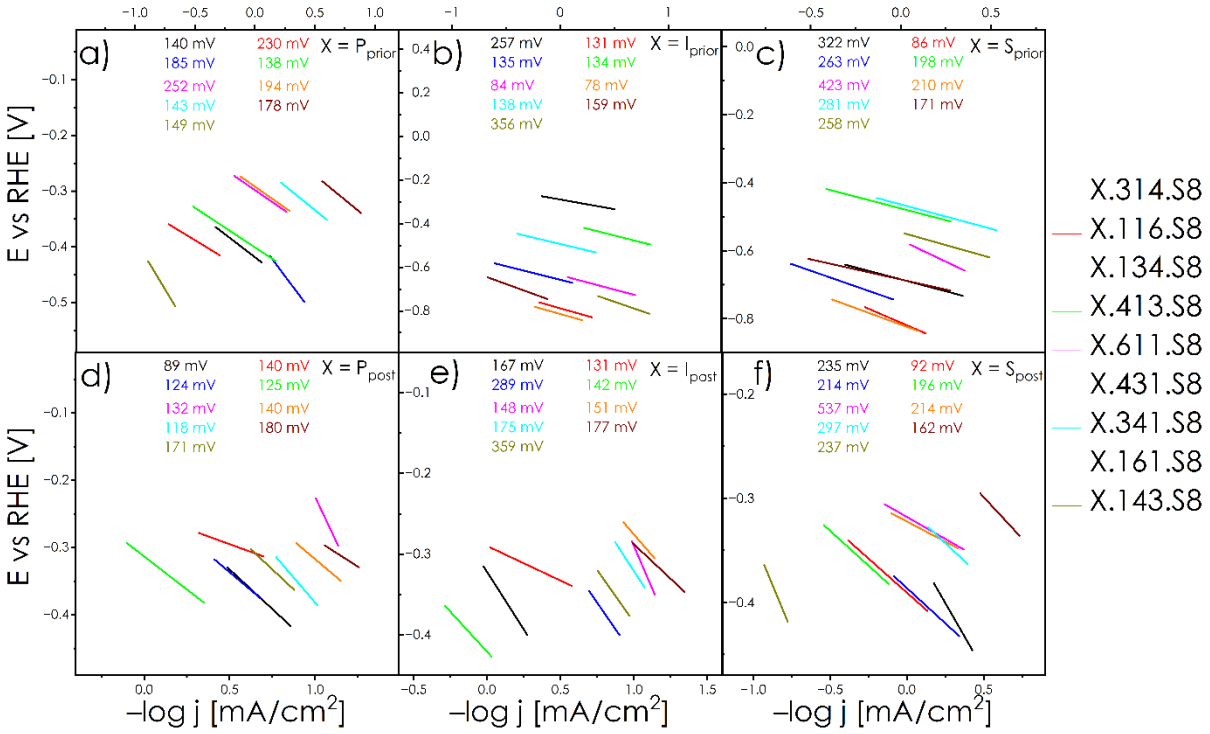

Figure 60. Tafel slope values recorded in 0.5 M H_2SO_4 at a 6.25 mV/s sweep rate and normalized to the geometric surface for $Co_{9-x-y}Fe_xN_yS_8$ series for: a) powder samples before chronoamperometry; b) ingot samples before chronoamperometry; c) pellet samples before chronoamperometry; d) powder samples after chronoamperometry; e) ingot samples after chronoamperometry and f) pellet samples after chronoamperometry.

4.3. $Co_{9-x-y}Fe_xNi_yS_4Se_4$ series

4.3.1. Structural investigation

4.3.1.1. XRD analysis

Among the Se-rich $Co_{9-x-y}Fe_xNi_yS_4Se_4$ compositions (Figure 61) the overall stability and cations solubility of the materials appears to be improved; however, secondary phases still emerge on some of the samples, particularly Ni-rich ones (e.g., P.116.S4 and P.134.S4) (Figure 61a). These secondary phases appear as precipitates of nickel and cobalt sulfides and selenides. Similar to the behavior observed in the sulfur-rich series, high-temperature treatment has an even more detrimental effect on the stability of materials with higher selenium content (Figure 61b). In this Se-rich series, not even one composition remains fully single-phase after temperature treatment, and the precipitates contain all the constituent elements of the original compositions. These observations suggest that pentlandite-like materials with non-equimolar or naturally occurring compositions are thermally unstable, especially under high-temperature conditions. Even the more stable high-Se compositions become unstable when exposed to elevated temperatures. This means that although selenium provides geometric space to accommodate increased iron or nickel content, it simultaneously weakens the overall structural integrity of the system, leading to destabilization rather than an improvement in thermodynamic stability, especially over time and under high-temperature treatment. Additional DFT studies on systems with critical Co, Fe, and Ni content show that their stability follows the trend: Co-rich > Ni-rich > Fe-rich.

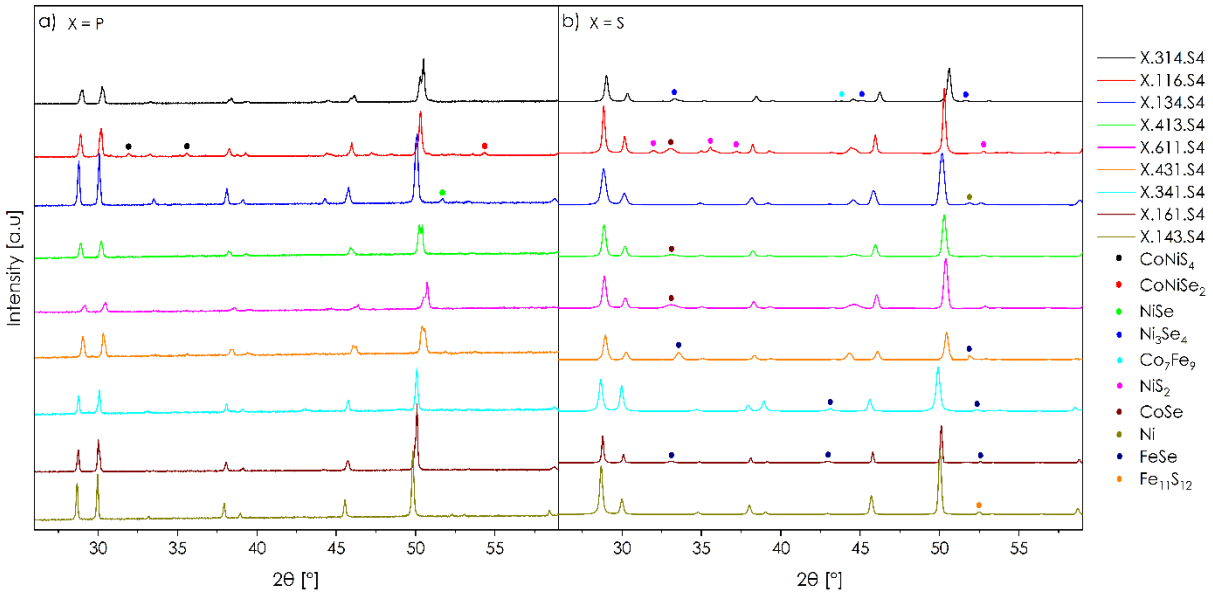

Figure 61. XRD patterns of $Co_{9-x-y}Fe_xNi_yS_4Se_4$ series in the form of a) powders and b) sinters.

4.3.1.2. SEM + EDS

The $Co_{9-x-y}Fe_xN_yS_4Se_4$ series shows noticeably improved phase purity and stability compared to the series with sulfur alone (Figure S24-Figure S28). As in the previous example, powders (Figure S24) exhibit Fe and FeS precipitates in a significant portion of the samples, but the ingots maintain a stable single-phase composition (Figure S25). High-temperature treatment affects the phase composition much less than in the previous example (Figure S26), with only small precipitates of Fe (S.314.S4, S.431.S4) and Co and Ni (S.161.S4) observed on the surfaces. This suggests an increase in the stability of the samples after the addition of selenium as a fifth component in amounts equal to sulfur, both at room and elevated temperatures, as selenium increases the lattice parameters of the unit cell, providing more space for metal atoms.

4.3.2. Catalytic properties

4.3.2.1. ECSA, RF, C_{dl}

In the $Co_{9-x-y}Fe_xN_yS_4Se_4$ series (Figure S29-Figure S34 show CV plots and Figure 62 shows C_{dl}), during the test of powder samples, redox peaks appear at slow scan rates, regardless of the material composition or measuring range, indicating the absence of a non-faradaic region. This issue disappears at higher scan rates due to the influence of C_{dl} and non-faraday currents that mask this effect, likely due to the presence of oxidized metallic compounds on the powder surface, which are formed during the milling process. Additionally, ingot samples exhibit irregularities, likely due to the randomness of orientation and uneven surface morphology, with brittle behavior especially evident in selenium-rich materials.

In this series, pellet samples exhibit the most pronounced changes in ECSA and RF values (Figure 63), indicating that the method of sample preparation has a substantial impact on catalytic behavior. These differences between pellets, ingots, and powders are primarily attributed to variations in microstructure and the extent of surface exposure. Among them, the S.161.S4 sample stands out, showing the highest RF value accompanied by a notable drop in ECSA. This behavior likely results from the catalytic activation driven by iron, which facilitates the formation of active sites – an effect observed also in the previous series. In the equimolar S–Se system, this iron-driven activation appears to be more pronounced than in S-rich compositions, possibly due to selenium-induced surface restructuring. However, in Fe-rich samples, partial decomposition of the pentlandite phase still occurs during electrochemical testing, which may hinder long-term stability. It should also be noted that such Fe-driven activation may partly originate from the partial dissolution of iron into the electrolyte. This effect would need to be verified by ICP-OES analysis of the post-measurement solutions; however, as in the previous series, such an analysis was not performed.

Almost all pellet samples (particularly S.161.S4, S.431.S4, and S.143.S4) show clear signs of electrochemical activation, as reflected by substantial changes in ECSA. This behavior may be attributed to the compact and relatively flat surface of the sintered pellets, which can locally concentrate electrochemical reactions and promote partial sulfur depletion. In contrast, ingot and powder

samples exhibit only minor ECSA changes during operation, likely due to their more porous or irregular surfaces, which facilitate a more stable distribution of active sites.

Compared to the $Co_{9-x-y}Fe_xNi_yS_8$ series, the activation process in the S_4Se_4 series is less pronounced. Here, the differences in catalytic activity appear to stem primarily from surface morphology rather than from chemical composition. Notably, RF values tend to decrease with increasing geometric surface area, closely following the trend observed for ECSA. The introduction of selenium once again seems to obscure the role of the cationic sublattice composition, making the observed differences more sensitive to sample preparation and microstructural variability. In contrast to the sulfur-only series, the equimolar S–Se compositions show higher ECSA values, suggesting a distinct mechanism of active site formation – possibly due to the longer TM–Se bonds, which localize catalytic activity closer to the metal centers and modify the overall HER pathway.

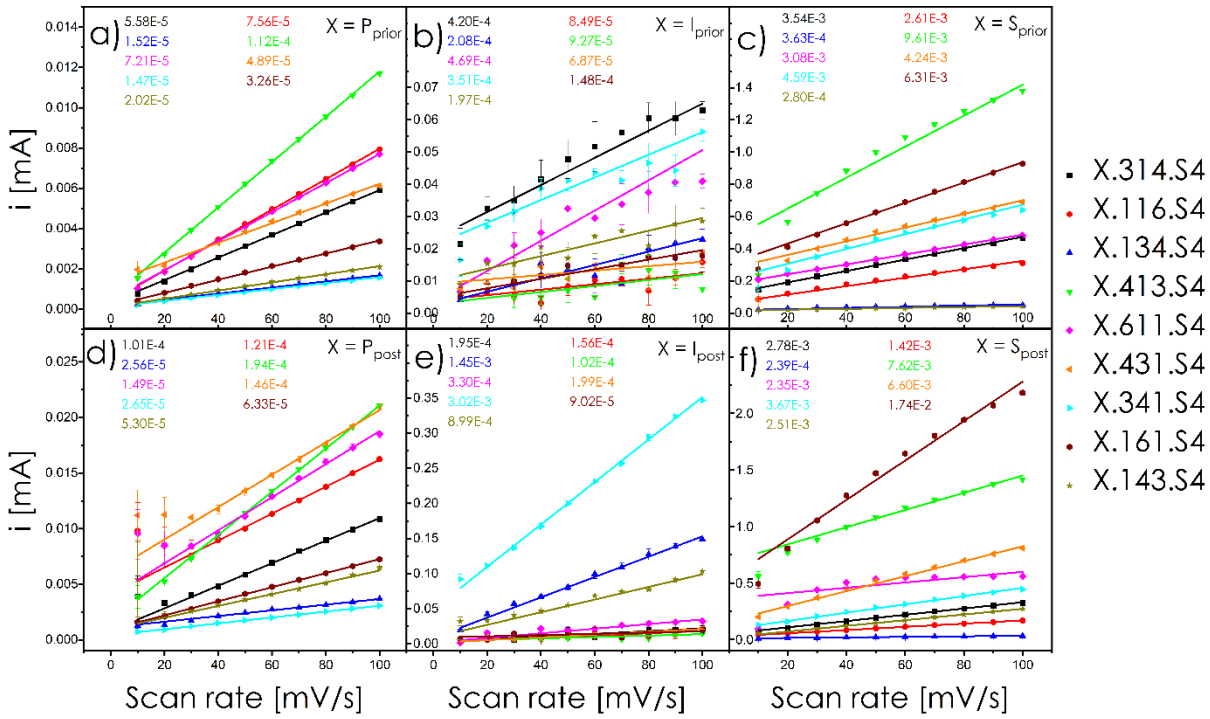

Figure 62. Charging current densities representing C_{dl} for $Co_{9-x-y}Fe_xNi_yS_4Se_4$ series for: a) pellets before; b) ingots before; c) powders before; d) pellets after; e) ingots after; f) powders after chronoamperometry. Numerical colored data indicates the slope - C_{DL}.

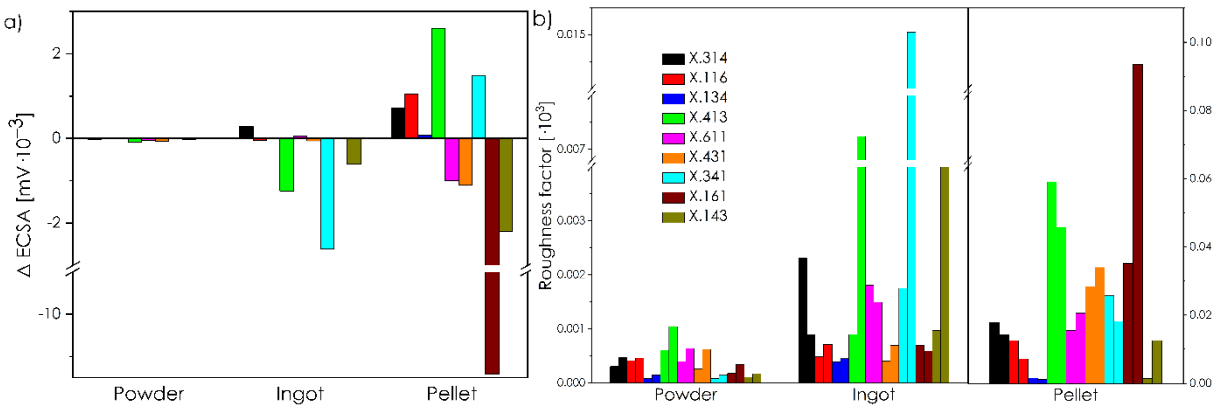

Figure 63. Graphical illustration of a) ΔECSA and b) RF for $Co_{9-x-y}Fe_xN_yS_4Se_4$ series.

4.3.2.2. EIS analysis

In the $Co_{9-x-y}Fe_xNi_yS_4Se_4$ series (Figure 64 and Table S4), R_{CT} values are noticeably lower than in S-rich compositions, suggesting enhanced conductivity due to the more metallic nature of Se-rich phases. Following the ECSA and RF analysis, and the general observation that selenium tends to mask the influence of cations while simultaneously increasing the metallic character and facilitating charge-transfer abilities, the EIS results indicate that, regardless of the material form, R_u and R_{CT} values do not show a systematic correlation with the cation sublattice occupancy. To a very limited extent, it can only be noted that Fe-rich compositions generally exhibit slightly lower R_{CT} values, which is particularly visible for S.161.S4 sample. The only consistent trend is that R_u decreases with increasing material consolidation. It should also be noted that sample P.314.S4 deviates from the rest of the series, most likely due to experimental errors.

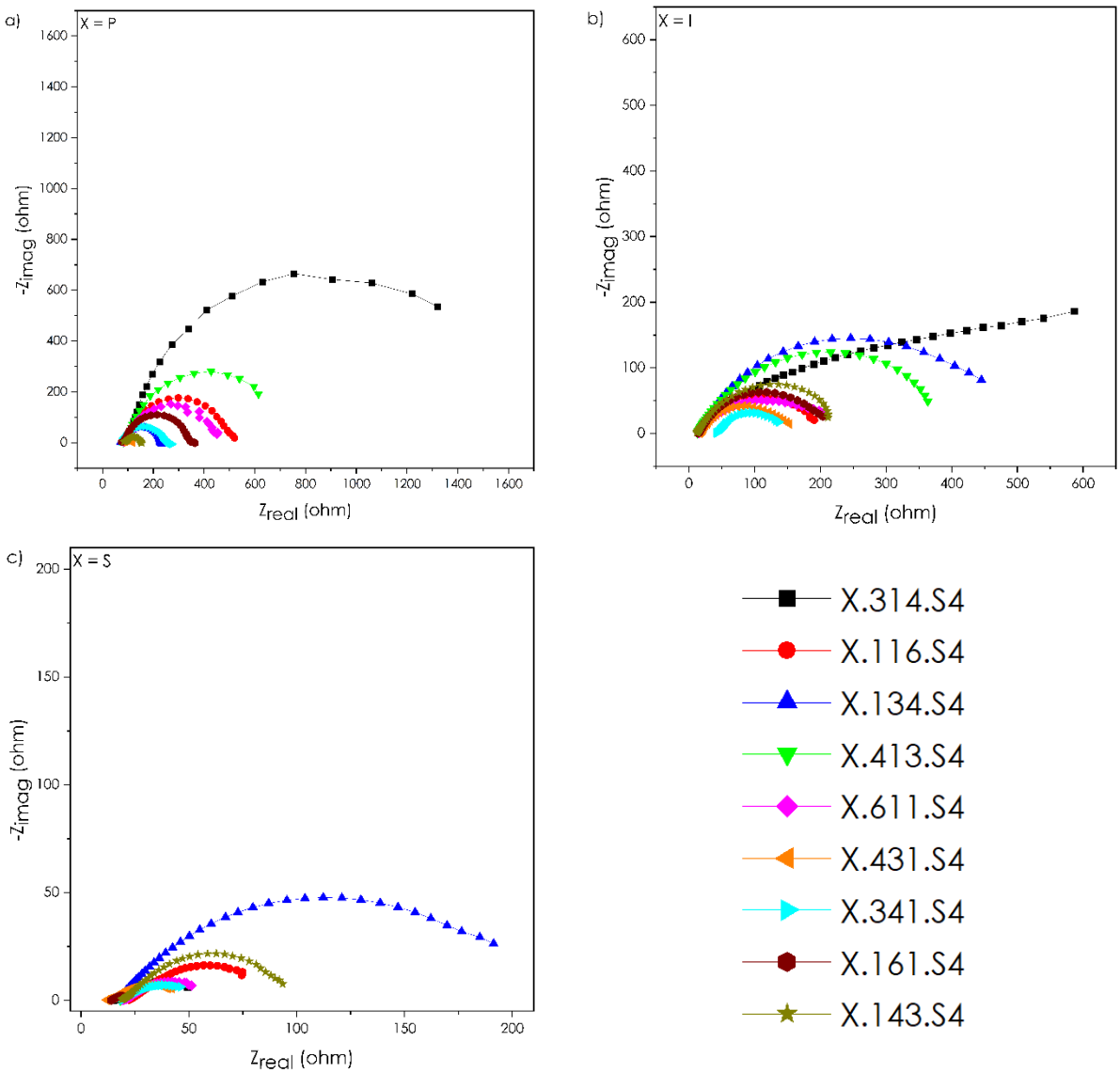

Figure 64. Nyquist plots for a) powders; b) ingots and c) pellets from the $Co_{9-x-y}Fe_xNi_yS_4Se_4$ series.

4.3.2.3. HER

In the case of the $Co_{9-x-y}Fe_xN_yS_4Se_4$ series, the conclusion that a large ECSA and RF correlate with HER performance is not as straightforward as expected. If this were true, the Co- and Fe-rich compositions should exhibit the best HER performance, but the situation is more complex. The LSV curves for this series, particularly those normalized to ECSA (Figure 65), highlight the influence of material morphology and changes in the cationic sublattice, with stability remaining a crucial factor. Normalizing the LSV currents to ECSA shows that the best performers are the ingot samples, which achieve the lowest overpotentials and highest current densities. Only three samples (I.314.S4, I.611.S4, and I.341.S4) show significantly lower HER performance compared to the others.

Powders show promising overpotentials and current densities (e.g., the best powder, P.143.S4, shows $\eta_{0.2ECSA}$ = 312.11 mV/cm^2), but the majority of the powder samples suffer from instability over time, likely due to the detachment of grains from the substrate. This indicates that Se-rich compositions exhibit a different surface charge distribution, resulting in poorer adhesion to the conductive substrate. Pellets perform the worst in this series, except for the S.143.S4 and S.134.S4 samples. However, the former shows instability over time, while S.134.S4, though showing $\eta_{0.2ECSAprior}$ = 435 mA/cm^2 and $\eta_{0.2ECSApost}$ = 383 mA/cm^2 both before and after stability testing, still results in the worst performance in the series.

Similar to the $Co_{9-x-y}Fe_xNi_yS_8$ series, this series exhibits comparable trends regarding the density of states near the Fermi level and the influence of metallic and bimetallic centers on the HER performance of the samples. However, this is affected by multiple factors such as the introduction of selenium, the presence of sulfur vacancies, and the iron content [251]. Typically, such modifications enhance catalytic activity, but auxiliary ΔG calculations reveal an interesting relationship in this case – namely, they lead to excessively strong hydrogen binding. While proton adsorption in the Volmer step is favored, the recombination reaction and desorption process in the Tafel step are limited, resulting in overly strong hydrogen binding and slowed reaction rates.

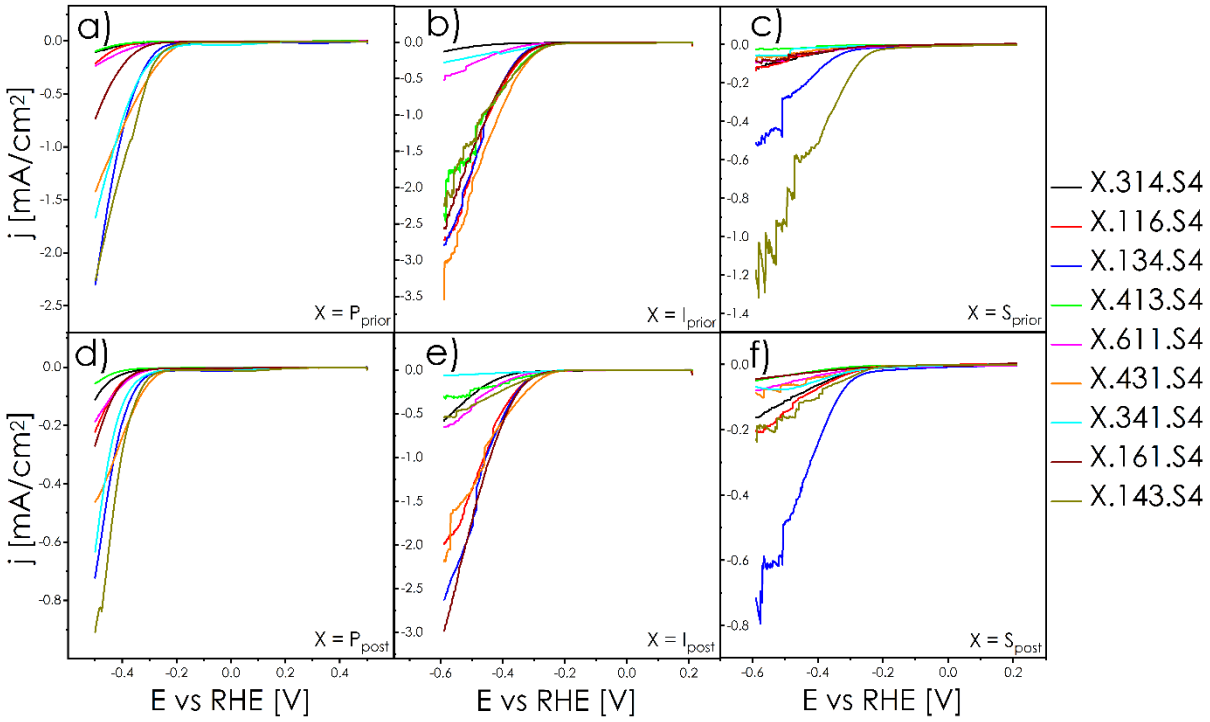

Figure 65. LSV voltammograms recorded at a sweep rate of a 6.25 mV/s in 0.5 M H_2SO_4 for $Co_{9-x-y}Fe_xNi_yS_4Se_4$ series normalized to ECSA for: a) powder samples before chronoamperometry; b) ingot samples before chronoamperometry; c) pellet samples before chronoamperometry; d) powder samples after chronoamperometry; e) ingot samples after chronoamperometry and f) pellet samples after chronoamperometry.

The LSV normalized to geometric are curves for the $Co_{9-x-y}Fe_xNi_yS_4Se_4$ series show that the current densities decrease as the sample density decreases. The highest currents are observed for sintered pellet samples, followed by ingots, with the lowest currents seen in powder samples on conductive substrates. These trends correlate with the previously discussed R_{CT} values and the inherent electrical properties of the materials. However, there is no clear correlation between overpotentials and chemical composition.

For the pellets (Figure 66), the best-performing compositions are S.161.S4 and S.431.S4, reaching η_{10} = 253.24 and 283.19 mA/cm^2, respectively, while the worst-performing composition is S.134.S4 (η_{10geo} = 451.08 mA/cm^2). Interestingly, for the S.161.S4 material, the situation is not entirely clear, particularly due to superior performance and non-zero cathodic currents observed in this material. Structural analysis indicates that the surface of S.161.S4 sample undergoes decomposition into Fe-rich areas, suggesting that despite its strong performance, the material may lack long-term stability. To confirm this, an XPS test was conducted on this composition (see 4.3.2.5).

For ingots and powders, no clear trends emerge linking performance to chemical composition. The best-performing ingots are I.413.S4 and I.143.S4 reaching η_{10geo} = 356.91 mA/cm^2 and 347.92 mA/cm^2, respectively, while the best powder is P.431.S4 (η_{10geo} = 340.89 mA/cm^2). In both series, the X.314.S4 composition exhibits the worst overpotentials. Although these values might seem random, in materials with both sulfur and selenium on anionic sublattice ("S_4Se_4"), surface morphology and sample preparation are far more significant factors, as demonstrated by the P.431.S4 sample. This sample stands

out due to its exceptionally small average particle size, making it noticeably superior to other powder samples.

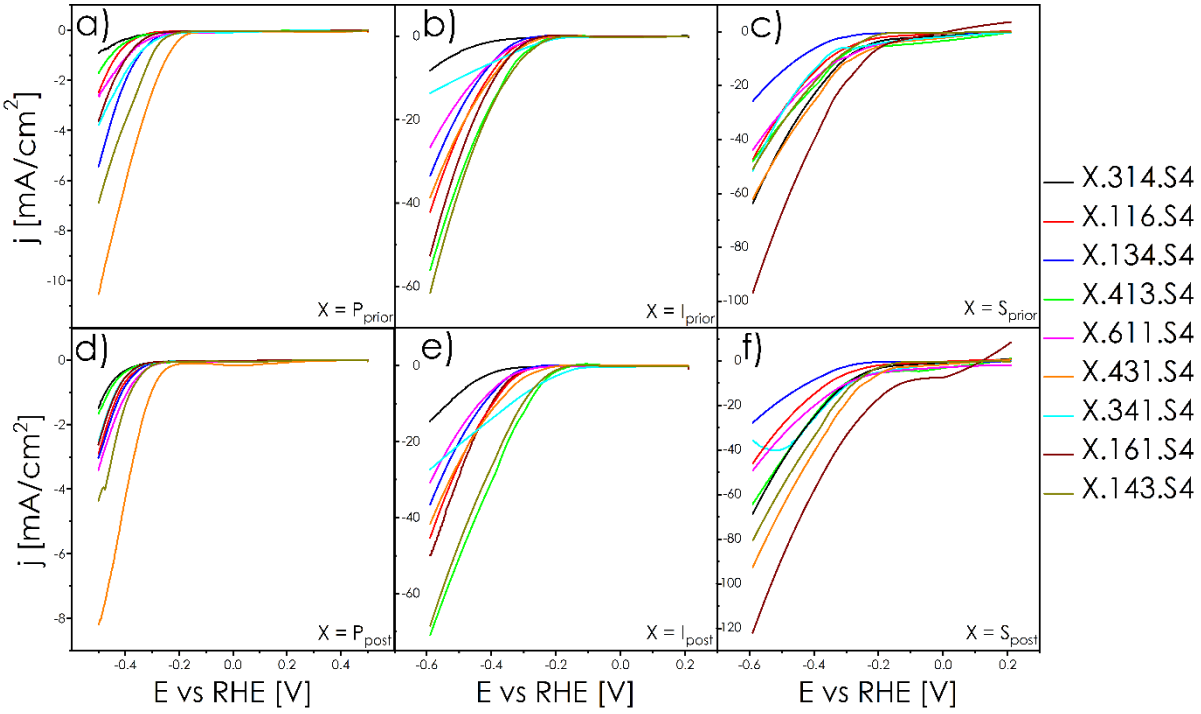

Figure 66. LSV voltammograms recorded at a sweep rate of a 6.25 mV/s in 0.5 M H_2SO_4 for $Co_{9-x-y}Fe_xNi_yS_4Se_4$ series normalized to geometric area for: a) powder samples before chronoamperometry; b) ingot samples before chronoamperometry; c) pellet samples before chronoamperometry; d) powder samples after chronoamperometry; e) ingot samples after chronoamperometry and f) pellet samples after chronoamperometry.

4.3.2.4. Tafel Slope

The Tafel slope normalized to the ECSA for the $Co_{9-x-y}Fe_xN_yS_4Se_4$ series (Figure 67) shows a trend consistent with the LSV results. Notably, both powder (Figure 67a and d) and ingot samples (Figure 67b and e) exhibit activation after chronoamperometry, attributed to *sulfur depletion*. This effect is more pronounced in the ingot samples, likely arises from their denser microstructure and lower surface area, which amplifies the impact of surface compositional changes on the overall catalytic activity. The best-performing powder sample displays a Tafel slope of approximately 100 mV/dec, although no clear correlation is observed between the Tafel values and chemical composition, nor between the values before and after the stability tests. Once again, this behavior reveals the masking effect of selenium on the influence of cations, consistent with the trends observed for R_u and R_{CT}.

Ingot samples generally show better kinetics than powders, with most exhibiting Tafel slopes below 100 mV/dec, except for samples I.314.S4, I.611.S4, and I.341.S4. These lower Tafel slope values suggest a preferred Volmer–Tafel mechanism, where fast proton chemisorption is followed by a rate-limiting recombination step. In contrast, the pellet samples (Figure 67c; f) – with lower surface development – exhibit the highest Tafel slopes, which again is consistent with literature data suggesting that Se-rich pentlandites are characterized by poorer kinetics, especially when ECSA is low [210,246]. Even the best-performing pellet samples, S.143.S4 and S.134.S4, show Tafel slopes above 100 mV/dec. The lowest Tafel slope of 114 mV/dec are identified for pellet S.143.S4 both before and after chronoamperometry.

These values indicate a non-preferred Volmer–Heyrovsky mechanism, suggesting that the high density in pellet surfaces significantly limits their catalytic activity.

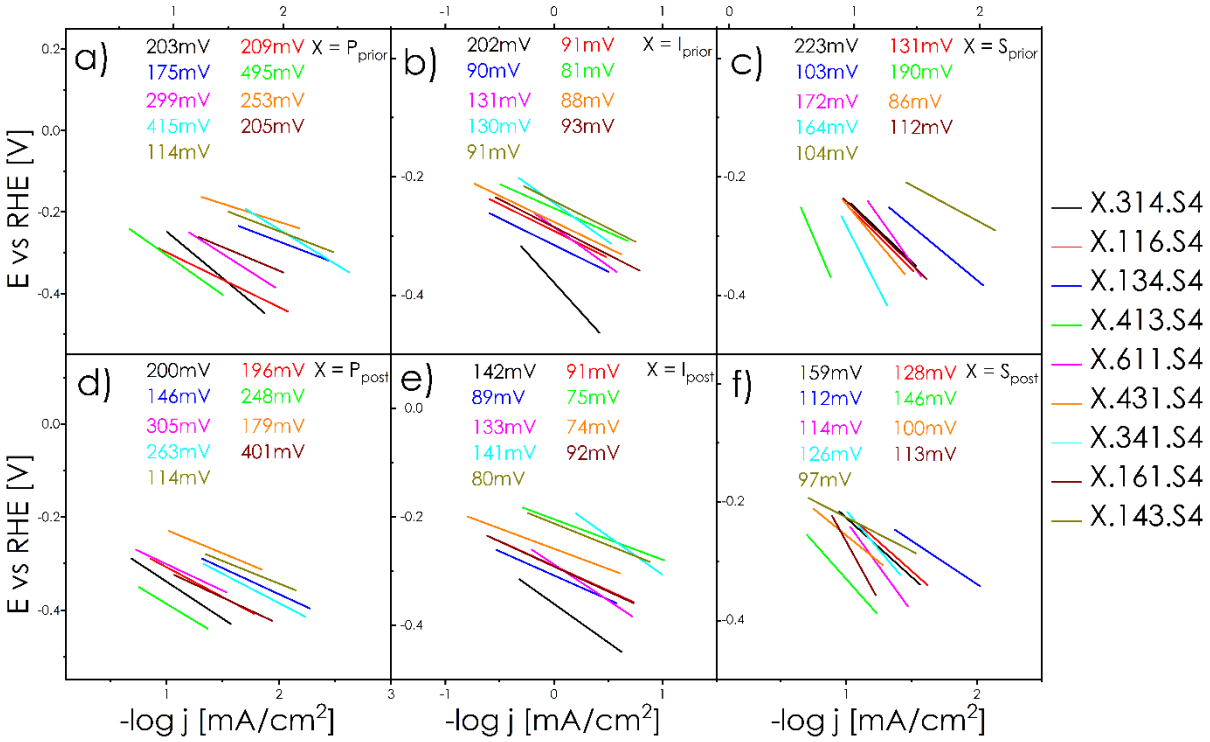

Figure 67. Tafel slope values recorded in 0.5 MH2SO4 at a 6.25 mV/s sweep rate and normalized to the ECSA for $Co_{9-x-y}Fe_xN_yS_4Se_4$ series for: a) powder samples before chronoamperometry; b) ingot samples before chronoamperometry; c) pellet samples before chronoamperometry; d) powder samples after chronoamperometry; e) ingot samples after chronoamperometry and f) pellet samples after chronoamperometry.

A very similar trend is observed for the $Co_{9-x-y}Fe_xN_yS_4Se_4$ series when Tafel slopes are normalized to the geometric area (Figure 68). Ingot samples (Figure 68b; e) continue to show the most favorable Tafel slope values, while pellet samples (Figure 68c; f) display the poorest hydrogen evolution kinetics. Powder samples (Figure 68a; d) exhibit slightly higher Tafel slopes than the ingots, with most values clustering around 100 mV/dec. Almost all ingot samples reach Tafel slopes close to 100 mV/dec, with the exception of three samples – I.314.S4, I.611.S4, and I.341.S4 – though the differences are relatively minor. Notably, ingot samples in this series exhibit Tafel slopes comparable to the I.S8 sample and significantly lower than those of the I.S4 sample, indicating superior HER kinetics. Pellet samples generally show high Tafel slopes above 100 mV/dec, indicative of a non-preferred Volmer-Heyrovsky mechanism. Most pellet samples also exhibit higher or comparable Tafel slopes relative to the S.S8 and S.S4 references. Only two pellet samples – S.143.S4 and S.134.S4 – approach Tafel slope values near 100 mV/dec. By analyzing Tafel slopes normalized to both ECSA and geometric area, the "143" sample stands out, showing the best average Tafel slope values. This is likely due to its composition, which closely resembles equimolar $Co_3Fe_3Ni_3S_4Se_4$ and contains a high Fe content that enhances reaction kinetics. The second-best performing sample, X.134.S4, further supports the conclusion that optimal "S_4Se_4" compositions tend to favor near-equimolar distributions of transition metals on the cationic sublattice.

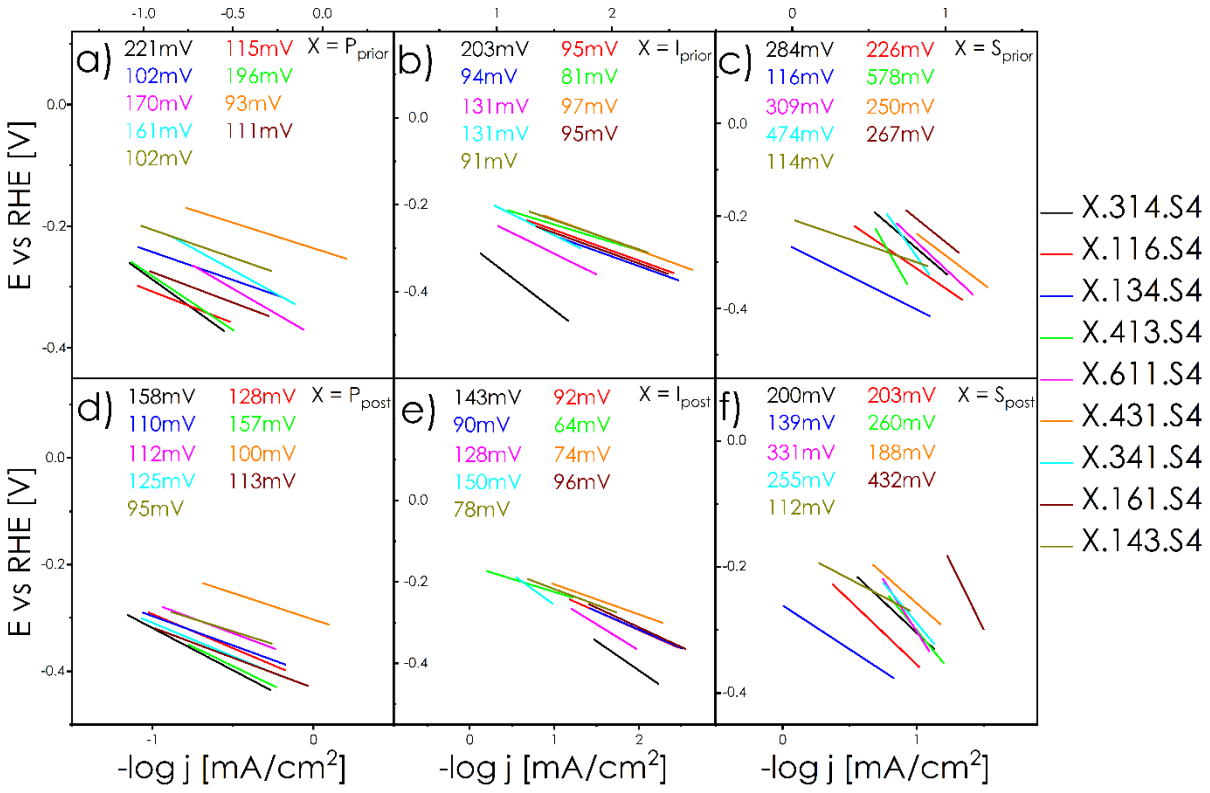

Figure 68. Tafel slope values recorded in 0.5 M H_2SO_4 at a sweep rate of 6.25 mV/s and normalized to the geometric surface for $Co_{9-x-y}Fe_xN_yS_4Se_4$ for: a) powder samples before chronoamperometry; b) ingot samples before chronoamperometry; c) pellet samples before chronoamperometry; d) powder samples after chronoamperometry; e) ingot samples after chronoamperometry and f) pellet samples after chronoamperometry.

The slow desorption process, which results in the low kinetics of the samples in this series, does not stem from geometric factors but rather from electronic ones. TM–Se bonds are longer than TM–S bonds, creating interatomic active centers, yet the optimized proton adsorption geometries in Se-rich structures are very similar to their sulfur analogues. Therefore, the kinetics are slowed down by the deepening of the d-band center caused by selenium. This, combined with the previously noted strong hydrogen binding and limited desorption, indicates that Se-rich pentlandites operate according to a different HER mechanism – the rate-limiting step is not related, as usual, to proton adsorption but rather to hydrogen release.

4.3.2.5. XPS test

To determine changes on the surface during the electrochemical tests of the S.161.S4 samples, the XPS test was conducted (Figure 69–Figure 72) for the sample before and after chronopotentiometry. Additionally, the same test was conducted for the S.S4 sample, for comparison.

All three transition metals exhibit mixed oxidation states, with Fe^0 being the most depleted in electrochemical tests – particularly in Fe-rich systems such as the S.161.S4 sample. This depletion suggests the presence of localized iron-rich regions within the material's volume, which dissolve into the electrolyte during electrochemical reactions and subsequently become oxidized. Verification of this effect by ICP-OES analysis of the post-reaction electrolyte would be highly valuable; however, such measurements were not performed in this study. This process accounts for the observed non-zero

cathodic currents (as shown in Figure 65 and Figure 66 for this sample) and supports the concept that Fe-rich materials with a pentlandite structure possess the lowest thermodynamic stability (Table S5), what is further supported by DFT results. Comparing the XPS spectra of selenium-rich materials to those containing only sulfur reveals significantly broader and more fragmented spectral envelopes in the former, which indicates a more complex surface chemistry and a more dynamic redox behavior [247]. An intriguing observation lies in the differing oxidation transitions of the transition metals: while Fe and Co exhibit shifts to higher oxidation states, Ni remains consistently at the +2 state. This suggests that Ni maintains near-zero net charge fluctuation and behaves as electrically inert throughout the redox cycle. Consequently, in Ni-rich systems, the role of charge compensation appears to shift toward Fe, which assumes a higher positive charge. This results (Figure S35) in partial filling of the *d* orbitals, which diminishes the catalytic activity of Ni-rich systems – as evident in the LSV curves – by effectively reducing the number of unoccupied states available for hydrogen adsorption. Conversely, in Fe-rich systems, iron tends to occupy the electronic roles typically favored by Ni, appearing with a lower net charge, closer to zero. This increases the availability of electron states, thereby enhancing HER activity. However, in critical cases – such as the S.161.S4 sample – this benefit comes at the expense of structural stability.

In addition, selenium – like iron – significantly shifts the *d*-band center, a key descriptor of catalytic activity [252,253], closer to the Fermi level. However, while Fe enhances electron accessibility at active sites, selenium exerts a much stronger effect, effectively overshadowing the subtle differences introduced by cationic substitutions. This explains why the best-performing Se-based pentlandites are those with Fe-rich or Fe-Co compositions, in contrast to selenium-free, sulfur-only pentlandites, where Ni-rich domains typically show higher activity [68]. Moreover, the incorporation of larger Se ions into the structure increases the formation energy, thereby reducing the structural stability of the pentlandite phase. This observation is consistent with results from the $Co_3Fe_3Ni_3S_{8-x}Se_x$ series and aligns with the literature [254], which reports that substituting sulfur with selenium leads to greater lattice distortion due to selenium's larger ionic radius and lower electronegativity. In summary, selenium not only enhances charge transfer but also fundamentally alters the influence of the cationic sublattice on catalytic behavior.

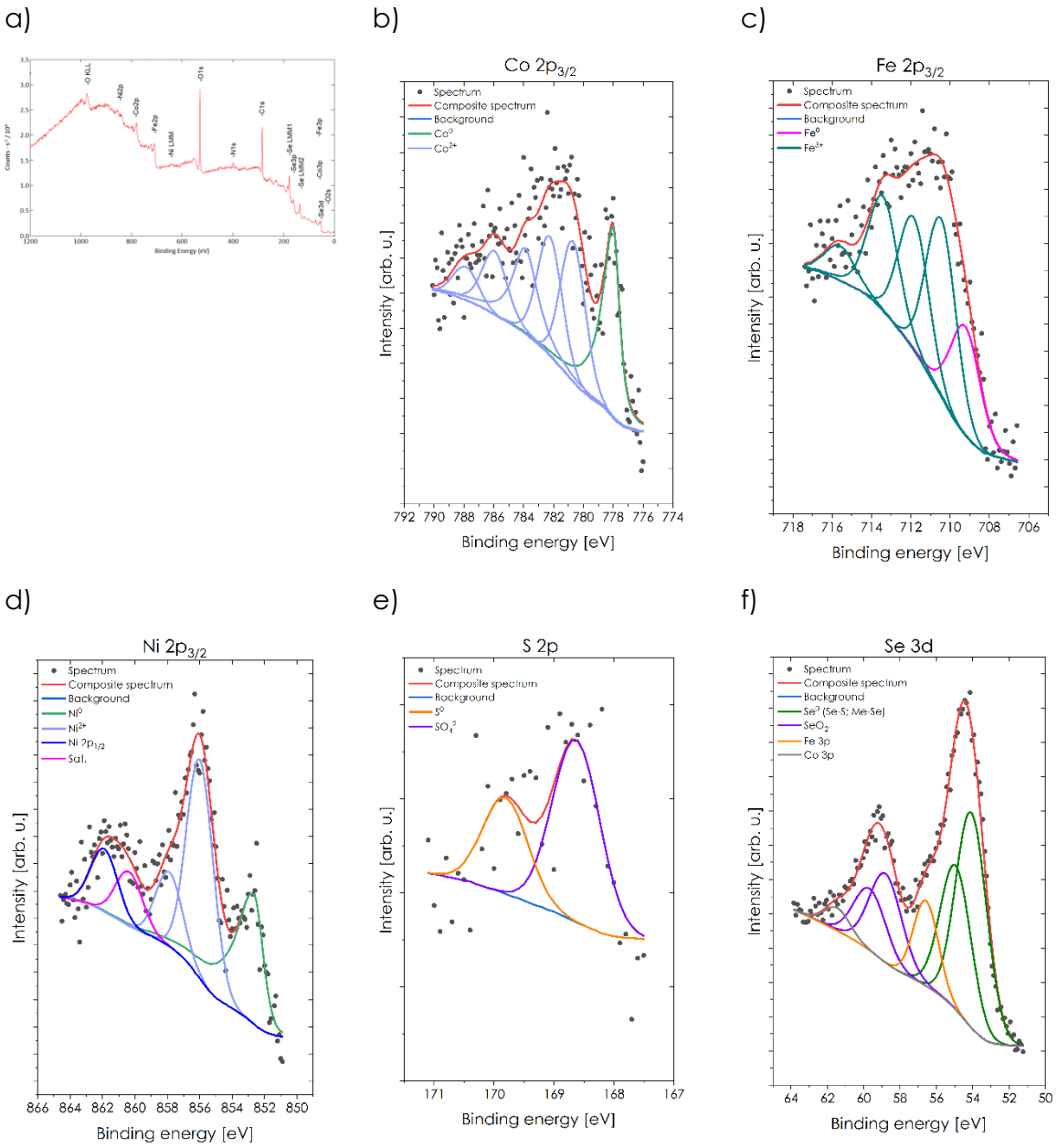

Figure 69. High-resolution spectra for pellet S.S4 sample before electrochemical tests: a) XPS survey spectrum; b) Co $2p_{2/3}$; c) Fe $2p_{3/2}$; d) Ni $2p_{3/2}$; e) S 2p; f) Se 3d.

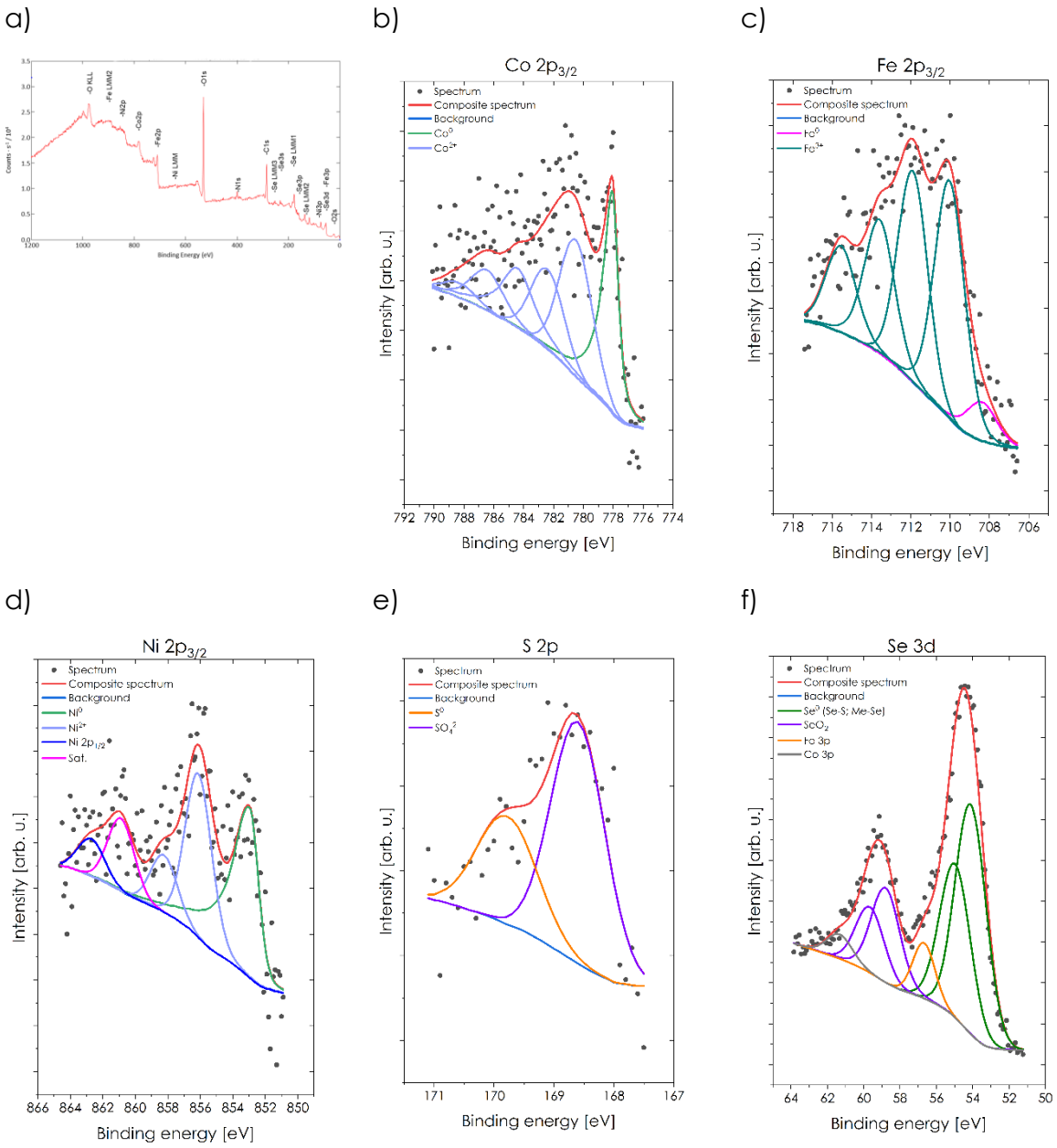

Figure 70. High-resolution spectra for pellet S.S4 sample after electrochemical tests: a) XPS survey spectrum; b) Co $2p_{2/3}$; c) Fe $2p_{3/2}$; d) Ni $2p_{3/2}$; e) S 2p; f) Se 3d.

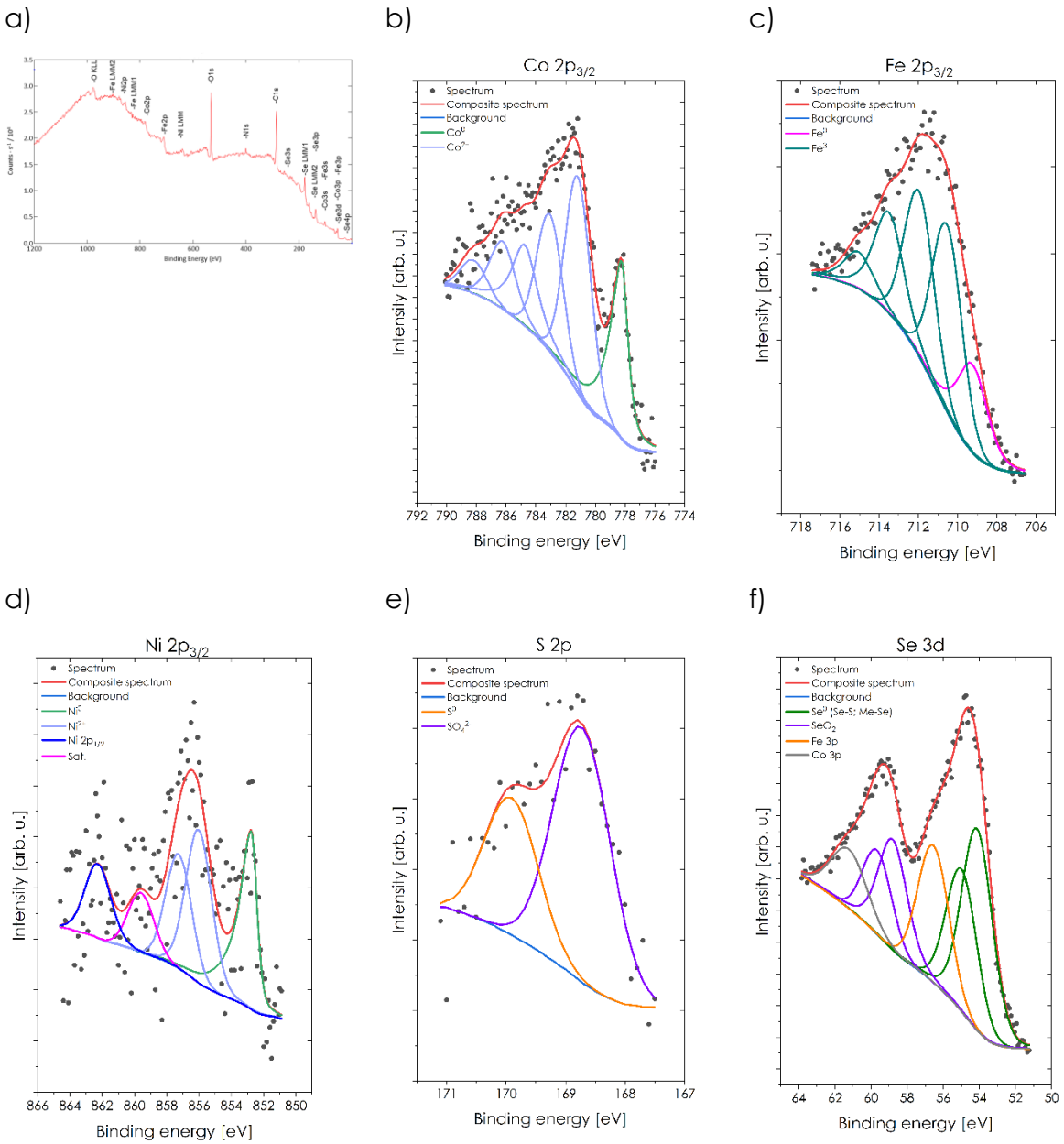

Figure 71. High-resolution spectra for pellet S.161.S4 sample before electrochemical tests: a) XPS survey spectrum; b) Co $2p_{2/3}$; c) Fe $2p_{3/2}$; d) Ni $2p_{3/2}$; e) S 2p; f) Se 3d.

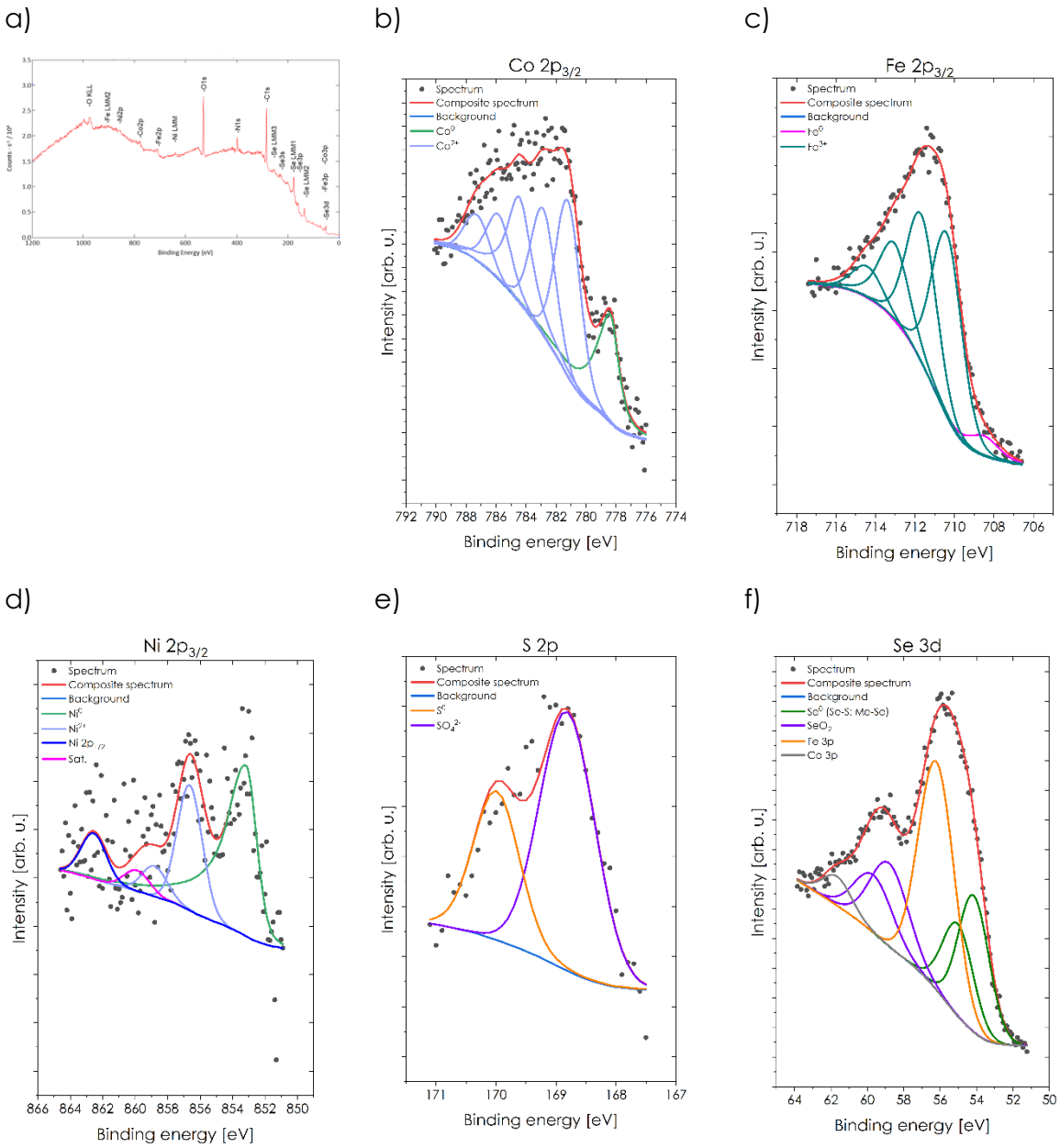

Figure 72. High-resolution spectra for pellet S.161.S4 sample after electrochemical tests: a) XPS survey spectrum; b) Co $2p_{2/3}$; c) Fe $2p_{3/2}$; d) Ni $2p_{3/2}$; e) S 2p; f) Se 3d.

4.4. Additional analyses

In this chapter, additional analyses are included, covering the optimization and the influence of sintering temperature on the properties of solid electrodes – which represents a central aspect of this dissertation – as well as clarifying specific mechanisms in pellet samples produced by non-normalized powders, and explaining the phenomenon observed in the Ni-rich composition S.116.S8.

4.4.1. Influence of sintering temperature on HER performance

As mentioned in the chapter dedicated to pellets (3.3.3), the $Co_3Fe_3Ni_3S_8$ and $Co_3Fe_3Ni_3S_4Se_4$ materials were sintered at different temperatures. Figure 73 presents XRD studies of S.S8 series and Figure 74 presents SEM+EDS studies of the S.S8 and S.S4 pellets sintered at 450 °C, 500 °C, and higher temperatures. As shown, when the sintering temperature is too high, the material begins to decompose. It is not visible in XRD, but SEM and EDS maps accurately show the decomposition of the material. This is clear in Figure 74b-d and f-g, that the higher temperatures cause the appearance of Fe and its subphases on the surface of the material. Typically, pentlandites are stable under inert (oxygen-free) conditions up to temperatures of around 700 °C [255]. However, decomposition observed in these materials occurs due to two main factors. The first is surface reduction driven by elevated temperatures under carbon-provided reducing conditions. The second, and more critical, factor is inductive hot pressing (IHP) sintering, during which eddy currents are generated [256]. These currents lead to intense electron movement, which, combined with the reducing environment, promotes redox reactions. Among the constituent metals, iron has the lowest standard reduction potential, which explains why iron-rich phases are the first to appear [87]. This decomposition is one of the reasons why all pellet samples, in the main part of the thesis, were sintered at a temperature of 400°C.

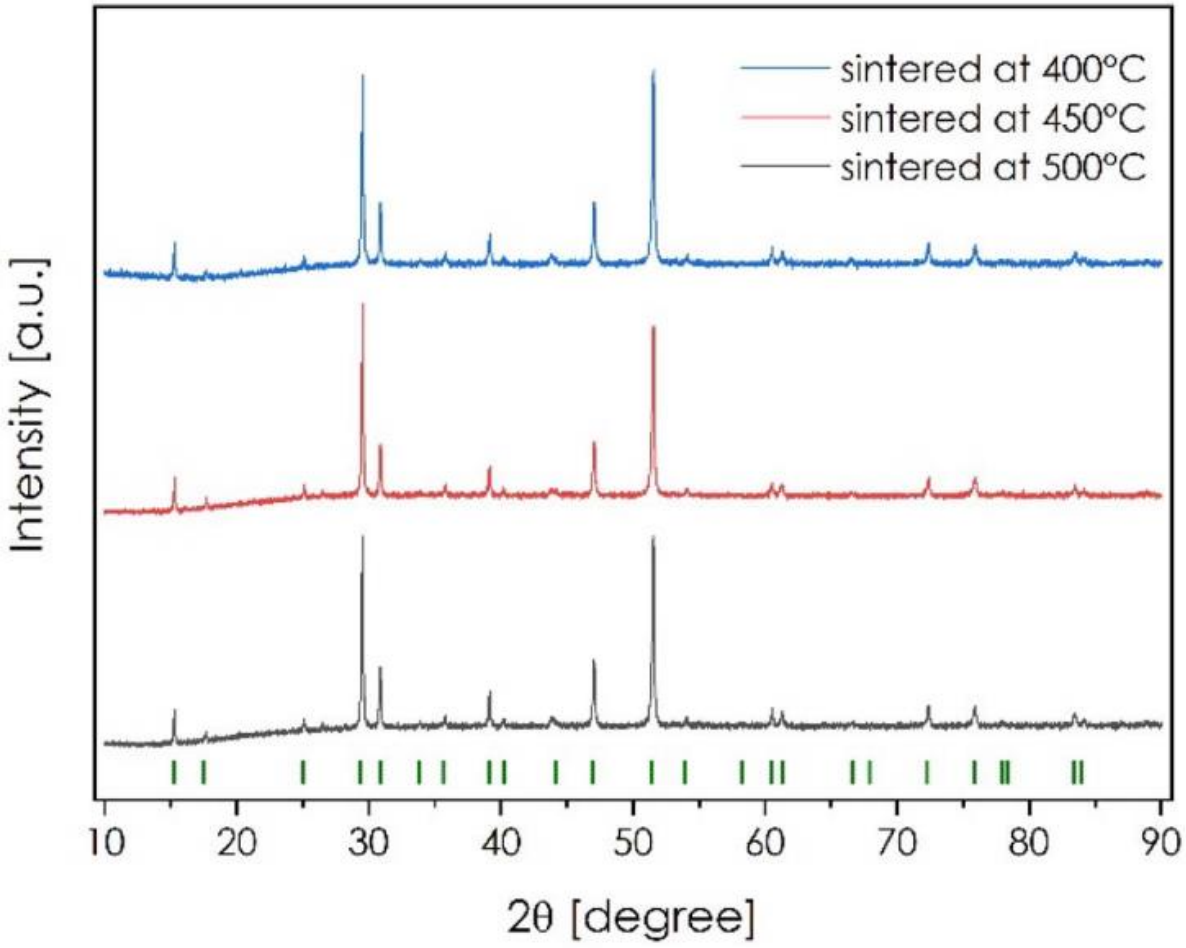

Figure 73. XRD patterns of the $Co_3Fe_3N_3S_8$ pentlandite pellets sintered at 400, 450 and 500 °C.

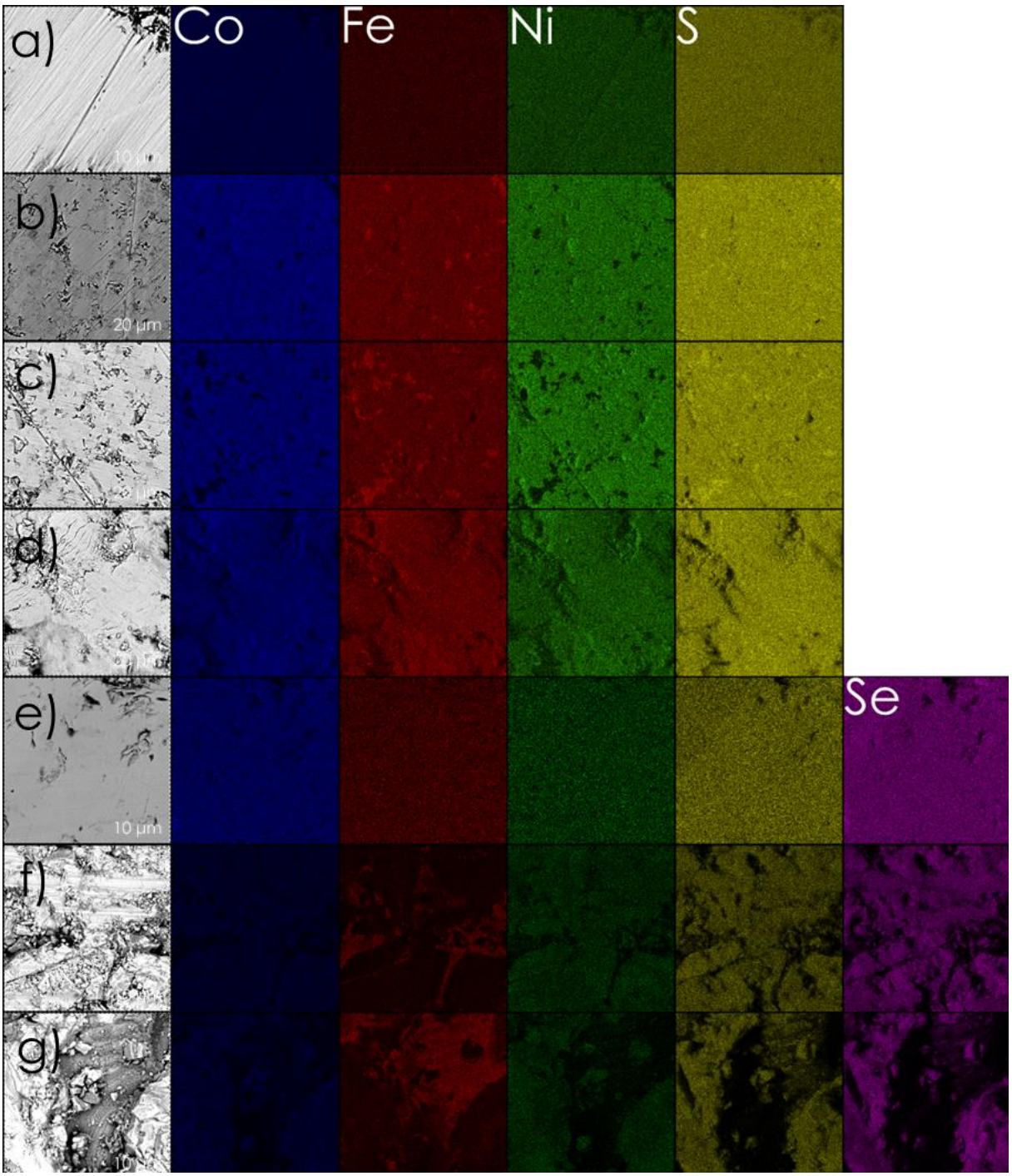

Figure 74. SEM of $Co_3Fe_3Ni_3S_8$ pellets sintered in: a) 400°C; b) 450°C; c) 500°C; and $Co_3Fe_3Ni_3S_4Se_4$ pellets sintered in: d) 400°C; e) 450°C; f) 500°C and g) 550°C.

The chemical compositions of all materials were determined using two different methods: SEM-EDS analysis and ICP-OES. The collected data were listed in Table S1, and discrepancies between the chemical compositions obtained by these two methods can be observed. The chemical compositions derived from ICP-OES are closer to the theoretical values than those obtained from the EDS method. This is because ICP-OES is a volume-based technique, while EDS is a surface-based method, making the latter more susceptible to random variations, which can significantly affect its accuracy, moreover, the measurement error of EDS is significantly higher than that of ICP [257]. This discrepancy is most evident in the $Co_{9-x-y}Fe_xN_yS_4Se_4$ series, where the values deviate notably from theoretical expectations.

This can be attributed to the limitations of the testing equipment, which may underestimate certain elements, such as sulfur, especially in the presence of selenium. Therefore, the values obtained from EDS should be considered as reference only, while further analysis will rely on the ICP-OES data. Overall, the elemental compositions in the obtained materials are close to the theoretical values, with deviations falling within acceptable limits — which, in the case of single-phase materials with a unimodal elemental distribution, can be emphasized as an unquestionable success, especially given the complexity of such a non-stoichiometric, multicomponent sulfide system.

An analysis of the relative density values of the obtained samples shows that all of them demonstrate stable values above 80%, often approaching 95% relative density. These values were measured using the Archimedes hydrostatic method and compared to the theoretical densities obtained via Rietveld analysis. Increased density can significantly influence the electrochemical properties of the materials (by altering the active surface area, electrical and thermal conductivity, the number of active centers, and other internal properties), making the measurement of these values crucial to this study.

Given these considerations, sintering conditions were tested in the IHP process, with sintering time and temperature manipulated. The collected density values are summarized in Table 10. When the sintering temperature is altered, the density increases up to 97.2 % but then begins to decrease. This reduction is likely due to the volatilization of sulfur at temperatures exceeding its evaporation threshold and subsequent phase decomposition. . Additionally, increasing the sintering time did not impact the density of the resulting pellets, so for both financial and time efficiency, a sintering time of 15 minutes was maintained.

Table 10. Density of $Co_3Fe_3Ni_3S_8$ and $Co_3Fe_3Ni_3S_4Se_4$ pellets after IHP sintering in non-standard conditions.

	$Co_3Fe_3Ni_3S_8$		**$Co_3Fe_3Ni_3S_4Se_4$**	
Conditions	**Measured density [g/cm^3]**	**Relative density [%]**	**Measured density [g/cm^3]**	**Relative density [%]**
400 °C (15 min)	4,69	91,6	4,82	81,4
450 °C (15 min)	4,79	93,3	5,2	87,8
500 °C (15 min)	4,98	97,2	5,69	96,2
550 °C (15 min)	4,88	95,4	x	x
600 °C (15 min)	4,80	93,7	x	x
650 °C (15 min)	4,80	93,7	x	x
15 min (400 °C)	4,38	85,5	4,82	81,4
20 min (400 °C)	4,40	85,9	4,87	82,3
25 min (400 °C)	4,40	86,0	4,86	82,1

Another test was conducted to assess the influence of sintering temperature on the catalytic activity of the pellets. As mentioned in 4.4.1, sintering temperatures above 500 °C led to phase composition of the pellet samples. Despite the presence of iron-rich precipitates, pentlandite remains the main phase at temperatures above 400 °C. Therefore, it was decided to investigate how the density and the possible presence of these precipitates affect the HER activity. Therefore, these tests were performed on $Co_3Fe_3Ni_3S_8$ (as the most stable composition) samples, sintered at 400 °C, 450 °C, and 500 °C, in two series: pellets sintered from hand-milled powders in an agate mortar and those sintered from normalized milled powders. A sulfur-only composition was chosen to avoid significant Se evaporation at higher sintering temperatures. Figure 75–Figure 77 show the LSV, C_{dl}, and Tafel slope charts for both non-normalized and normalized pellet series.

The results confirm the exceptional HER capabilities of pentlandites in this regard. It was found that current densities at a given overpotential could be significantly improved by applying higher sintering temperatures, which is linked to achieving near-theoretical density in the samples and a high defect concentration. As shown in Figure 74, the average sulfur concentration per area decreases from 45 mol% to 43 mol%, and finally to 41 mol% for the pellets sintered at 400 °C, 450 °C, and 500 °C, respectively. This confirms the observation of sulfur evaporation as the sintering temperature increases.

This test also revealed that the high defect concentration, in combination with the material density, results in the conventional and random precipitation of the active phase as a non-stoichiometric iron sulfide. These phases are anchored to the highly conductive and catalytically active surface in the form of pentlandite. This phenomenon led to the appearance of unpredictable synergistic effects, yielding solid electrodes with high efficiency.

In both series, samples sintered at higher temperatures (450 °C and 500 °C) exhibited higher current densities compared to those sintered at 400 °C. However, surprisingly, the hand-milled series provided more consistent and intuitive results, with a clear correlation between increasing temperature and improved HER efficiency (Figure 75a), as well as a decrease in ECSA (Figure 76a).

Furthermore, the increase in sintering temperature had a significant impact on both overpotential (Figure 75) and Tafel slopes (Figure 77). The Tafel slopes of samples sintered at higher temperatures were significantly lower (90 mV for non-normalized and 83 mV for normalized pellets sintered at 500 °C) compared to those sintered at 400 °C (268 mV for non-normalized and 209 mV for normalized pellets).

The positive influence of temperature treatment was also observed in the normalized series (Figure 75b). However, the HER performance of these samples was significantly worse compared to the non-normalized ones. Moreover, the sample sintered at 450 °C outperformed the one sintered at 500 °C, suggesting that the larger extent of Fe-rich precipitation at 500 °C reduced the contribution of the pentlandite surface. Although the Fe-rich precipitates themselves are catalytically active, their excessive formation diminishes the relative pentlandite area, thereby weakening the synergistic effect

between the two active phases. Similar to the case of selenium concentration, this indicates the existence of a critical sintering temperature at which the balance of defects and phase proportions leads to the highest performance.

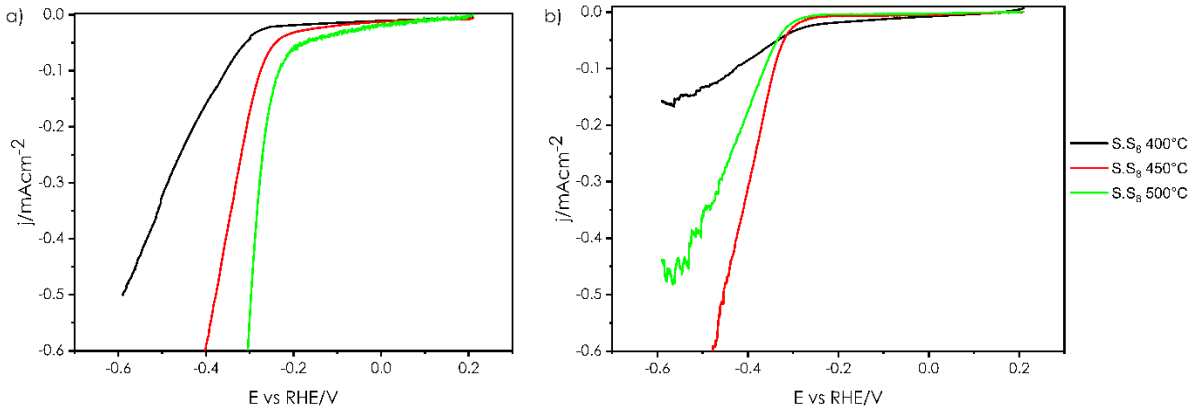

Figure 75. LSV curves as a function of Se concentration normalized to ECSA, recorded at sweep rate of 6.25 mV/s[1]int 0.5 M H_2SO_4: a) pellets with random particle sizes and b) pellets with normalized particle sizes.

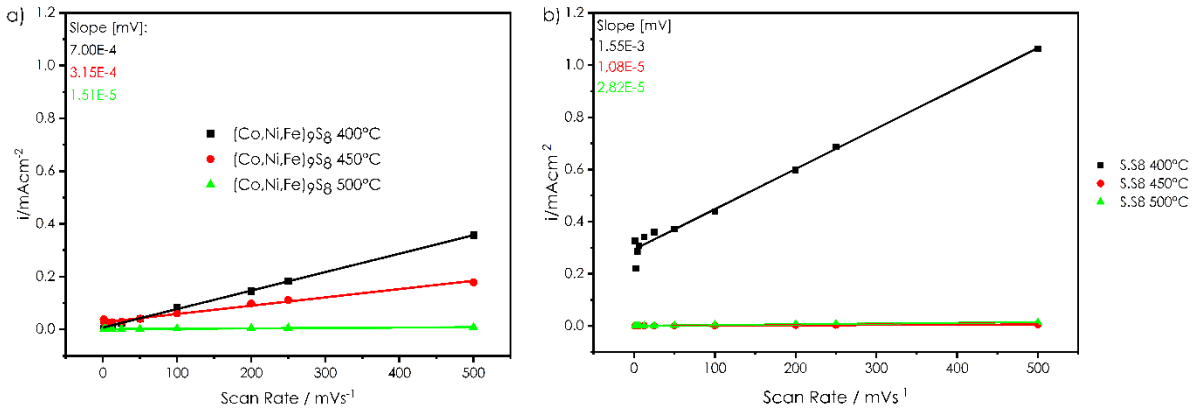

Figure 76. Charging current densities representing C_{dl} for $Co_3Fe_3Ni_3S_8$ pellets sintered in different temperatures for a) random particle sizes and b) pellets with normalized particle sizes.

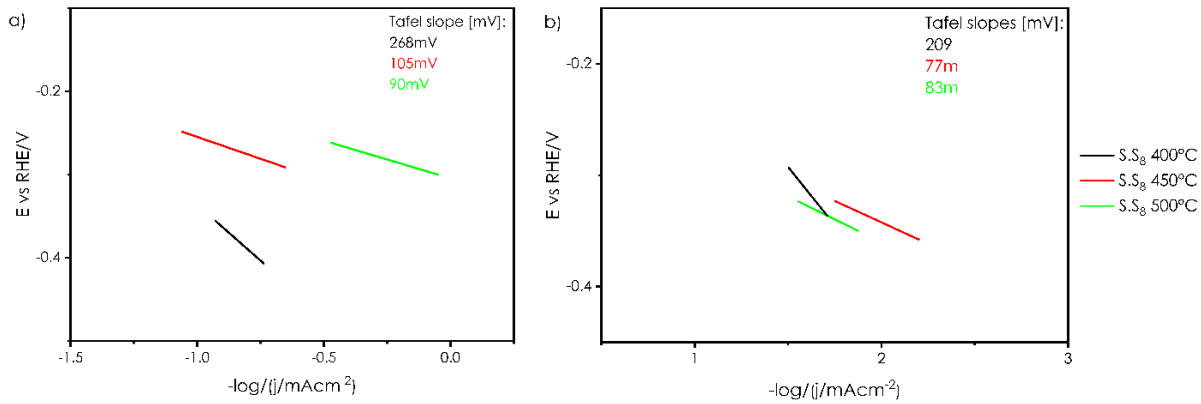

Figure 77. Tafel slopes of pellets with a) random particle sizes and b) pellets with normalized particle sizes.

Summarizing the observations about pellets sintered from non-normalized powders and the impact of higher sintering temperatures, several conclusions emerge. First and foremost, the preparation of the electrode itself, including its surface treatment and pre-test processing, plays a crucial role in determining HER performance. Second, the non-normalized milling process, which results in a random particle size distribution, significantly affects the current densities of the materials. The

same effect is observed for the density and the precipitates with high efficiency on the surface, which are influenced and modified by the sintering temperature. The key takeaway is that electrode preparation and the pre-test treatment of the material are essential when comparing materials with different chemical compositions, as each of these variables has a significant impact on the HER performance of pentlandite materials.

4.4.2. S.116.S8 phenomenon

The "S.116.S8 phenomena" was previously mentioned during the LSV test of the $Co_{9-x-y}Fe_xNi_yS_8$ series, where the S.116.S8 sample exhibited a strong non-cathodic current after the stability test. This sample was also the best performer in both measurements: before and after chronoamperometry. The S.116.S8 composition is multi-phase immediately after synthesis and undergoes further decomposition during sintering, resulting in the formation of nickel sulfide-based phases distributed throughout the material. NiS phases are catalytically active, creating a favorable yet unpredictable scenario where a catalyst is anchored to another catalyst - pentlandite (similarly as in the case of pellets sintered above 400 °C). In this context, despite achieving low overpotentials, the kinetics of the HER reaction are reduced, due to the NiS precipitates block active sites on the pentlandite surface (and related *sulfur depletion* mechanism).

It is worth noting that the S.116.S8 sample behaves similarly in the initial stages, where the amount of nickel sulfide phases increases from about 4% after synthesis to approximately 12% upon sintering. These actively segregated nickel sulfide phases contribute to excellent HER efficiency, as shown in Figure 78, both as a function of ECSA (Figure 78a) and geometric area (Figure 78b), reaching $\eta_{0.2ECSA}$ = 291 mV and η_{10geo} = 341 mV, respectively. In both cases, the characteristic bend in the LSV curve, associated with the NiS reduction reaction (Ni^{2+} to metallic Ni) can be observed.

To further test its unusual behavior, this material underwent additional processing following the scheme shown on Figure 36. After the first chronoamperometry measurement, the material's properties significantly deteriorated, resulting in overpotentials of $\eta_{0.2}$ = 356 mV and η_{10} = 388 mV, based on ECSA and geometric area, respectively. Notably, subsequent chronoamperometry and LSV measurements did not cause further significant changes in the catalytic performance of this material.

Structural analysis of S.116.S8 (Figure 79) shows that under operating conditions, the nickel sulfide contamination (Figure 79a) disappears (Figure 79b), and the remaining Ni-rich pentlandite becomes a single-phase system. In other words, there is no further decomposition, and a thermodynamic equilibrium is established, indicating the limit of nickel solubility in this system is near the $Co_{1.42}Fe_{1.37}Ni_{5.21}S_8$ composition (based on SEM-EDS). This equilibrium is clearly shown in Figure 79c, which compares areas affected and unaffected by HER processing.

This conclusion is confirmed by changes in ECSA and RF values at each processing stage (Table 10). After the first chronoamperometry cycle, both parameters increased due to the removal of NiS, which

had blocked active sites on the pentlandite surface. The second cycle led to a further increase, now attributed to the typical activation process observed in pentlandite materials. These findings highlight a dual effect of NiS: it can initially enhance HER performance by lowering overpotentials, but at the same time, it reduces ECSA, limits the formation of active sites, and slows down reaction kinetics in an uncontrolled manner.

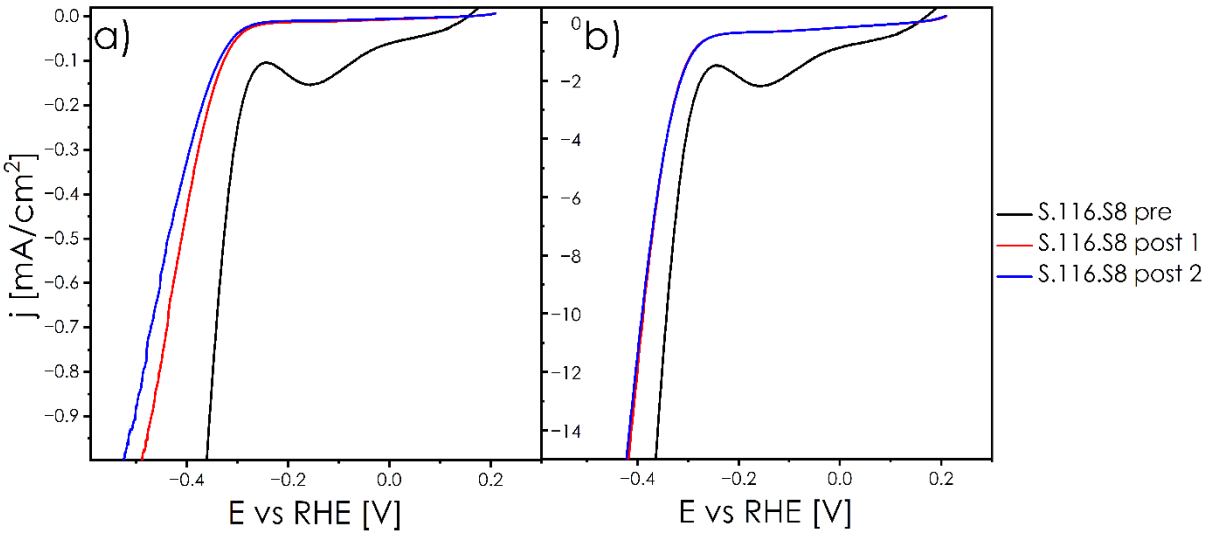

Figure 78. LSV curves recorded in 0.5 M H_2SO_4 at a 6.25 mV/s sweep rate and normalized to: a) ECSA and b) geometrical area for $Co_{1,5}Fe_{1,5}Ni_6S_8$ pellet.

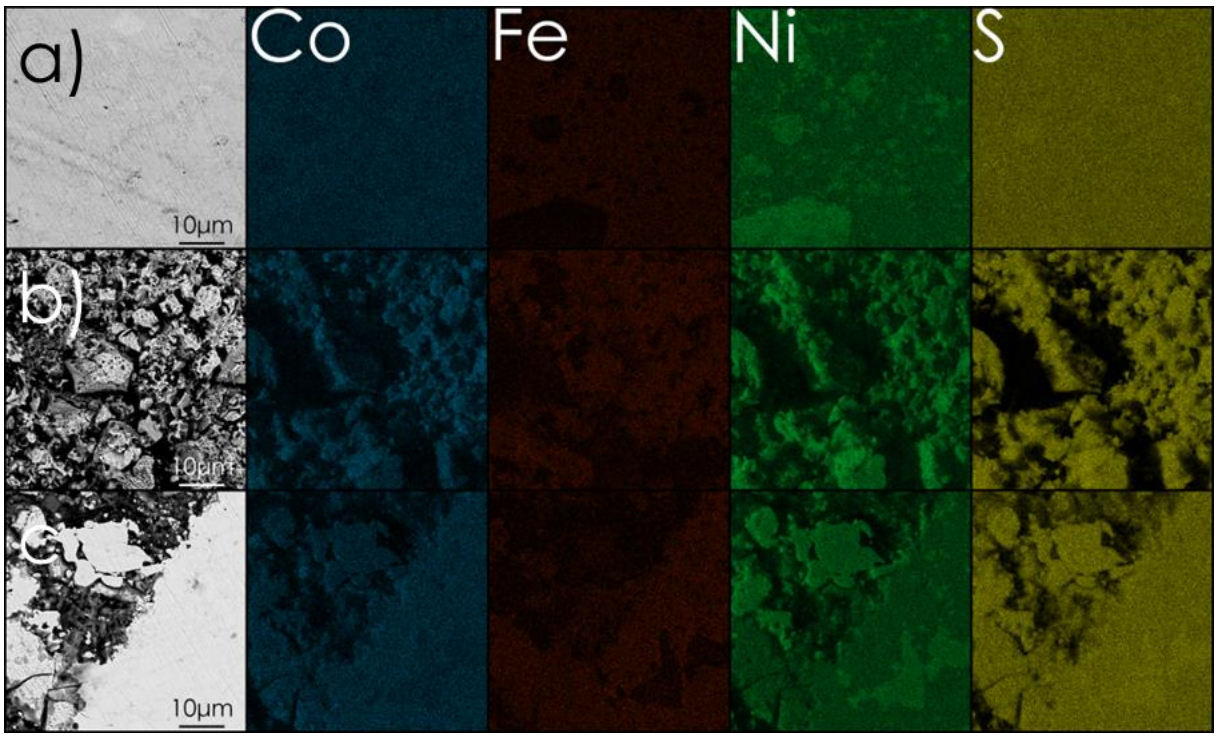

Figure 79. SEM micrographs together with EDS elemental mapping for $Co_{1.5}Fe_{1.5}Ni_6S_8$ sintered pellet: a) pre-measurement area; b) post-measurement area; and c) border of areas affected (top-left) and unaffected (bottom-righ) by HER processing.

Table 11. ECSA and RF values for $Co_{1.5}Fe_{1.5}Ni_6S_8$ pellet.

	ECSA [$cm^{-2} \cdot 10^3$]	RF [$-\cdot 10^3$]
Prior	1.72	14.23
Post 1	3.32	27.46
Post 2	4.24	35.08

4.4.3. Pellets sintered from randomly milled powders

The second additional analysis focused on evaluating the HER performance of sintered pellets made from randomly distributed, milled powders. Typically, all powders, whether for preparing powder electrodes or sintering pellets, are milled in a planetary mill for the same duration for each sample. However, for the $Co_3Fe_3Ni_3S_{8-x}Se_x$ series, an additional test was conducted in which pellets were sintered from powders ground in a hand-agate mortar, resulting in randomly distributed particle sizes rather than following the standard milling procedure. This test aimed to investigate the impact of particle distribution on electrocatalytic performance. The LSV measurements normalized to ECSA for these pellets are shown in Figure 80a.

As presented, the pellets made from these powders do not exhibit a clear trend with respect to the chemical composition. The three best-performing compositions are the extremes: $Co_3Fe_3Ni_3S_8$, $Co_3Fe_3Ni_3S_4Se_4$, and $Co_3Fe_3Ni_3S_3Se_5$ (with HER performance reaching $\eta_{0.2ECSA}$ = 428 mV, 384 mV, and 362 mV, respectively), with the two pellets containing the highest Se concentrations performing the best. This is particularly interesting, as it contrasts with the bimetallic compositions [210]. For the normalized pellets, the $S.S_4$ and $S.S_3$ compositions show nearly identical results, confirming that selenium strongly influences the overpotentials and masks the effects of both cations and microstructure. At the same time, the S.S8 sample performs almost equally well, indicating that in sulfur-rich materials the random grain distribution and associated microstructural features become more important, as they expose numerous active sites related to sulfur-vacancy formation.

Analyzing the C_{dl} (Figure 80b) and Tafel slopes (Figure 80c) of the non-standardized pellets reveals a clear observation: both values appear random and do not correlate with Se concentration. For example, the Tafel slope of non-standardized $Co_3Fe_3Ni_3S_7Se$ (the highest in this series) is 397 mV, whereas the "normalized" $Co_3Fe_3Ni_3S_7Se$ has a Tafel slope of 154 mV – the lowest and best in this series. This test shows that the most important factor affecting kinetics and ECSA in such studies is the precise and reproducible preparation of electrodes before measurements.

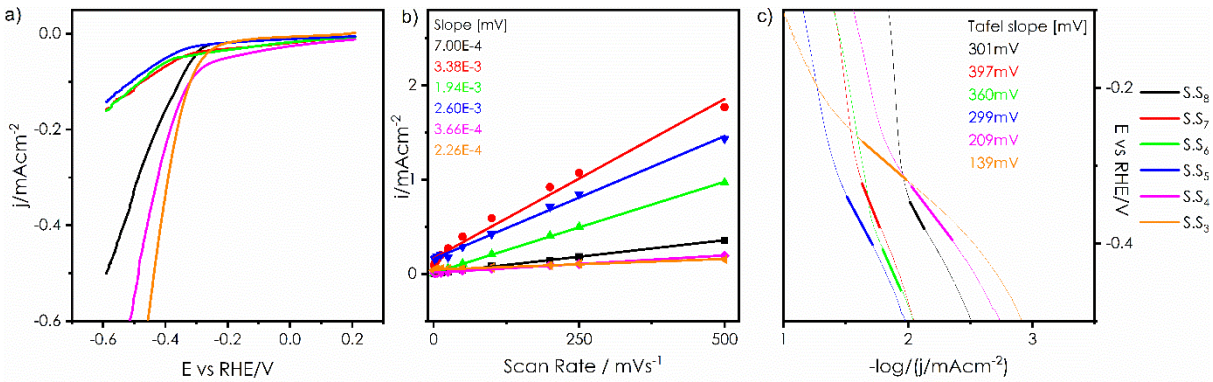

Figure 80. a) LSV curves normalized to ECSA, b) C_{dl} values, and c) Tafel slopes for non-normalized $Co_3Fe_3Ni_3S_{8-x}Se_x$ pellet series.

4.4.4. Another approach to powders

Due to challenges in interpreting the performance of powder-based electrocatalysts in the hydrogen evolution reaction – particularly due to the significant influence of Nafion, the substrate, and the uneven distribution and size of powder grains on electrode surfaces – it was decided to conduct an additional analysis. As not all samples achieved standard current densities (e.g., η_{10}) the comparison was made based on the potential at which the HER reaction began for each sample. Figure 81 shows the LSV curves for all samples, both before and after chronoamperometry, normalized to the ECSA. The points at which the reaction appeared to start – onset potential – are indicated by vertical lines in colors corresponding to each LSV curve. It is important to note that this is not a standardized method; rather, it represents an alternative approach proposed in this work, where the onset values were determined manually and are intended to illustrate general trends rather than provide precise HER onset potentials. Additionally, Figure 82 graphically presents the onset potential obtained for all three series, offering a visual representation of the observed trends. Table 12 lists the corresponding onset potential values for each sample, before and after the chronoamperometric test.

Within the $Co_3Fe_3Ni_3S_{8-x}Se_x$ series, the best-performing sample is P.S7, with HER onset potentials of 346 mV and 403 mV vs. RHE before and after chronoamperometry, respectively, confirming the consistent observation that the X.S7 composition tends to outperform others. In contrast, the poorest performance is observed for P.S4, which exhibits an onset potential of 549 mV prior to chronoamperometry, standing out as an outlier within the series.

The $Co_{9-x-y}Fe_xNi_yS_4Se_4$ series shows overall the best performance, particularly among Fe-rich compositions. Samples P.341.S4, P.161.S4, and P.143.S4 display the lowest onset potentials prior to chronoamperometry (225 mV, 313 mV, and 215 mV, respectively). After chronoamperometric testing, almost all samples in this series retain onset potentials below 400 mV, and in some cases even below 300 mV. The only exception is P.413.S4, with a post-test onset of ~446 mV, which is still ~50 mV lower than the equimolar P.S4 sample. Overall, Fe-rich samples consistently show the most favorable onset values in this series.

By contrast, the $Co_{9-x-y}Fe_xNi_yS_8$ series generally exhibits the highest onset potentials, often exceeding that of the equimolar P.S8 sample. Only one Fe-rich sample, P.161.S8, and several near-equimolar, low-Fe compositions show promising values. Furthermore, in most cases no improvement is observed that could be attributed to the sulfur-depletion mechanism. The notable exception is P.314.S8, where the onset potential decreases dramatically from 710 mV to 350 mV after chronoamperometry, indicating a potential activation. although it is most likely related to a measurement error.

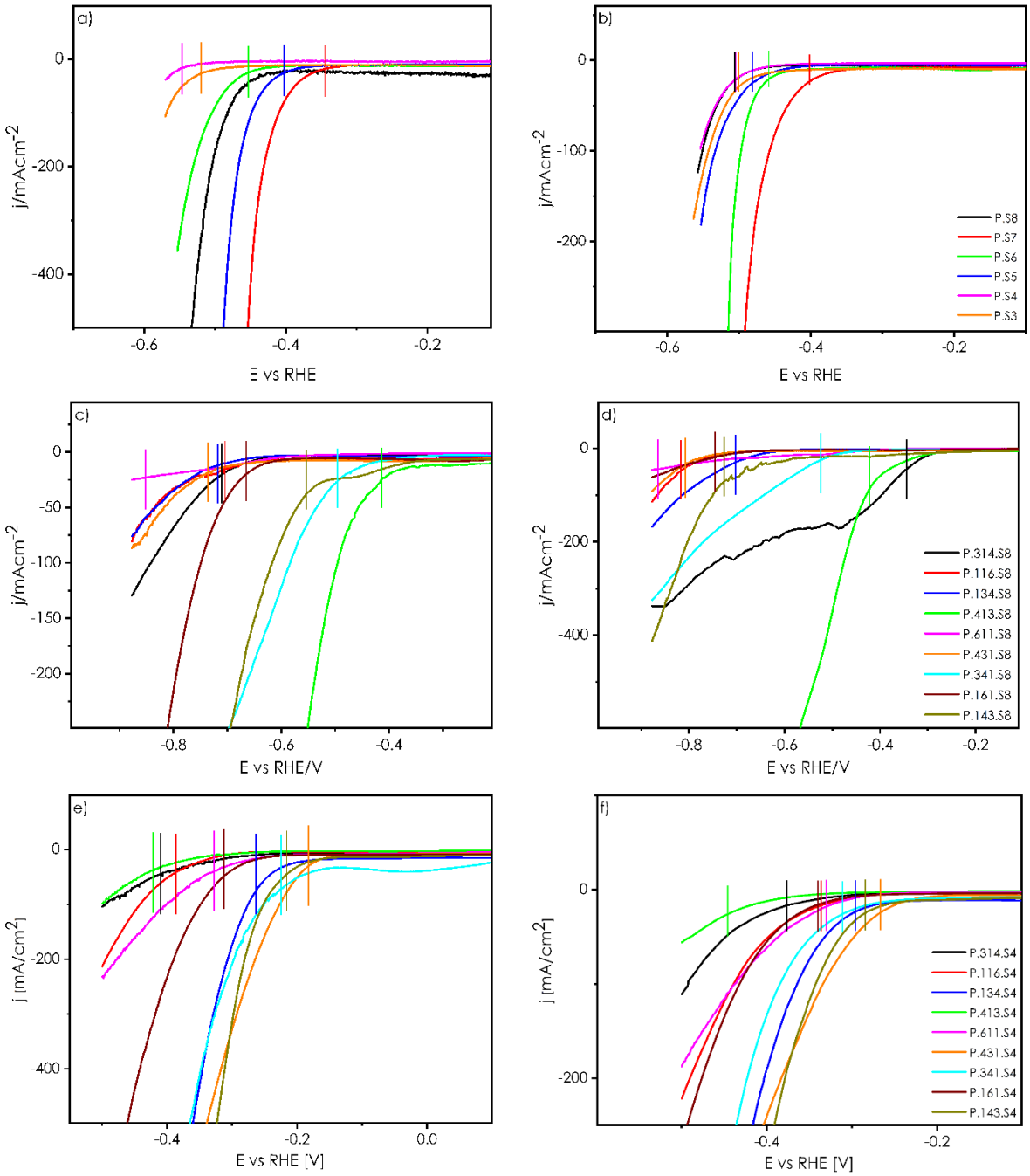

Figure 81. Onset potential of HER reaction of powders for: a) $Co_3Fe_3Ni_3S_{8-x}Se_x$ series before chronopotentiometry; b) $Co_3Fe_3Ni_3S_{8-x}Se_x$ series after chronopotentiometry; c) $Co_{9-x-y}Fe_xNi_yS_8$ series before chronopotentiometry; d) $Co_{9-x-y}Fe_xNi_yS_8$ series after chronopotentiometry; e) $Co_{9-x-y}Fe_xNi_yS_4Se_4$ series before chronopotentiometry; f) $Co_{9-x-y}Fe_xNi_yS_4Se_4$ series after chronopotentiometry.

This experimental approach of analyzing the HER performance of powder samples confirms that, among the metal-equimolar compositions, the best-performing sample is the one with a small selenium addition (P.S7). Selenium positively influences the electronic structure while still leaving sufficient sulfur content, so that the sulfur-depletion mechanism is not limited**.** Additionally, when using a variable-metal composition strategy, non-equimolar samples – particularly those with a high iron content (e.g., P.161.S4) – show favorable HER performance, but only when combined with a high selenium content. In contrast, for pentlandites with high sulfur content, the best-performing samples are those with near-equimolar (P.413.S8, P.314.S8) or equimolar (P.S8) compositions. However, even these exhibit significantly lower HER activity compared to other groups. While this experimental method is not ideal and involves a degree of subjectivity, it provides a more accurate comparison of the intrinsic performance of pure powder catalysts by minimizing the influence of substrate effects and surface distribution. Importantly, although not a perfect methodology, this approach demonstrates that results which in the main series of powders often deviated from general trends show much greater consistency with the overall observations when analyzed in this way.

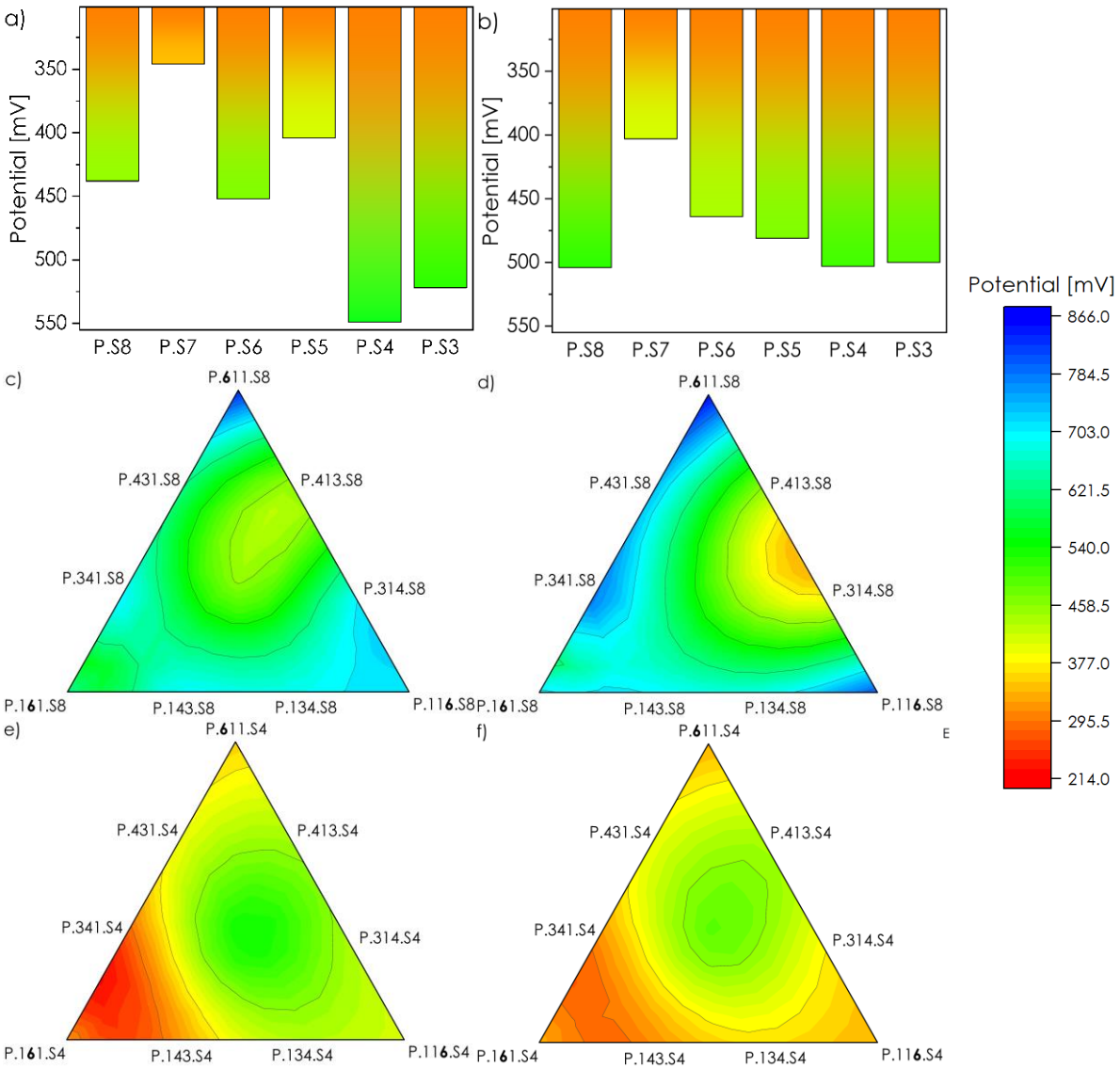

Figure 82. Graphical representation of HER reaction onset trends for powders from: a) $Co_3Fe_3Ni_3S_{8-x}Se_x$ series before chronopotentiometry; b) $Co_3Fe_3Ni_3S_{8-x}Se_x$ series after chronopotentiometry; c) $Co_{9-x-y}Fe_xNi_yS_8$ series before chronopotentiometry; d) $Co_{9-x-y}Fe_xNi_yS_8$ series after chronopotentiometry; e) $Co_{9-x-y}Fe_xNi_yS_4Se_4$ series after chronopotentiometry; f) $Co_{9-x-y}Fe_xNi_yS_4Se_4$ series after chronopotentiometry.

Table 12. Onset potentials of HER reaction for the tested powder electrrodes from all series.

Sample	Onset potential [mV]:		Sample	Onset potential [mV]:		Sample	Onset potential [mV]:	
	Prior	**Post**		**Prior**	**Post**		**Prior**	**Post**
$Co_3Fe_3Ni_3S_{8-x}Se_x$ series			**$Co_{9-x-y}Fe_xNi_yS_8$ series**			**$Co_{9-x-y}Fe_xNi_yS_4Se_4$ series**		
S8	438	504	**P.314.S8**	710	350	**P.314.S4**	410	376
S7	346	403	**P.116.S8**	705	817	**P.116.S4**	388	336
S6	452	464	**P.134.S8**	715	702	**P.134.S4**	263	294
S5	404	481	**P.413.S8**	415	426	**P.413.S4**	421	446
S4	549	503	**P.611.S8**	851	866	**P.611.S4**	329	330
S3	522	500	**P.431.S8**	735	802	**P.431.S4**	182	267
			P.341.S8	496	523	**P.341.S4**	225	311
			P.161.S8	666	746	**P.161.S4**	313	340
			P.143.S8	555	726	**P.143.S4**	215	284

5. Discussion

5.1. Phase and chemical stability of pentlandites

Table S1. Summary of all samples from all three series and all three forms, with chemical compositions determined by EDS and ICP-OES, other phases in the material determined by XRD analysis, elementary cell size, Goodness of Fit, Weighted R profile determined by Rietveld analysis and relative density for ingot and pellet samples.

The initial aim of this thesis was to investigate the solubility limits of individual elements in trimetallic pentlandites, as illustrated in Figure 83. This section focuses on: a) the solubility of selenium in an equimolar pentlandite structure ($Co_3Fe_3Ni_3S_{8-x}Se_x$ series, Figure 83a and Figure 83b), b) the solubility of different amounts of transition metals on the cationic sublattice in a sulfur-only pentlandites ($Co_{9-x-y}Fe_xNi_yS_8$ series, Figure 83c and Figure 83d), and c) the same transition metal substitutions in a system containing equimolar amounts of sulfur and selenium ($Co_{9-x-y}Fe_xNi_yS_4Se_4$ series, Figure 83e and Figure 83f).

As shown in Figure 83a, substituting sulfur with selenium does not disrupt the single-phase pentlandite structure up to approximately 65% selenium substitution, corresponding to composition P.S5. Further substitution results in the appearance of secondary phases: 8.3% CoSe and 1.3% NiS for P.S6. With increasing selenium content, decomposition into dominant secondary phases occurs – 43.4% CoSe and 31% FeSe for P.S7, and 70.1% FeSe and 12.3% CoNiSe for P.S8, but this is not caused by the amount of selenium itself, but rather, as confirmed by DFT analyses and formation energies, reflects the thermodynamic preference for the formation of these secondary phases instead of a selenium-rich pentlandite Thermal treatment of this series (Figure 83b) does not induce decomposition of the single-phase materials; even P.S5 remains single-phase after heat treatment. Based on these results, the solubility limit for selenium in cationic equimolar compositions of pentlandite is defined as $Co_3Fe_3Ni_3S_3Se_5$ which is the same as that determined for the corresponding bimetallic systems [210].

Variation in the amounts of transition metals on the cationic sublattice in the sulfur-rich series (Figure 83c and Figure 83d) reveals a significant impact on the phase stability of the pentlandite structure. For the $Co_{9-x-y}Fe_xNi_yS_8$ powders (Figure 83c), most compositions remain single-phase, with the exception of three materials that deviate significantly from the stoichiometry of naturally occurring pentlandite. These exceptions – Fe- and Ni-rich compositions (P.161.S8, P.116.S8, and P.341.S8) – exhibit the formation of secondary phases. In P.116.S8 and P.341.S8, minor amounts of NiS (3.7%) and FeS (5.7%), respectively, are observed, while the Fe-rich composition P.161.S8 shows more substantial decomposition, with 24.3% FeS and 4.8% elemental Fe detected. Thermal treatment of these samples (Figure 83d) leads to further decomposition, ultimately resulting in only two compositions – S.413.S8 and S.611.S8 – retaining a single-phase structure. Notably, these compositions

are close to that of naturally occurring pentlandite (Co_9S_8), indicating that this stoichiometry represents a thermodynamically stable configuration, due to the local order enabled by the stabilizing role of cobalt. The results suggest that synthesizing single-phase materials significantly deviating from this natural composition is difficult, if not impossible. Overall, the observed solubility limits are in good agreement with values previously reported in the literature [68].

Investigations of the next series – comprising equimolar sulfur and selenium ($Co_{9-x-y}Fe_xNi_yS_4Se_4$, Figure 83e and Figure 83f) – revealed several noteworthy observations. Due to the larger unit cell size resulting from selenium's greater atomic radius compared to sulfur, some powder compositions more readily retain a single-phase structure (Figure 83e). However, Ni-rich compositions exhibit the formation of secondary phases, such as 10.5% of $CoNiS_4$ and 6.3% of $CoNiSe_2$ for P.116.S4, and 2.4% of NiSe for P.134.S4. While the minor amount of NiSe precipitate in P.134.S4 does not significantly alter the material's overall character, this composition still cannot be considered single-phase. Upon thermal treatment (Figure 83f), additional foreign phases appear in all compositions. While in some cases the precipitates are minor (e.g., 1.4% $Fe_{11}S_{12}$ in S.143.S4), in most samples they are more pronounced – such as 19% FeSe in S.611.S4 and 23.7% FeSe in S.341.S4. These results show that even the most stable compositions from the sulfur-only series do not retain their single-phase character when equimolar amounts of sulfur and selenium are used. However, the incorporation of selenium increases the solubility range of individual cations compared to S-only pentlandites, although the overall stability of these Se-rich systems remains moderate.

In summary, direct synthesis from elements allows for the creation of four- and five-element materials with pentlandite structures. Additionally, it is possible to tailor the chemical compositions on both the cationic and anionic sublattices, though within limited ranges. The pentlandite structure forms solid solutions within the TM_9S_8-S_3Se_5 series, where the addition of selenium increases the lattice parameters, in accordance with Vegard's rule. However, exceeding a certain selenium content leads to material decomposition.

Similarly, manipulation of the metal content in the cationic sublattice is feasible, but compositions deviating significantly from naturally occurring pentlandite ores (Co_9S_8; $Fe_{4.5}Ni_{4.5}S_8$) are unstable. This means that compositions with high iron or nickel content will be unstable in practice. Moreover, substituting sulfur with selenium improves the stability of the material, enabling the synthesis of pentlandites with more extreme metal compositions. Effective screening of pentlandite materials to identify the best HER catalysts is possible within broad but limited stoichiometric ranges, with their performance strongly depending on the material's form. It is important to note that selenium masks cationic effects in solid electrodes, facilitating higher current densities but simultaneously drastically reducing reaction kinetics and the number of active sites.

Heat treatment and sintering by IHP method often lead to the formation of additional phases in the material, particularly Fe-rich ones. This occurs for two reasons: iron has the lowest reduction

potential and the IHP process takes place under reducing conditions, plus it has the highest number of electrons. Additionally, eddy currents in IHP are difficult to control. In this case, the addition of selenium increases the stability of pentlandite, although it slightly negatively affects its density [226,245,247].

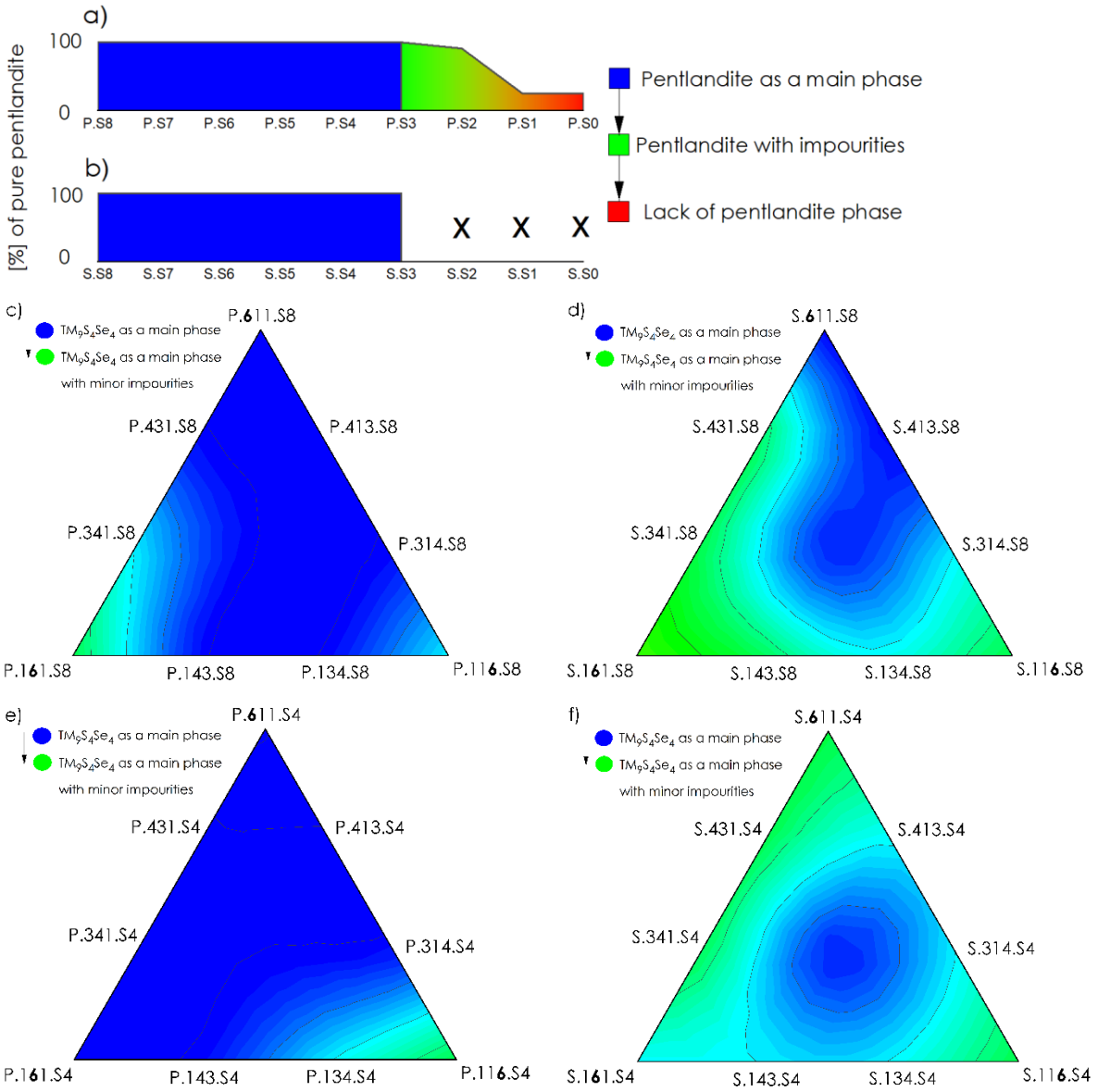

Figure 83. Stability of pentlandite structures represented by ternary diagrams for individual series: a) $Co_3Fe_3Ni_3S_{8-x}Se_x$ powders; b) $Co_3Fe_3Ni_3S_{8-x}Se_x$ pellets; c) $Co_{9-x-y}Fe_xNi_yS_8$ powders; d) $Co_{9-x-y}Fe_xNi_yS_8$ pellets; e) $Co_{9-x-y}Fe_xNi_yS_4Se_4$ powders; f) $Co_{9-x-y}Fe_xNi_yS_4Se_4$ pellets.

5.2. HER

5.2.1. HER normalized to ECSA

For the measurements normalized to ECSA, an overpotential at a current density of 0.2 mA/cm^2 ($\eta_{0.2ECSA}$) was chosen as the basis for comparing the HER performance of all materials. The observed trends for each series – $Co_3Fe_3Ni_3S_{8-x}Se_x$, $Co_{9-x-y}Fe_xNi_yS_8$, and $Co_{9-x-y}Fe_xNi_yS_4Se_4$ – are shown in Figure 84–Figure 86, respectively. To enable comparison across all tested compositions, those that did not reach $\eta_{0.2}$ had the maximum measurable value (804 mV) manually assigned. Analysis of $\eta_{0.2ECSA}$ across all series reveals several key observations. First, ingot samples consistently exhibit the best performance, often achieving overpotentials near or even below 300 mV, what is likely due to their higher phase purity and structural homogeneity compared to pelletized samples, as well as the absence of substrate-related effects observed in powder-based electrodes. While certain samples, such as S.S5 (209 mV) and several powders from the $Co_{9-x-y}Fe_xNi_yS_4Se_4$ series, demonstrate superior performance, the ingot form generally performs best across all compositions.

In the $Co_3Fe_3Ni_3S_{8-x}Se_x$ series (Figure 84), two interesting trends emerge: among low-density materials (powders and ingots), the best HER performance is observed in samples with low selenium content (e.g., P.S7 and I.S7), whereas for high-density materials (pellets), the sample with equimolar sulfur and selenium (S.S4) performs best, because the addition of selenium masks the effects of microstructure and cation influence, whereas a high sulfur content – indicating the absence of selenium's impact – is beneficial for materials with a high surface area. In the $Co_{9-x-y}Fe_xNi_yS_8$ series (Figure 85), ingots again show superior HER performance. Notably, across all material forms, Fe-rich compositions exhibit the poorest performance, while Ni-rich – and to a lesser extent, Co-rich – samples perform the best. An opposite trend is observed in the $Co_{9-x-y}Fe_xNi_yS_4Se_4$ series (Figure 86), where ingot samples also display strong HER activity, particularly those with near-equimolar compositions or enriched in Co or Fe/Ni. A general trend observed across all series indicates that single-phase materials consistently exhibit significantly higher HER activity than those containing secondary phases or impurities. Unfortunately, nearly all samples tested exhibited a decline in HER activity after the two-hour stability test, indicating degradation over time. This degradation likely results from the decomposition of the pentlandite phase into residual compounds and/or the dissolution of certain elements, such as iron, into the electrolyte.

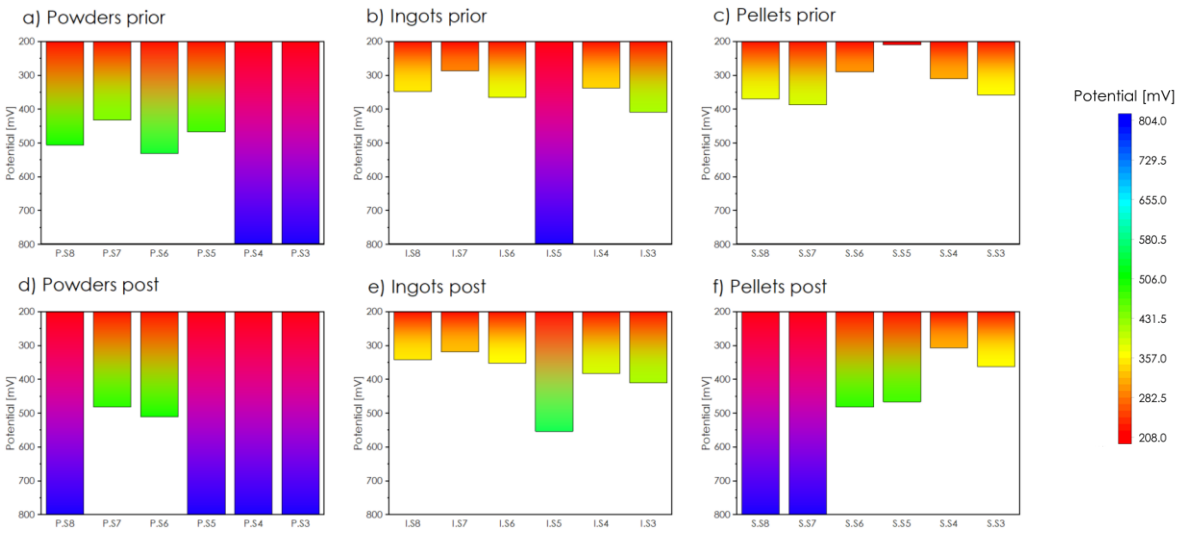

Figure 84. $\eta_{0.2ECSA}$ values of $Co_3Fe_3Ni_3S_{8-x}Se_x$ series for: a) powder samples before chronoamperometry; b) ingot samples before chronoamperometry; c) pellet samples before chronoamperometry; d) powder samples after chronoamperometry; e) ingot samples after chronoamperometry and f) pellet samples after chronoamperometry.

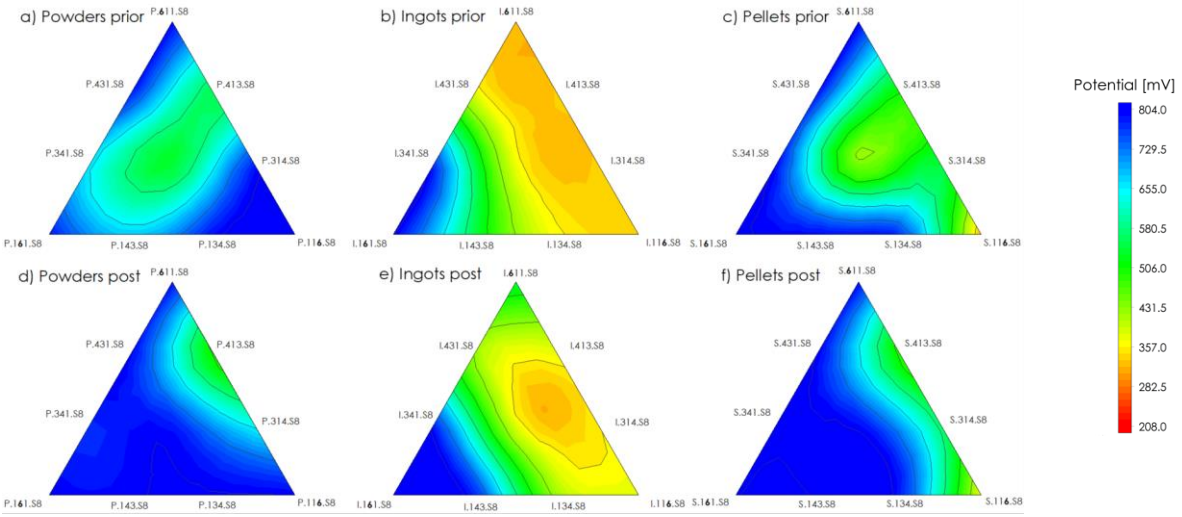

Figure 85.Ternary diagrams representing $\eta_{0.2ECSA}$ values of $Co_{9-x-y}Fe_xNi_yS_8$ series for: a) powder samples before chronoamperometry; b) ingot samples before chronoamperometry; c) pellet samples before chronoamperometry; d) powder samples after chronoamperometry; e) ingot samples after chronoamperometry and f) pellet samples after chronoamperometry.

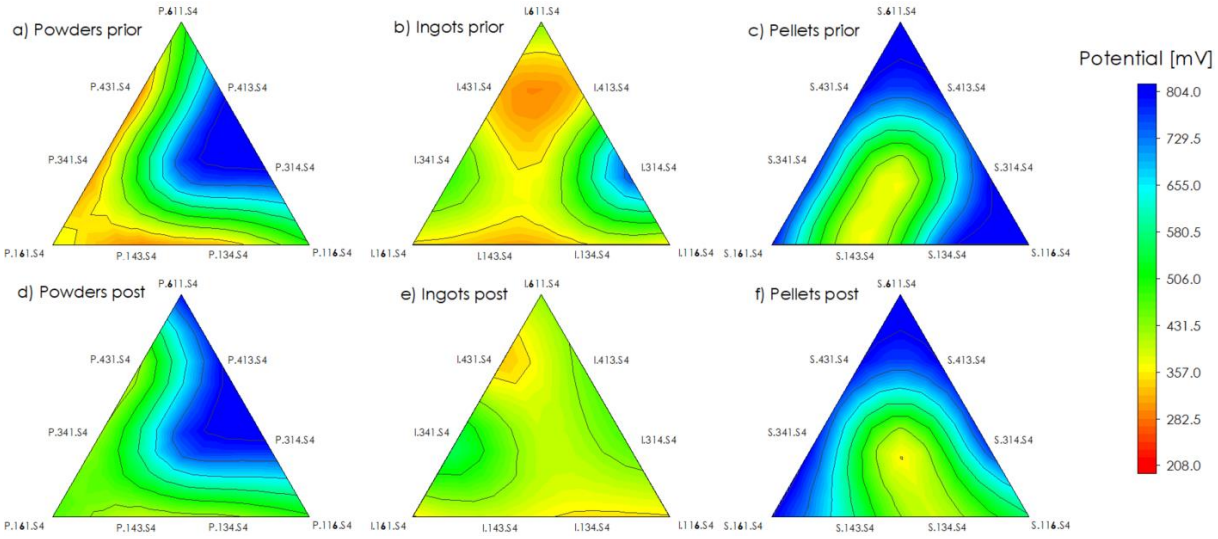

Figure 86. Ternary diagrams representing $\eta_{0.2ECSA}$ values of $Co_{9-x-y}Fe_xNi_yS_4Se_4$ series for: a) powder samples before chronoamperometry; b) ingot samples before chronoamperometry; c) pellet samples before chronoamperometry; d) powder samples after chronoamperometry; e) ingot samples after chronoamperometry and f) pellet samples after chronoamperometry.

5.2.2. HER normalized to geometric area

While overpotential normalized to ECSA is widely accepted in the literature as a parameter for comparing the HER performance of materials, the geometrical normalization approach also offers valuable insights – especially when directly compared with ECSA-based results. In this thesis, overpotential at 10 mA/cm^2 based on geometric area (η_{10geo}) is used to assess HER performance across the different material forms, as shown in Figure 87 – Figure 89. In this geometrical approach, the best-performing form across all series is the high-density material – pellets – followed by ingots, with powders showing the lowest HER performance. This trend highlights how sample density affects the apparent catalytic activity normalized to the geometric surface area, which in turn influences charge-transfer performance.

In the $Co_3Fe_3Ni_3S_{8-x}Se_x$ series (Figure 87), the same trend observed in the ECSA-based analysis is partially maintained: for pellets, the best-performing sample is S.S4, which has equimolar amounts of sulfur and selenium. For lower-density forms (ingots and powders), the best performance is again observed for compositions with a moderate selenium substitution (I.S7 and P.S7). In the $Co_{9-x-y}Fe_xNi_yS_8$ series (Figure 88), a clear contrast to the ECSA-normalized results emerges. Here, Fe- and Co-rich compositions (e.g., S.341.S8 and S.431.S8) show the best HER. This highlights the strong influence of individual transition metals on both ECSA and HER activity, depending on the normalization method. Specifically, Fe- and Co-rich materials exhibit higher ECSA values, which dilutes their performance when normalized to ECSA. However, when normalized to geometric area, their intrinsic catalytic activity becomes more apparent. It should be noted, though, that these parameters are also affected by phase purity, which is not consistent across all samples. Therefore, the interpretation of these results remains at least partially speculative. For the $Co_{9-x-y}Fe_xNi_yS_4Se_4$ series (Figure 89), pellets again show the best HER performance, with Fe- and Co-rich compositions (e.g., S.341.S4 and S.431.S4) outperform

others. Among ingots, the best-performing samples are those with low Ni content and compositions close to equimolar. Powders follow a similar trend to the $Co_{9-x-y}Fe_xNi_yS_8$ series, confirming the influence of elemental composition in high-surface-area materials, where the masking effect of selenium is less critical. Interestingly, across nearly all samples and series, the HER performance – as measured by overpotential – either remains stable or improves slightly after the two-hour chronopotentiometry stability test, indicating reasonable durability under operational conditions.

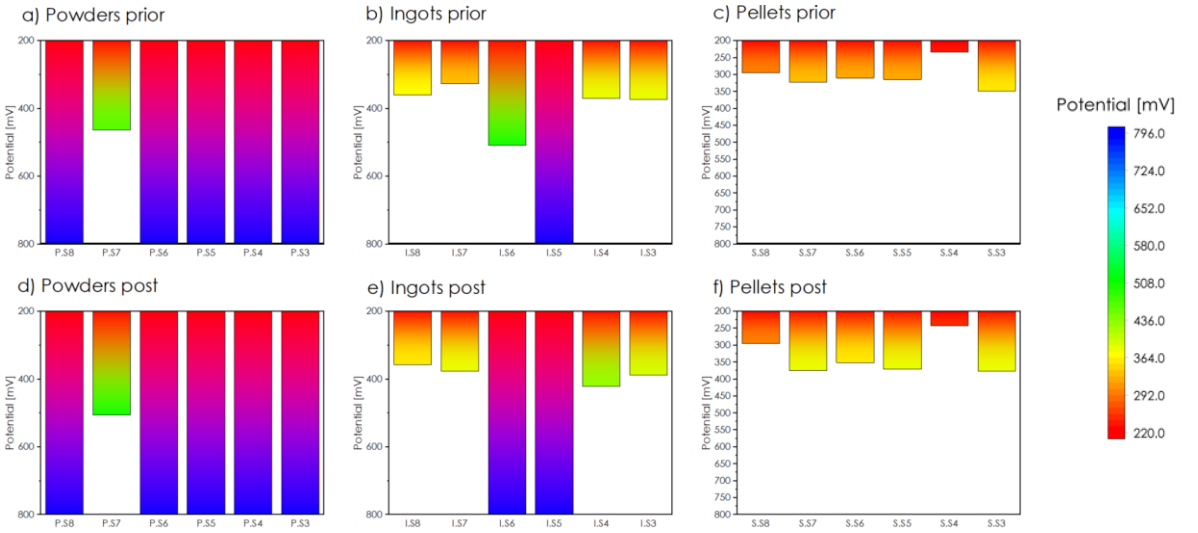

Figure 87. η_{10geo} values of $Co_3Fe_3Ni_3S_{8-x}Se_x$ series for: a) powder samples before chronoamperometry; b) ingot samples before chronoamperometry; c) pellet samples before chronoamperometry; d) powder samples after chronoamperometry; e) ingot samples after chronoamperometry and f) pellet samples after chronoamperometry.

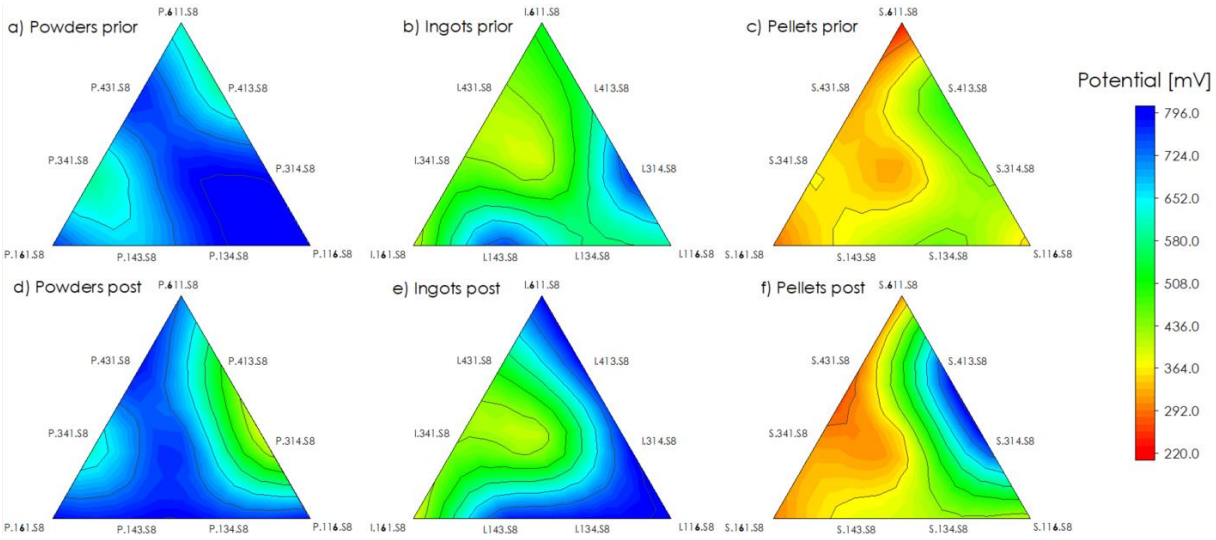

Figure 88. Ternary diagrams representing η_{10geo} values of $Co_{9-x-y}Fe_xNi_yS_8$ series for: a) powder samples before chronoamperometry; b) ingot samples before chronoamperometry; c) pellet samples before chronoamperometry; d) powder samples after chronoamperometry; e) ingot samples after chronoamperometry and f) pellet samples after chronoamperometry.

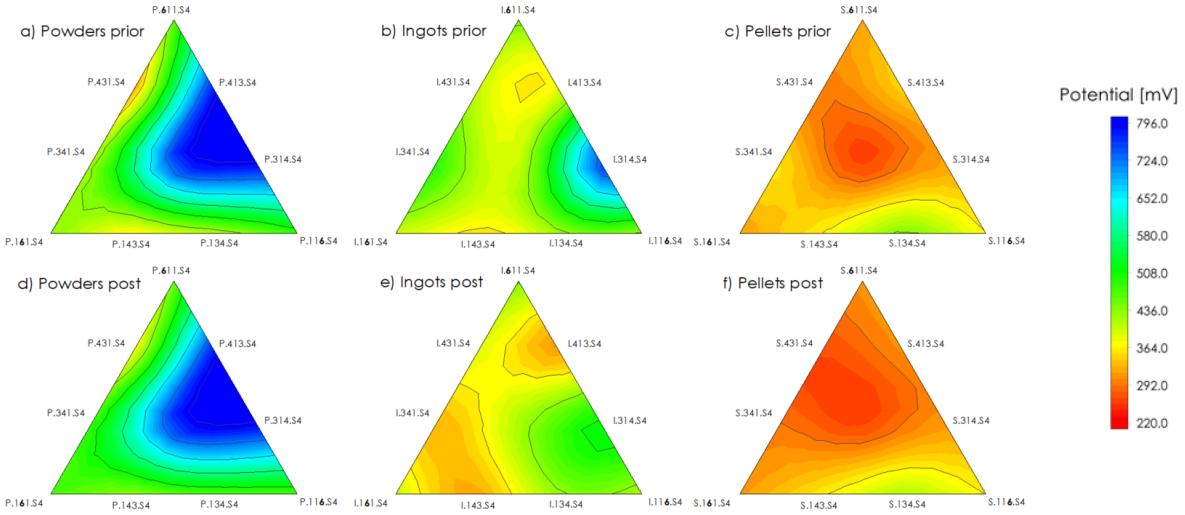

Figure 89. Ternary diagrams representing η_{10geo} values of $Co_{9-x-y}Fe_xNi_yS_4Se_4$ series for: a) powder samples before chronoamperometry; b) ingot samples before chronoamperometry; c) pellet samples before chronoamperometry; d) powder samples after chronoamperometry; e) ingot samples after chronoamperometry and f) pellet samples after chronoamperometry.

5.2.3. HER – summary

These observations suggest that selenium may mask the effect of cations due to strong influence on electronic structure and increased metallic character, making the sample preparation process – and the surface condition of the materials – crucial for electrochemical performance. Therefore, for bulk materials, the surface condition is paramount, while for powders, particle size is a key factor. In the $Co_{9-x-y}Fe_xNi_yS_8$ series, the best-performing samples were those with nearly equimolar chemical compositions, but rich in Fe. However, this trend does not appear in the $Co_{9-x-y}Fe_xNi_yS_4Se_4$ series, making the results more random. Collectively, these findings imply that the absorption mechanism in these materials differs fundamentally from that in classical TM_9S_8-type pentlandites, with a hidden influence from cationic sublattice occupancy. This seems especially plausible, as selenium shifts the d-band center towards the Fermi level, similarly to sulfur vacancy. Given the relatively low sulfur content on the surface (S:Se = 1:1), this effect appears justified.

For materials with equimolar cationic compositions, two key features determine their catalytic behavior: the formation of sulfur vacancies, which provides additional active sites, and the presence of a small selenium addition, which optimizes the electronic structure while leaving sufficient sulfur to sustain the vacancy-driven activation. Specifically, the $Co_3Fe_3Ni_3S_7Se$ material demonstrates a stable composition, highlighting the favorable effects of selenium addition in conjunction with sulfur vacancies. This amount of selenium was identified as a “critical concentration” that shifts the electronic structure of the material toward more favorable values while retaining a high sulfur content on the surface, enabling its detachment. Additionally, XRD analysis reveals that Se predominantly occupies the 8c crystallographic sites, as indicated by changes in the intensity of reflections in the doublet around 30° 2θ, leaving vacancies at the 24e positions free, which can serve as adsorption sites for hydrogen. These interactions significantly influence the electronic structure and catalytic

properties, showing a clear correlation between HER performance, activation mechanisms, and intermetallic interactions – especially in sulfur-rich samples such as powders.

For ingots, high sulfur content combined with a slight Se:S substitution proves advantageous due to favorable d-band center position and longer TM-Ch bonds. The later weakens the bonds with sulfur, facilitating sulfur detachment from the structure, supported by DFT [246]. This effect becomes more pronounced in pellet form, where increasing selenium content correlates with enhanced HER efficiency, despite lower ECSA. This enhancement, in addition to the shifting of the d-band center and the elongation of TM-Ch bonds, is linked with the creation of the new type of active sites.

Thus, without considering the influence of varying metal amounts on the cationic sublattice, sulfur-rich compositions outperform others in both powder and ingot forms, while selenium-rich compositions excel as pellet materials. Notably, among the $Co_3Fe_3Ni_3S_{8-x}Se_x$ series, pellets perform the best, although higher selenium content increasingly diminishes this advantage. On the other hand, the $Co_3Fe_3Ni_3S_7Se$ composition stands out as the most efficient across all forms, highlighting the importance of single S→Se substitution, as well as the sulfur-depletion mechanism, in enhancing the catalytic activity of pentlandite materials**.**

When the number of metals on the cationic sublattice begins to change, while sulfur remains the only element on the anionic sublattice, several observations can be made. For pellet and ingot materials, clear trends emerge: the best performance is observed in Fe- and Co-rich compositions, while Ni-rich materials exhibit the poorest activity, as nickel shifts the electronic levels toward less favorable values for catalytic efficiency [245]. In these systems, the catalytic performance correlates well with the position of the d_{bc} and, to some extent, with electrochemical parameters such as R_{CT}, while the correlation with ECSA alone is less apparent. This indicates that both the composition of the cationic sublattice (particularly Co–Fe-rich systems) and the material form strongly influence charge-transfer abilities and catalytic activity. Phase homogeneity also plays an important role, as single-phase materials tend to exhibit predictable behavior and favorable catalytic parameters. In contrast, materials with surface precipitates – such as FeS or NiS – may display lower overpotentials but simultaneously block the pentlandite surface, thereby altering HER kinetics.

The cases of sulfur-rich pentlandites with various metals on the cationic sublattice serve as an excellent example of a system in which a multi-component approach, synergistic effects, and intrinsic properties yield to surface effects, especially in solid electrode forms. These effects are related to the formation of vacancies, the presence of metallic active sites, and the role of individual elements in enhancing stability.

Substituting sulfur with selenium in the series containing varying amounts of metals in the cationic sublattice increases the solubility of Fe and Ni due to the expansion of the material's geometric space. However, this substitution simultaneously reduces the stability of these compositions over time, as selenium weakens the overall structural integrity of the system, particularly during prolonged

exposure and under high-temperature conditions. This trend is especially evident in the Fe-rich composition, which achieved the best overpotentials and current densities, but also destabilized the fastest during operation. As previously mentioned, supporting DFT studies confirm these observations, ranking the stability of the respective systems in descending order as follows: Co-rich, Ni-rich, and Fe-rich. Selenium also enables the metals to shift toward the adsorbed hydrogen, which leads to the elongation and weakening of TM–Se bonds, particularly around iron atoms, contributing to material degradation and dissolution during operation.

Additionally, a different adsorption mechanism seems to be involved compared to the sulfur-rich series. Specifically, the traditional hydrogen absorption mechanism in pentlandites – typically relying on simple adsorption into sulfur vacancy sites – does not fully account for the observed behavior in these materials. Computational analysis suggests that an alternative absorption mechanism may be involved, characterized by more complex interactions at the atomic level. These interactions could be linked to selenium's influence on the material's electronic structure and intermetallic active sites. While this may enhance the material's ability to adsorb hydrogen more efficiently, the binding strength seems excessively high, which hinders desorption and negatively affects hydrogen evolution kinetics.

Among all series, one notable phenomenon observed during chronoamperometry is the activation process, which refers to cases where long-term processes, such as *sulfur depletion*, enhance the electrochemical performance of the materials. In this thesis, the "activation process" is defined as the situation where the difference between the ECSA before and after chronoamperometry is negative, indicating an increase in the electrochemically active surface, likely due to mechanisms like *sulfur depletion*. A careful analysis of the changes in ECSA and RF values during chronoamperometry – a short-term stability test – revealed that the *sulfur depletion* mechanism predominated in the case of all pentlandite materials with high sulfur content, leading to an increase in RF values, particularly for materials with higher surface areas.

As mentioned in the theoretical section, the addition of a third metal into the cationic sublattice does not significantly improve HER performance to a level surpassing the best-performing samples reported in the literature, such as $Fe_{4.5}Ni_{4.5}S_8$ or $Fe_{4.5}Ni_{4.5}S_4Se_4$, which reaching η_{10} = 280 mA/cm^2 and 300 mA/cm^2, respectively [210]. However, materials with varying elemental compositions within the cationic sublattice exhibit superior catalytic efficiency compared to literature values (e.g. $Fe_2Co_4Ni_3S_8$ reaching η_{10} values of 378 mA/cm^2 [68]), particularly in the case of ingot-type samples, which achieve $n_{0.2}$ values close to 300 mA/cm^2. Unfortunately, it is not possible to compare the last material series with literature data, as this type of system is described for the first time in this work.

In the case of these tests, which include both the cationic and anionic sublattices, and involve changes in the material's form, interpreting the results can be complicated. However, the interpretation of ECSA values and their differences from chronoamperometry tests can reveal the electrocatalytic properties of the materials and help identify the best-performing catalysts. The RF, which serves a similar purpose

as ECSA but is less dependent on the geometric surface area, is an even more reliable metric for describing the electrochemical performance of the material. Moreover, the R_{CT} values – particularly for bulk samples – also provide a good indicator of the final HER performance, complementing the information obtained from ECSA and RF.

5.3. Tafel slope

Tafel slopes, alongside overpotential, are critical parameters for evaluating HER performance, as they describe the reaction kinetics. Although Tafel slopes can be determined from LSV data normalized to either ECSA or geometric area, the trends are consistent between both approaches. Therefore, in this section, only the Tafel slopes obtained from ECSA-normalized LSVs are analyzed in detail (Figure 90 –Figure 92).

Interestingly, and in contrast to overpotential trends, the best Tafel slope values across all series are observed for powder samples. In the $Co_3Fe_3Ni_3S_{8-x}Se_x$ series (Figure 90), all powder samples exhibit Tafel slopes close to or below 100 mV/dec, with only two ingot samples – I.S8 and I.S7 – achieving comparable values. Other ingots, as well as all pellet samples, show significantly higher Tafel slopes, often exceeding 100 mV/dec and in some cases surpassing 200 mV/dec, indicating two to three times slower reaction kinetics compared to the low-density forms. This observation makes the advantage of maximizing surface development in potential applications quite obvious. However, within the scope of this work, it is of particular importance for the discussion of bulk samples in the context of their possible use in flow-cell configurations.

In both variable-transition-metal series ($Co_{9-x-y}Fe_xNi_yS_8$ and $Co_{9-x-y}Fe_xNi_yS_4Se_4$), a clear trend persists: powders exhibit the lowest Tafel slopes, followed by ingots with slightly higher values, and pellets with the highest, often one to three times greater. In the $Co_{9-x-y}Fe_xNi_yS_8$ series (Figure 91), two powder compositions – P.611.S8 and P.116.S8 – along with a few ingots (e.g., I.314.S8, I.143.S8, and I.134.S8), display exceptionally high Tafel slopes. In contrast, the $Co_{9-x-y}Fe_xNi_yS_4Se_4$ series (Figure 92) shows more consistent performance, with no extremely poor-performing powder or ingot samples. While a few weaker-performing examples exist, such as P.314.S4 and I.314.S4, their Tafel slopes still fall within the general range of other samples, particularly after the stability test.

Among pellet samples, only S.116.S8 and two $Co_{9-x-y}Fe_xNi_yS_4Se_4$ compositions (S.143.S4 and S.134.S4) reach Tafel slopes around 100 mV/dec. However, even these are significantly worse than the best-performing low-density materials. Notably, Tafel slope values tend to improve for nearly all samples following the two-hour chronopotentiometry test, indicating enhanced reaction kinetics after prolonged operation.

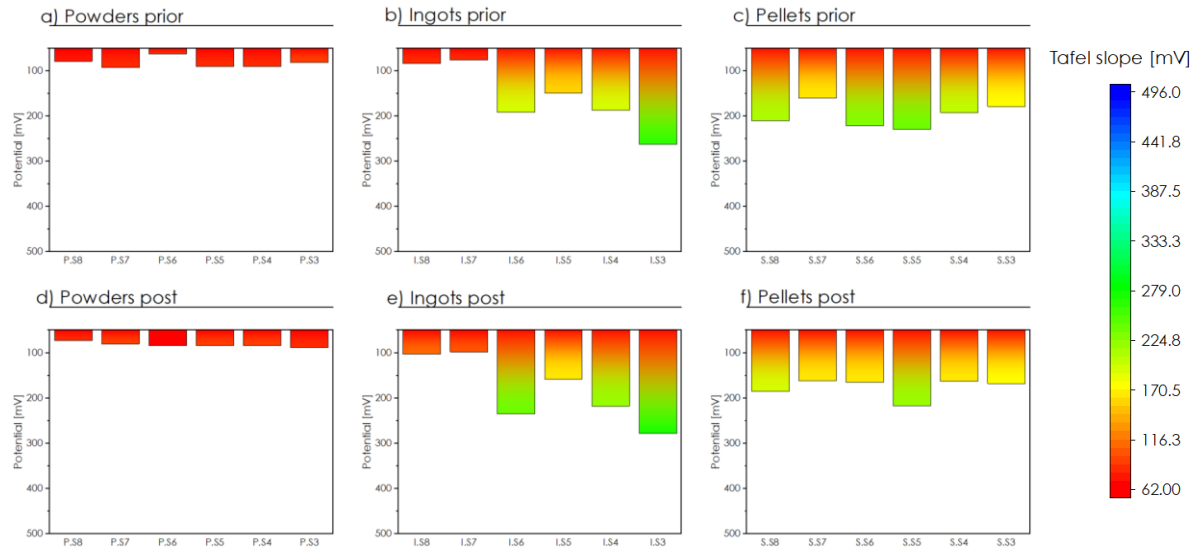

Figure 90. Tafel slope values of $Co_3Fe_3Ni_3S_{8-x}Se_x$ series normalized to ECSA for: a) powder samples before chronoamperometry; b) ingot samples before chronoamperometry; c) pellet samples before chronoamperometry; d) powder samples after chronoamperometry; e) ingot samples after chronoamperometry and f) pellet samples after chronoamperometry.

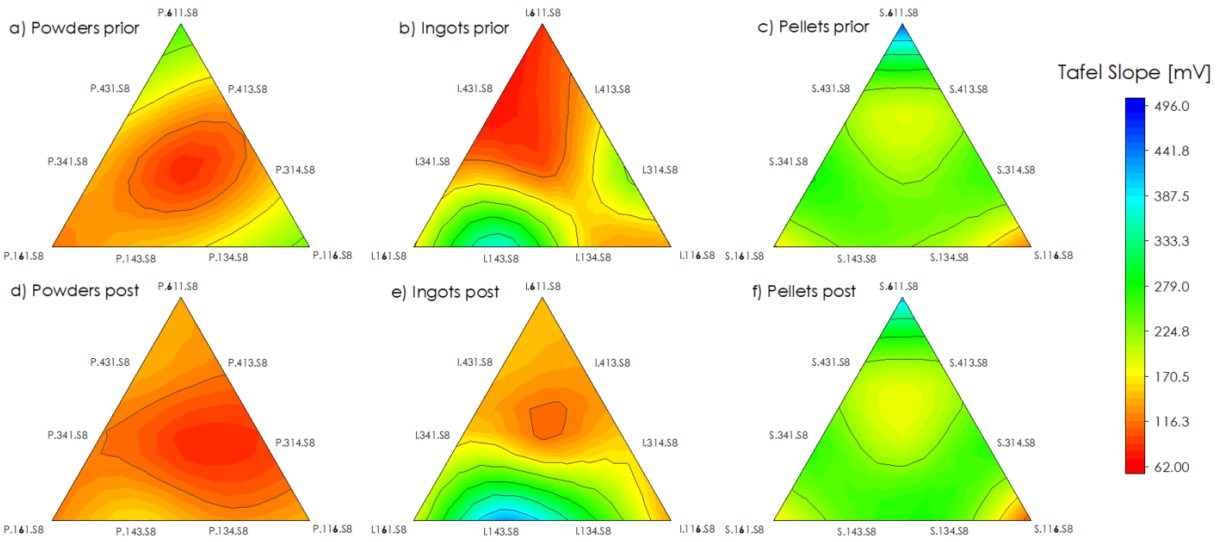

Figure 91. Ternary diagrams representing Tafel slope values of $Co_{9-x-y}Fe_xNi_yS_8$ series normalized to ECSA for: a) powder samples before chronoamperometry; b) ingot samples before chronoamperometry; c) pellet samples before chronoamperometry; d) powder samples after chronoamperometry; e) ingot samples after chronoamperometry and f) pellet samples after chronoamperometry.

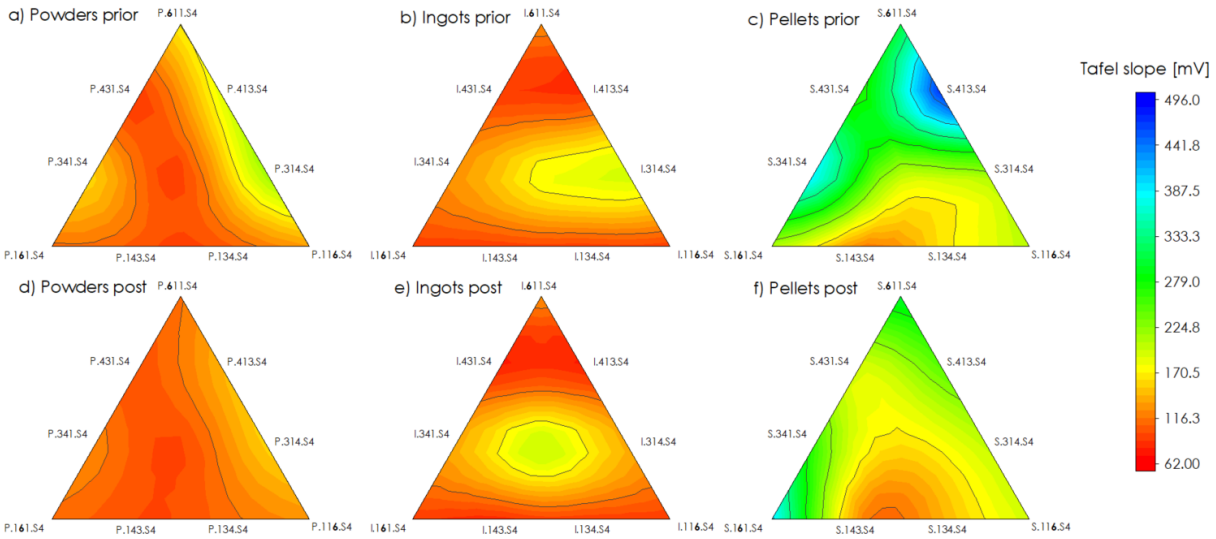

Figure 92. Ternary diagrams representing Tafel slope values of $Co_{9-x-y}Fe_xNi_yS_4Se_4$ series normalized to ECSA for: a) powder samples before chronoamperometry; b) ingot samples before chronoamperometry; c) pellet samples before chronoamperometry; d) powder samples after chronoamperometry; e) ingot samples after chronoamperometry and f) pellet samples after chronoamperometry.

Overall, the main observation from the $Co_3Fe_3Ni_3S_{8-x}Se_x$ series is that HER kinetics tend to slow down with increasing material consolidation, due to the reduced surface area and the lower amount of free sulfur, whose vacancies form active sites preferable for proton adsorptions. This is particularly evident in sintered pellets, though compositional effects on their performance remain speculative.

Studies on the $Co_{9-x-y}Fe_xN_yS_8$ series highlight several key factors that influence HER kinetics and performance. One of the key aspects is phase homogeneity – single-phase materials consistently exhibit more favorable catalytic properties due to their clean surfaces and the absence of precipitates that could block the active species. The presence of catalytically active phases on the surface, such as iron and nickel sulfides, can enhance HER activity; however, excessive surface segregation or formation of secondary phases may block active sites of pentlandite itself and thus reduce reaction kinetics.

In the $Co_{9-x-y}Fe_xN_yS_4Se_4$ series, the most effective compositions are those close to equimolar $Co_3Fe_3N_3S_4Se_4$ pentlandite, particularly with a higher Ni content. Increased Ni appears to raise the density of active sites, thereby improving HER kinetics. This is probably due to the partial dissolution of Ni into the electrolyte, although this effect has not been confirmed. Interestingly, the typical HER mechanism associated with pentlandites does not fully account for the observed behavior in this series. This suggests the involvement of alternative adsorption mechanisms, likely driven by more complex atomic-level interactions. These may stem from selenium's impact on the material's electronic structure and the nature of intermetallic active sites – in Se-rich pentlandites, the primary active sites are those located at intermetallic positions (demonstrated by supporting DFT calculations). While selenium can enhance hydrogen adsorption, it may also increase binding strength excessively, thereby hindering hydrogen desorption and negatively impacting overall HER kinetics.

The Tafel slope values obtained for the materials in this study are comparable to those reported in the literature. For equimolar bimetallic Se-rich materials, the lowest Tafel slope was recorded for $Fe_{4.5}Ni_{4.5}S_8$ at 76 mV/dec [210]. However, for other selenium-containing samples (e.g., $Fe_{4.5}Ni_{4.5}S_7Se$ and $Fe_{4.5}Ni_{4.5}S_4Se_4$), the values were less favorable, reaching 120 mV/dec. In the case of the trimetallic materials presented in this work, the lowest Tafel slopes were obtained for bulk samples – 76 mV/dec for the I.S7 and 160 mV/dec for the S.S7 – further highlighting the superior performance of the ingot-type materials. For materials with variable metal compositions in the cationic sublattice, the most favorable Tafel slope reported in the literature was 92 mV/dec for $Fe_3CoNi_5S_8$ [68]. In comparison, the present study achieved even lower values of 75 mV/dec and 87 mV/dec for I.431.S8 and I.611.S8, respectively, and 113 mV/dec for S.116.S8 – again underscoring the improved performance of ingot samples. As with the previous case, a comparison for the final selenium-containing trimetallic series is not possible due to the lack of prior literature reports on such types of trimetallic pentlandites.

Summarizing the Tafel slope analysis across all series yields several key conclusions:

- Pellet samples, which have the lowest surface area development, consistently show the highest Tafel slope values, likely due to the reduced number of accessible active sites.
- In compositions with equimolar metal content, modifications of the anionic sublattice significantly influence reaction kinetics.
- Replacing sulfur with selenium generally increases the Tafel slopes, indicating slower kinetics, particularly in powders. In bulk materials, however, selenium substitution tends to decrease the Tafel slopes, suggesting an improvement in kinetics. The notable exception is $Co_3Fe_3Ni_3S_7Se$, which consistently exhibits improved values regardless of the material form.
- Comparing the HER mechanisms across the different series reveals a clear distinction in the dominant steps and controlling factors of the reaction. In the $Co_{9-x-y}Fe_xN_yS_8$ series, HER appears to follow a more traditional mechanism, driven by hydrogen adsorption at sulfur vacancies. Compositions with an excess of Co, Fe, or Ni perform the best here. In contrast, the $Co_{9-x-y}Fe_xN_yS_4Se_4$ series exhibits more complex kinetic behavior, likely dominated by selenium-induced modifications to the electronic structure, which in turn makes them more susceptible to surface preparation, with reduced cation influence. These changes enhance hydrogen adsorption but may also limit desorption, creating a bottleneck in HER kinetics. As a result, compositions close to the equimolar pentlandite stoichiometry are most effective in balancing adsorption and desorption steps.

5.4. Summary

After reviewing all available materials, it is difficult to identify a single most favorable pentlandite composition, however, several trends can help guide the selection of an optimal form and composition for HER applications. Most importantly, only the equimolar cation series exhibits single-phase compositions and long-term stability up to the $Co_3Fe_3Ni_3S_3Se_5$ composition. This is a crucial property for the potential widespread use of these materials in the future.

Within $Co_3Fe_3Ni_3S_{8-x}Se_x$ series, additional insights can be drawn based on material density. For high-density samples, such as ingots and pellets, the $Co_3Fe_3Ni_3S_4Se_4$ composition demonstrates the best HER performance and reaction kinetics. This correlates with a low ECSA, a low R_{CT}, a position of the d-band center close to the Fermi level, and the progressive elongation of TM–Ch bonds, which may lead to the formation of new active site types. In contrast, for low-density materials such as powders, the $Co_3Fe_3Ni_3S_7Se$ composition shows the highest performance. This is attributed to the strong tendency of S-rich pentlandites to form sulfur vacancies, along with a stable arrangement of selenium additives and the coexisting sulfur vacancies. These structural features significantly influence the electronic properties and catalytic behavior of the material. Across the entire series, the $Co_3Fe_3Ni_3S_7Se$ composition consistently stands out as the most promising and interesting candidate for HER applications, regardless of the form of the material.

Interestingly, all non-equimolar compositions in the $Co_{9-x-y}Fe_xNi_yS_8$ series outperform the $Co_3Fe_3Ni_3S_8$ composition. A comparison of overpotentials, Tafel slopes, and RF values indicates that composition deviating from the natural $Fe_{4.5}Ni_{4.5}S_8$, particularly those enriched in Fe or Co, tend to show better HER performance. As shown in Figure 93, a general trend emerges: Ni-rich pentlandites exhibit the poorest HER performance, while Fe-rich compositions perform the best. Notably, compositions close to $Fe_{4.5}Ni_{4.5}S_8$, regardless of Co content, show the weakest activity and stability. However, a key drawback of the Fe-rich compositions is that they do not form single-phase structures, either before or after high-temperature treatment. Considering phase purity, stability, and the performance-related factors mentioned above, the $Co_{4.5}Fe_{1.5}Ni_3S_8$ composition appears to be the best-performing material within this series.

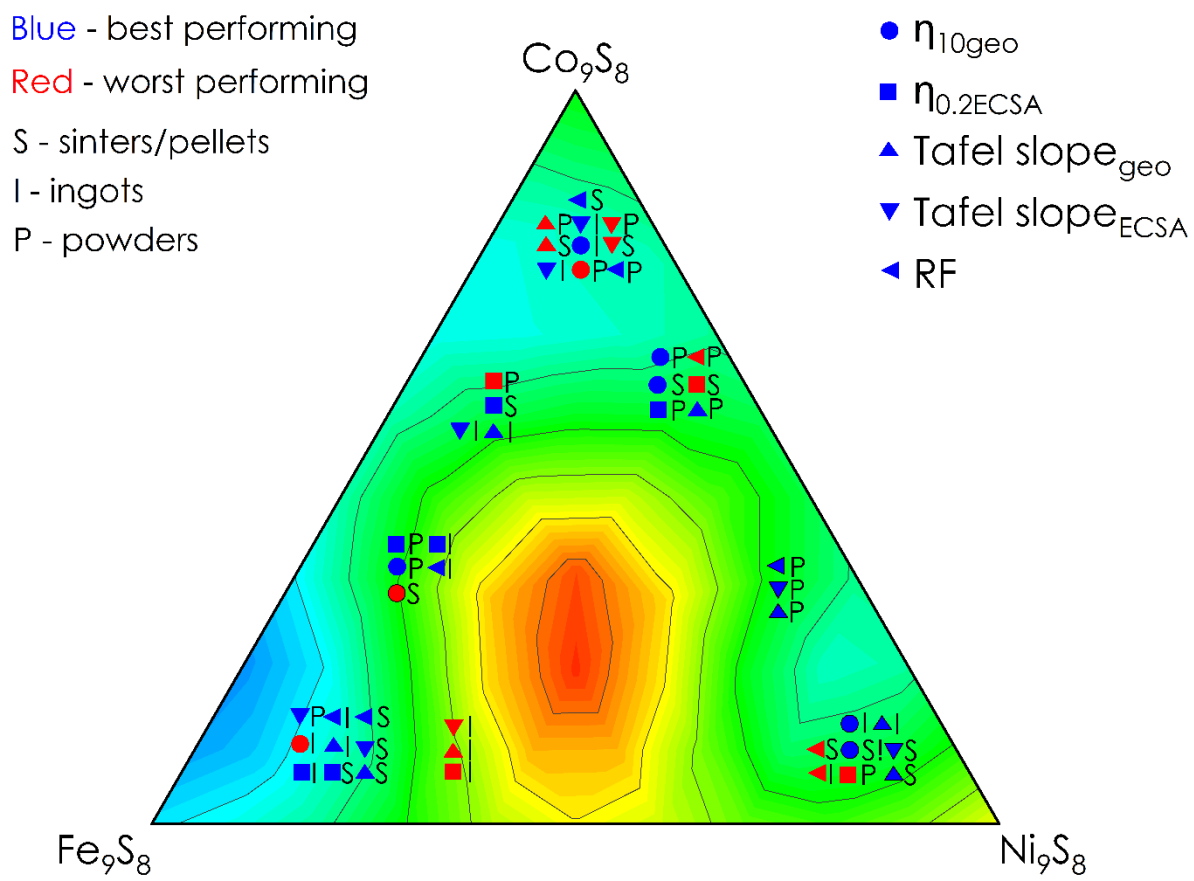

Figure 93. Ternary diagram summarizing the most significant electrochemical parameters of the $Co_{9-x-y}Fe_xNi_yS_8$ series.

In the $Co_{9-x-y}Fe_xNi_yS_4Se_4$ series, the situation is similar – but not identical – to that observed in the S-rich materials. Once again, Ni-rich compositions demonstrate the poorest HER performance and, notably, do not form single-phase structures even before high-temperature treatment. In contrast to the $Co_{9-x-y}Fe_xNi_yS_8$ series, the Fe-rich compositions in the $Co_{9-x-y}Fe_xNi_yS_4Se_4$ series do not remain single-phase before heat treatment and exhibit the best HER activity, particularly when the cobalt content is above the minimum level. As shown in Figure 94, the best-performing compositions in this series are found between the $Co_{1.5}Fe_6Ni_{1.5}S_4Se_4$ and $Co_3Fe_{4.5}Ni_{1.5}S_4Se_4$ compositions. However, it is important to note that none of the compositions in this series remain a single-phase structure prior to high-temperature treatment. Despite this limitation, these findings highlight the potential of these materials in the form of ingots. Ingot samples are stable and demonstrate better Tafel slopes and η_{ECSA} values compared to pellets, and do not require any further processing when constructing the working electrode, making them particularly interesting for HER applications, especially in flow-cell systems where a certain degree of porosity combined with surface development is advantageous.

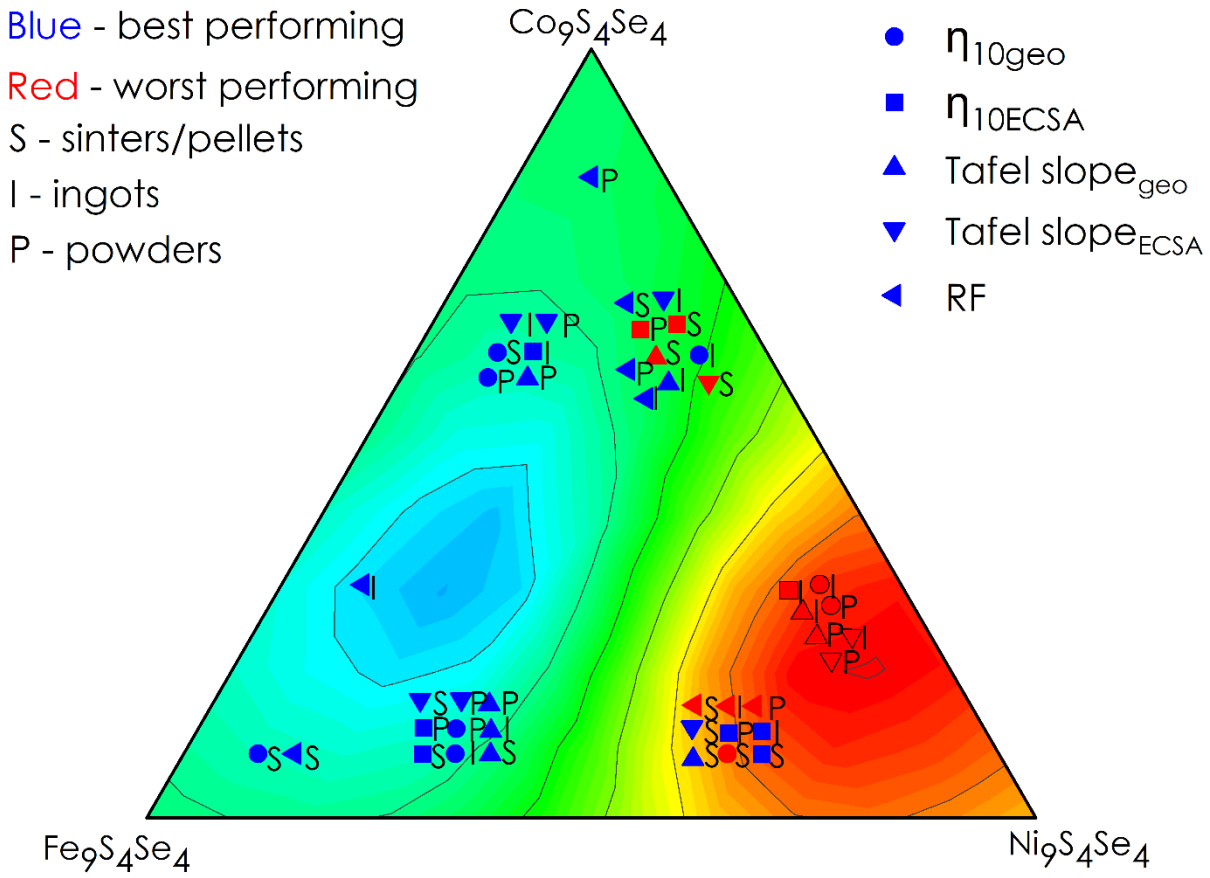

Figure 94. Ternary diagram summarizing the most significant electrochemical parameters of the $Co_{9-x-y}Fe_xNi_yS_4Se_4$ series.

6. Conclusions

The research presented in this thesis offers a novel and innovative perspective on the application of pentlandite materials in the hydrogen evolution reaction (HER). Among the forms studied – bulk ingots, pellets, and powders – this work provides the first comprehensive evaluation of these five-component materials for water splitting applications. Among the tested morphologies, ingots emerged as particularly promising due to their simplicity and robustness, making them attractive for practical applications such as conventional electrolyzers and flow-cell systems.

This study also explores the solubility of selenium in the anionic sublattice and various transition metals (TMs) in the cationic sublattice in both S- and Se-rich pentlandites. It was demonstrated that selenium can substitute sulfur to form $Co_3Fe_3Ni_3S_3Se_5$, which remains single-phase both after synthesis and high-temperature treatments like sintering. Changes in the cationic sublattice typically reduce pentlandite stability. Most compositions initially remain single-phase, excluding Fe-rich compositions in the $Co_{9-x-y}Fe_xNi_yS_8$ series and Ni-rich compositions in the $Co_{9-x-y}Fe_xNi_yS_4Se_4$ series.

Sulfur depletion is a key factor influencing HER performance. While sulfur vacancies significantly impact HER kinetics, they are not the sole determining factor. Variations in composition and material form reveal additional critical factors. In the $Co_3Fe_3Ni_3S_{8-x}Se_x$ series, the $Co_3Fe_3Ni_3S_7Se$ composition – especially in powder form – shows optimal performance and stability due to the synergy between sulfur vacancies and the extended TM-chalcogen (TM-Ch) bonds introduced by selenium. However, in denser materials (ingots and pellets), $Co_3Fe_3Ni_3S_4Se_4$ performs best, combining low electrochemically active surface area (ECSA), excellent charge-transfer capabilities (R_{CT}), favorable d-band center position, and elongated TM–Ch bonds that create new active sites for HER.

In non-equimolar compositions, single-phase materials generally outperform multi-phase ones. In the $Co_{9-x-y}Fe_xNi_yS_8$ series, multi-phase materials rich in Fe and Ni sulfides demonstrate lower overpotentials but suffer from slower HER kinetics. Conversely, all compositions in the $Co_{9-x-y}Fe_xNi_yS_4Se_4$ series decompose during HER, rendering them unsuitable for performance evaluation. An intriguing exception is the $Co_{1.5}Fe_{1.5}Ni_6S_8$ pellet (P.116.S8), which starts as a multi-phase material but transitions to a stable single-phase composition ($Co_{1.42}Fe_{1.37}Ni_{5.21}S_8$) during HER, leading to excellent performance.

Another notable observation is the formation of high-performance subphases on material surfaces following IHP treatment above 400 °C. Although the materials are multi-phase, these surface phases could offer promising directions for future research if proven stable over time and under operational conditions.

6.1. Main conclusions

This thesis presents a comprehensive study of trimetallic pentlandite-type materials for the hydrogen evolution reaction (HER), focusing on the relationships between composition, structure, morphology, and electrochemical performance. Three material series with varying cationic and anionic sublattice compositions were investigated in multiple physical forms (powders, pellets, and ingots), using a consistent and comparative methodology. The results provide clear structure–activity relationships and mechanistic insights that can guide further design of earth-abundant HER catalysts.

The key findings are as follows:

- **Single-phase stability and sulfur substitution**: Only the equimolar cationic series ($Co_3Fe_3Ni_3S_{8-x}Se_x$) retained phase purity after both synthesis and high-temperature treatments. Selenium can substitute sulfur up to $Co_3Fe_3Ni_3S_3Se_5$ without destabilizing the pentlandite structure. In contrast, deviations from equimolarity (especially Fe- or Ni-rich compositions) led to secondary phases, particularly in the $Co_{9-x-y}Fe_xNi_yS_8$ and $Co_{9-x-y}Fe_xNi_yS_4Se_4$ series.

- **HER activity and material form**: The physical form of the material strongly affects HER performance depending on the normalization approach. Powders generally exhibit the best Tafel slopes and highest ECSA but suffer from mechanical instability and limited long-term applicability. Pellets demonstrate enhanced performance when normalized to geometric area, likely due to improved interparticle connectivity and reduced resistance, yet they remain mechanically fragile. Ingots offer a practical compromise by combining relatively high electrochemical activity with superior mechanical robustness and long-term stability. Among all tested morphologies, $Co_3Fe_3Ni_3S_7Se$ emerged as the most promising candidate, showing high HER activity, stable performance, and no requirement for mechanical processing or post-synthesis modifications. This exceptional behavior can be attributed not only to the material's bulk and surface properties, but also to its partially substituted anionic framework (S_7Se), which should be regarded as a critical factor. This exceptional behavior can be attributed to the unique synergy of selenium substitution and sulfur vacancy retention, making $Co_3Fe_3Ni_3S_7Se$ the most promising non-noble HER catalyst in this family.

- **S-rich vs. Se-rich performance**: Se-rich compositions generally outperform sulfur-rich analogs when tested in the form of solid electrodes (e.g., ingots and pellets), likely due to enhanced bulk conductivity, structural ordering, and the aforementioned masking of cationic disorder. However, this benefit becomes less pronounced – or even detrimental – for low-density samples (e.g., powders), where the HER performance is dominated by surface effects and sulfur vacancy-related activation mechanisms.

- **Stabilizing role of cobalt across all systems**: Cobalt plays a key structural role across all investigated compositions, including both sulfur- and selenium-rich systems. It remains fully soluble across the entire tested compositional range, which is crucial for maintaining the pentlandite framework despite variations in Fe and Ni content. Its presence stabilizes the structure and enables

the formation of single-phase materials even at higher degrees of compositional complexity, improving the long-term durability of the materials under HER conditions. However, cobalt does not systematically enhance catalytic activity, indicating that its role is predominantly structural rather than electronic or catalytic.

- **Surface effects and activation mechanisms**: Sulfur-rich compositions undergo HER-driven surface reconstruction involving *sulfur depletion*, vacancy formation, and d-band shifts. These effects increase the real surface area and create new active sites, especially in low-density materials. The presence of selenium further enhances HER performance by elongating TM–Ch bonds facilitating sulfur detachment, and modifying the electronic structure, though excessive Se leads to stronger hydrogen binding and limited desorption.
- **Composition–performance relationships**: In non-equimolar series, Fe-rich materials consistently outperform Ni-rich ones, despite the former often being multiphase. Ni-rich materials exhibit low intrinsic activity and instability. Interestingly, some initially multiphase samples (e.g., P.116.S8) self-reconstruct during HER into single-phase, high-performance compositions, suggesting that in situ activation may be a viable strategy for performance enhancement.
- **Role of cations in S-rich and Se-rich systems**: The catalytic performance of pentlandites is strongly governed by the cationic sublattice configuration. In sulfur-rich systems, Co and Fe enhance HER activity by promoting sulfur vacancy formation and balancing hydrogen adsorption/desorption energetics. In Se-rich systems, the role of cations becomes more nuanced: Fe-rich compositions remain catalytically superior, but the influence of Co is shifted toward structural stabilization. In both cases, Ni-rich compositions tend to show the lowest HER activity and stability, likely due to unfavorable electronic structure and surface speciation effects.
- **Mechanistic implications**: Traditional HER models based on sulfur vacancy adsorption sites do not fully explain the performance trends observed in Se-substituted pentlandites. The data suggest an alternative adsorption mechanism influenced by cationic sublattice configuration and chalcogen electronic effects. This highlights the need to revisit the mechanistic assumptions for TM_9Ch_8-type materials in HER catalysis.

In summary, this work identifies a clear link between structural order, chalcogen substitution, cationic distribution, and HER performance. It demonstrates that carefully balanced compositions offer a viable path toward low-cost, durable, and efficient HER catalysts without relying on noble metals. The findings also establish key design principles for further development of pentlandite-derived materials in electrochemical water splitting.

6.2. Fulfilment of research objectives

Objective 1: To synthesize single-phase four- and/or five-component materials with the pentlandite (TM_9Ch_8) structure.

Multiple single-phase pentlandite-type compositions were successfully synthesized, including quaternary materials in the Co–Fe–Ni–S system and quinary materials in the Co–Fe–Ni–S–Se system.

Objective 2: To determine the solubility limits of individual components (Co, Fe, Ni, S, Se) within the pentlandite structure across different compositions.

Selenium substitution was shown to be limited to 5 out of 8 anionic sites in stable single-phase systems, while cobalt demonstrated full solubility across all tested compositions, contributing significantly to phase stability. In S-rich series, nickel is soluble up to 4.5 atoms per 9, similar to iron, although iron only reaches this level when cobalt is present in small amounts (1.5 atoms). For the $Co_{9-x-y}Fe_xNi_yS_4Se_4$ series, iron exhibits complete solubility only when all three metals (Co, Fe, Ni) are simultaneously present, whereas nickel dissolves up to a maximum of 4.5 atoms, and only when the amount of iron is minimal.

Objective 3: To fabricate materials in three distinct forms: pellets, ingots, and powders deposited on conductive substrates.

All target compositions were prepared in pellet, ingot, and powder form, enabling consistent, comparative analysis of HER activity and stability as a function of material form.

Objective 4: To identify sustainable and stable material compositions and forms.

The most durable and phase-stable systems were found within the $Co_3Fe_3Ni_3S_{8-x}Se_x$ series, with ingots showing superior mechanical robustness and long-term HER performance.

Objective 5: To evaluate the electrochemical performance of all synthesized materials and determine the optimal composition and form for HER applications.

Among all tested variants, $Co_3Fe_3Ni_3S_7Se$ emerged as the optimal composition, especially in ingot form. While Fe-rich and Ni-rich compositions exhibit favorable features (e.g., higher current densities or R_{CT}), they lack compositional predictability and long-term stability.

6.3. Recommendations and design guidelines for future HER catalyst development

Based on the results presented in this work, several general design principles can be formulated:

- Equimolar $Co_3Fe_3Ni_3S_7Se$should be considered a benchmark composition for future studies, given its balance of stability, activity, and durability.
- Slight compositional shifts toward Fe- and Co-enrichment, such as $Co_4Fe_4NiS_7Se$ or $Co_{3.5}Fe_{3.5}Ni_2S_7Se$, may further improve HER performance by reinforcing the structural framework while enhancing the activity associated with Fe–S and Co–S bonding environments.
- The role of cobalt should be emphasized in future materials, as it enhances phase stability without significantly interfering with catalytic properties.
- The concept of ingots directly used after synthesis is particularly promising, combining processing simplicity with mechanical robustness.

Given their compact form, conductivity, and mechanical stability, ingot-based pentlandites (and sintered pellet) are suitable not only for classical electrolyzers but also for flow-cell architectures, where long-term stability and integration with scalable hardware are critical.

7. References

1. Bower, V. E. *et al.* Recalculation of the Faraday Constant Due To a New Value for the Atomic Weight of Silver. *J. Res. Natl. Bur. Stand. (United States)* **87**, 21–22 (1982).

2. Cimbala, A. J. M. The Ideal Gas. *Stat. Phys.* 79–112 (2006) doi:10.1007/0-387-25099-9_4.

3. Wang, S., Lu, A. & Zhong, C. J. Hydrogen production from water electrolysis: role of catalysts. *Nano Converg.* **8**, (2021).

4. Carmo, M., Fritz, D. L., Mergel, J. & Stolten, D. A comprehensive review on PEM water electrolysis. *Int. J. Hydrogen Energy* **38**, 4901–4934 (2013).

5. Molenda, J. Fundamentalne znaczenie badañ naukowych dla rozwoju gospodarki wodorowej. *Polityka Energ.* **11**, 61–68 (2008).

6. Nørskov, J. K., Bligaard, T., Rossmeisl, J. & Christensen, C. H. Towards the computational design of solid catalysts. *Nat. Chem.* **1**, 37–46 (2009).

7. Abe, J. O., Popoola, A. P. I., Ajenifuja, E. & Popoola, O. M. Hydrogen energy, economy and storage: Review and recommendation. *Int. J. Hydrogen Energy* **44**, 15072–15086 (2019).

8. May, M. M., Lewerenz, H. J., Lackner, D., Dimroth, F. & Hannappel, T. Efficient direct solar-to-hydrogen conversion by in situ interface transformation of a tandem structure. *Nat. Commun.* **6**, 4–10 (2015).

9. Ajanovic, A., Sayer, M. & Haas, R. The economics and the environmental benignity of different colors of hydrogen. *Int. J. Hydrogen Energy* **47**, 24136–24154 (2022).

10. Le, P. A. *et al.* The current status of hydrogen energy: an overview. *RSC Adv.* **13**, 28262–28287 (2023).

11. Panić, I., Cuculić, A. & Ćelić, J. Color-Coded Hydrogen: Production and Storage in Maritime Sector. *J. Mar. Sci. Eng.* **10**, (2022).

12. Blank, T. K. & Molly, P. Hydrogen's Decarbonization Impact for Industry. 13 (2020).

13. Newborough, M. & Cooley, G. Developments in the global hydrogen market: The spectrum of hydrogen colours. *Fuel Cells Bull.* **2020**, 16–22 (2020).

14. Noussan, M., Raimondi, P. P., Scita, R. & Hafner, M. The role of green and blue hydrogen in the energy transition—a technological and geopolitical perspective. *Sustain.* **13**, 1–26 (2021).

15. Incer-Valverde, J., Korayem, A., Tsatsaronis, G. & Morosuk, T. "Colors" of hydrogen: Definitions and carbon intensity. *Energy Convers. Manag.* **291**, 117294 (2023).

16. Cheng, W. & Lee, S. How Green Are the National Hydrogen Strategies? *Sustain.* **14**, 1–33 (2022).

17. Ramantani, T., Evangeliou, V., Kormentzas, G. & Kondarides, D. I. Hydrogen production by steam reforming of propane and LPG over supported metal catalysts. *Appl. Catal. B Environ.* **306**, 121129 (2022).

18. Schädel, B. T., Duisberg, M. & Deutschmann, O. Steam reforming of methane, ethane, propane, butane, and natural gas over a rhodium-based catalyst. *Catal. Today* **142**, 42–51 (2009).

19. Amin, A. M., Croiset, E. & Epling, W. Review of methane catalytic cracking for hydrogen production. *Int. J. Hydrogen Energy* **36**, 2904–2935 (2011).

20. Alharthi, A. I. *et al.* Mg and Cu incorporated CoFe2O4 catalyst: characterization and methane cracking performance for hydrogen and nano-carbon production. *Ceram. Int.* **47**, 27201–27209 (2021).

21. Banu, A. & Bicer, Y. Review on COx-free hydrogen from methane cracking: Catalysts, solar energy integration and applications. *Energy Convers. Manag. X* **12**, 100117 (2021).

22. Saxena, S. K., Drozd, V. & Durygin, A. A fossil-fuel based recipe for clean energy. *Int. J. Hydrogen Energy* **33**, 3625–3631 (2008).

23. Farmer, T. C., McFarland, E. W. & Doherty, M. F. Membrane bubble column reactor model for the production of hydrogen by methane pyrolysis. *Int. J. Hydrogen Energy* **44**, 14721–14731 (2019).

24. Sánchez-Bastardo, N., Schlögl, R. & Ruland, H. Methane Pyrolysis for Zero-Emission Hydrogen Production: A Potential Bridge Technology from Fossil Fuels to a Renewable and Sustainable Hydrogen Economy. *Ind. Eng. Chem. Res.* **60**, 11855–11881 (2021).

25. Boretti, A. White is the color of hydrogen from concentrated solar energy and thermochemical water splitting cycles. *Int. J. Hydrogen Energy* **46**, 20790–20791 (2021).

26. Dincer, I. & Acar, C. Review and evaluation of hydrogen production methods for better sustainability. *Int. J. Hydrogen Energy* **40**, 11094–11111 (2014).

27. Pinsky, R., Sabharwall, P., Hartvigsen, J. & O'Brien, J. Comparative review of hydrogen production technologies for nuclear hybrid energy systems. *Prog. Nucl. Energy* **123**, 103317 (2020).

28. Poullikkas, A. Implementation of distributed generation technologies in isolated power systems. *Renew. Sustain. Energy Rev.* **11**, 30–56 (2007).

29. Clark, W. W. & Rifkin, J. A green hydrogen economy. *Energy Policy* **34**, 2630–2639 (2006).

30. Bošnjakovi, M., Katanić, M., Santa, R. & Marić, D. Wind Turbine Technology Trends. *Appl. Sci.* 124–134 (2018) doi:10.4324/9781315232140-14.

31. Zhong, X., Sun, X. & Wu, Y. A Capacity Optimization Method for a Hybrid Energy Storage Microgrid System Based on an Augmented ε- Constraint Method. *Energies* **15**, (2022).

32. Dincer, I. Green methods for hydrogen production. *Int. J. Hydrogen Energy* **37**, 1954–1971 (2012).

33. Zeng, M. & Li, Y. Recent advances in heterogeneous electrocatalysts for the hydrogen evolution reaction. *J. Mater. Chem. A* **3**, 14942–14962 (2015).

34. Zoulias, E., Varkaraki, E., Lymberopoulos, N., Christodoulou, C. N. & Karagiorgis, G. N. A REVIEW ON WATER ELECTROLYSIS Related papers Hydrogen and Fuel Cell Syst ems.

35. Kreuter, W. & Hofmann, H. Electrolysis: the important energy transformer in a world of sustainable energy. *Int. J. Hydrogen Energy* **23**, 661–666 (1998).

36. Şahin, M. E. An Overview of Different Water Electrolyzer Types for Hydrogen Production. *Energies* **17**, (2024).

37. Pape, S. V. *et al.* Performance data extraction from dynamic long-term operation of proton exchange membrane and alkaline water electrolysis cells. *Int. J. Hydrogen Energy* **127**, 51–63 (2025).

38. Raveendran, A., Chandran, M. & Dhanusuraman, R. A comprehensive review on the electrochemical parameters and recent material development of electrochemical water splitting electrocatalysts. *RSC Adv.* **13**, 3843–3876 (2023).

39. Wang, Y. *et al.* Recent advances in transition metal carbide electrocatalysts for oxygen evolution reaction. *Catalysts* **10**, 1–30 (2020).

40. Yan, Y., Xia, B. Y., Zhao, B. & Wang, X. A review on noble-metal-free bifunctional heterogeneous catalysts for overall electrochemical water splitting. *J. Mater. Chem. A* **4**, 17587–17603 (2016).

41. Schuring, J., Schulz, H. D., Fischer, W. R., Bottcher, J. & Duijnisveld, W. H. M. *Redox: Fundamentals, Processes and Applications*. vol. (1999).

42. Garnett, P. J. & Treagust, D. F. Conceptual difficulties experienced by senior high school students of electrochemistry: Electrochemical (galvanic) and electrolytic cells. *J. Res. Sci. Teach.* **29**, 1079–1099 (1992).

43. Kulikovsky, A. A. *et al.* DMFC: Galvanic or electrolytic cell? *Electrochem. commun.* **8**, 754–760 (2006).

44. Petrucii, R., Herring, G., Madura, J. & Bissonnette, C. *General Chemistry - Principles and Modern Applications 12e*. (2023).

45. Hong, W. T. *et al.* Charge-transfer-energy-dependent oxygen evolution reaction mechanisms for perovskite oxides. *Energy Environ. Sci.* **10**, 2190–2200 (2017).

46. Sun, J. *et al.* One simple strategy towards nitrogen and oxygen codoped carbon nanotube for efficient electrocatalytic oxygen reduction and evolution. *Catalysts* **9**, 1–13 (2019).

47. Wang, J. *et al.* The application of CeO2-based materials in electrocatalysis. *J. Mater. Chem. A* **7**,

17675–17702 (2019).

48. Lenne, Q., Leroux, Y. R. & Lagrost, C. Surface Modification for Promoting Durable, Efficient, and Selective Electrocatalysts. *ChemElectroChem* **7**, 2345–2363 (2020).

49. Ishikawa, Y., Mateo, J. J., Tryk, D. A. & Cabrera, C. R. Direct molecular dynamics and density-functional theoretical study of the electrochemical hydrogen oxidation reaction and underpotential deposition of H on Pt(1 1 1). *J. Electroanal. Chem.* **607**, 37–46 (2007).

50. Tan, Y., Wei, Y., Liang, K., Wang, L. & Zhang, S. Facile in-situ deposition of Pt nanoparticles on nano-pore stainless steel composite electrodes for high active hydrogen evolution reaction. *Int. J. Hydrogen Energy* **46**, 26340–26346 (2021).

51. Koper, M. T. M. Thermodynamic theory of multi-electron transfer reactions: Implications for electrocatalysis. *J. Electroanal. Chem.* **660**, 254–260 (2011).

52. Liang, L. *et al.* Ultra-small platinum nanoparticles segregated by nickle sites for efficient ORR and HER processes. *J. Energy Chem.* **65**, 48–54 (2021).

53. Sarno, M. & Ponticorvo, E. Continuous flow HER and MOR evaluation of a new Pt/Pd/Co nano electrocatalyst. *Appl. Surf. Sci.* **459**, 105–113 (2018).

54. Saito, Y. & Kikuchi, T. *Voltammetry: Theory, Types and Applications*. *Protests and Riots Past: Present and future perspectives* (2018). doi:10.1016/j.arthro.2012.05.044.

55. Giuffredi, G., Asset, T., Liu, Y., Atanassov, P. & Di Fonzo, F. Transition Metal Chalcogenides as a Versatile and Tunable Platform for Catalytic CO2and N2Electroreduction. *ACS Mater. Au* **1**, 6–36 (2021).

56. Podlovchenko, B. I. & Maksimov, Y. M. Peculiarities of surface layer formation at galvanic displacement of lead by platinum. Activity of Pt0(Pb) composites in FAOR. *J. Electroanal. Chem.* **801**, 319–327 (2017).

57. Shi, Z. *et al.* Recent advances in the electrochemical hydrogenation of unsaturated hydrocarbons. *Curr. Opin. Electrochem.* **28**, 100713 (2021).

58. Li, J., He, L., Liu, X., Cheng, X. & Li, G. Electrochemical Hydrogenation with Gaseous Ammonia. *Angew. Chemie* **131**, 1773–1777 (2019).

59. Russo, C. *et al.* eHydrogenation: Hydrogen-free Electrochemical Hydrogenation. *Angew. Chemie - Int. Ed.* **62**, (2023).

60. Woldu, A. R., Huang, Z., Zhao, P., Hu, L. & Astruc, D. Electrochemical CO2 reduction (CO2RR) to multi-carbon products over copper-based catalysts. *Coord. Chem. Rev.* **454**, 214340 (2022).

61. He, J., Li, Y., Huang, A., Liu, Q. & Li, C. *Electrolyzer and Catalysts Design from Carbon Dioxide*

to Carbon Monoxide Electrochemical Reduction. *Electrochemical Energy Reviews* vol. 4 (Springer Singapore, 2021).

62. Chialvo, M. R. G. de & Chialvo, A. C. The Resolution of the Volmer-Heyrovsky-Tafel Mechanism with a Normal Distribution of the Standart Gibbs Energy of Adsorption. *J. Braz. Chem. Soc.* **5**, 137–143 (1994).

63. M. R. Gennero, de C. & Cesar, A. C. Hydrogen evolution reaction : Analysis of the Volmer-Heyrovsky-Tafel mechanism with a generalized adsorption model. *J. Electroanal. Chem.* **372**, 209–223 (2014).

64. Ďurovič, M., Hnát, J. & Bouzek, K. Electrocatalysts for the hydrogen evolution reaction in alkaline and neutral media. A comparative review. *J. Power Sources* **493**, (2021).

65. Shinagawa, T., Garcia-Esparza, A. T. & Takanabe, K. Insight on Tafel slopes from a microkinetic analysis of aqueous electrocatalysis for energy conversion. *Sci. Rep.* **5**, 1–21 (2015).

66. Dubouis, N. & Grimaud, A. The hydrogen evolution reaction: From material to interfacial descriptors. *Chem. Sci.* **10**, 9165–9181 (2019).

67. Conway, B. E. & Tilak, B. V. Interfacial processes involving electrocatalytic evolution and oxidation of H2, and the role of chemisorbed H. *Electrochim. Acta* **47**, 3571–3594 (2002).

68. Smialkowski, M. *et al.* Trimetallic Pentlandites (Fe,Co,Ni)9S8for the Electrocatalytical HER in Acidic Media. *ACS Mater. Au* **2**, 474–481 (2022).

69. Chakrabartty, S., Karmakar, S. & Raj, C. R. An Electrocatalytically Active Nanoflake-Like Co9S8-CoSe2Heterostructure for Overall Water Splitting. *ACS Appl. Nano Mater.* **3**, 11326–11334 (2020).

70. Gao, W. *et al.* Molybdenum Carbide Anchored on Graphene Nanoribbons as Highly Efficient All-pH Hydrogen Evolution Reaction Electrocatalyst. *ACS Sustain. Chem. Eng.* **4**, 6313–6321 (2016).

71. Seunghwa, L., Aliki, M., You-Chiuan, C., Chen, H. M. & Xile, H. Tracking high-valent surface iron species in the oxygen evolution reaction on cobalt iron (oxy)hydroxides. *AIChE Annu. Meet. Conf. Proc.* **2019-Novem**, 1–8 (2019).

72. Lu, L., Yu, S. & Tian, H. Theoretical insight into surface structures of pentlandite toward hydrogen evolution. *J. Colloid Interface Sci.* **607**, 645–654 (2022).

73. Smialkowski, M., Tetzlaff, D., Hensgen, L., Siegmund, D. & Apfel, U. P. Fe/Co and Ni/Co-pentlandite type electrocatalysts for the hydrogen evolution reaction. *Chinese J. Catal.* **42**, 1360–1369 (2021).

74. Zegkinoglou, I. *et al.* Operando Phonon Studies of the Protonation Mechanism in Highly Active Hydrogen Evolution Reaction Pentlandite Catalysts. *J. Am. Chem. Soc.* **139**, 14360–14363 (2017).

75. Suen, N. T. *et al.* Electrocatalysis for the oxygen evolution reaction: Recent development and future perspectives. *Chem. Soc. Rev.* **46**, 337–365 (2017).

76. Song, J. *et al.* A review on fundamentals for designing oxygen evolution electrocatalysts. *Chem. Soc. Rev.* **49**, 2196–2214 (2020).

77. Amin, H. M. A. & Apfel, U. P. Metal-Rich Chalcogenides as Sustainable Electrocatalysts for Oxygen Evolution and Reduction: State of the Art and Future Perspectives. *Eur. J. Inorg. Chem.* **2020**, 2679–2690 (2020).

78. Zhou, J. *et al.* Revealing the effect of anion-tuning in bimetallic chalcogenides on electrocatalytic overall water splitting. *Nano Res.* **14**, 4548–4555 (2021).

79. Linnemann, J., Kanokkanchana, K. & Tschulik, K. Design Strategies for Electrocatalysts from an Electrochemist's Perspective. *ACS Catal.* **11**, 5318–5346 (2021).

80. Kim, D., Yun, N., Du, H., Moreno Jimenez, D. A. & Rossi, R. Flow field design for zero-gap microbial electrolysis cells using synthetic and real wastewater. *J. Power Sources* **630**, 236077 (2025).

81. Phillips, R. & Dunnill, C. W. Zero gap alkaline electrolysis cell design for renewable energy storage as hydrogen gas. *RSC Adv.* **6**, 100643–100651 (2016).

82. Rad, R. *et al.* A hybrid bioelectrochemical system coupling a zero-gap cell and a methanogenic reactor for carbon dioxide reduction using a wastewater-derived catholyte. *Cell Reports Phys. Sci.* **4**, 101526 (2023).

83. Dryfe, R. A. W. *Handbook of Electrochemistry*. *Handbook of Electrochemistry* (2007).

84. Achterberg, E. Laboratory techniques in electroanalytical chemistry. **75**, 7996 (1995).

85. Christian, G., Dasgupta, P. & Schug, K. *Analytical chemistry, seventh edition*. *Journal of Chemical Education* vol. 63 (1986).

86. Bockris, J. O. & Reddy, A. K. N. *Modern electrochemistry 2B*. *Sustainability (Switzerland)* vol. 11 (2019).

87. de Rooij, D. M. R. Electrochemical Methods: Fundamentals and Applications. *Anti-Corrosion Methods Mater.* **50**, 91–92 (2003).

88. Elgrishi, N. *et al.* A Practical Beginner's Guide to Cyclic Voltammetry. *J. Chem. Educ.* **95**, 197–206 (2018).

89. Garlyyev, B. *et al.* Revealing the nature of active sites in electrocatalysis. *Chem. Sci.* **10**, 8060–8075 (2019).

90. Zambelli, T., Wintterlin, J., Trost, J. & Ertl, G. Identification of the 'active sites' of a surface-

catalyzed reaction. *Science (80-.).* **273**, 1688–1690 (1996).

91. Nørskov, J. K. *et al.* The nature of the active site in heterogeneous metal catalysis. *Chem. Soc. Rev.* **37**, 2163–2171 (2008).

92. Easton, E. B. & Pickup, P. G. An electrochemical impedance spectroscopy study of fuel cell electrodes. *Electrochim. Acta* **50**, 2469–2474 (2005).

93. Connor, P., Schuch, J., Kaiser, B. & Jaegermann, W. The Determination of Electrochemical Active Surface Area and Specific Capacity Revisited for the System MnOx as an Oxygen Evolution Catalyst. *Zeitschrift fur Phys. Chemie* **234**, 979–994 (2020).

94. Morales, D. M. & Risch, M. Seven steps to reliable cyclic voltammetry measurements for the determination of double layer capacitance. *JPhys Energy* **3**, (2021).

95. Shao, M., Odell, J. H., Choi, S. Il & Xia, Y. Electrochemical surface area measurements of platinum- and palladium-based nanoparticles. *Electrochem. commun.* **31**, 46–48 (2013).

96. McCrory, C. C. L. *et al.* Benchmarking Hydrogen Evolving Reaction and Oxygen Evolving Reaction Electrocatalysts for Solar Water Splitting Devices. *J. Am. Chem. Soc.* **137**, 4347–4357 (2015).

97. McCrory, C. C. L., Jung, S., Peters, J. C. & Jaramillo, T. F. Benchmarking heterogeneous electrocatalysts for the oxygen evolution reaction. *J. Am. Chem. Soc.* **135**, 16977–16987 (2013).

98. Wood, M. A. The Effect of Synthesis Methods on Activity Measurements for Transition Metal Phosphides (TMPs) for the Hydrogen Evolution Reaction (HER) APPROVED BY SUPERVISING COMMITTEE : 1–27 (2023).

99. Sarac, A. S. *et al.* Nanofiber network of electropolymerized 3,4-(2-benzylpropylenedioxy) thiophene on single carbon fiber microelectrode. *J. Nanosci. Nanotechnol.* **10**, 8043–8053 (2010).

100. Advanced Materials - 2024 - Park - Conversion of Layered WS2 Crystals into Mixed-Domain Electrochemical Catalysts by.pdf.

101. Sobhanie, E., Hosseini, M., Faridbod, F. & Ganjali, M. R. Sensitive detection of H2O2 released from cancer cells with electrochemiluminescence sensor based on electrochemically prepared polypyrrole@Ce: Dy tungstate/polyluminol. *J. Electroanal. Chem.* **932**, 117244 (2023).

102. Wu, L. & Hofmann, J. P. Comparing the Intrinsic HER Activity of Transition Metal Dichalcogenides: Pitfalls and Suggestions. *ACS Energy Lett.* **6**, 2619–2625 (2021).

103. Marković, N. M., Grgur, B. N. & Ross, P. N. Temperature-dependent hydrogen electrochemistry on platinum low-index single-crystal surfaces in acid solutions. *J. Phys. Chem. B* **101**, 5405–5413 (1997).

104. Hansen, J. N. *et al.* Is There Anything Better than Pt for HER? *ACS Energy Lett.* **6**, 1175–1180 (2021).

105. Geiger, S. *et al.* The stability number as a metric for electrocatalyst stability benchmarking. *Nat. Catal.* **1**, 508–515 (2018).

106. Frydendal, R. *et al.* Benchmarking the Stability of Oxygen Evolution Reaction Catalysts: The Importance of Monitoring Mass Losses. *ChemElectroChem* **1**, 2075–2081 (2014).

107. Yoon, Y., Yan, B. & Surendranath, Y. Suppressing Ion Transfer Enables Versatile Measurements of Electrochemical Surface Area for Intrinsic Activity Comparisons. *J. Am. Chem. Soc.* **140**, 2397–2400 (2018).

108. Zhu, S., Zhang, X., Sun, J. & Wang, D. A study of misaligned compliant journal bearings lubricated by non-Newtonian fluid considering surface roughness. *Tribol. Int.* **179**, 108138 (2023).

109. Abellán-Nebot, J. V., Vila Pastor, C. & Siller, H. R. A Review of the Factors Influencing Surface Roughness in Machining and Their Impact on Sustainability. *Sustain.* **16**, (2024).

110. Lasia, A. *Electrochemical Impedance Spectroscopy and its Applications*. *Comprehensive Microsystems* vol. 1 (2014).

111. Orazem, M. & Tribollet, B. *Electrochemical impedance spectroscopy*. *Electrochimica Acta* (2008). doi:10.1016/0013-4686(88)80076-8.

112. Inc., G. I. Basics of Electrochemical Impedance Spectroscopy Impedance Values. *Appl. Note Rev. 2.0* 1–28 (2014).

113. Macdonald, J. R. & Barsoukov, E. *Impedance Spectroscopy Theory, Experiment, and Applications*.

114. Lazanas, A. C. & Prodromidis, M. I. Electrochemical Impedance Spectroscopy─A Tutorial. *ACS Meas. Sci. Au* **3**, 162–193 (2023).

115. Fabbri, E., Habereder, A., Waltar, K., Kötz, R. & Schmidt, T. J. Developments and perspectives of oxide-based catalysts for the oxygen evolution reaction. *Catal. Sci. Technol.* **4**, 3800–3821 (2014).

116. Anantharaj, S. *et al.* Membrane free water electrolysis under 1.23 V with Ni 3 Se 4 /Ni anode in alkali and Pt cathode in acid. *Appl. Surf. Sci.* **478**, 784–792 (2019).

117. De Silva Muñoz, L., Bergel, A., Féron, D. & Basséguy, R. Hydrogen production by electrolysis of a phosphate solution on a stainless steel cathode. *Int. J. Hydrogen Energy* **35**, 8561–8568 (2010).

118. Jerkiewicz, G. Standard and Reversible Hydrogen Electrodes: Theory, Design, Operation, and Applications. *ACS Catal.* **10**, 8409–8417 (2020).

119. Jerkiewicz, G. Hydrogen Sorption at/in electrodes. *Science (80-.).* **57**, 137–186 (1998).

120. Coridan, R. H. *et al.* Methods for comparing the performance of energy-conversion systems for use in solar fuels and solar electricity generation. *Energy Environ. Sci.* **8**, 2886–2901 (2015).

121. Anantharaj, S. *et al.* Recent Trends and Perspectives in Electrochemical Water Splitting with an Emphasis on Sulfide, Selenide, and Phosphide Catalysts of Fe, Co, and Ni: A Review. *ACS Catal.* **6**, 8069–8097 (2016).

122. Anantharaj, S., Karthik, P. E., Subramanian, B. & Kundu, S. Pt Nanoparticle Anchored Molecular Self-Assemblies of DNA: An Extremely Stable and Efficient HER Electrocatalyst with Ultralow Pt Content. *ACS Catal.* **6**, 4660–4672 (2016).

123. Anantharaj, S., Jayachandran, M. & Kundu, S. Unprotected and interconnected Ru0 nano-chain networks: Advantages of unprotected surfaces in catalysis and electrocatalysis. *Chem. Sci.* **7**, 3188–3205 (2016).

124. Zou, X. & Zhang, Y. Noble metal-free hydrogen evolution catalysts for water splitting. *Chem. Soc. Rev.* **44**, 5148–5180 (2015).

125. Liu, K. *et al.* Recent advances in metal-nitrogen-carbon catalysts for electrochemical water splitting. *Mater. Chem. Front.* **1**, 2155–2173 (2017).

126. Zhang, L., Shi, X. L., Yang, Y. L. & Chen, Z. G. Flexible thermoelectric materials and devices: From materials to applications. *Mater. Today* **46**, 62–108 (2021).

127. Sheng, W., Gasteiger, H. A. & Shao-Horn, Y. Hydrogen Oxidation and Evolution Reaction Kinetics on Platinum: Acid vs Alkaline Electrolytes. *J. Electrochem. Soc.* **157**, B1529 (2010).

128. Strmcnik, D., Lopes, P. P., Genorio, B., Stamenkovic, V. R. & Markovic, N. M. Design principles for hydrogen evolution reaction catalyst materials. *Nano Energy* **29**, 29–36 (2016).

129. Elsodany, M. N., Abdel Rahim, M. A., Shalaby, N. H. & Sultan, M. A. Nickel and/or platinum modified crystalline silicon–carbon composites and their electrochemical behaviour towards the hydrogen evolution reaction. *J. Appl. Electrochem.* **54**, 531–546 (2024).

130. Konkena, B. *et al.* Pentlandite rocks as sustainable and stable efficient electrocatalysts for hydrogen generation. *Nat. Commun.* **7**, 1–8 (2016).

131. HORIUTI, J., MATSUDA, A., ENYO, M. & KITA, H. the Mechanism of the Hydrogen Evolution Reaction. *Electrochemistry* 750–779 (1965) doi:10.1016/b978-1-4831-9831-6.50063-1.

132. Conway, B. E. & O'M Bockris, J. Electrolytic hydrogen evolution kinetics and its relation to the electronic and adsorptive properties of the metal. *J. Chem. Phys.* **26**, 532–541 (1957).

133. Ma, J., Habrioux, A. & Alonso-Vante, N. Enhanced HER and ORR behavior on photodeposited Pt nanoparticles onto oxide-carbon composite. *J. Solid State Electrochem.* **17**, 1913–1921 (2013).

134. Petrik, L. F., Godongwana, Z. G. & Iwuoha, E. I. Platinum nanophase electro catalysts and composite electrodes for hydrogen production. *J. Power Sources* **185**, 838–845 (2008).

135. Razavi, M. *et al.* Molybdenum Disulfide Nanosheets Decorated with Platinum Nanoparticle as a High Active Electrocatalyst in Hydrogen Evolution Reaction. *Nanoscale Res. Lett.* **17**, (2022).

136. Abbas, S. A. *et al.* Synergistic effect of nano-Pt and Ni spine for HER in alkaline solution: Hydrogen spillover from nano-Pt to Ni spine. *Sci. Rep.* **8**, 1–9 (2018).

137. Nairan, A. *et al.* Proton selective adsorption on Pt-Ni nano-thorn array electrodes for superior hydrogen evolution activity. *Energy Environ. Sci.* **14**, 1594–1601 (2021).

138. Yin, Y. *et al.* Confining nano-sized platinum in nitrogen doped ordered mesoporous carbon: An effective approach toward efficient and robust hydrogen evolution electrocatalyst. *J. Colloid Interface Sci.* **530**, 595–602 (2018).

139. Chen, J. *et al.* Diversity of platinum-sites at platinum/fullerene interface accelerates alkaline hydrogen evolution. *Nat. Commun.* **14**, 1–12 (2023).

140. Mohan, A. & Sharma, S. In-situ carbon integration on atomically dispersed platinum metal oxide nanocomposites for hydrogen evolution reaction. *Electrochim. Acta* **508**, 145218 (2024).

141. Soliman, A. B. *et al.* Pt Immobilization within a Tailored Porous-Organic Polymer-Graphene Composite: Opportunities in the Hydrogen Evolving Reaction. *ACS Catal.* **7**, 7847–7854 (2017).

142. Kumar Manna, B., Samanta, R., Kumar Trivedi, R., Chakraborty, B. & Barman, S. Hydrogen spillover inspired bifunctional Platinum/Rhodium Oxide-Nitrogen-Doped carbon composite for enhanced hydrogen evolution and oxidation reactions in base. *J. Colloid Interface Sci.* **670**, 258–271 (2024).

143. Yu, F. Y. *et al.* Pt-O bond as an active site superior to Pt0 in hydrogen evolution reaction. *Nat. Commun.* **11**, (2020).

144. Ljiljana, M. & Grgur, B. N. Study of gold-platinum and platinum-gold surface modification. *J. Serbian Chem. Soc.* **70**, 231–242 (2005).

145. Liu, S. Q. *et al.* Amorphous Ni(OH)2 encounter with crystalline CuS in hollow spheres: A mesoporous nano-shelled heterostructure for hydrogen evolution electrocatalysis. *Nano Energy* **44**, 7–14 (2018).

146. Lafforgue, C., Maillard, F., Martin, V., Dubau, L. & Chatenet, M. Degradation of Carbon-Supported Platinum-Group-Metal Electrocatalysts in Alkaline Media Studied by in Situ Fourier Transform Infrared Spectroscopy and Identical-Location Transmission Electron Microscopy. *ACS Catal.* **9**, 5613–5622 (2019).

147. Park, H. *et al.* Canonic-Like HER Activity of Cr1–xMoxB2 Solid Solution: Overpowering Pt/C at High Current Density. *Adv. Mater.* **32**, 2–7 (2020).

148. Conway, B. E. & Bai, L. Determination of adsorption of OPD H species in the cathodic hydrogen

evolution reaction at Pt in relation to electrocatalysis. *J. Electroanal. Chem.* **198**, 149–175 (1986).

149. Chi, J. Q. *et al.* N-Doped Sandwich-Structured Mo2C@C@Pt Interface with Ultralow Pt Loading for pH-Universal Hydrogen Evolution Reaction. *ACS Appl. Mater. Interfaces* **11**, 4047–4056 (2019).

150. Chen, J. *et al.* Enhanced activity for hydrogen evolution reaction over CoFe catalysts by alloying with small amount of Pt. *ACS Appl. Mater. Interfaces* **9**, 3596–3601 (2017).

151. Yan, X. *et al.* Pt nanoparticles decorated high-defective graphene nanospheres as highly efficient catalysts for the hydrogen evolution reaction. *Carbon N. Y.* **137**, 405–410 (2018).

152. Saha, S., Martin, B., Leonard, B. & Li, D. Probing synergetic effects between platinum nanoparticles deposited: Via atomic layer deposition and a molybdenum carbide nanotube support through surface characterization and device performance. *J. Mater. Chem. A* **4**, 9253–9265 (2016).

153. Cheng, X. *et al.* Highly active, stable oxidized platinum clusters as electrocatalysts for the hydrogen evolution reaction. *Energy Environ. Sci.* **10**, 2450–2458 (2017).

154. Chao, T. *et al.* Atomically Dispersed Copper–Platinum Dual Sites Alloyed with Palladium Nanorings Catalyze the Hydrogen Evolution Reaction. *Angew. Chemie - Int. Ed.* **56**, 16047–16051 (2017).

155. Tian, H. *et al.* Oxygen vacancy-assisted hydrogen evolution reaction of the Pt/WO3 electrocatalyst. *J. Mater. Chem. A* **7**, 6285–6293 (2019).

156. Yu, P. *et al.* Earth abundant materials beyond transition metal dichalcogenides: A focus on electrocatalyzing hydrogen evolution reaction. *Nano Energy* **58**, 244–276 (2019).

157. Gupta, S., Patel, M. K., Miotello, A. & Patel, N. Metal Boride-Based Catalysts for Electrochemical Water-Splitting A Review. (2020) doi:https://doi.org/10.1002/adfm.201906481.

158. Chen, W. F. *et al.* Highly active and durable nanostructured molybdenum carbide electrocatalysts for hydrogen production. *Energy Environ. Sci.* **6**, 943–951 (2013).

159. Tavakkoli, M. *et al.* Single-Shell Carbon-Encapsulated Iron Nanoparticles: Synthesis and High Electrocatalytic Activity for Hydrogen Evolution Reaction. *Angew. Chemie - Int. Ed.* **54**, 4535–4538 (2015).

160. Raj, I. A. & Vasu, K. I. Transition metal-based hydrogen electrodes in alkaline solution - electrocatalysis on nickel based binary alloy coatings. *J. Appl. Electrochem.* **20**, 32–38 (1990).

161. Cui, X., Ren, P., Deng, D., Deng, J. & Bao, X. Single layer graphene encapsulating non-precious metals as high-performance electrocatalysts for water oxidation. *Energy Environ. Sci.* **9**, 123–129 (2016).

162. Garcia-Esparza, A. T. *et al.* Tungsten carbide nanoparticles as efficient cocatalysts for photocatalytic overall water splitting. *ChemSusChem* **6**, 168–181 (2013).

163. Pan, L. *et al.* Molybdenum carbide stabilized on graphene with high electrocatalytic activity for hydrogen evolution reaction. *Chem. Commun.* **50**, 13135–13137 (2014).

164. Liao, L. *et al.* A nanoporous molybdenum carbide nanowire as an electrocatalyst for hydrogen evolution reaction. *Energy Environ. Sci.* **7**, 387–392 (2014).

165. Chen, W. F. *et al.* Hydrogen-evolution catalysts based on non-noble metal nickel-molybdenum nitride nanosheets. *Angew. Chemie - Int. Ed.* **51**, 6131–6135 (2012).

166. Xie, J. *et al.* Atomically-thin molybdenum nitride nanosheets with exposed active surface sites for efficient hydrogen evolution. *Chem. Sci.* **5**, 4615–4620 (2014).

167. Ma, L., Ting, L. R. L., Molinari, V., Giordano, C. & Yeo, B. S. Efficient hydrogen evolution reaction catalyzed by molybdenum carbide and molybdenum nitride nanocatalysts synthesized via the urea glass route. *J. Mater. Chem. A* **3**, 8361–8368 (2015).

168. Zhao, Y., Kamiya, K., Hashimoto, K. & Nakanishi, S. Hydrogen Evolution by Tungsten Carbonitride Nanoelectrocatalysts Synthesized by the Formation of a Tungsten Acid/Polymer Hybrid In Situ. *Angew. Chemie* **125**, 13883–13886 (2013).

169. Vrubel, H. & Hu, X. Molybdenum boride and carbide catalyze hydrogen evolution in both acidic and basic solutions. *Angew. Chemie - Int. Ed.* **51**, 12703–12706 (2012).

170. Alameda, L. T., Holder, C. F., Fenton, J. L. & Schaak, R. E. Partial Etching of Al from MoAlB Single Crystals to Expose Catalytically Active Basal Planes for the Hydrogen Evolution Reaction. *Chem. Mater.* **29**, 8953–8957 (2017).

171. Popczun, E. J. *et al.* Nanostructured nickel phosphide as an electrocatalyst for the hydrogen evolution reaction. *J. Am. Chem. Soc.* **135**, 9267–9270 (2013).

172. Xu, Y., Wu, R., Zhang, J., Shi, Y. & Zhang, B. Anion-exchange synthesis of nanoporous FeP nanosheets as electrocatalysts for hydrogen evolution reaction. *Chem. Commun.* **49**, 6656–6658 (2013).

173. Popczun, E. J., Read, C. G., Roske, C. W., Lewis, N. S. & Schaak, R. E. Highly active electrocatalysis of the hydrogen evolution reaction by cobalt phosphide nanoparticles. *Angew. Chemie - Int. Ed.* **53**, 5427–5430 (2014).

174. McEnaney, J. M. *et al.* Electrocatalytic hydrogen evolution using amorphous tungsten phosphide nanoparticles. *Chem. Commun.* **50**, 11026–11028 (2014).

175. Tan, X., Tahini, H. A. & Smith, S. C. P-Doped Graphene/Graphitic Carbon Nitride Hybrid Electrocatalysts: Unraveling Charge Transfer Mechanisms for Enhanced Hydrogen Evolution Reaction Performance. *ACS Catal.* **6**, 7071–7077 (2016).

176. Shalom, M. *et al.* Controlled Carbon Nitride Growth on Surfaces for Hydrogen Evolution Electrodes.

Angew. Chemie **126**, 3728–3732 (2014).

177. Zheng, Y. *et al.* Toward design of synergistically active carbon-based catalysts for electrocatalytic hydrogen evolution. *ACS Nano* **8**, 5290–5296 (2014).

178. Cui, W., Liu, Q., Cheng, N., Asiri, A. M. & Sun, X. Activated carbon nanotubes: a highly-active metal-free electrocatalyst for hydrogen evolution reaction. *Chem. Commun.* **50**, 9340–9342 (2014).

179. Xu, Y. F., Gao, M. R., Zheng, Y. R., Jiang, J. & Yu, S. H. Nickel/nickel(II) oxide nanoparticles anchored onto cobalt(IV) diselenide nanobelts for the electrochemical production of hydrogen. *Angew. Chemie - Int. Ed.* **52**, 8546–8550 (2013).

180. McKone, J. R., Sadtler, B. F., Werlang, C. A., Lewis, N. S. & Gray, H. B. Ni-Mo nanopowders for efficient electrochemical hydrogen evolution. *ACS Catal.* **3**, 166–169 (2013).

181. Kumar, R. *et al.* Nano-structured hybrid molybdenum carbides/nitrides generated: In situ for HER applications. *J. Mater. Chem. A* **5**, 7764–7768 (2017).

182. Zeradjanin, A. R. *et al.* What is the trigger for the hydrogen evolution reaction? - Towards electrocatalysis beyond the Sabatier principle. *Phys. Chem. Chem. Phys.* **22**, 8768–8780 (2020).

183. Petrii, O. A. & Tsirlina, G. A. Electrocatalytic activity prediction for hydrogen electrode reaction: intuition, art, science. *Electrochim. Acta* **39**, 1739–1747 (1994).

184. Bockris, J. O. & Potter, E. C. The Mechanism of the Cathodic Hydrogen Evolution Reaction. *J. Electrochem. Soc.* **99**, 169 (1952).

185. Roger, B. Y. The rate of electrolytic hydrogen and the heat of adsorption of hydrogen. *Trans. Faraday Soc.* 1053–1063 (1957).

186. Wodrich, M. D., Sawatlon, B., Busch, M. & Corminboeuf, C. The Genesis of Molecular Volcano Plots. *Acc. Chem. Res.* **54**, 1107–1117 (2021).

187. Exner, K. S. Does a Thermoneutral Electrocatalyst Correspond to the Apex of a Volcano Plot for a Simple Two-Electron Process? *Angew. Chemie* **132**, 10320–10324 (2020).

188. Laursen, A. *et al.* Electrochemical Hydrogen Evolution: Sabatier's Principle and the Volcano Plot. *Chem. Educ.* (2005).

189. Hinnemann, B. *et al.* Biomimetic Hydrogen Evolution: MoS2 Nanoparticles as Catalyst for Hydrogen Evolution. *J. Am. Chem. Soc.* **127**, 5308–5309 (2005).

190. Gao, W. *et al.* Determining the adsorption energies of small molecules with the intrinsic properties of adsorbates and substrates. *Nat. Commun.* **11**, (2020).

191. Anantharaj, S., Kundu, S. & Noda, S. Progress in nickel chalcogenide electrocatalyzed hydrogen evolution reaction. *J. Mater. Chem. A* **8**, 4174–4192 (2020).

192. Luty, S. PATENTOWEGO. (1966).

193. Mann, J. B., Meek, T. L., Knight, E. T., Capitani, J. F. & Allen, L. C. Configuration energies of the d-block elements. *J. Am. Chem. Soc.* **122**, 5132–5137 (2000).

194. Ortiz-Rodríguez, J. C. *et al.* Stabilizing Hydrogen Adsorption through Theory-Guided Chalcogen Substitution in Chevrel-Phase Mo6X8(X=S, Se, Te) Electrocatalysts. *ACS Appl. Mater. Interfaces* **12**, 35995–36003 (2020).

195. Geng, X. *et al.* Two-Dimensional Water-Coupled Metallic MoS2 with Nanochannels for Ultrafast Supercapacitors. *Nano Lett.* **17**, 1825–1832 (2017).

196. Miao, R. *et al.* Mesoporous iron sulfide for highly efficient electrocatalytic hydrogen evolution. *J. Am. Chem. Soc.* **139**, 13604–13607 (2017).

197. Li, Y. *et al.* High-index faceted CuFeS2 nanosheets with enhanced behavior for boosting hydrogen evolution reaction. *Nanoscale* **9**, 9230–9237 (2017).

198. Scofield, M. E. *et al.* Role of chemical composition in the enhanced catalytic activity of Pt-based alloyed ultrathin nanowires for the hydrogen oxidation reaction under alkaline conditions. *ACS Catal.* **6**, 3895–3908 (2016).

199. Yin, J. *et al.* Optimized Metal Chalcogenides for Boosting Water Splitting. *Adv. Sci.* **7**, (2020).

200. Li, W. *et al.* Hydrothermal Synthesis of Monolithic Co3Se4 Nanowire Electrodes for Oxygen Evolution and Overall Water Splitting with High Efficiency and Extraordinary Catalytic Stability. *Adv. Energy Mater.* **7**, 1–7 (2017).

201. Amin, B. G., Swesi, A. T., Masud, J. & Nath, M. CoNi2Se4 as an efficient bifunctional electrocatalyst for overall water splitting. *Chem. Commun.* **53**, 5412–5415 (2017).

202. Zhao, M. *et al.* One Step Hydrothermal Synthesis of Ni-MoS2-RGO Bifunctional Electrocatalysts for HER and OER. *Int. J. Electrochem. Sci.* **16**, 1–8 (2021).

203. Li, Y. *et al.* MoS2 nanoparticles grown on graphene: An advanced catalyst for the hydrogen evolution reaction. *J. Am. Chem. Soc.* **133**, 7296–7299 (2011).

204. Sundara Venkatesh, P., Kannan, N., Ganesh Babu, M., Paulraj, G. & Jeganathan, K. Transition metal doped MoS2 nanosheets for electrocatalytic hydrogen evolution reaction. *Int. J. Hydrogen Energy* **47**, 37256–37263 (2022).

205. Tian, T., Huang, L., Ai, L. & Jiang, J. Surface anion-rich NiS2 hollow microspheres derived from metal-organic frameworks as a robust electrocatalyst for the hydrogen evolution reaction. *J. Mater. Chem. A* **5**, 20985–20992 (2017).

206. Mikuła, A. *et al.* Synthesis, properties and catalytic performance of the novel, pseudo-spinel,

multicomponent transition-metal selenides. *J. Mater. Chem. A* 5337–5349 (2023) doi:10.1039/d2ta09401k.

207. Zang, N., Wu, Z., Wang, J. & Jin, W. Rational design of Cu-Co thiospinel ternary sheet arrays for highly efficient electrocatalytic water splitting. *J. Mater. Chem. A* **8**, 1799–1807 (2020).

208. Kang, Z. *et al.* Engineering an Earth-Abundant Element-Based Bifunctional Electrocatalyst for Highly Efficient and Durable Overall Water Splitting. *Adv. Funct. Mater.* **29**, 1–10 (2019).

209. Chuancang, Z., Hongyu, W., Feipeng, Z. & Yigao, M. Cobalt, Ferrum Co-Doped Ni3Se4 Nano-Flake Array: An Efficient Electrocatalyst for the Alkaline Hydrogen Evolution and Overall Water Splitting. *Crystal* (2022) doi:doi.org/10.3390/ cryst12050666.

210. Smialkowski, M. *et al.* Seleno-analogues of pentlandites (Fe4.5Ni4.5S8-: YSey, y = 1-6): Tuning bulk Fe/Ni sulphoselenides for hydrogen evolution. *Chem. Commun.* **55**, 8792–8795 (2019).

211. Vincent, K. A., Parkin, A. & Armstrong, F. A. Investigating and exploiting the electrocatalytic properties of hydrogenases. *Chem. Rev.* **107**, 4366–4413 (2007).

212. Knop, O. & Ibrahim, M. A. Chalkogenides of the transition elements: II. Existence of the π phase in the M9S8 section of the system Fe−Co−Ni−S. *Can. J. Chem* **39**, 297–317 (1961).

213. Kaneda, H., Takenouchi, S. & Shoji, T. Stability of pentlandite in the Fe-Ni-Co-S system. *Miner. Depos.* **21**, 169–180 (1986).

214. Feng, L. L. *et al.* Metallic Co9S8 nanosheets grown on carbon cloth as efficient binder-free electrocatalysts for the hydrogen evolution reaction in neutral media. *J. Mater. Chem. A* **4**, 6860–6867 (2016).

215. Lai, C. H., Lu, M. Y. & Chen, L. J. Metal sulfide nanostructures: Synthesis, properties and applications in energy conversion and storage. *J. Mater. Chem.* **22**, 19–30 (2012).

216. Tang, Y. *et al.* Phase-pure pentlandite Ni4.3Co4.7S8 binary sulfide as an efficient bifunctional electrocatalyst for oxygen evolution and hydrogen evolution. *Nanoscale* **10**, 10459–10466 (2018).

217. Piontek, S. *et al.* Influence of the Fe:Ni Ratio and Reaction Temperature on the Efficiency of (FexNi1-x)9S8 Electrocatalysts Applied in the Hydrogen Evolution Reaction. *ACS Catal.* **8**, 987–996 (2018).

218. Dou, S., Tao, L., Huo, J., Wang, S. & Dai, L. Etched and doped Co9S8/graphene hybrid for oxygen electrocatalysis. *Energy Environ. Sci.* **9**, 1320–1326 (2016).

219. Tetzlaff, D. *et al.* Sustainable and rapid preparation of nanosized Fe/Ni-pentlandite particles by mechanochemistry. *Chem. Sci.* **11**, 12835–12842 (2020).

220. Qin, W., Hu, B., Bao, D. & Gao, P. The preparation of Co9S8 and CoS2 nanoparticles by a high energy ball-milling method and their electrochemical hydrogen storage properties. *Int. J. Hydrogen*

Energy **39**, 9300–9306 (2014).

221. Zhang, Y., Gao, Q. & Wang, S. Hydrothermal impregnation synthesis of cobalt pentlandite as anode material of H2S SOFC. *Ionics (Kiel).* **22**, 743–749 (2016).

222. Bezverkhyy, I., Afanasiev, P. & Danot, M. Preparation of highly dispersed pentlandites (M,M′)9S 8 (M, M′ = Fe, Co, Ni) and their catalytic properties in hydrodesulfurization. *J. Phys. Chem. B* **108**, 7709–7715 (2004).

223. Bezverkhyy, I., Danot, M. & Afanasiev, P. New low-temperature preparations of some simple and mixed Co and Ni dispersed sulfides and their chemical behavior in reducing atmosphere. *Inorg. Chem.* **42**, 1764–1768 (2003).

224. Sugaki, A. & Kitakaze, A. High form of pentlandite and its thermal stability. *Am. Mineral.* **83**, 133–140 (1998).

225. Amin, H. M. A., Attia, M., Tetzlaff, D. & Apfel, U. P. Tailoring the Electrocatalytic Activity of Pentlandite FexNi9-XS8 Nanoparticles via Variation of the Fe : Ni Ratio for Enhanced Water Oxidation. *ChemElectroChem* **8**, 3863–3874 (2021).

226. Mikuła, A. *et al.* Search for mid- And high-entropy transition-metal chalcogenides - investigating the pentlandite structure. *Dalt. Trans.* **50**, 9560–9573 (2021).

227. Electroanal, I. & Milano, U. Surface area measurements. *Appl. Catal. A Gen.* **144**, N3–N4 (1996).

228. Liang, Y. *et al.* Co3O4 nanocrystals on graphene as a synergistic catalyst for oxygen reduction reaction. *Nat. Mater.* **10**, 780–786 (2011).

229. Kelly, P. J. & Arnell, R. D. Magnetron sputtering: A review of recent developments and applications. *Vacuum* **56**, 159–172 (2000).

230. Wang, C. H., Liu, J. L. & Huang, H. Y. Pseudocapacitive performance of Co(OH)2 enhanced by Ni(OH)2 formation on porous Ni/Cu electrode. *Electrochim. Acta* **182**, 47–60 (2015).

231. Puring, K. J. *et al.* Simple methods for the preparation of non-noble metal bulk-electrodes for electrocatalytic applications. *J. Vis. Exp.* **2017**, 4–9 (2017).

232. Cao, B. X., Wang, C., Yang, T. & Liu, C. T. Cocktail effects in understanding the stability and properties of face-centered-cubic high-entropy alloys at ambient and cryogenic temperatures. *Scr. Mater.* **187**, 250–255 (2020).

233. Yeh, J. W. *et al.* Nanostructured high-entropy alloys with multiple principal elements: Novel alloy design concepts and outcomes. *Adv. Eng. Mater.* **6**, 299–303 (2004).

234. Rost, C. M. Entropy-Stabilized Oxides: Explorations of a Novel Class of Multicomponent Materials by. *North Carolina State Univ.* 227 (2016).

235. Gibbs, W. Gibbs-Equilibrium of Heterogeneous Substances. *Equilib. Heterog. Subst.* 441–458 (1876).

236. Senthamaraikannan, T. G., Lim, D. H. & Han, Y. S. First-principles investigation of hydrogen evolution reaction on doped 2D transition metal sulfides in mackinawite structures. *Int. J. Hydrogen Energy* **97**, 1461–1471 (2024).

237. Heins, T. P., Harms, N., Schramm, L. S. & Schröder, U. Development of a new Electrochemical Impedance Spectroscopy Approach for Monitoring the Solid Electrolyte Interphase Formation. *Energy Technol.* **4**, 1509–1513 (2016).

238. Pierozynski, B. & Mikolajczyk, T. On the Temperature Dependence of Hydrogen Evolution Reaction at Nickel Foam and Pd-Modified Nickel Foam Catalysts. *Electrocatalysis* **6**, 51–59 (2015).

239. LI, A. & CHUAN, X. Effect of activation temperature on the properties of double layer capacitance of diatomite-templated carbon. *Acta Geol. Sin. - English Ed.* **91**, 161–162 (2017).

240. Fletcher, S. I. *et al.* The effects of temperature on the performance of electrochemical double layer capacitors. *J. Power Sources* **195**, 7484–7488 (2010).

241. Cho, K. H. *et al.* Uniform, Assembled 4 nm Mn3O4 Nanoparticles as Efficient Water Oxidation Electrocatalysts at Neutral pH. *Adv. Funct. Mater.* **30**, 1–9 (2020).

242. Sanden, S. A. *et al.* Ternary Pentlandites as Hydrogen Evolution Catalysts in Alkaline Media. *Adv. Energy Sustain. Res.* (2024) doi:10.1002/aesr.202400128.

243. Tetzlaff, D. *et al.* Mechanochemical one-pot synthesis of heterostructured pentlandite-carbon composites for the hydrogen evolution reaction. *Chem. Sci.* **14**, 11790–11797 (2023).

244. Nesselberger, M. *et al.* The particle size effect on the oxygen reduction reaction activity of Pt catalysts: Influence of electrolyte and relation to single crystal models. *J. Am. Chem. Soc.* **133**, 17428–17433 (2011).

245. Mikuła, A., Kubowicz, M., Smialkowski, M., Sanden, S. & Apfel, U.-P. Tuning the Electrocatalytic Properties of Trimetallic Pentlandites: Stability and Catalytic Activity as a Function of Material Form and Selenium Concentration. *ACS Mater. Lett.* **6**, 1581–1592 (2024).

246. Kubowicz, M., Kożusznik, M., Kurek, T., Mars, K. & Mikuła, A. Role of Foreign Phases, Synergistic Effects, and Morphology in the HER Performance of Trimetallic Pentlandites with Non-Equimolar Co:Fe:Ni Ratio. *Energies* **17**, (2024).

247. Mikuła, A. *et al.* Tailoring the electrocatalytic activity of multicomponent (Co,Fe,Ni)9S8−xSex pentlandite solid electrodes. *J. Mater. Chem. A* 7526–7538 (2023) doi:10.1039/d2ta08893b.

248. Scounakis, S., Sideris, C. & Economou, M. A new natural occurrence of Co9S8 in pyrrhotite ore from the ophiolite complex of Pindos, Greece. 169–174 (1982).

249. Zhang, P., Xu, B., Gao, C., Chen, G. & Gao, M. Facile Synthesis of Co9Se8 Quantum Dots as Charge Traps for Flexible Organic Resistive Switching Memory Device. *ACS Appl. Mater. Interfaces* **8**, 30336–30343 (2016).

250. Jiang, N. *et al.* Nickel sulfides for electrocatalytic hydrogen evolution under alkaline conditions: A case study of crystalline NiS, NiS2, and Ni3S2 nanoparticles. *Catal. Sci. Technol.* **6**, 1077–1084 (2016).

251. Zhang, R. *et al.* Ternary NiCo2Px Nanowires as pH-Universal Electrocatalysts for Highly Efficient Hydrogen Evolution Reaction. *Adv. Mater.* **29**, 2–7 (2017).

252. Lee, H. *et al.* Enhancing Bifunctional Electrocatalytic Activities via Metal d-Band Center Lift Induced by Oxygen Vacancy on the Subsurface of Perovskites. *ACS Catal.* **10**, 4664–4670 (2020).

253. Singstock, N. R. *et al.* Machine Learning Guided Synthesis of Multinary Chevrel Phase Chalcogenides. *J. Am. Chem. Soc.* **143**, 9113–9122 (2021).

254. Huber, K. P. & Herzberg, G. *Molecular Spectra and Molecular Structure: IV. Constants of diatomic molecules*. *Physics Today* vol. IV (1979).

255. Zhu, H., Chen, J., Deng, J., Yu, R. & Xing, X. Oxidation behavior and mechanism of pentlandite at 973 K (700 °C) in air. *Metall. Mater. Trans. B Process Metall. Mater. Process. Sci.* **43**, 494–502 (2012).

256. Heins, G., Ionel, D. M., Patterson, D., Stretz, S. & Thiele, M. Combined Experimental and Numerical Method for Loss Separation in Permanent-Magnet Brushless Machines. *IEEE Trans. Ind. Appl.* **52**, 1405–1412 (2016).

257. Haley, S. M., Tappin, A. D., Bond, P. R. & Fitzsimons, M. F. A comparison of SEM-EDS with ICP-AES for the quantitative elemental determination of estuarine particles. *Environ. Chem. Lett.* **4**, 235–238 (2006).

(I1) https://www.hydrogenfuelnews.com/what-is-yellow-hydrogen/8552843/

(I2) https://www.enapter.com/blog/hydrogen-clearing-up-the-colours/

(I3) https://www.williams.com/2021/04/23/what-are-the-colors-of-hydrogen/

(I4) https://www.jdpower.com/cars/shopping-guides/whats-the-difference-between-gray-blue-and-green-hydrogen

(I5) https://hydrogeneurope.eu/in-a-nutshell/

(I6) https://www.eea.europa.eu/en/analysis/indicators/greenhouse-gas-emission-intensity-of-1

8. Supplementary materials

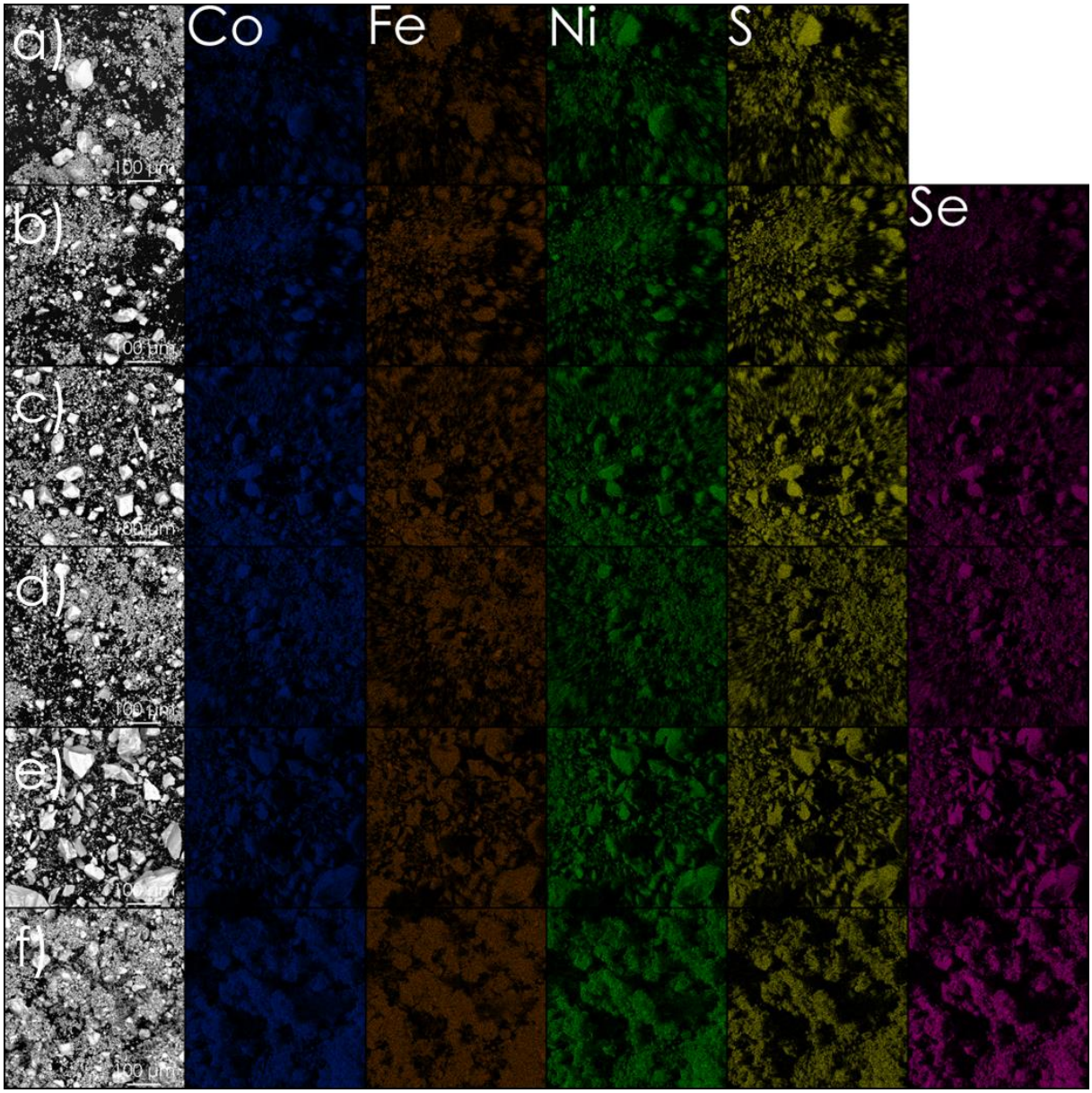

Figure S1. SEM images and EDS elemental maps of $TM_9S_{8-x}Se_x$ series: a) P.S8; b) P.S7; c) P.S6; d) P.S5; e) P.S4; f) P.S3.

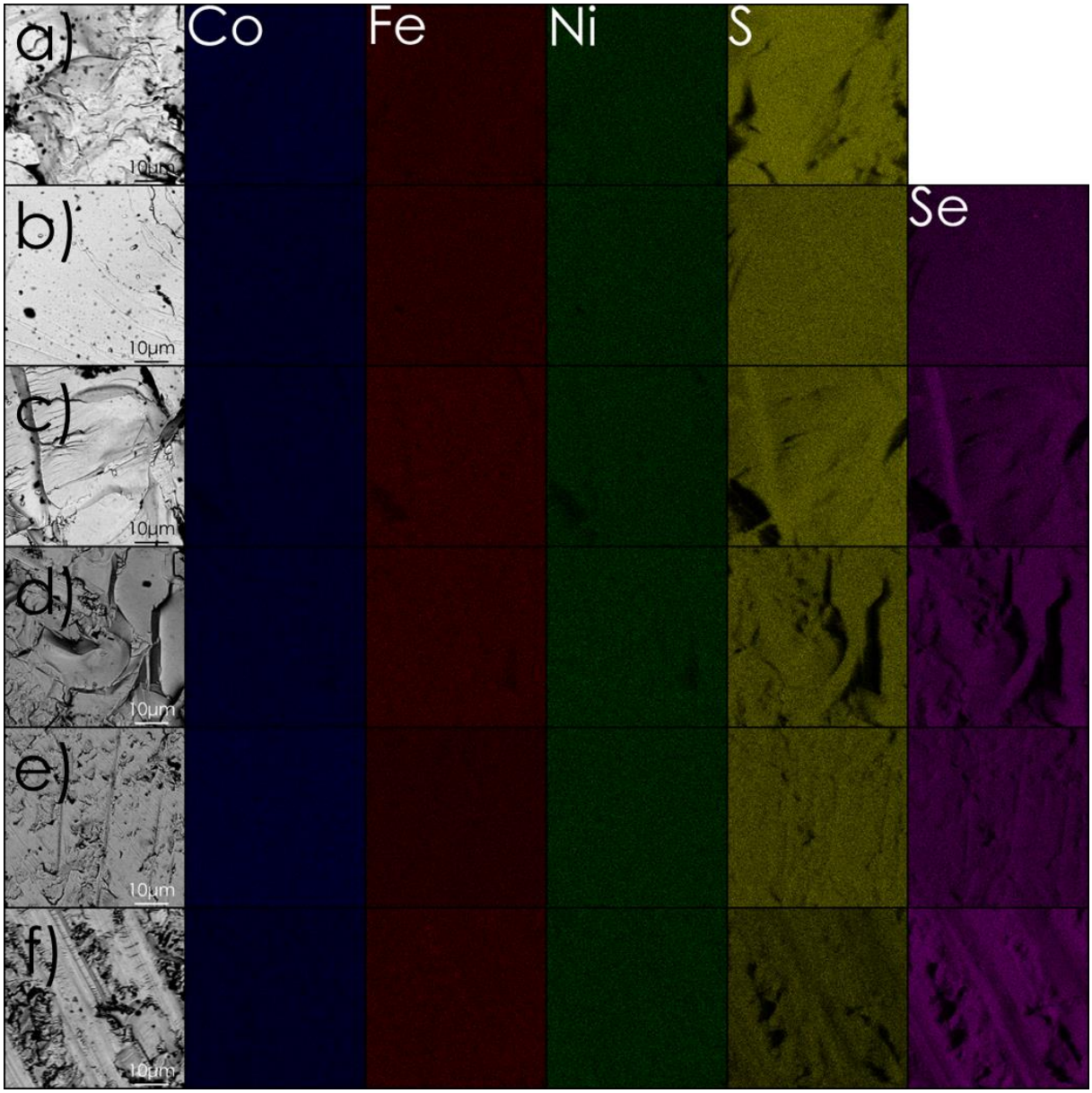

Figure S2. SEM images and EDS elemental maps of $TM_9S_{8-x}Se_x$ series: a) I.S8; b) I.S7; c) I.S6; d) I.S5; e) I.S4; f) I.S3.

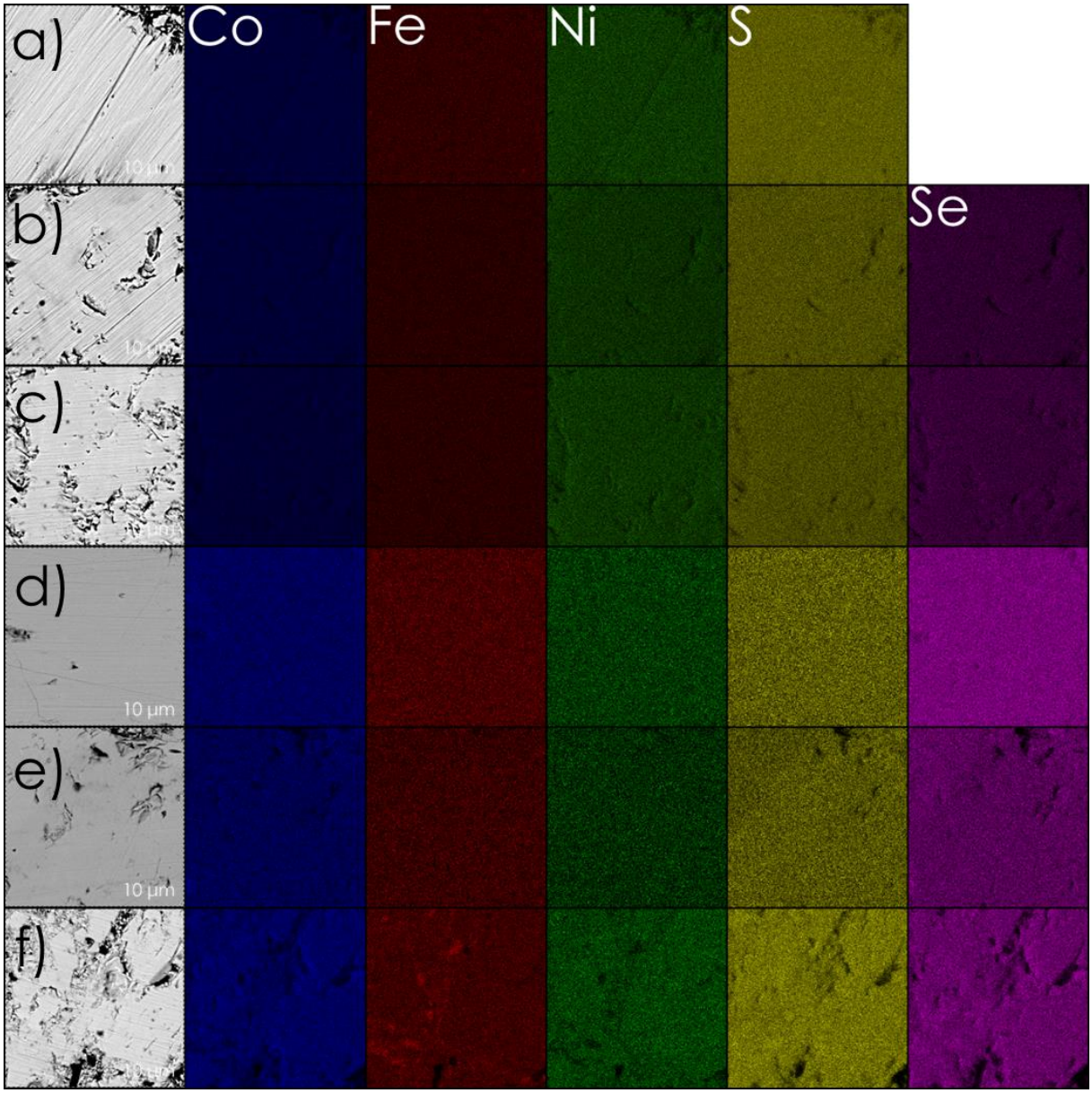

Figure S3. SEM images and EDS elemental maps of $TM_9S_{8-x}Se_x$ series: a) S.S8; b) S.S7; c) S.S6; d) S.S5; e) S.S4; f) S.S3.

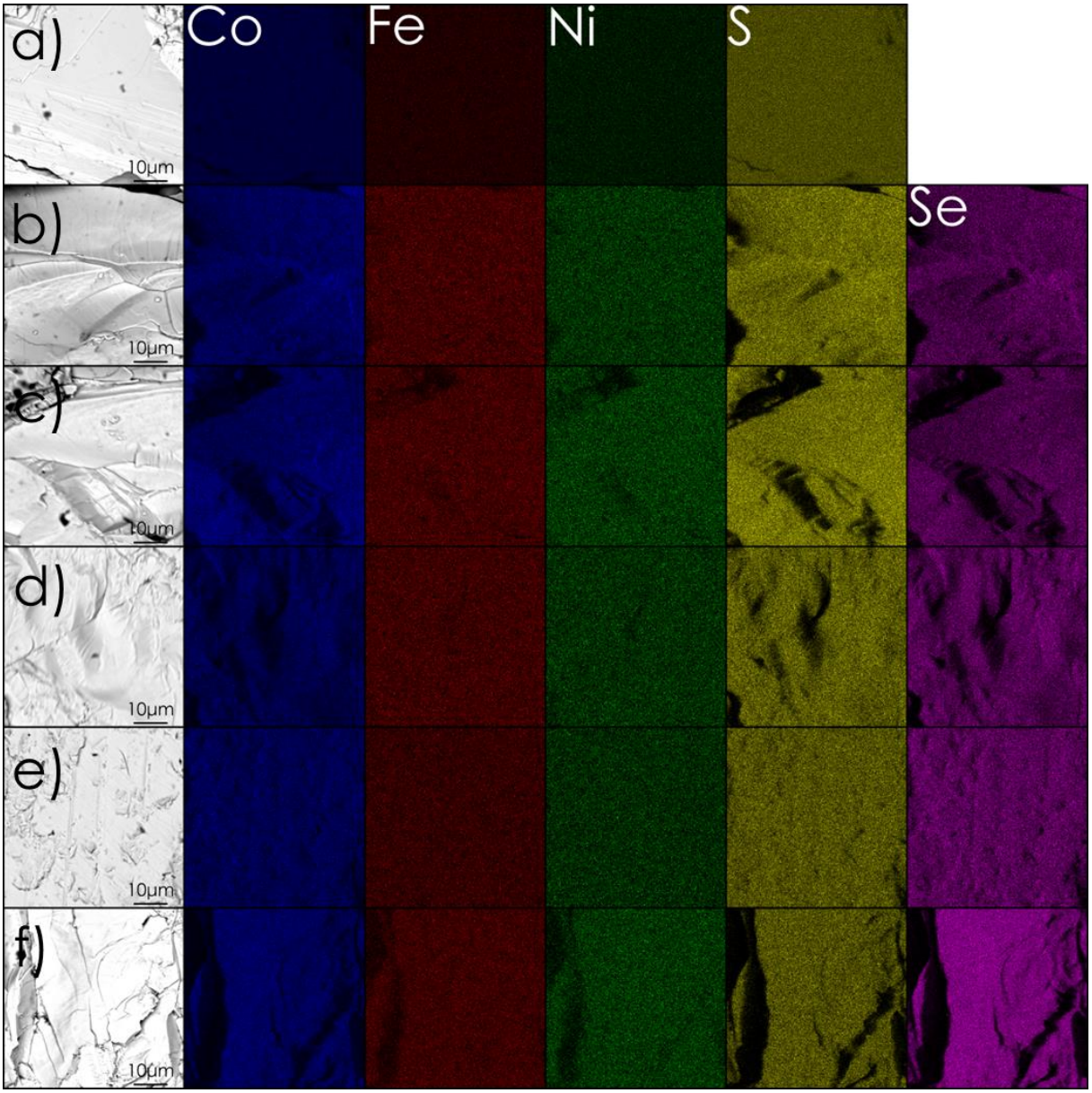

Figure S4. SEM images and EDS elemental maps of $TM_9S_{8-x}Se_x$ series: a) I.S8; b) I.S7; c) I.S6; d) I.S5; e) I.S4; f) I.S3 after chronoamperometry.

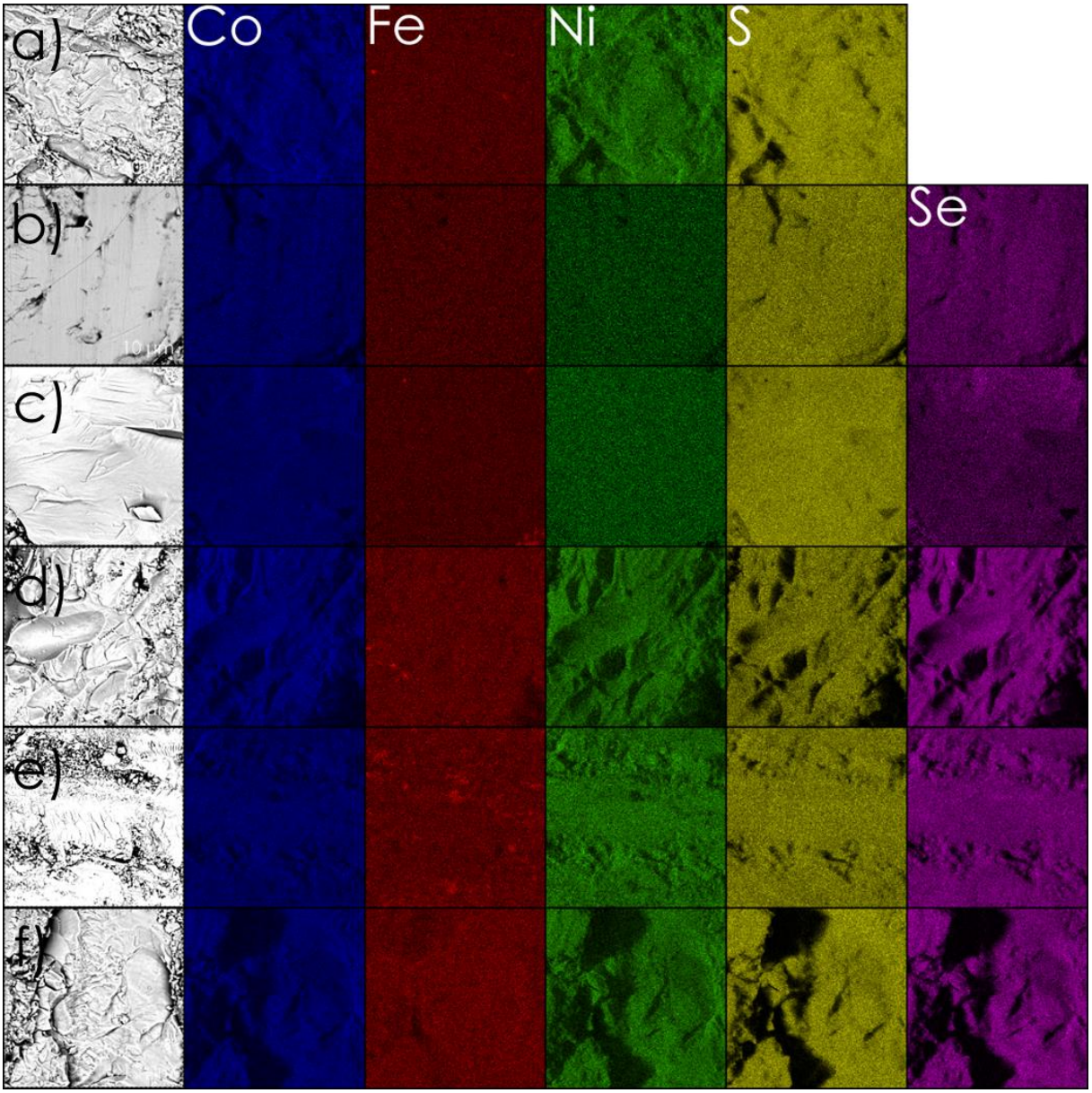

Figure S5. SEM images and EDS elemental maps of $TM_9S_{8-x}Se_x$ series: a) S.S8; b) S.S7; c) S.S6; d) S.S5; e) S.S4; f) S.S3 after chronoamperometry.

The surface area of the bulk electrodes studied on the *Anko* system was determined using the *ImageJ* software. Figure S6 show the calculation process in example of I.S8 sample. In Figure S6a, the original photograph is shown, while Figure S6b presents the marked and analyzed region. Based on the area of this marked region and the known reference length of 1 cm (provided by the grid paper placed above the electrode), the geometric surface area of the working electrode was calculated.

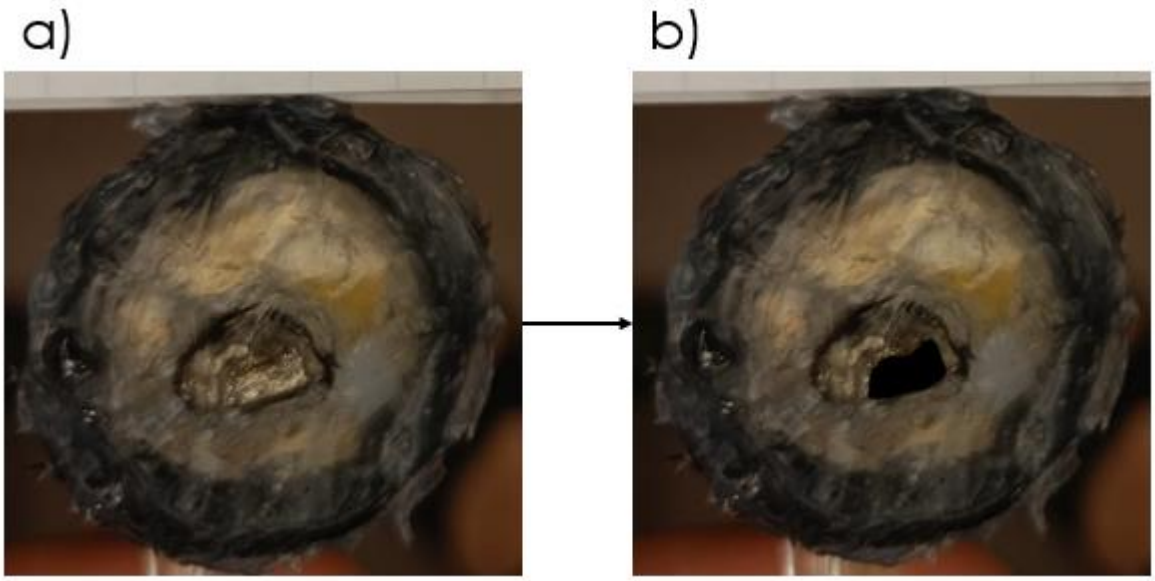

Figure S6. a) original photography of I.S8 sample; b) photography with marked surface area.

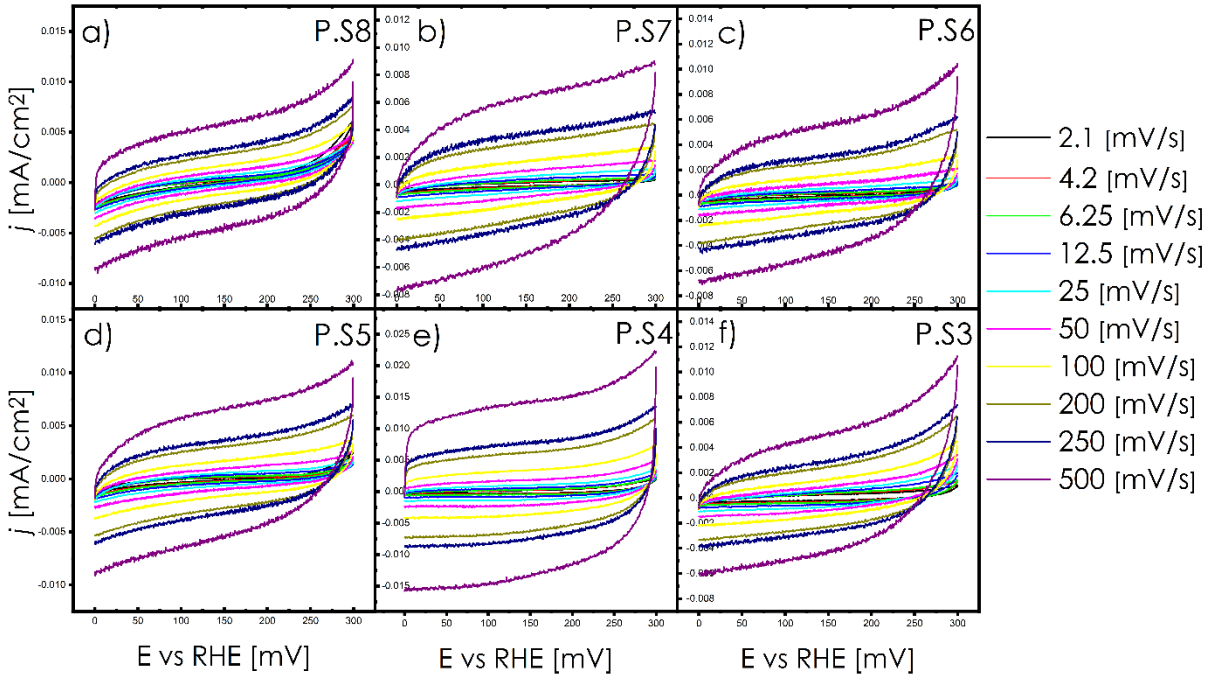

Figure S7. CV curves for powders from $Co_3Fe_3Ni_3S_{8-x}Se_x$ before chronoamperometry.

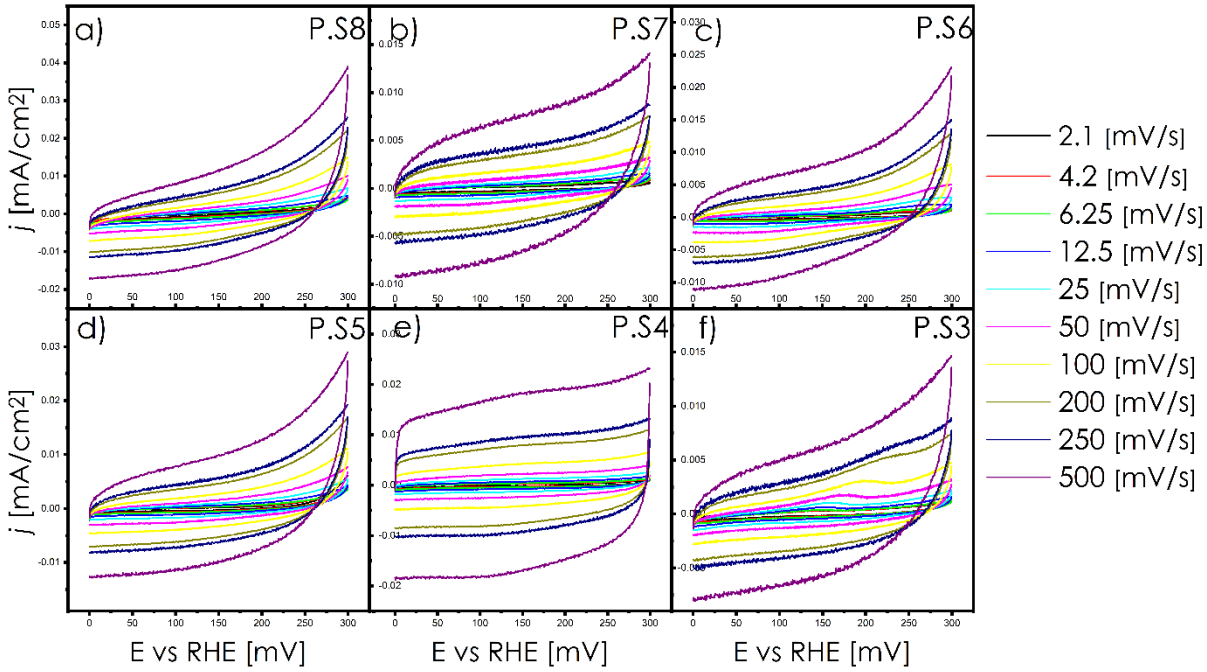

Figure S8. CV curves for powders from $Co_3Fe_3Ni_3S_{8-x}Se_x$ after chronoamperometry.

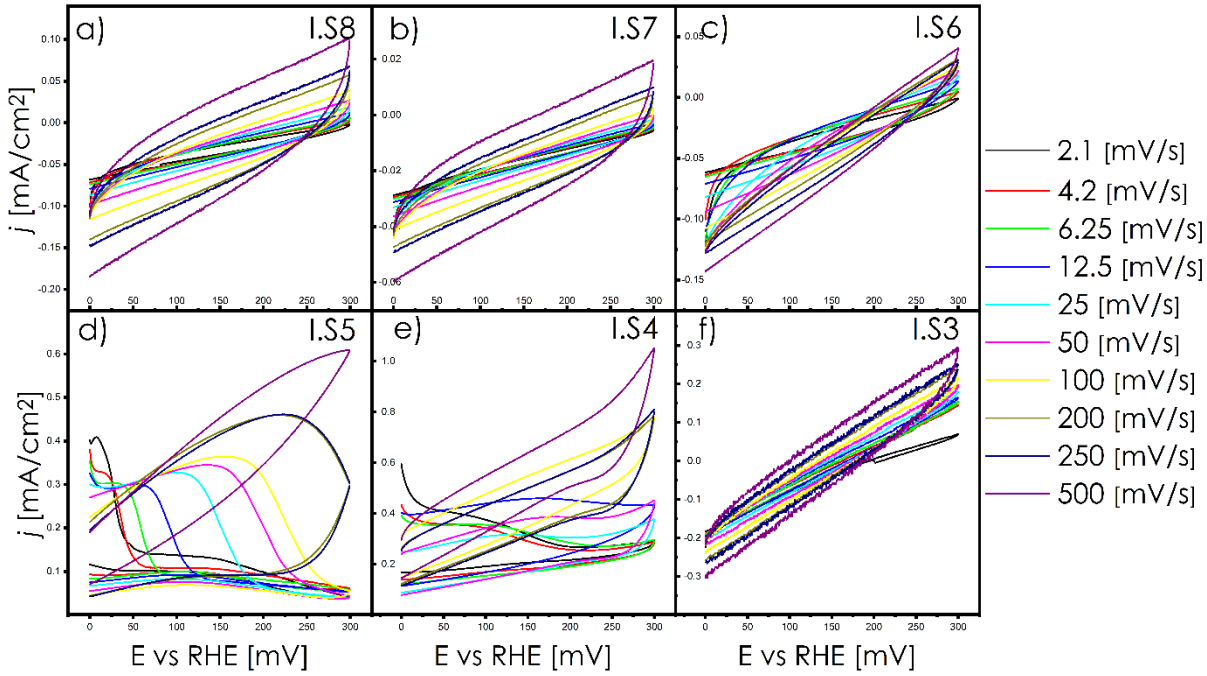

Figure S9. CV curves for ingots from $Co_3Fe_3Ni_3S_{8-x}Se_x$ before chronoamperometry.

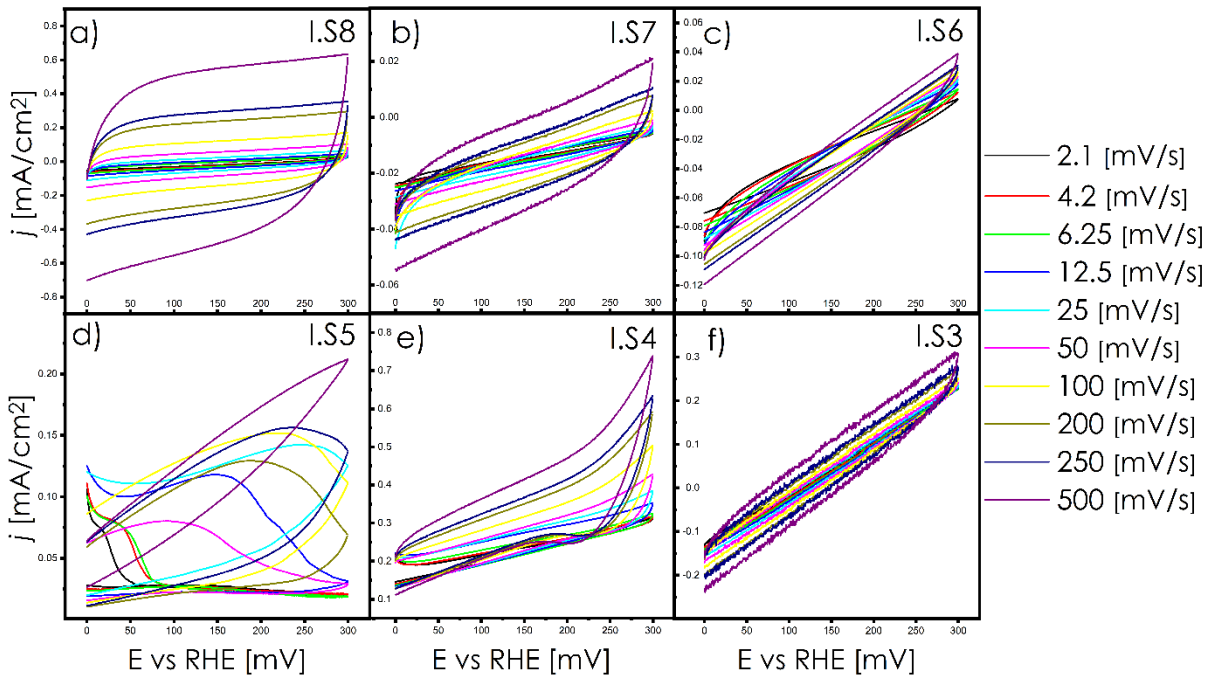

Figure S10. CV curves for ingots from $Co_3Fe_3Ni_3S_{8-x}Se_x$ after chronoamperometry.

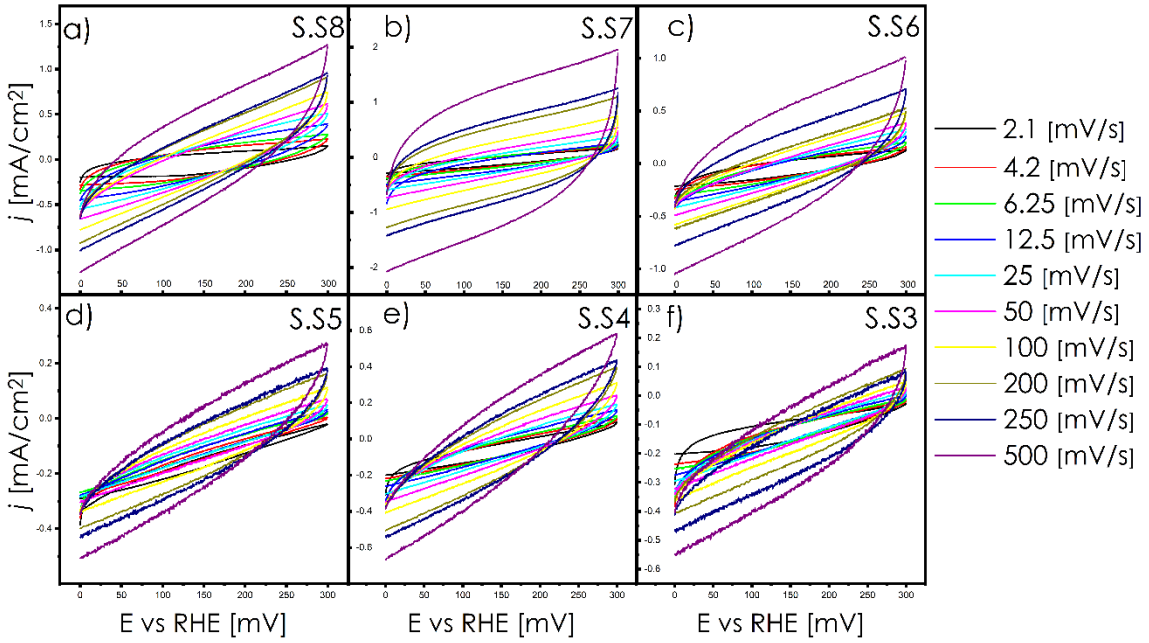

Figure S11. CV curves for pellets from $Co_3Fe_3Ni_3S_{8-x}Se_x$ before chronoamperometry.

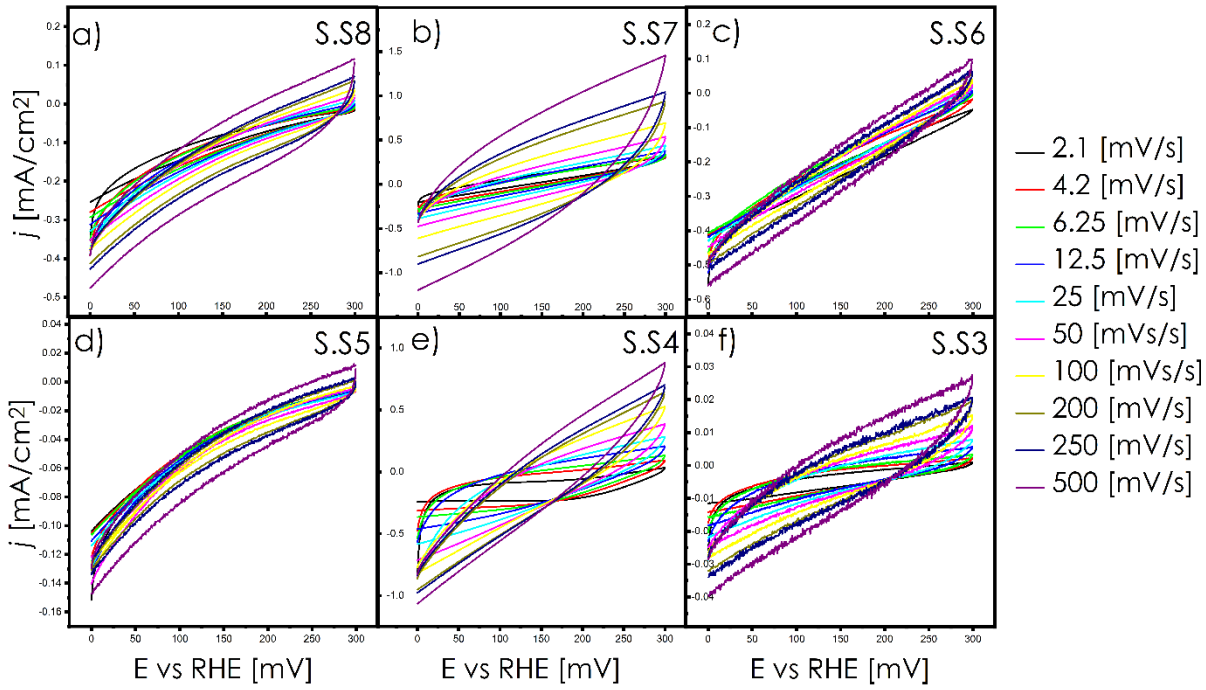

Figure S12. CV curves for pellets from $Co_3Fe_3Ni_3S_{8-x}Se_x$ after chronoamperometry.

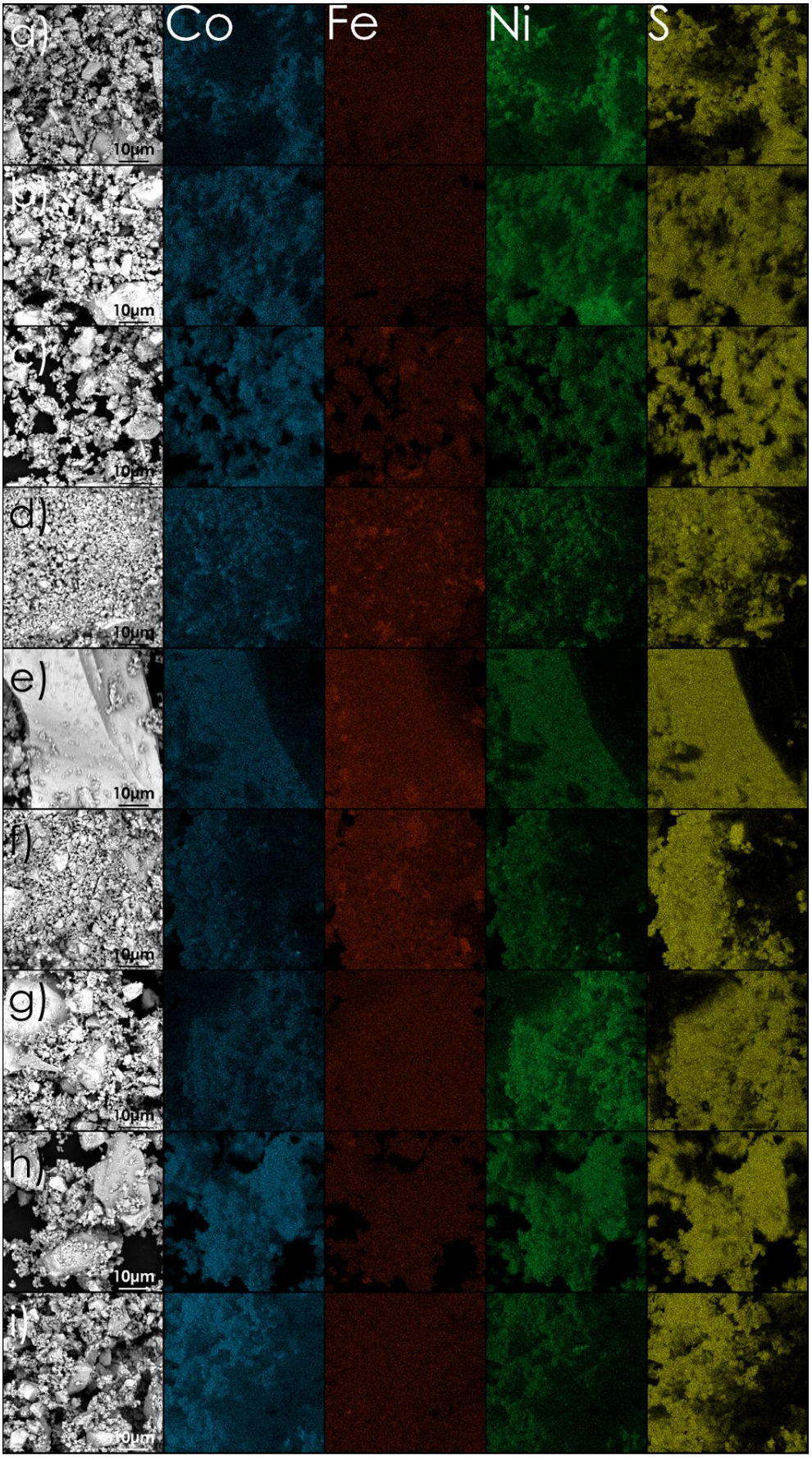

Figure S13. SEM images and EDS elemental maps of $Co_{9-x-y}Fe_xN_yS_8$ series: a) P.314.S8; b) P.116.S8; c) P.134.S8; d) P.413.S8; e) P.611.S8; f) P.431.S8; g) P.341.S8; h) P.161.S8; i) P.143.S8.

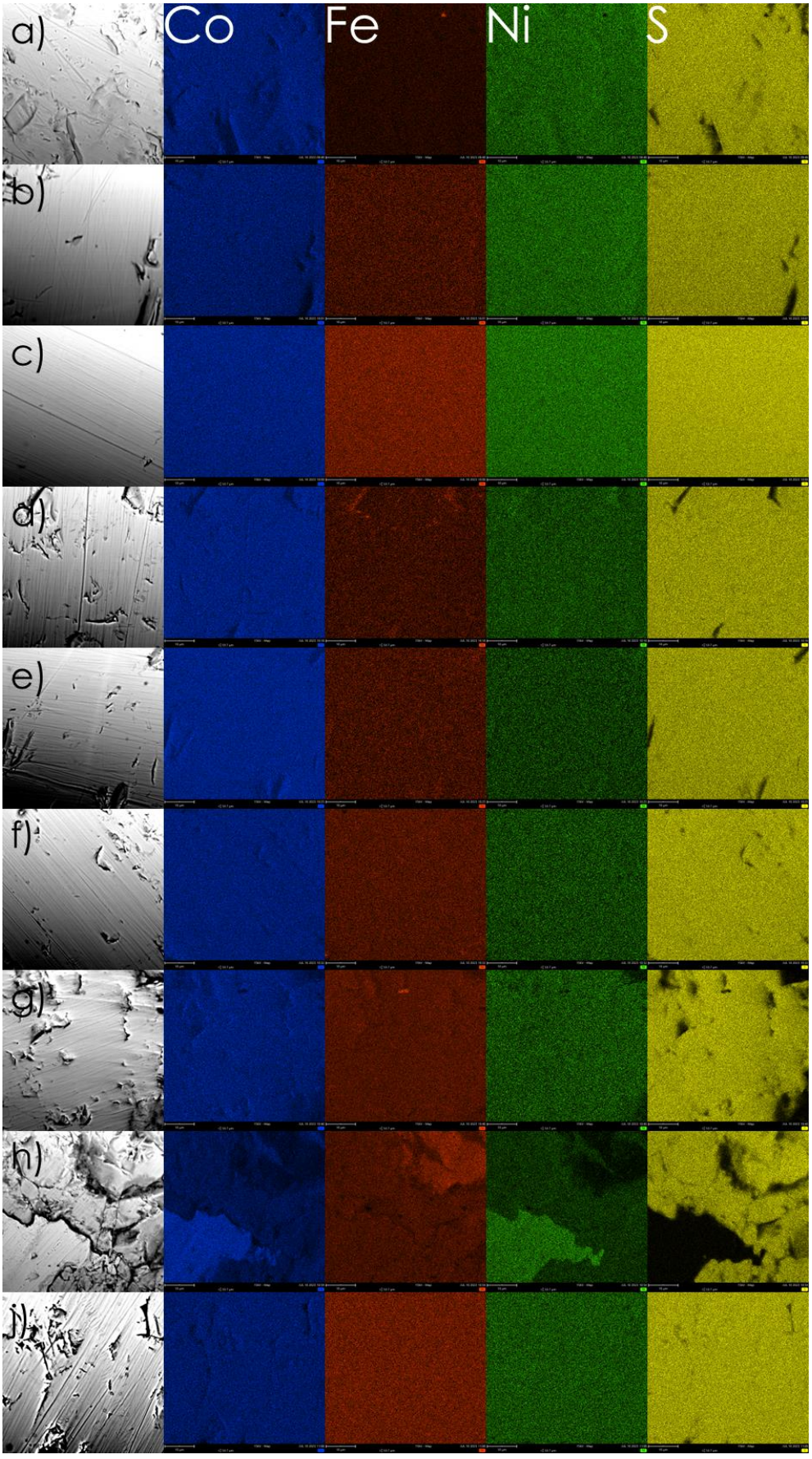

Figure S14. SEM images and EDS elemental maps of $Co_{9-x-y}Fe_xN_yS_8$ series: a) I.314.S8; b) I.116.S8; c) I.134.S8; d) I.413.S8; e) I.611.S8; f) I.431.S8; g) I.341.S8; h) I.161.S8; i) I.143.S8.

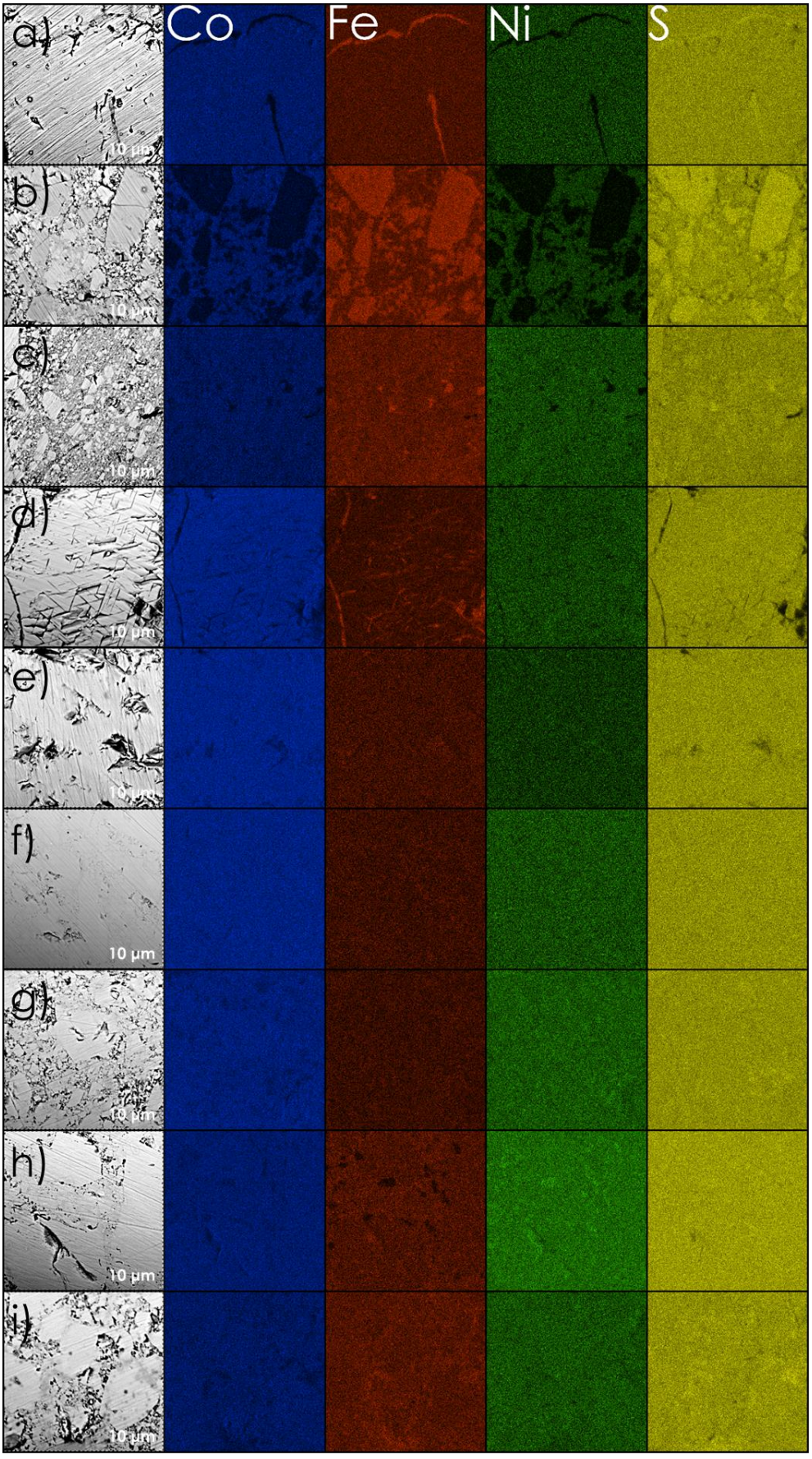

Figure S15. SEM images and EDS elemental maps of $Co_{9-x-y}Fe_xN_yS_8$ series: a) S.314.S8; b) S.116.S8; c) S.134.S8; d) S.413.S8; e) S.611.S8; f) S.431.S8; g) S.341.S8; h) S.161.S8; i) S.143.S8.

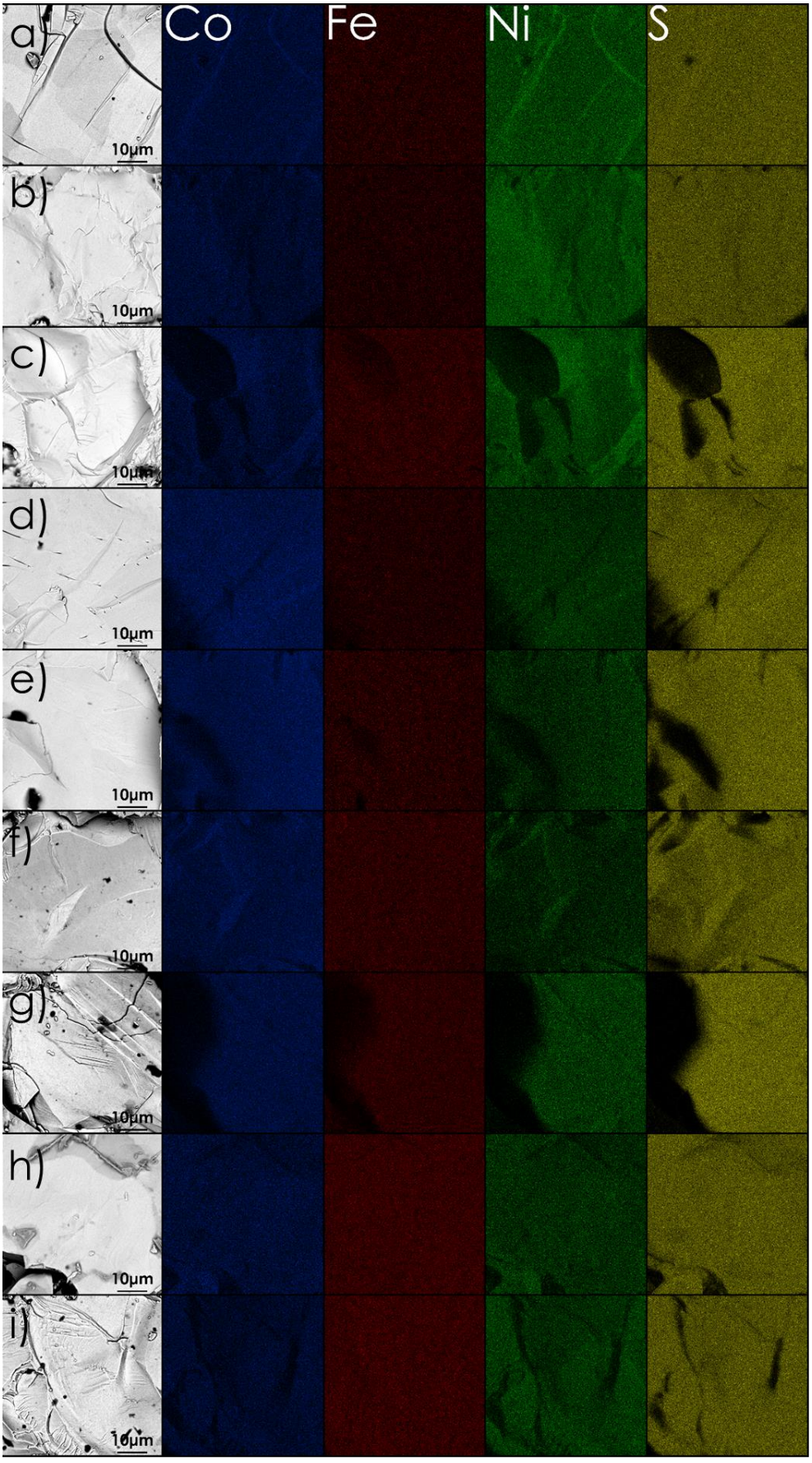

Figure S16. SEM images and EDS elemental maps of $Co_{9-x-y}Fe_xN_yS_8$ series: a) I.314.S8; b) I.116.S8; c) I.134.S8; d) I.413.S8; e) I.611.S8; f) I.431.S8; g) I.341.S8; h) I.161.S8; i) I.143.S8 after chronoamperometry.

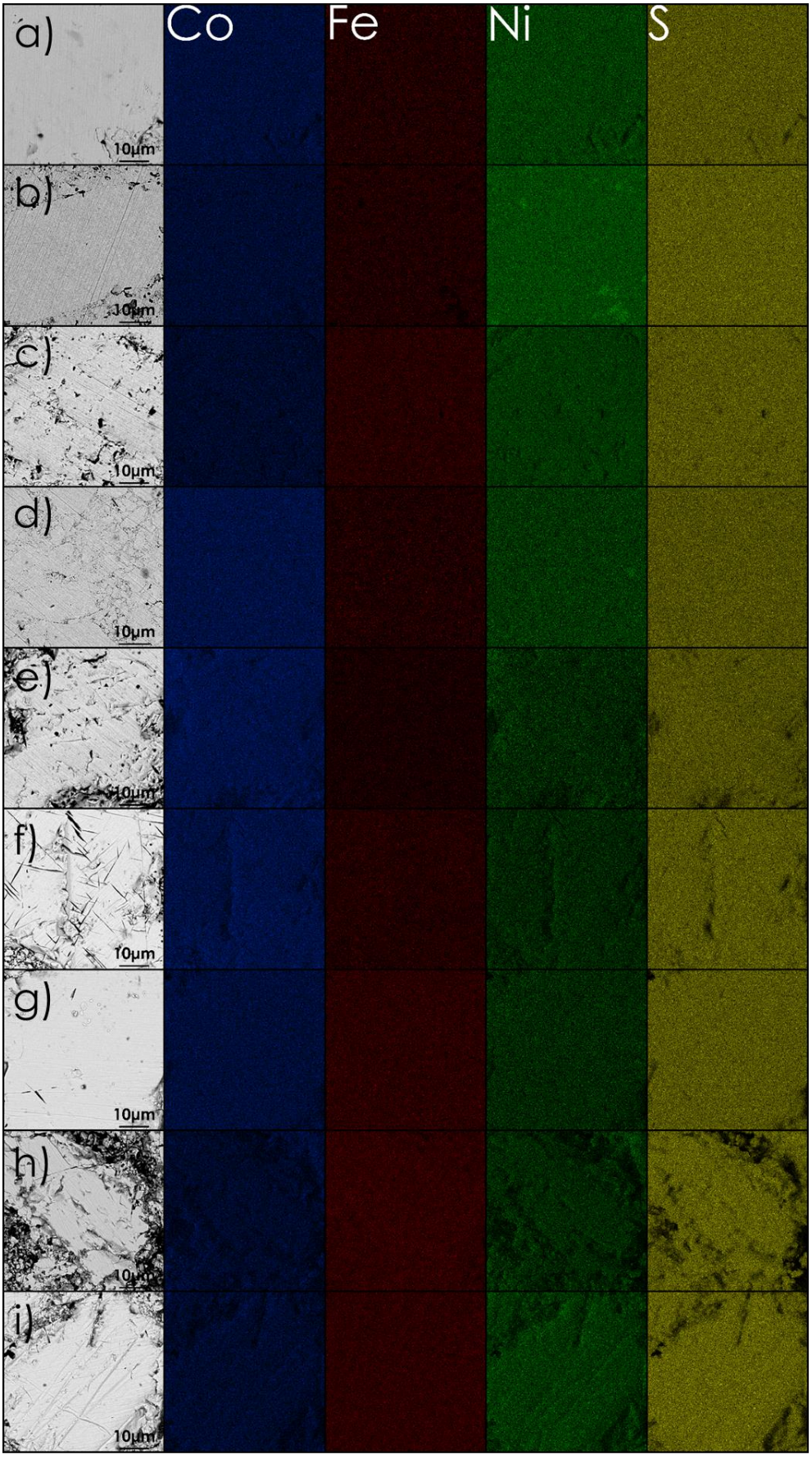

Figure S17. SEM images and EDS elemental maps of $Co_{9-x-y}Fe_xN_yS_8$ series: a) S.314.S8; b) S.116.S8; c) S.134.S8; d) S.413.S8; e) S.611.S8; f) S.431.S8; g) S.341.S8; h) S.161.S8; i) S.143.S8 chronoamperometry.

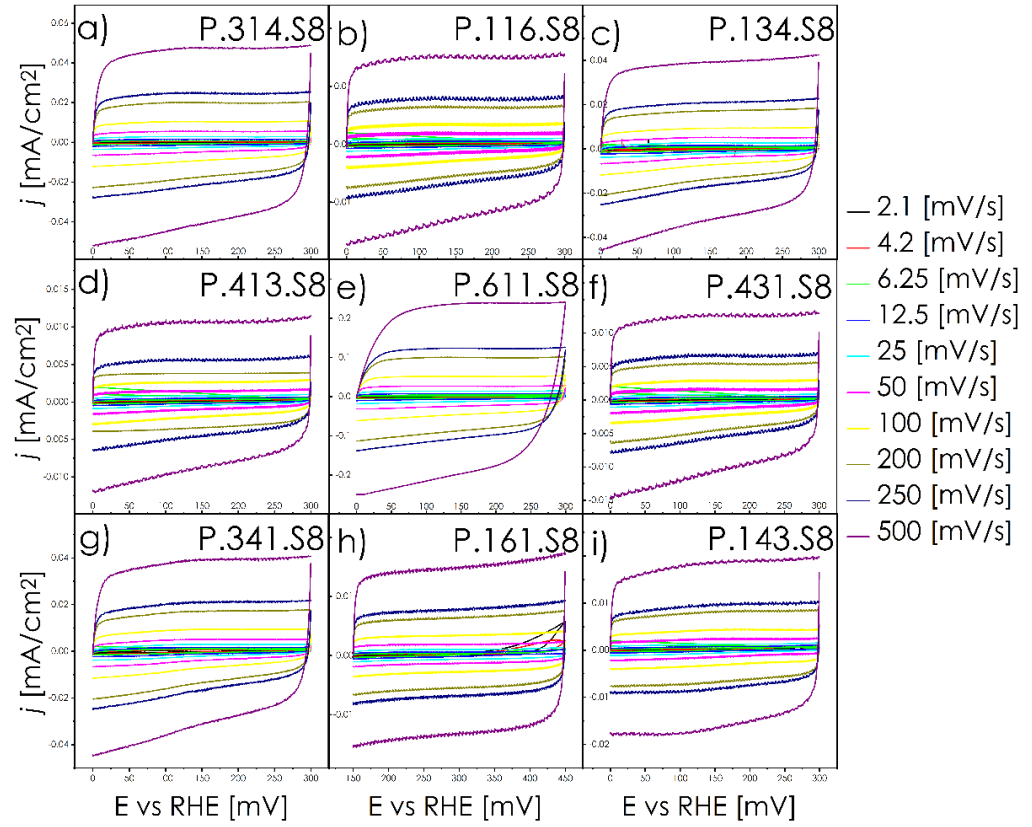

Figure S18. CV curves for powders from $Co_{9-x-y}Fe_xNi_yS_8$ before chronoamperometry.

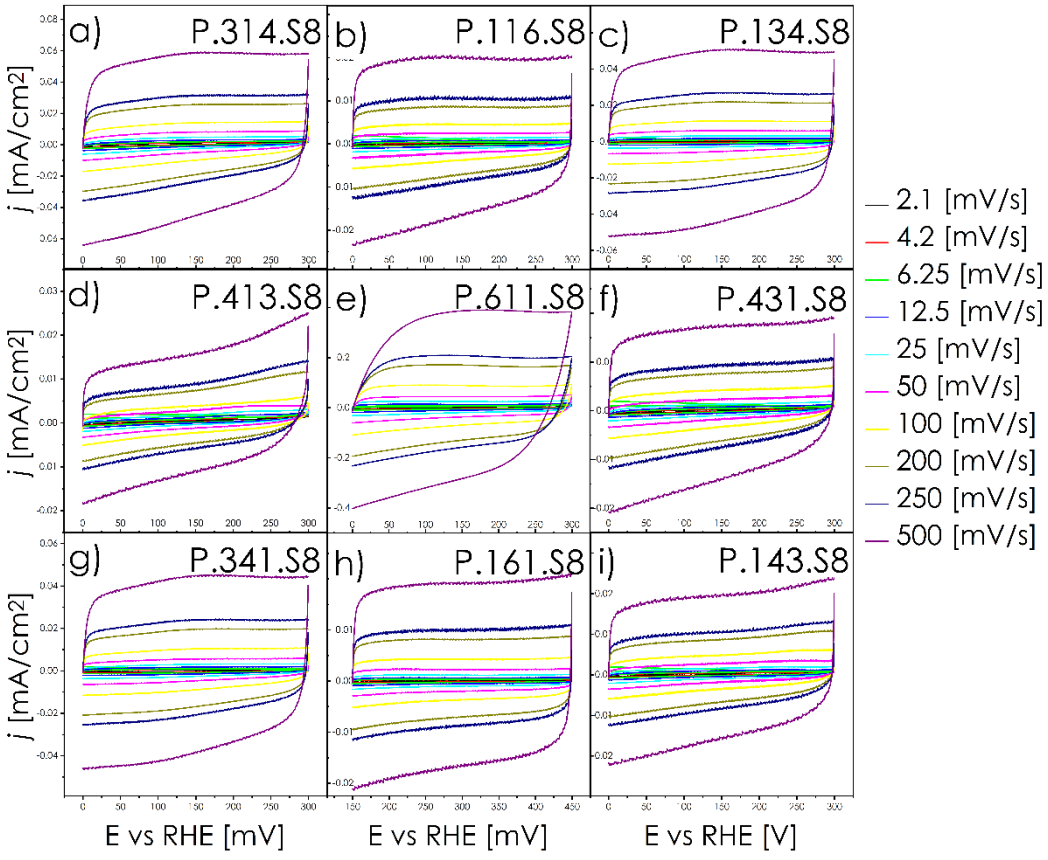

Figure S19. CV curves for powders from $Co_{9-x-y}Fe_xNi_yS_8$ after chronoamperometry.

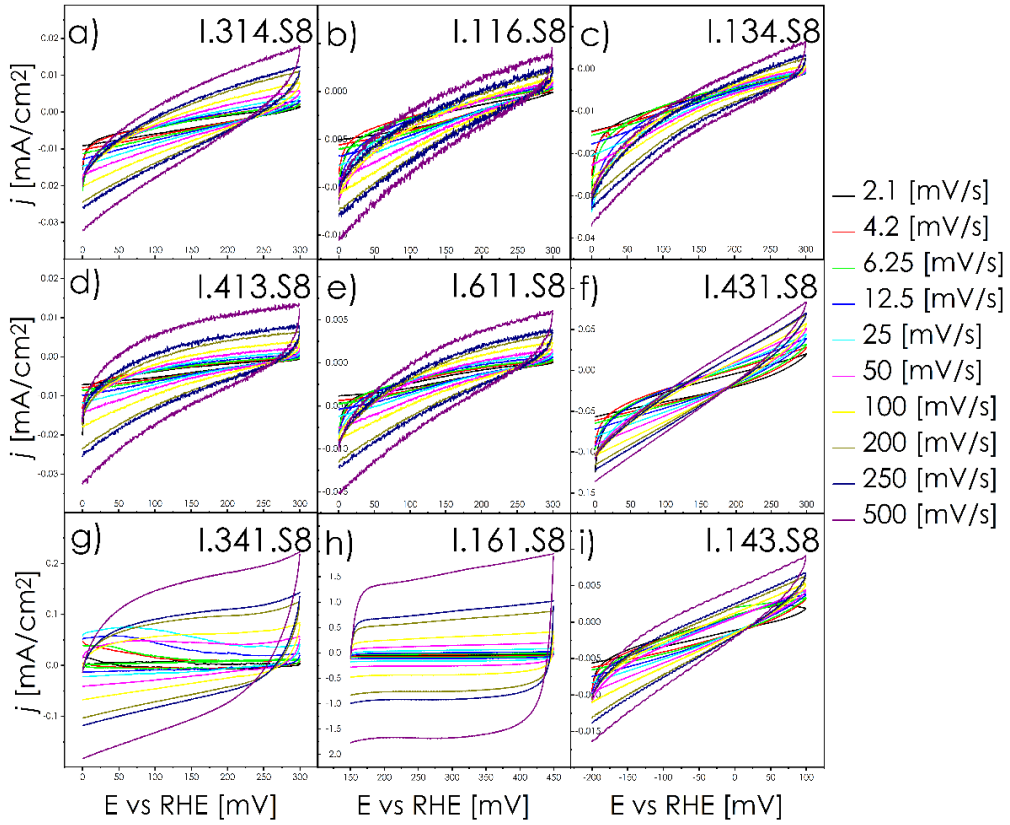

Figure S20. CV curves for ingots from $Co_{9-x-y}Fe_xNi_yS_8$ before chronoamperometry.

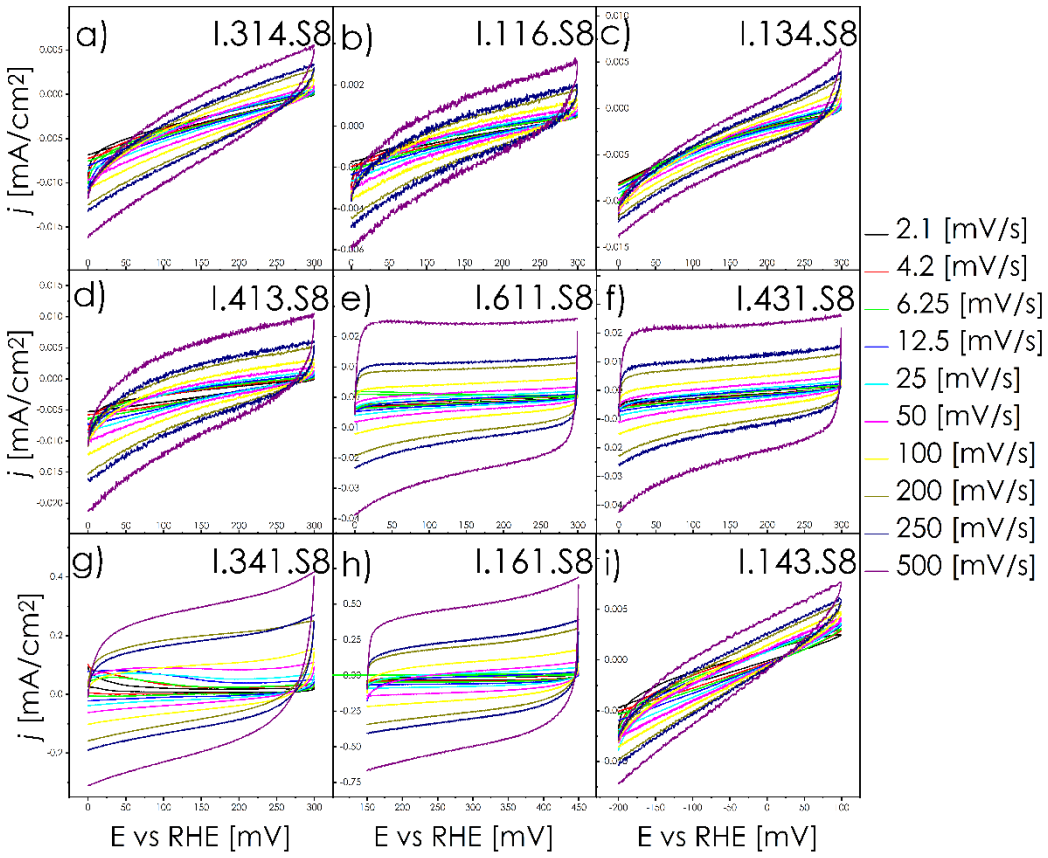

Figure S21. CV curves for ingots from $Co_{9-x-y}Fe_xNi_yS_8$ after chronoamperometry.

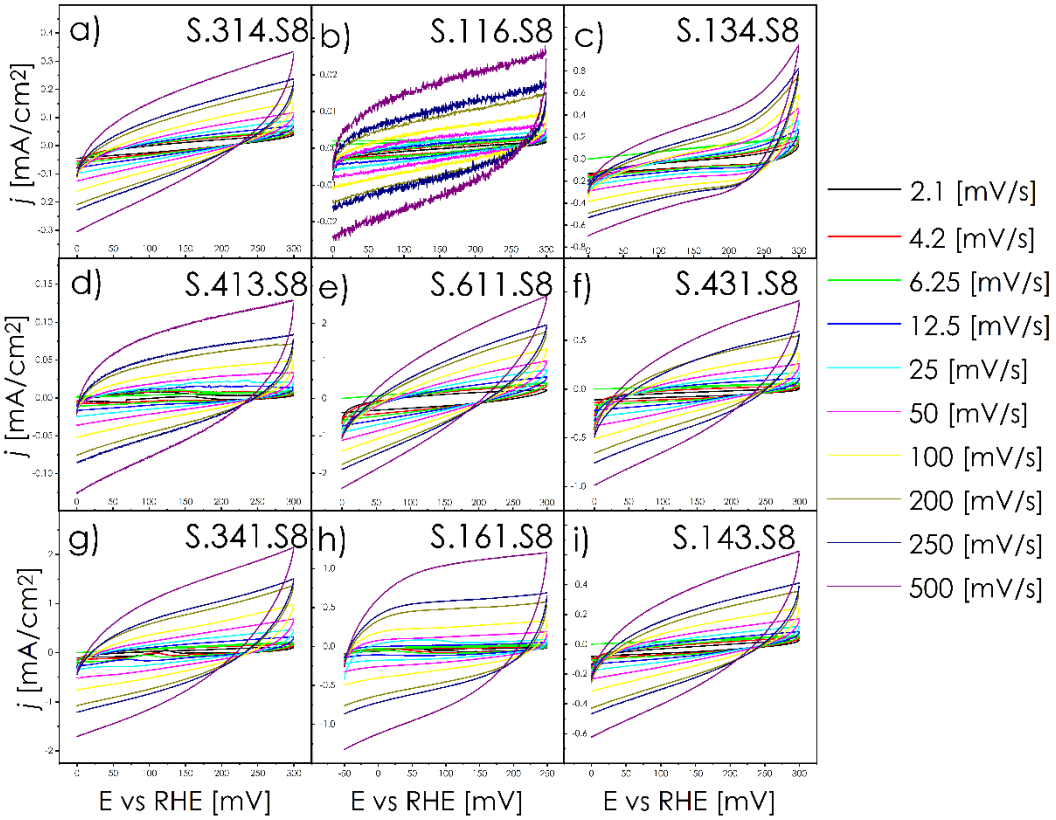

Figure S22. CV curves for pellets from $Co_{9-x-y}Fe_xNi_yS_8$ before chronoamperometry.

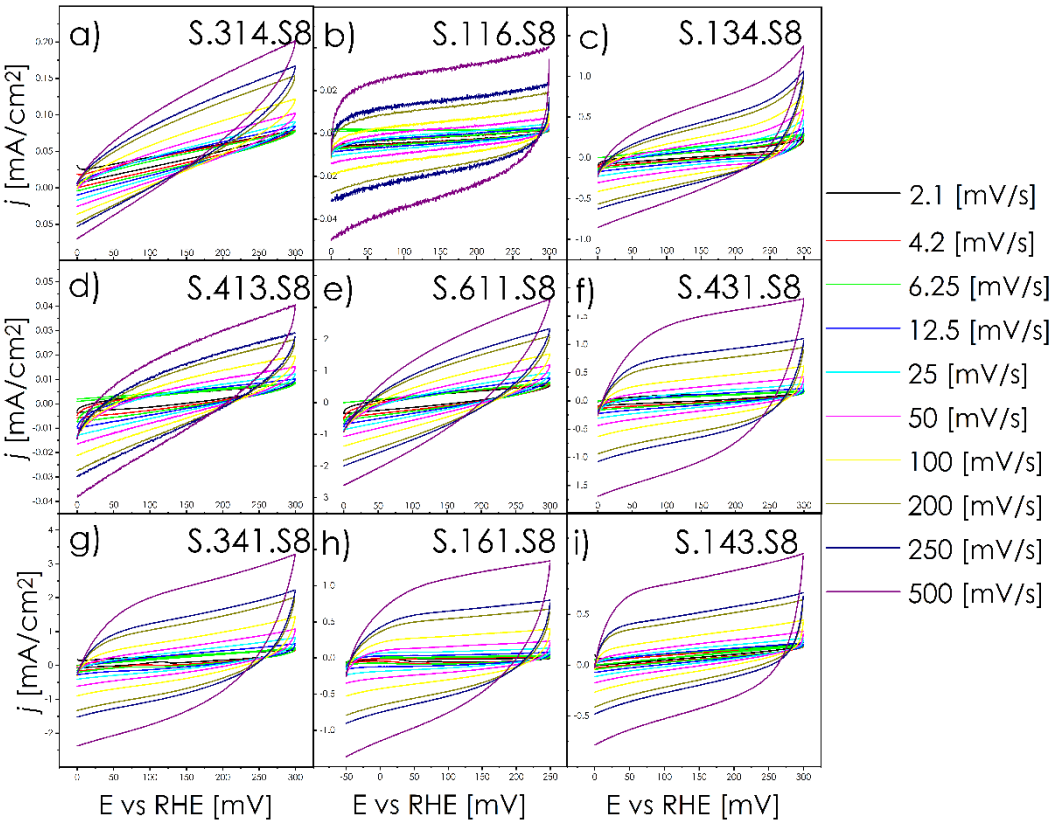

Figure S23. CV curves for pellets from $Co_{9-x-y}Fe_xNi_yS_8$ after chronoamperometry.

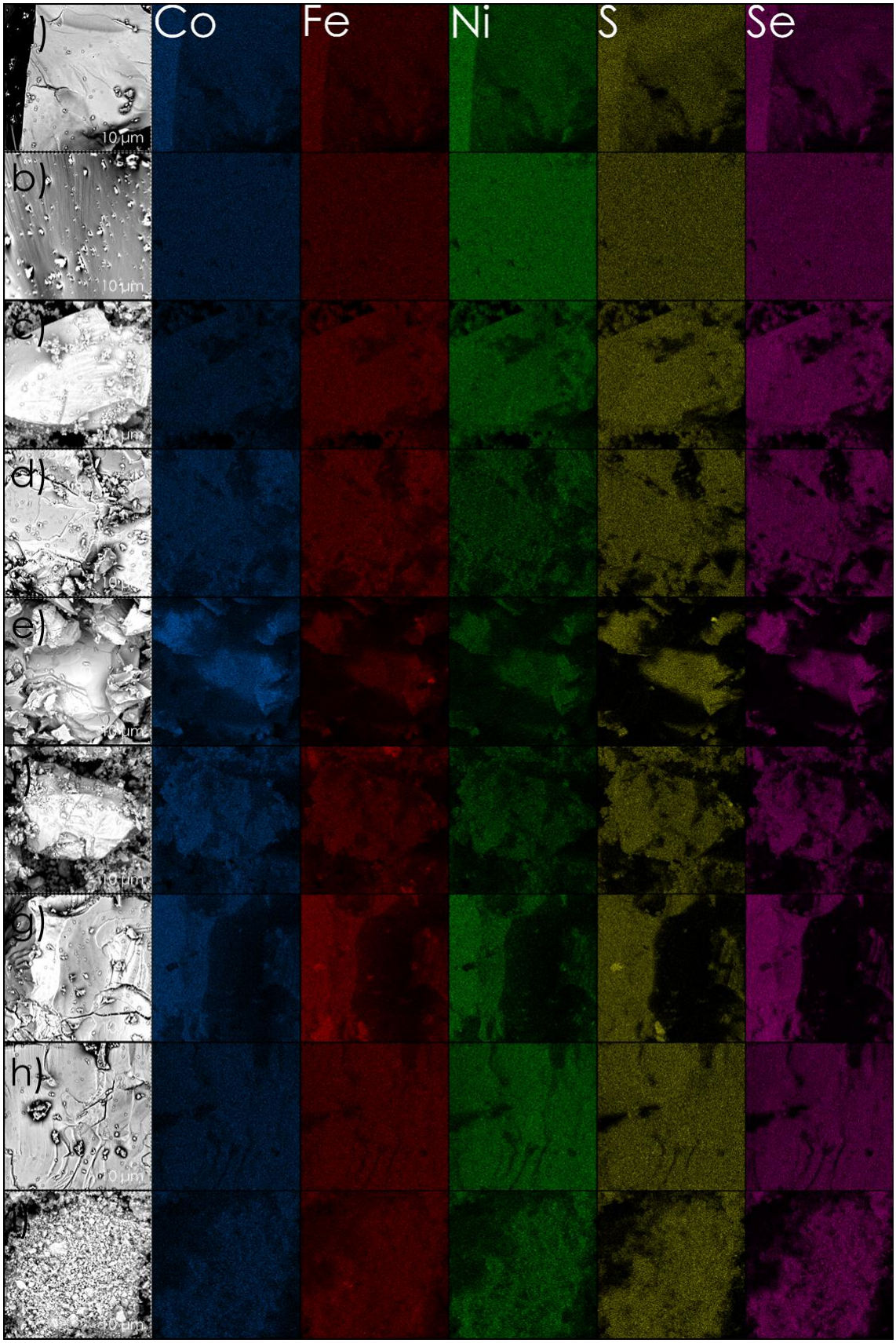

Figure S24. SEM images and EDS elemental maps of $Co_{9-x-y}Fe_xN_yS_4Se_4$ series: a) P.314.S4; b) P.116.S4; c) P.134.S4; d) P.413.S4; e) P.611.S4; f) P.431.S4; g) P.341.S4; h) P.161.S4; i) P.143.S4.

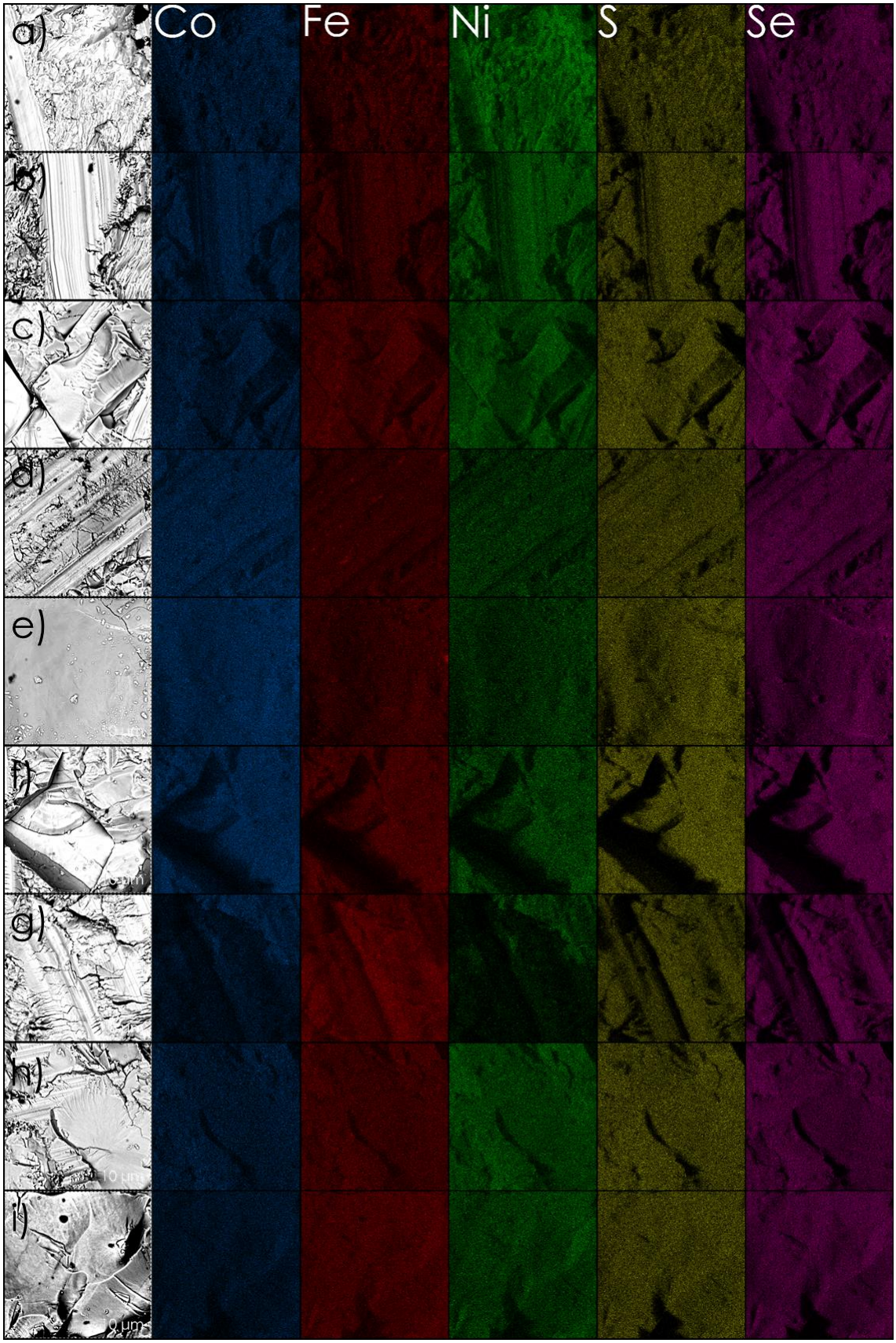

Figure S25. SEM images and EDS elemental maps of $Co_{9-x-y}Fe_xN_yS_4Se_4$ series: a) I.314.S4; b) I.116.S4; c) I.134.S4; d) I.413.S4; e) I.611.S4; f) I.431.S4; g) I.341.S4; h) I.161.S4; i) I.143.S4.

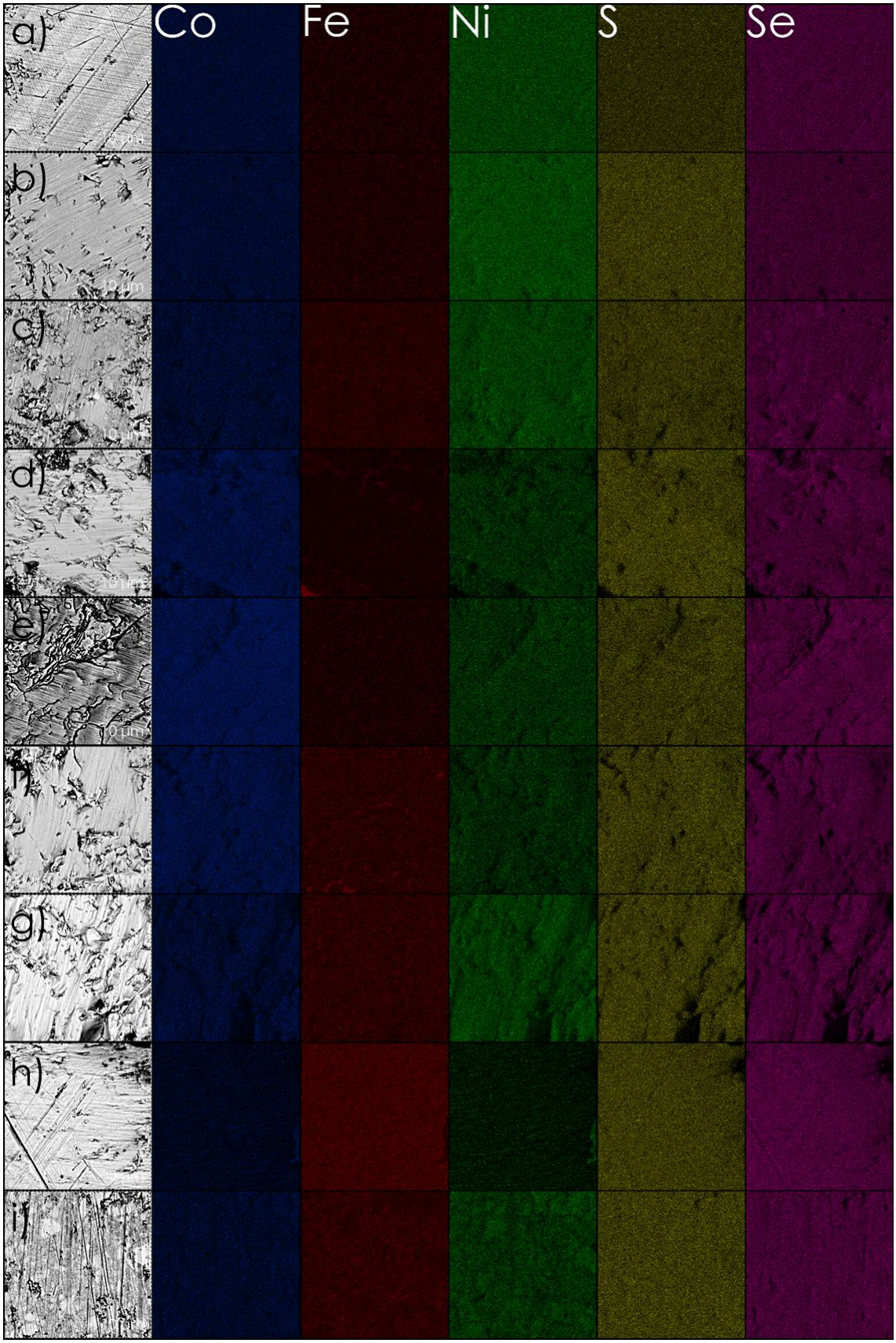

Figure S26. SEM images and EDS elemental maps of $Co_{9-x-y}Fe_xN_yS_4Se_4$ series: a) S.314.S4; b) S.116.S4; c) S.134.S4; d) S.413.S4; e) S.611.S4; f) S.431.S4; g) S.341.S4; h) S.161.S4; i) S.143.S4.

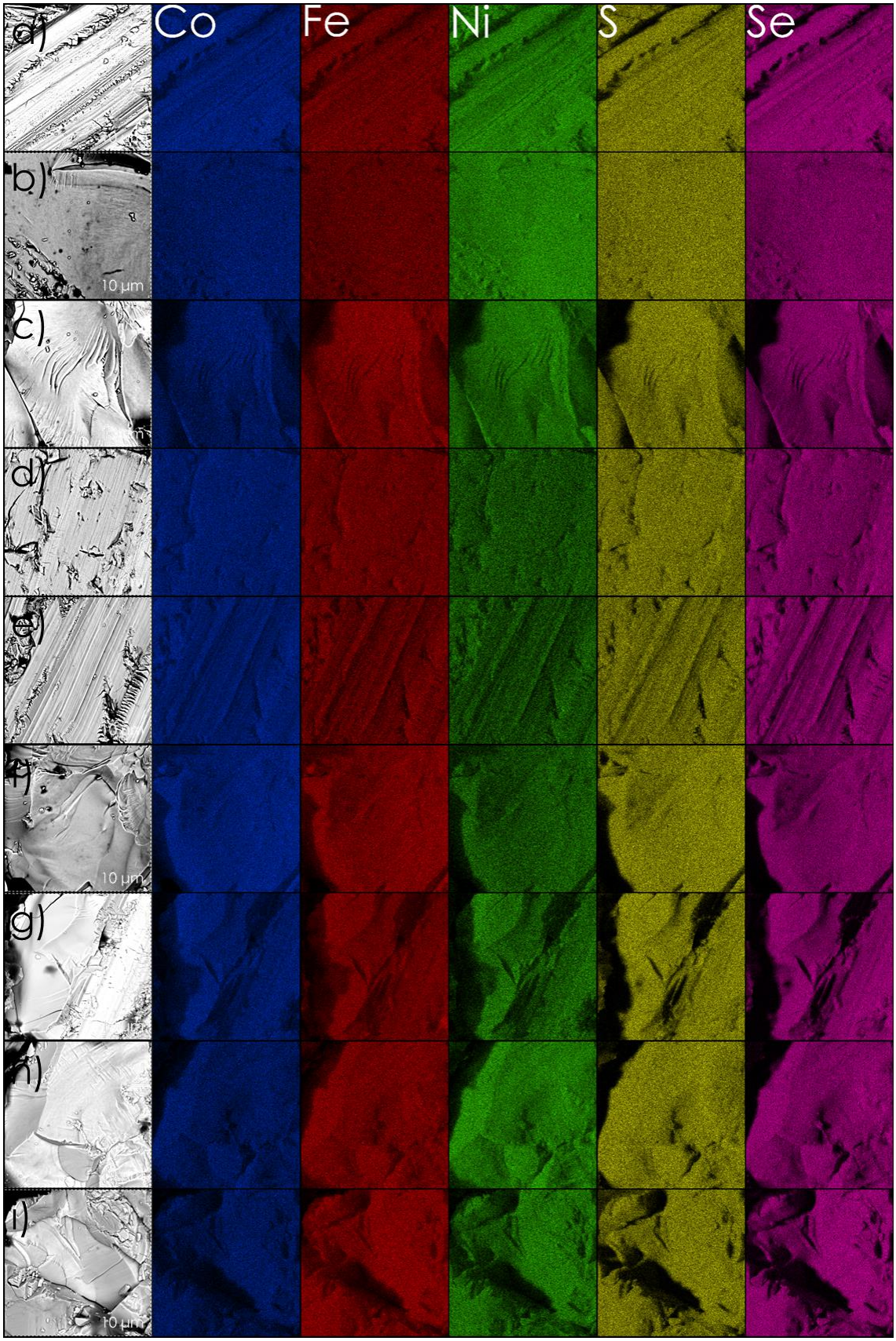

Figure S27. SEM images and EDS elemental maps of $Co_{9-x-y}Fe_xN_yS_4Se_4$ series: a) I.314.S4; b) I.116.S4; c) I.134.S4; d) I.413.S4; e) I.611.S4; f) I.431.S4; g) I.341.S4; h) I.161.S4; i) I.143.S4 after chronoamperometry.

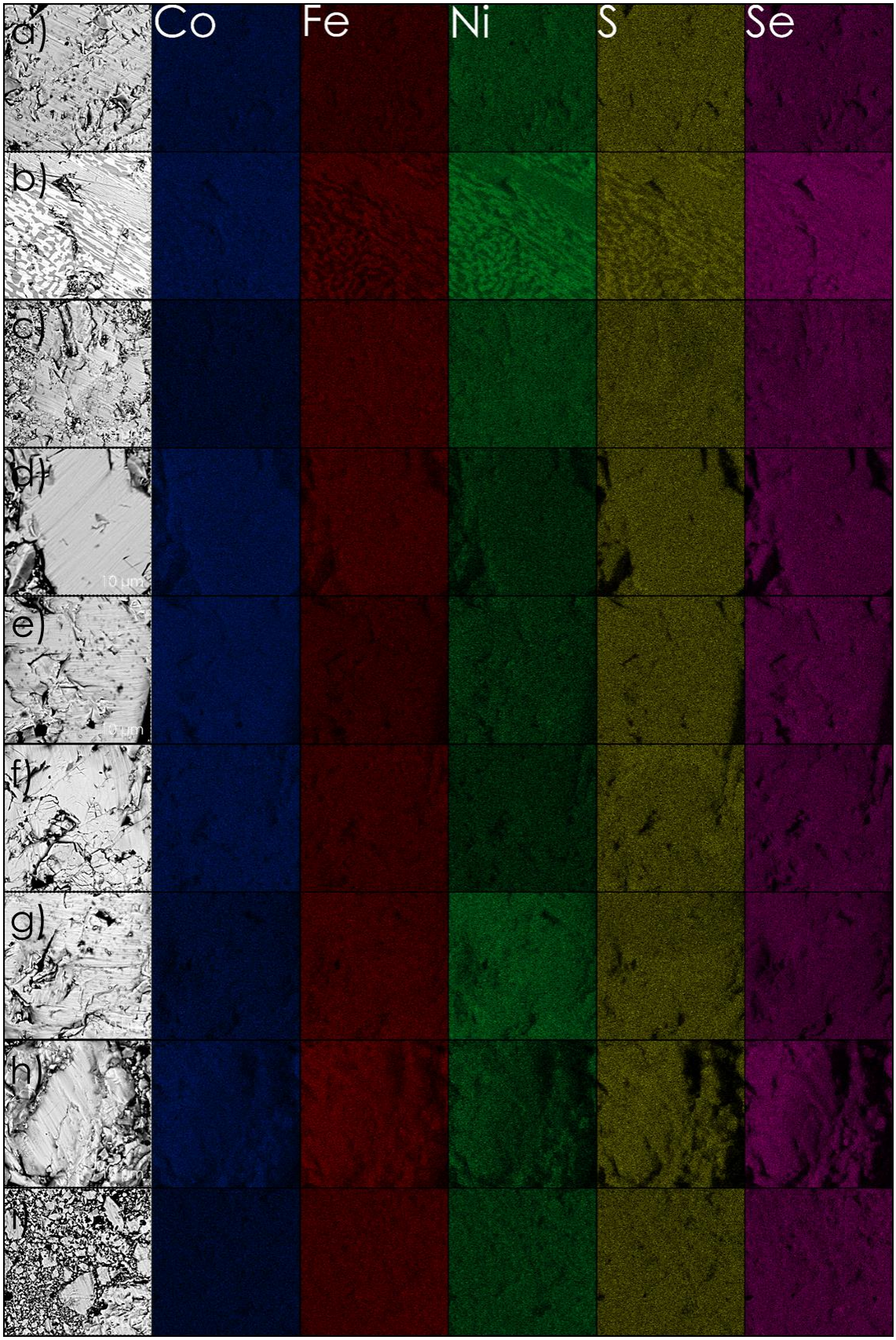

Figure S28. SEM images and EDS elemental maps of $Co_{9-x-y}Fe_xN_yS_4Se_4$ series: a) I.314.S4; b) I.116.S4; c) I.134.S4; d) I.413.S4; e) I.611.S4; f) I.431.S4; g) I.341.S4; h) I.161.S4; i) I.143.S4 after chronoamperometry.

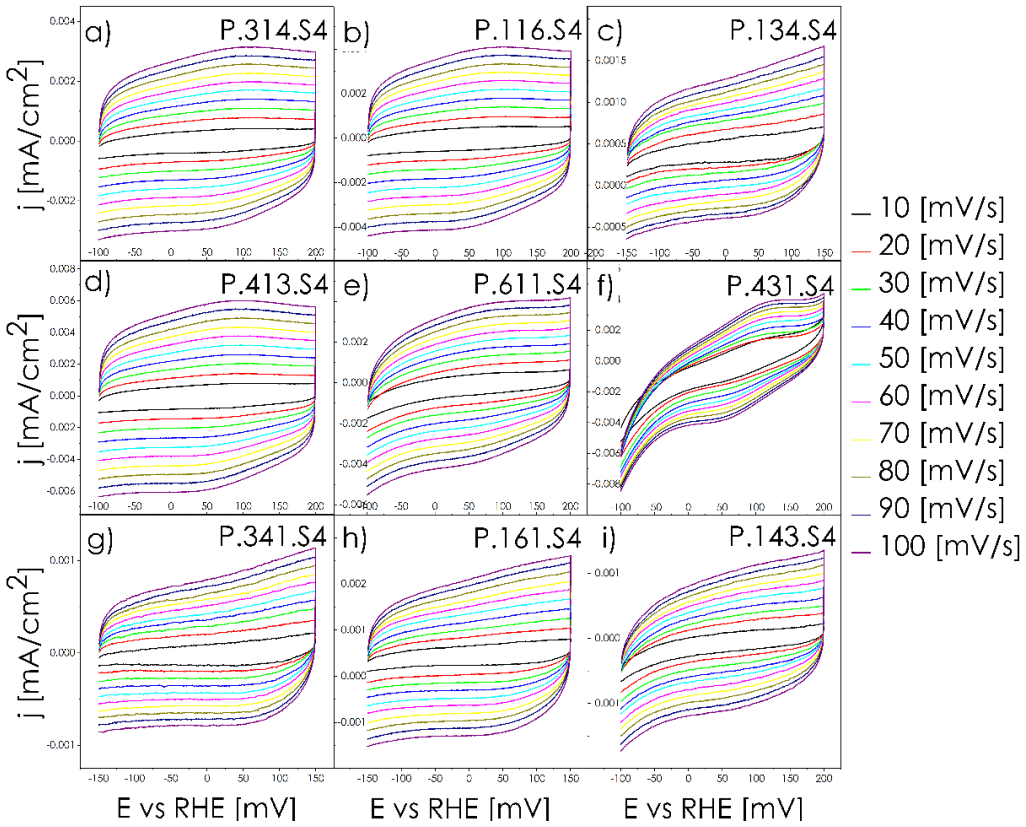

Figure S29. CV curves for powders from $Co_{9-x-y}Fe_xNi_yS_4Se_4$ before chronoamperometry.

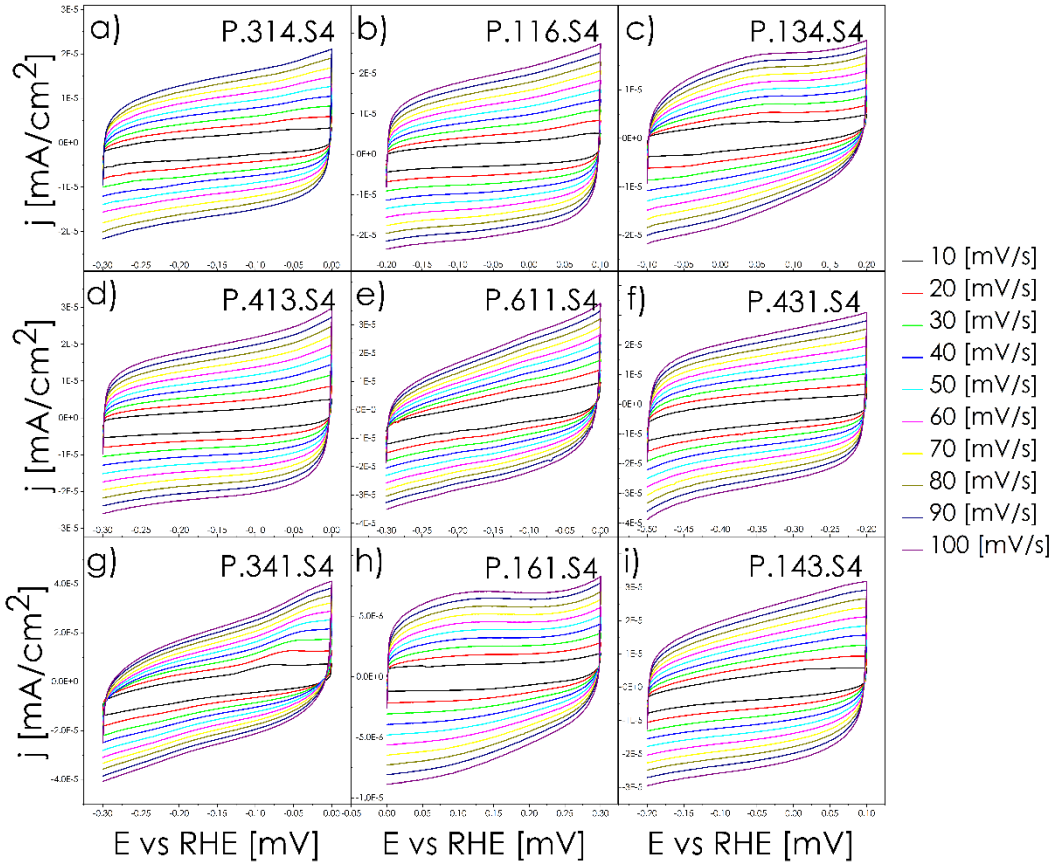

Figure S30. CV curves for powders from $Co_{9-x-y}Fe_xNi_yS_4Se_4$ after chronoamperometry.

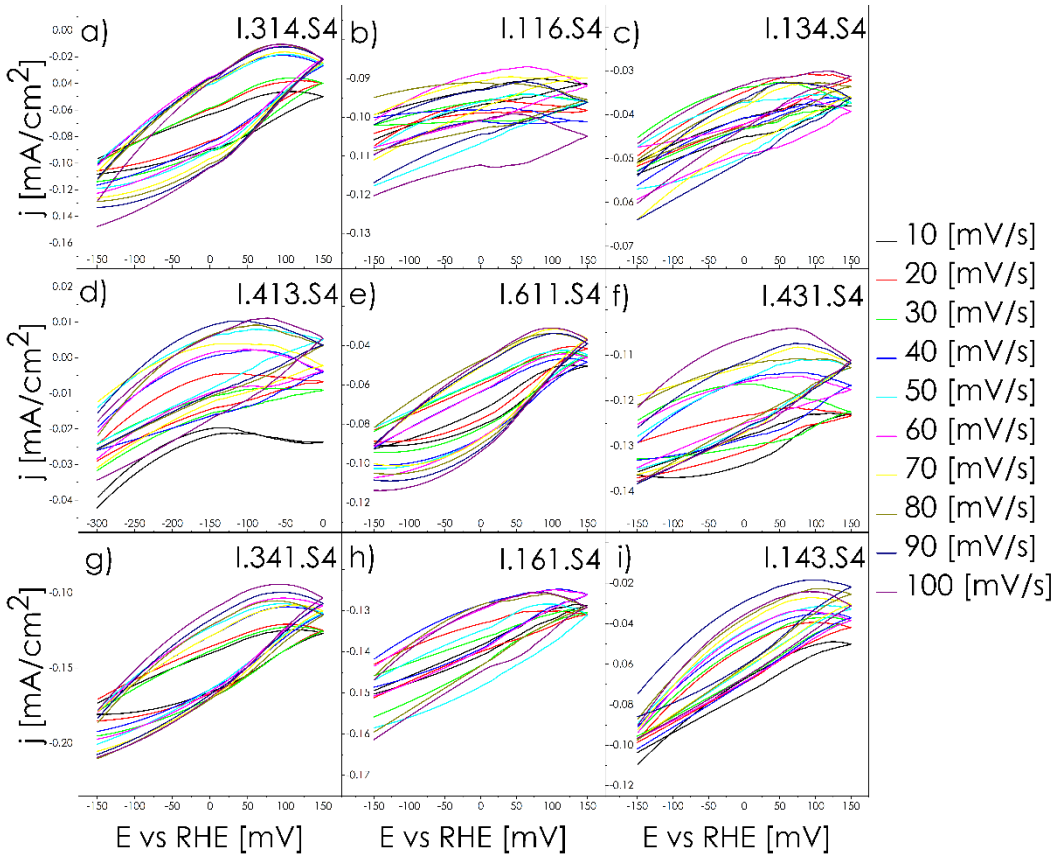

Figure S31. CV curves for ingots from $Co_{9-x-y}Fe_xNi_yS_4Se_4$ before chronoamperometry.

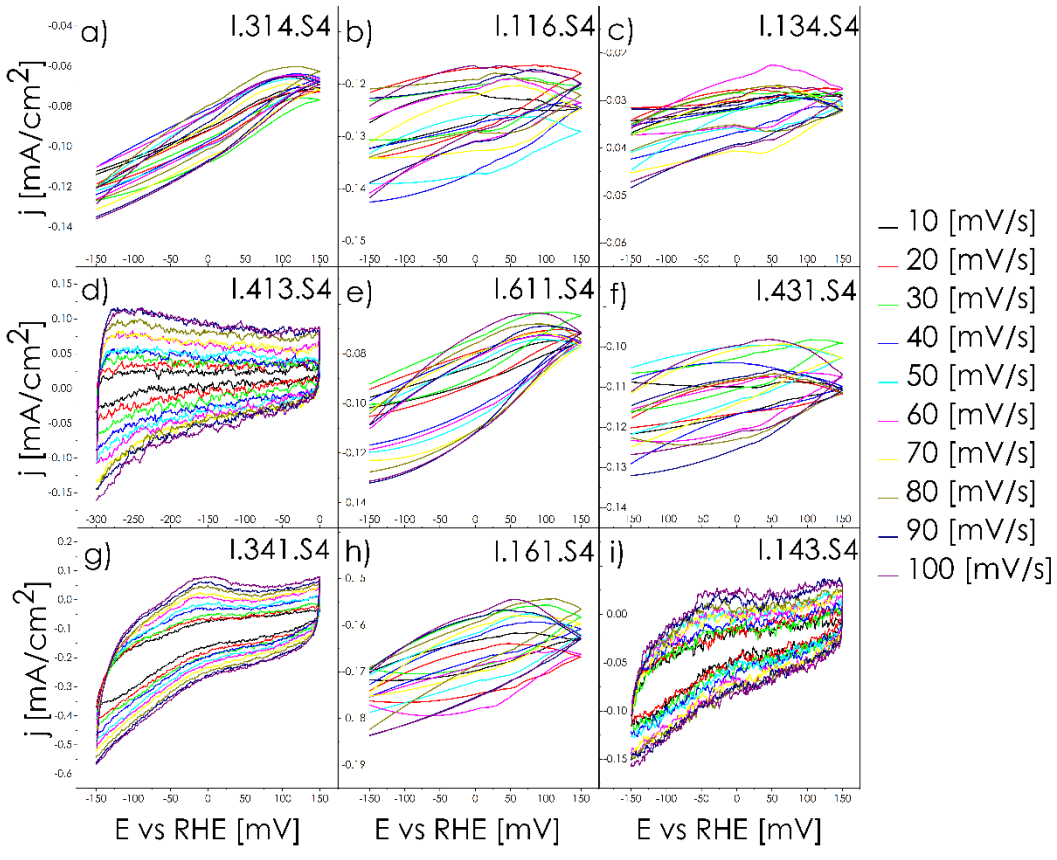

Figure S32. CV curves for ingots from $Co_{9-x-y}Fe_xNi_yS_4Se_4$ after chronoamperometry.

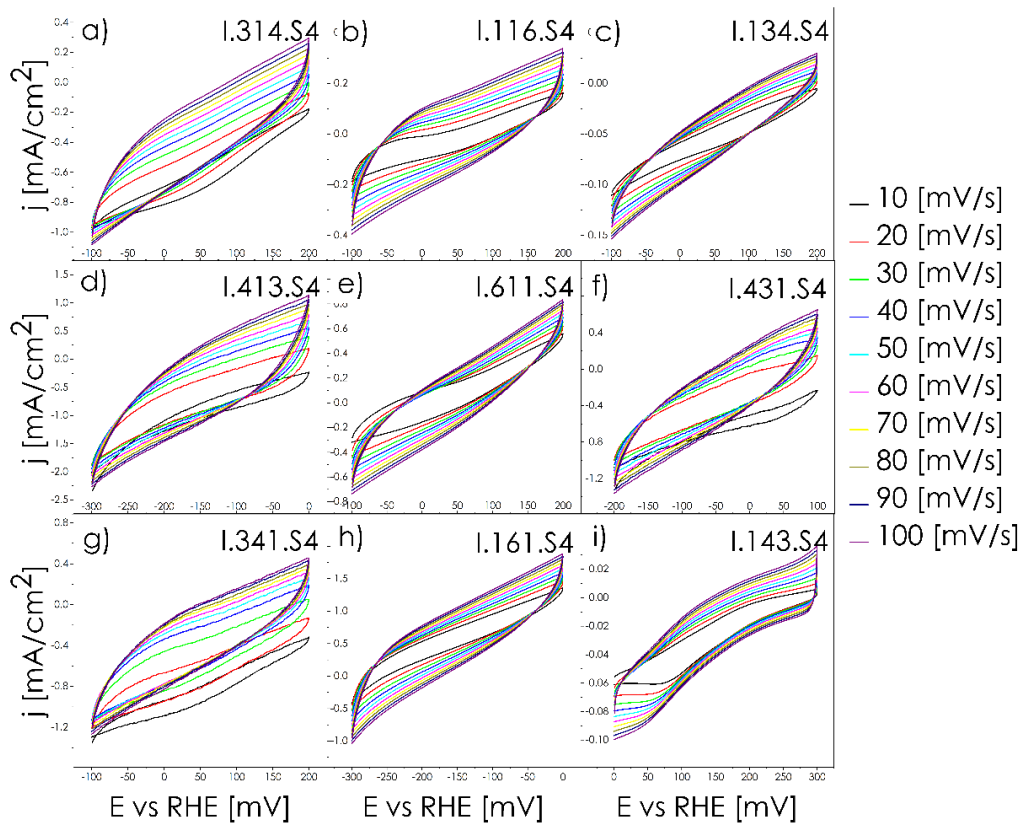

Figure S33. CV curves for pellets from $Co_{9-x-y}Fe_xNi_yS_4Se_4$ before chronoamperometry.

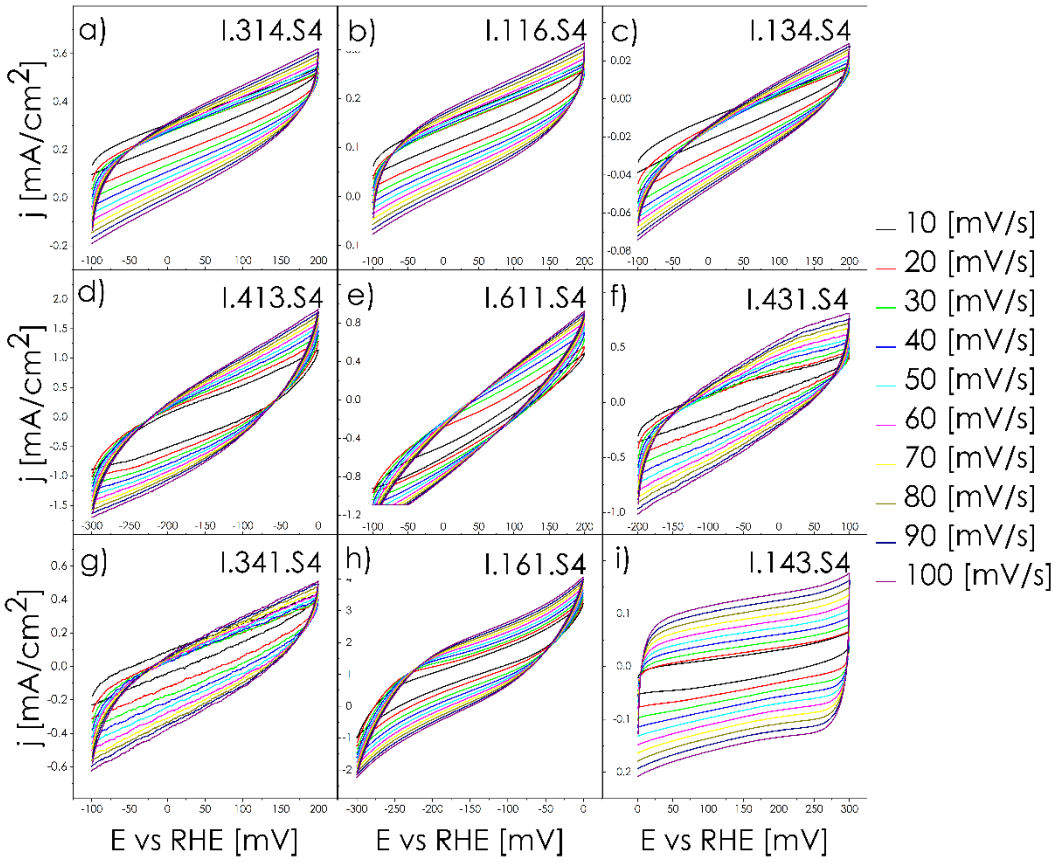

Figure S34. CV curves for pellets from $Co_{9-x-y}Fe_xNi_yS_4Se_4$ after chronoamperometry.

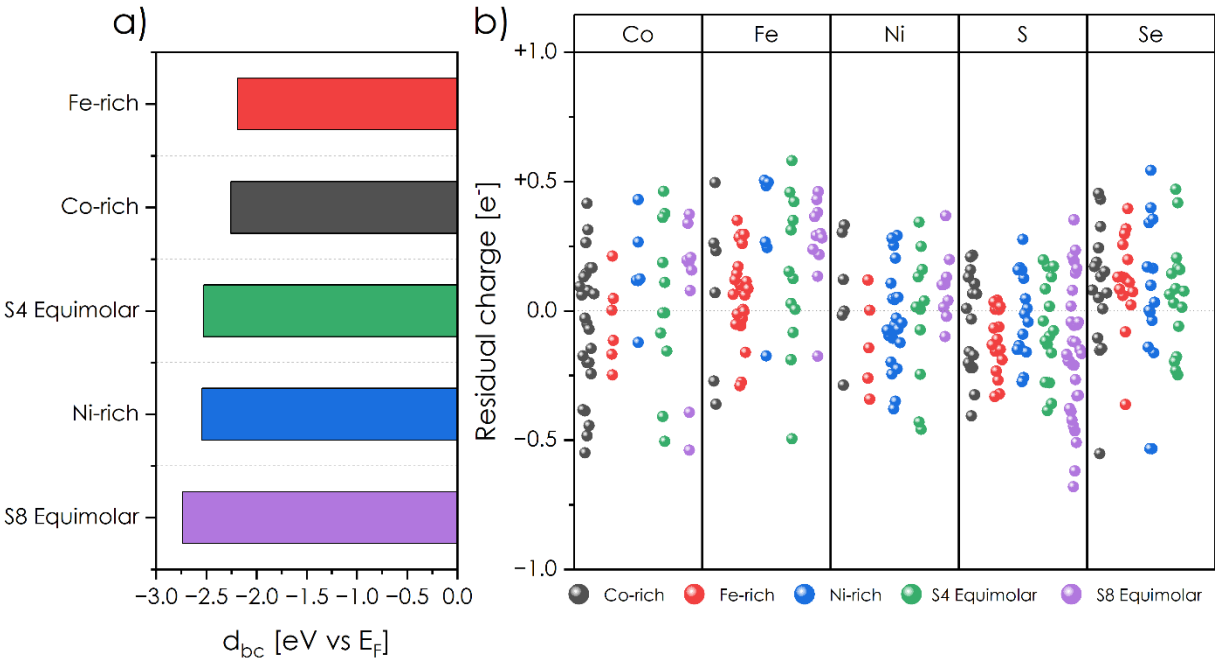

Figure S35. a) D-band centers with respect to Fermi Energy of samples from $Co_{9-x-y}Fe_xNi_yS_8$ and $Co_{9-x-y}Fe_xNi_yS_4Se_4$ series; b) Residual charge distribution of atoms in samples from $Co_{9-x-y}Fe_xNi_yS_8$ and $Co_{9-x-y}Fe_xNi_yS_4Se_4$ series derived from Bader analysis.

Table S1. Summary of all samples from all three series and all three forms, with chemical compositions determined by EDS and ICP-OES, other phases in the material determined by XRD analysis, elementary cell size, Goodness of Fit, Weighted R profile determined by Rietveld analysis and relative density for ingot and pellet samples.

Sample	Nominal composition	Chemical composition (EDS)	Chemical composition (ICP-OES)	Other phases in material	a=b=c [Å]	GoF	wRp	Relative density [%]
			$Co_3Fe_3Ni_3S_{8-x}Se_x$ series					
P.S8	$Co_3Fe_3Ni_3S_8$	$Co_{3.59}Fe_{3.33}Ni_{3.22}S_8$	$Co_{3.14}Fe_{3.08}Ni_{3.07}S_8$	-	10.01	1.46	3.14	-
P.S7	$Co_3Fe_3Ni_3S_7Se$	$Co_{3.64}Fe_{3.64}Ni_{3.24}S_{6.91}Se_{1.09}$	$Co_{3.08}Fe_{3.17}Ni_{2.94}S_{6.95}Se_{1.05}$	-	10.08	2.05	4.22	-
P.S6	$Co_3Fe_3Ni_3S_6Se_2$	$Co_{3.04}Fe_{3.08}Ni_{2.75}S_{5.90}Se_{2.10}$	$Co_{3.07}Fe_{3.19}Ni_{2.94}S_{5.97}Se_{2.03}$	-	10.15	2.32	4.32	-
P.S5	$Co_3Fe_3Ni_3S_5Se_3$	$Co_{3.51}Fe_{3.55}Ni_{3.15}S_{4.78}Se_{3.22}$	$Co_{3.03}Fe_{3.16}Ni_{2.87}S_{4.91}Se_{3.09}$	-	10.22	2.50	4.63	-
P.S4	$Co_3Fe_3Ni_3S_4Se_4$	$Co_{3.65}Fe_{3.53}Ni_{3.30}S_{3.90}Se_{4.10}$	$Co_{3.06}Fe_{3.04}Ni_{2.98}S_{3.99}Se_{4.01}$	-	10.24	3.98	5.19	-
P.S3	$Co_3Fe_3Ni_3S_3Se_5$	$Co_{3.67}Fe_{3.59}Ni_{3.37}S_{2.76}Se_{5.24}$	$Co_{2.97}Fe_{3.07}Ni_{2.81}S_{2.99}Se_{5.01}$	-	10.35	5.68	6.61	-
P.S2	$Co_3Fe_3Ni_3S_2Se6$	-	-	8.3% CoSe + 1.3% NiS	-	4.74	5.71	-
P.S1	$Co_3Fe_3Ni_3SSe_7$	-	-	43.4% CoSe + 31% FeSe	-	7.23	5.78	-
P.S0	$Co_3Fe_3Ni_3Se_8$	-	-	70.1% FeSe + 12.3% CoNiSe	-	6.86	8.77	-
I.S8	$Co_3Fe_3Ni_3S_8$	$Co_{3.08}Fe_{2.80}Ni_{3.29}S_8$	Same as powders					92.9
I.S7	$Co_3Fe_3Ni_3S_7Se$	$Co_{3.28}Fe_{2.62}Ni_{2.83}S_{6.42}Se_{1.58}$						82.1
I.S6	$Co_3Fe_3Ni_3S_6Se_2$	$Co_{2.68}Fe_{3.39}Ni_{2.52}S_{5.40}Se_{2.60}$						84.2
I.S5	$Co_3Fe_3Ni_3S_5Se_3$	$Co_{3.12}Fe_{2.96}Ni_{2.96}S_{4.36}Se_{3.64}$						91.2
I.S4	$Co_3Fe_3Ni_3S_4Se_4$	$Co_{2.97}Fe_{2.92}Ni_{2.88}S_{3.35}Se_{4.65}$						86.2
I.S3	$Co_3Fe_3Ni_3S_3Se_5$	$Co_{2.65}Fe_{2.69}Ni_{2.24}S_{2.24}Se_{5.76}$						79.6
S.S8	$Co_3Fe_3Ni_3S_8$	$Co_{3.12}Fe_{3.00}Ni_{3.01}S_8$	$Co_{3,09}Fe_{3,04}Ni_{3,10}S_8$	-	10.02	1.63	2.74	90.2
S.S7	$Co_3Fe_3Ni_3S_7Se$	$Co_{3.04}Fe_{3.22}Ni_{2.91}S_{6.40}Se_{1.60}$	$Co_{3,12}Fe_{3,21}Ni_{2,98}S_{6,92}Se_{1,08}$	-	10.09	2.00	4.04	91.1
S.S6	$Co_3Fe_3Ni_3S_6Se_2$	$Co_{3.12}Fe_{3.47}Ni_{2.95}S_{5.51}Se_{2.49}$	$Co_{3,10}Fe_{3,21}Ni_{2,97}S_{5,95}Se_{2,05}$	-	10.15	3.48	4.24	92.6
S.S5	$Co_3Fe_3Ni_3S_5Se_3$	$Co_{2.58}Fe_{2.68}Ni_{2.60}S_{4.63}Se_{3.36}$	$Co_{3,04}Fe_{3,07}Ni_{2,81}S_{4,92}Se_{3,08}$	-	10.21	4.66	4.90	92.6
S.S4	$Co_3Fe_3Ni_3S_4Se_4$	$Co_{3.02}Fe_{3.00}Ni_{2.95}S_{3.43}Se_{4.57}$	$Co_{3,08}Fe_{3,23}Ni_{2,85}S_{3,93}Se_{4,07}$	-	10.27	3.58	4.84	90.9
S.S3	$Co_3Fe_3Ni_3S_3Se_5$	$Co_{2.78}Fe_{2.55}Ni_{2.58}S_{2.44}Se_{5.56}$	$Co_{3,02}Fe_{3,13}Ni_{2,86}S_{2,88}Se_{5,12}$	-	10.36	3.43	4.43	91.2

			$Co_{9-x-y}Fe_xN_yS_8$ series					
P.314.S8	$Co_3Fe_{1.5}Ni4.5S_8$	$Co_{2.39}Fe_{1.34}Ni_{4.27}S_8$	$Co_{3.11}Fe_{1.46}Ni_{5.93}S_8$	-	10.00	1.26	2.61	-
P.116.S8	$Co_{1.5}Fe_{1.5}Ni_6S_8$	$Co_{1.62}Fe_{1.47}Ni_{5.90}S_8$	$Co_{1.72}Fe_{1.66}Ni_{6.94}S_8$	3.7% NiS	10.05	3.49	5.55	-
P.134.S8	$Co_{1.5}Fe_3Ni_{4.5}S_8$	$Co_{1.59}Fe_{3.06}Ni_{4.36}S_8$	$Co_{1.76}Fe_{3.64}Ni_{5.19}S_8$	-	10.05	1.37	3.08	-
P.413.S8	$Co_{4.5}Fe_{1.5}Ni_3S_8$	$Co_{4.51}Fe_{1.46}Ni_{3.03}S_8$	$Co_{4.65}Fe_{1.29}Ni_{4.70}S_8$	-	9.90	1.58	2.91	-
P.611.S8	$Co_6Fe_{1.5}Ni_{1.5}S_8$	$Co_{5.99}Fe_{1.54}Ni_{1.47}S_8$	$Co_{6.66}Fe_{1.16}Ni_{2.57}S_8$	-	9.98	1.09	2.55	-
P.431.S8	$Co_{4.5}Fe_3Ni_{1.5}S_8$	$Co_{4.53}Fe_{2.96}Ni_{1.51}S_8$	$Co_{5.15}Fe_{3.07}Ni_{2.26}S_8$	-	10.01	1.25	2.95	-
P.341.S8	$Co_3Fe_{4.5}Ni_{1.5}S_8$	$Co_{3.15}Fe_{4.51}Ni_{1.34}S_8$	$Co_{3.72}Fe_{5.41}Ni_{1.87}S_8$	5.7% Pyrrhotite (FeS)	10.05	1.51	2.83	-
P.161.S8	$Co_{1.5}Fe_6Ni_{1.5}S_8$	$Co_{1.66}Fe_{6.03}Ni_{1.31}S_8$	$Co_{1.69}Fe_{7.27}Ni_{1.59}S_8$	4.8% Fe + 24.3% Troilite (FeS)	10.09	1.60	2.64	-
P.143.S8	$Co_{1.5}Fe_{4.5}Ni_3S_8$	$Co_{1.67}Fe_{4.71}Ni_{2.62}S_8$	$Co_{1.81}Fe_{5.05}Ni_{3.97}S_8$	-	10.08	2.12	3.63	-
I.314.S8	$Co_3Fe_{1.5}Ni_{4.5}S_8$	$Co_{2.98}Fe_{1.52}Ni_{4.49}S_8$						90.77
I.116.S8	$Co_{1.5}Fe_{1.5}Ni_6S_8$	$Co_{1.55}Fe_{1.56}Ni_{5.89}S_8$						91.43
I.134.S8	$Co_{1.5}Fe_3Ni_{4.5}S_8$	$Co_{1.51}Fe_{2.93}Ni_{4.56}S_8$						91.68
I.413.S8	$Co_{4.5}Fe_{1.5}Ni_3S_8$	$Co_{4.41}Fe_{1.51}Ni_{3.01}S_8$						95.02
I.611.S8	$Co_6Fe_{1.5}Ni_{1.5}S_8$	$Co_{5.95}Fe_{1.50}Ni_{1.55}S_8$		Same as powders				90.08
I.431.S8	$Co_{4.5}Fe_3Ni_{1.5}S_8$	$Co_{4.68}Fe_{2.75}Ni_{1.57}S_8$						88.69
I.341.S8	$Co_3Fe_{4.5}Ni_{1.5}S_8$	$Co_{3.42}Fe_{3.85}Ni_{1.75}S_8$						87.31
I.161.S8	$Co_{1.5}Fe_6Ni_{1.5}S_8$	$Co_{1.46}Fe_{5.29}Ni_{2.25}S_8$						85.24
I.143.S8	$Co_{1.5}Fe_{4.5}Ni_3S_8$	$Co_{1.59}Fe_{4.08}Ni_{3.33}S_8$						89.92
S.314.S8	$Co_3Fe_{1.5}Ni_{4.5}S_8$	$Co_{3.07}Fe_{1.46}Ni_{4.47}S_8$	$Co_{3.37}Fe_{1.67}Ni_{5.07}S_8$	4% Fe	10.01	1.72	3.30	88.14
S.116.S8	$Co_{1.5}Fe_{1.5}Ni_6S_8$	$Co_{1.61}Fe_{1.54}Ni_{5.85}S_8$	$Co_{1.47}Fe_{1.45}Ni_{6.01}S_8$	12.1% NiS	10.04	6.33	7.06	92.87
S.134.S8	$Co_{1.5}Fe_3Ni_{4.5}S_8$	$Co_{1.52}Fe_{3.07}Ni_{4.41}S_8$	$Co_{1.54}Fe_{2.97}Ni_{4.63}S_8$	3% Fe	10.04	1.77	3.54	86.38
S.413.S8	$Co_{4.5}Fe_{1.5}Ni_3S_8$	$Co_{4.47}Fe_{1.52}Ni_{3.01}S_8$	$Co_{1.54}Fe_{2.97}Ni_{4.63}S_8$	-	9.98	1.91	3.05	92.77
S.611.S8	$Co_6Fe_{1.5}Ni_{1.5}S_8$	$Co_{5.93}Fe_{1.56}Ni_{1.51}S_8$	$Co_{6.05}Fe_{1.63}Ni_{1.47}S_8$	-	9.97	1.28	2.56	79.84
S.431.S8	$Co_{4.5}Fe_3Ni_{1.5}S_8$	$Co_{4.15}Fe_{2.35}Ni_{1.50}S_8$	$Co_{4.48}Fe_{3.06}Ni_{1.51}S_8$	15.3% Pyrrhotite (FeS)	9.98	1.03	2.25	80.52
S.341.S8	$Co_3Fe_{4.5}Ni_{1.5}S_8$	$Co_{2.94}Fe_{3.42}Ni_{1.63}S_8$	$Co_{3.24}Fe_{5.08}Ni_{1.55}S_8$	22% Troilite (FeS)	10.02	1.07	2.46	84.56
S.161.S8	$Co_{1.5}Fe_6Ni_{1.5}S_8$	$Co_{1.25}Fe_{5.58}Ni_{1.16}S_8$	$Co_{1.72}Fe_{7.39}Ni_{1.68}S_8$	35.3% Troilite (FeS) + 11.3% Pyrrhotite (FeS)	10.07	1.62	2.64	91.08
S.143.S8	$Co_{1.5}Fe_{4.5}Ni_3S_8$	$Co_{1.38}Fe_{3.99}Ni_{2.63}S_8$	$Co_{1.52}Fe_{4.87}Ni_{3.00}S_8$	16.9% Pyrrhotite (FeS)	10.06	1.26	2.79	83.46

			$Co_{9-x-y}Fe_xN_yS4Se_4$ series					
P314.S4	$Co_3Fe_{1.5}Ni_{4.5}S_4Se_4$	$Co_{4.26}Fe_{2.20}Ni_{6.48}S_4Se_{5.79}$ $Co_{2.95}Fe_{1.52}Ni_{4.48}S_{2.76}Se_4$	$Co_{3.05}Fe_{1.55}Ni_{4.53}S_4Se_{3.97}$	-	10.24	5.71	8.02	-
P.116.S4	$Co_{1.5}Fe_{1.5}Ni_6S_4Se_4$	$Co_{1.47}Fe_{1.54}Ni_{5.74}S_4Se_{6.00}$ $Co_{1.45}Fe_{1.50}Ni_{5.78}S_{2.86}Se_4$	$Co_{1.54}Fe_{1.53}Ni_{6.20}S_4Se_{4.03}$	10.5% $CoNiS_4$ + 6.3% $CoNiSe_2$	10.26	7.21	9.64	-
P.134.S4	$Co_{1.5}Fe_3Ni_{4.5}S_4Se_4$	$Co_{1.93}Fe_{3.85}Ni_{5.58}S_4Se_{5.73}$ $Co_{1.34}Fe_{2.69}Ni_{3.89}S_{2.79}Se_4$	$Co_{1.52}Fe_{3.01}Ni_{4.63}S_4Se_{4.01}$	2.4% NiSe	10.32	4.28	5.93	-
P.413.S4	$Co_{4.5}Fe_{1.5}Ni_3S_4Se_4$	$Co_{6.50}Fe_{2.34}Ni_{4.44}S_4Se_{6.10}$ $Co_{4.26}Fe_{1.53}Ni_{2.91}S_{2.62}Se_4$	$Co_{4.78}Fe_{1.72}Ni_{3.21}S_4Se_{3.93}$	-	10.27	3.61	5.32	-
P.611.S4	$Co_6Fe_{1.5}Ni_{1.5}S_4Se_4$	$Co_{7.31}Fe_{1.83}Ni_{2.10}S_4Se_{6.01}$ $Co_{6.52}Fe_{1.55}Ni_{1.73}S_{2.66}Se_4$	$Co_{6.09}Fe_{1.53}Ni_{1.46}S_4Se_{3.96}$	-	10.20	2.90	4.98	-
P.431.S4	$Co_{4.5}Fe_3Ni_{1.5}S_4Se_4$	$Co_{7.42}Fe_{5.50}Ni_{2.44}S_4Se_{5.37}$ $Co_{5.53}Fe_{4.10}Ni_{1.82}S_{2.98}Se_4$	$Co_{5.50}Fe_{3.05}Ni_{1.50}S_4Se_{3.94}$	-	10.26	3.40	4.33	-
P.341.S4	$Co_3Fe_{4.5}Ni_{1.5}S_4Se_4$	$Co_{5.76}Fe_{6.59}Ni_{2.76}S_4Se_{6.04}$ $Co_{3.81}Fe_{4.37}Ni_{1.83}S_{2.65}Se_4$	$Co_{3.35}Fe_{4.56}Ni_{1.57}S_4Se_{4.15}$	-	10.32	3.40	5.00	-
P.161.S4	$Co_{1.5}Fe_6Ni_{1.5}S_4Se_4$	$Co_{1.79}Fe_{3.53}Ni_{5.31}S_4Se_{5.79}$ $Co_{1.23}Fe_{2.45}Ni_{3.68}S_{2.77}Se_4$	$Co_{1.61}Fe_{6.59}Ni_{1.37}S_4Se_{4.07}$	-	10.31	7.48	9.96	-
P.143.S4	$Co_{1.5}Fe_{4.5}Ni_3S_4Se_4$	$Co_{2.42}Fe_{7.33}Ni_{4.62}S_4Se_{5.67}$ $Co_{1.71}Fe_{5.18}Ni_{3.26}S_{2.82}Se_4$	$Co_{1.46}Fe_{4.54}Ni_{2.99}S_4Se_{3.98}$	-	10.37	2.84	4.70	-
I.314.S4	$Co_3Fe_{1.5}Ni_{4.5}S_4Se_4$	$Co_{4.14}Fe_{2.08}Ni_{6.39}S_4Se_{6.68}$ $Co_{2.48}Fe_{1.24}Ni_{3.82}S_{2.39}Se_4$	Same as powders					90.09
I.116.S4	$Co_{1.5}Fe_{1.5}Ni_6S_4Se_4$	$Co_{1.74}Fe_{1.57}Ni_{9.26}S_4Se_{6.98}$ $Co_{1.00}Fe_{0.90}Ni_{5.30}S_{2.29}Se_4$						87.41
I.134.S4	$Co_{1.5}Fe_3Ni_{4.5}S_4Se_4$	$Co_{1.75}Fe_{3.54}Ni_{5.12}S_4Se_{5.62}$ $Co_{1.25}Fe_{2.59}Ni_{3.64}S_{2.85}Se_4$						83.46
I.413.S4	$Co_{4.5}Fe_{1.5}Ni_3S_4Se_4$	$Co_{4.92}Fe_{1.85}Ni_{3.35}S_4Se_{6.92}$ $Co_{4.11}Fe_{1.41}Ni_{2.57}S_{2.52}Se_4$						81.72
I.611.S4	$Co_6Fe_{1.5}Ni_{1.5}S_4Se_4$	$Co_{8.38}Fe_{1.93}Ni_{2.02}S_4Se_{4.67}$ $Co_{7.17}Fe_{1.65}Ni_{1.73}S_{3.42}Se_4$						89.13
I.431.S4	$Co_{4.5}Fe_3Ni_{1.5}S_4Se_4$	$Co_{5.87}Fe_{3.76}Ni_{1.93}S_4Se_{5.55}$ $Co_{4.23}Fe_{2.71}Ni_{1.39}S_{2.88}Se_4$						80.12
I.341.S4	$Co_3Fe_{4.5}Ni_{1.5}S_4Se_4$	$Co_{3.76}Fe_{4.28}Ni_{1.92}S_4Se_{5.97}$						88.16

		$Co_{2.52}Fe_{2.86}Ni_{1.28}S_{2.68}Se_4$						
I.161.S4	$Co_{1.5}Fe_6Ni_{1.5}S_4Se_4$	$Co_{0.81}Fe_{7.46}Ni_{0.41}S_4Se_{5.11}$ $Co_{0.63}Fe_{5.83}Ni_{0.31}S_{3.13}Se_4$						86.15
I.143.S4	$Co_{1.5}Fe_{4.5}Ni_3S_4Se_4$	$Co_{1.77}Fe_{5.28}Ni_{3.56}S_4Se_{5.73}$ $Co_{1.24}Fe_{3.69}Ni_{2.49}S_{2.79}Se_4$						86.63
S.314.S4	$Co_3Fe_{1.5}Ni_{4.5}S_4Se_4$	$Co_{3.38}Fe_{1.61}Ni_{5.35}S_4Se_{6.44}$ $Co_{2.10}Fe_{1.00}Ni_{3.32}S_{2.48}Se_4$	$Co_{2.99}Fe_{1.51}Ni_{4.41}S_4Se_{3.90}$	1.1% Co_7Fe_9 + 8.8% Ni_3Se_4	10.19	4.39	4.10	88.86
S.116.S4	$Co_{1.5}Fe_{1.5}Ni_6S_4Se_4$	$Co_{1.67}Fe_{1.82}Ni_{5.69}S_4Se_{4.80}$ $Co_{1.40}Fe_{1.52}Ni_{4.74}S_{3.33}Se_4$	$Co_{1.53}Fe_{1.53}Ni_{6.15}S_4Se_{4.00}$	8.0% NiS_2 + 9.9% CoSe	10.25	3.61	9.37	93.52
S.134.S4	$Co_{1.5}Fe_3Ni_{4.5}S_4Se_4$	$Co_{1.73}Fe_{3.45}Ni_{5.09}S_4Se_{5.88}$ $Co_{1.18}Fe_{2.34}Ni_{3.46}S_{2.72}Se_4$	$Co_{1.51}Fe_{2.96}Ni_{4.62}S_4Se_{4.00}$	6.4% Ni	10.31	8.10	6.33	94.86
S.413.S4	$Co_{4.5}Fe_{1.5}Ni_3S_4Se_4$	$Co_{5.06}Fe_{3.06}Ni_{1.81}S_4Se_{5.18}$ $Co_{3.91}Fe_{2.37}Ni_{1.39}S_{3.09}Se_4$	$Co_{4.25}Fe_{1.41}Ni_{2.85}S_4Se_{3.69}$	7.4% CoSe	10.26	4.99	4.31	90.22
S.611.S4	$Co_6Fe_{1.5}Ni_{1.5}S_4Se_4$	$Co_{6.83}Fe_{1.82}Ni_{2.03}S_4Se_{6.57}$ $Co_{4.15}Fe_{1.11}Ni_{1.24}S_{2.43}Se_4$	$Co_{6.04}Fe_{1.47}Ni_{1.46}S_4Se_{3.95}$	12.3% CoSe	10.23	9.84	7.30	86.79
S.431.S4	$Co_{4.5}Fe_3Ni_{1.5}S_4Se_4$	$Co_{5.34}Fe_{3.63}Ni_{1.94}S_4Se_{6.33}$ $Co_{3.38}Fe_{2.30}Ni_{1.22}S_{2.53}Se_4$	$Co_{4.46}Fe_{2.98}Ni_{1.47}S_4Se_{3.90}$	19% FeSe	10.23	3.77	3.69	83.80
S.341.S4	$Co_3Fe_{4.5}Ni_{1.5}S_4Se_4$	$Co_{3.52}Fe_{5.00}Ni_{1.74}S_4Se_{5.24}$ $Co_{2.69}Fe_{3.82}Ni_{1.33}S_{3.05}Se_4$	$Co_{2.98}Fe_{4.41}Ni_{1.50}S_4Se_{3.90}$	23.7% FeSe	10.34	4.95	4.66	86.66
S.161.S4	$Co_{1.5}Fe_6Ni_{1.5}S_4Se_4$	$Co_{1.44}Fe_{7.18}Ni_{0.37}S_4Se_{5.47}$ $Co_{1.05}Fe_{5.25}Ni_{0.27}S_{2.93}Se_4$	$Co_{1.51}Fe_{5.97}Ni_{1.44}S_4Se_{3.90}$	7.9% FeSe	10.30	3.47	4.81	80.36
S.143.S4	$Co_{1.5}Fe_{4.5}Ni_3S_4Se_4$	$Co_{1.66}Fe_{5.25}Ni_{3.33}S_4Se_{5.71}$ $Co_{1.16}Fe_{3.68}Ni_{2.33}S_{2.80}Se_4$	$Co_{1.45}Fe_{4.50}Ni_{2.96}S_4Se_{3.95}$	1.4% $Fe_{11}S_{12}$	10.29	5.03	7.78	95.33

Table S2. Summary of geometric area of all tested samples assigned to test equipment.

Sample	Geometric area [cm^2]	Sample	Geometric area [cm^2]	Sample	Geometric area [cm^2]
$Co_3Fe_3Ni_3S_{8-x}Se_x$ series		**$Co_{9-x-y}Fe_xN_yS_8$ series**		**$Co_{9-x-y}Fe_xN_yS_4Se_4$ series**	
	MTM Anko				*Gamry*
P.S8	0.094	**P.314.S8**	0.067	**P314.S4**	0.187
P.S7	0.058	**P.116.S8**	0.061	**P.116.S4**	0.187
P.S6	0.070	**P.134.S8**	0.074	**P.134.S4**	0.187
P.S5	0.066	**P.413.S8**	0.077	**P.413.S4**	0.187
P.S4	0.095	**P.611.S8**	0.028	**P.611.S4**	0.187
P.S3	0.056	**P.431.S8**	0.067	**P.431.S4**	0.187
		P.341.S8	0.063	**P.341.S4**	0.187
		P.161.S8	0.048	**P.161.S4**	0.187
		P.143.S8	0.069	**P.143.S4**	0.187
I.S8	0.094	**I.314.S8**	0.156	**I.314.S4**	0.196
I.S7	0.105	**I.116.S8**	0.121	**I.116.S4**	0.196
I.S6	0.116	**I.134.S8**	0.217	**I.134.S4**	0.196
I.S5	0.115	**I.413.S8**	0.218	**I.413.S4**	0.196
I.S4	0.111	**I.611.S8**	0.186	**I.611.S4**	0.196
I.S3	0.108	**I.431.S8**	0.127	**I.431.S4**	0.196
		I.341.S8	0.251	**I.341.S4**	0.196
		I.161.S8	0.114	**I.161.S4**	0.196
		I.143.S8	0.181	**I.143.S4**	0.196

S.S8	0.114	**S.314.S8**	0.188	**S.314.S4**	0.196
S.S7	0.921	**S.116.S8**	0.144	**S.116.S4**	0.196
S.S6	0.228	**S.134.S8**	0.051	**S.134.S4**	0.196
S.S5	0.174	**S.413.S8**	0.246	**S.413.S4**	0.196
S.S4	0.228	**S.611.S8**	0.072	**S.611.S4**	0.196
S.S3	0.324	**S.431.S8**	0.140	**S.431.S4**	0.196
		S.341.S8	0.153	**S.341.S4**	0.196
		S.161.S8	0.237	**S.161.S4**	0.196
		S.143.S8	0.115	**S.143.S4**	0.196

Table S3. Summaries of C_{dl}, ECSA and RF values of all tested samples with the Δ ECSA and noted activation process.

Sample	Before stability test			After stability test			Δ ECSA	Activation process
	C_{dl}	ECSA	RF	C_{dl}	ECSA	RF		
$Co_3Fe_3Ni_3S_{8-x}Se_x$ series								
P.S8	$1.95\cdot10^{-5}$	$5.58\cdot10^{-1}$	5.91	$4.69\cdot10^{-5}$	1.34	$1.42\cdot10^{1}$	$-7.81\cdot10^{-1}$	+
P.S7	$2.25\cdot10^{-5}$	$6.43\cdot10^{-1}$	$1.10\cdot10^{1}$	$2.80\cdot10^{-5}$	7.99	$1.35\cdot10^{1}$	$-1.55\cdot10^{-1}$	+
P.S6	$1.98\cdot10^{-5}$	$05.66\cdot10^{-1}$	8.06	$3.02\cdot10^{-5}$	$8.63\cdot10^{-1}$	$1.23\cdot10^{1}$	$-2.97\cdot10^{-1}$	+
P.S5	$2.38\cdot10^{-5}$	$6.81\cdot10^{-1}$	$1.02\cdot10^{1}$	$3.90\cdot10^{-5}$	1.11	$1.67\cdot10^{1}$	$-4.33\cdot10^{-1}$	+
P.S4	$5.49\cdot10^{-5}$	1.57	$1.65\cdot10^{1}$	$7.01\cdot10^{-5}$	2.00	$2.11\cdot10^{1}$	$-4.34\cdot10^{-1}$	+
P.S3	$1.81\cdot10^{-5}$	$5.16\cdot10^{-1}$	7.90	$2.33\cdot10^{-5}$	$6.65\cdot10^{-1}$	$1.02\cdot10^{1}$	$-1.49\cdot10^{-1}$	+
I.S8	$2.25\cdot10^{-4}$	6.44	$6.79\cdot10^{1}$	$2.09\cdot10^{-3}$	$5.96\cdot10^{1}$	$6.28\cdot10^{2}$	$-5.31\cdot10^{1}$	+
I.S7	$6.13\cdot10^{-5}$	1.75	$1.66\cdot10^{1}$	$6.49\cdot10^{-5}$	1.85	$1.76\cdot10^{1}$	$-9.72\cdot10^{-2}$	+
I.S6	$4.26\cdot10^{-5}$	1.22	$1.05\cdot10^{1}$	$3.51\cdot10^{-5}$	1.00	8.67	$2.12\cdot10^{-1}$	–
I.S5	$4.66\cdot10^{-4}$	1.33	$1.15\cdot10^{2}$	$9.04\cdot10^{-5}$	2.58	$2.24\cdot10^{1}$	$1.07\cdot10^{1}$	–
I.S4	$1.19\cdot10^{-4}$	3.39	$3.05\cdot10^{1}$	$2.81\cdot10^{-4}$	8.02	$7.21\cdot10^{1}$	-4.62	+
I.S3	$2.57\cdot10^{-4}$	7.35	6.78	$2.37\cdot10^{-4}$	6.77	$6.24\cdot10^{1}$	$5.77\cdot10^{-1}$	–
S.S8	$1.56\cdot10^{-3}$	$4.46\cdot10^{1}$	$3.90\cdot10^{2}$	$2.92\cdot10^{-4}$	8.34	$7.30\cdot10^{1}$	$3.62\cdot10^{1}$	–
S.S7	$4.85\cdot10^{-3}$	$1.37\cdot10^{2}$	$1.49\cdot10^{2}$	$2.47\cdot10^{-3}$	$7.06\cdot10^{1}$	$7.67\cdot10^{1}$	$6.65\cdot10^{1}$	–
S.S6	$1.81\cdot10^{-3}$	$3.00\cdot10^{1}$	$1.32\cdot10^{2}$	$2.21\cdot10^{-4}$	6.32	$2.77\cdot10^{1}$	$2.37\cdot10^{1}$	–
S.S5	$5.72\cdot10^{-4}$	$1.66\cdot10^{1}$	$9.56\cdot10^{1}$	$6.53\cdot10^{-5}$	1.86	$1.07\cdot10^{1}$	$1.47\cdot10^{1}$	–
S.S4	$8.50\cdot10^{-4}$	$2.45\cdot10^{1}$	$1.07\cdot10^{2}$	$6.04\cdot10^{-4}$	$1.73\cdot10^{1}$	$7.56\cdot10^{1}$	7.24	–
S.S3	$4.86\cdot10^{-4}$	$1.32\cdot10^{1}$	$4.08\cdot10^{1}$	$3.45\cdot10^{-4}$	$9.87\cdot10^{-1}$	3.05	$1.22\cdot10^{1}$	–

$Co_{9-x-y}Fe_xN_yS_8$ series								
P.314.S8	$1.77 \cdot 10^{-4}$	5.06	$7.59 \cdot 10^{1}$	$2.07 \cdot 10^{-4}$	5.92	$8.89 \cdot 10^{1}$	$-8.63 \cdot 10^{-1}$	+
P.116.S8	$5.57 \cdot 10^{-5}$	1.59	$2.61 \cdot 10^{1}$	$7.21 \cdot 10^{-5}$	2.06	$3.37 \cdot 10^{1}$	$-4.69 \cdot 10^{-1}$	+
P.134.S8	$1.43 \cdot 10^{-4}$	4.08	$5.53 \cdot 10^{1}$	$1.90 \cdot 10^{-4}$	5.43	$7.35 \cdot 10^{1}$	-1.35	+
P.413.S8	$3.80 \cdot 10^{-5}$	1.09	$1.41 \cdot 10^{1}$	$5.33 \cdot 10^{-5}$	1.52	1.98	$-4.35 \cdot 10^{-1}$	+
P.611.S8	$9.33 \cdot 10^{-4}$	$2.49 \cdot 10^{1}$	$8.90 \cdot 10^{2}$	$1.14 \cdot 10^{-3}$	$3.86 \cdot 10^{1}$	$1.38 \cdot 10^{3}$	$-1.37 \cdot 10^{1}$	+
P.431.S8	$4.65 \cdot 10^{-5}$	1.33	$2.00 \cdot 10^{1}$	$6.24 \cdot 10^{-5}$	1.78	$2.68 \cdot 10^{1}$	$-4.54 \cdot 10^{-1}$	+
P.341.S8	$1.40 \cdot 10^{-4}$	4.00	$6.30 \cdot 10^{1}$	$1.67 \cdot 10^{-4}$	4.76	$7.51 \cdot 10^{1}$	$-7.68 \cdot 10^{-1}$	+
P.161.S8	$5.67 \cdot 10^{-5}$	1.62	$3.36 \cdot 10^{1}$	$7.19 \cdot 10^{-5}$	2.05	$4.26 \cdot 10^{1}$	$-4.33 \cdot 10^{-1}$	+
P.143.S8	$7.09 \cdot 10^{-5}$	2.02	$2.93 \cdot 10^{1}$	$7.02 \cdot 10^{-5}$	2.01	$2.90 \cdot 10^{1}$	$1.91 \cdot 10^{-2}$	-
I.314.S8	$3.36 \cdot 10^{-5}$	$9.61 \cdot 10^{-1}$	5.12	$1.43 \cdot 10^{-5}$	$4.09 \cdot 10^{-1}$	2.17	$5.52 \cdot 10^{-1}$	-
I.116.S8	$8.91 \cdot 10^{-6}$	$2.54 \cdot 10^{-1}$	1.76	$6.87 \cdot 10^{-6}$	$1.96 \cdot 10^{-1}$	1.36	$5.80 \cdot 10^{-2}$	-
I.134.S8	$1.75 \cdot 10^{-5}$	$5.00 \cdot 10^{-1}$	9.7	$1.07 \cdot 10^{-5}$	$3.06 \cdot 10^{-1}$	5.97	$1.94 \cdot 10^{-1}$	-
I.413.S8	$3.86 \cdot 10^{-5}$	1.10	4.48	$2.84 \cdot 10^{-5}$	$8.11 \cdot 10^{-1}$	3.30	$2.91 \cdot 10^{-1}$	-
I.611.S8	$1.45 \cdot 10^{-5}$	$4.14 \cdot 10^{-1}$	5.78	$9.66 \cdot 10^{-5}$	2.76	$3.86 \cdot 10^{1}$	-2.35	+
I.431.S8	$5.72 \cdot 10^{-5}$	1.63	$1.17 \cdot 10^{1}$	$9.31 \cdot 10^{-5}$	2.66	$1.90 \cdot 10^{1}$	-1.03	+
I.341.S8	$5.13 \cdot 10^{-4}$	$1.47 \cdot 10^{1}$	$9.56 \cdot 10^{1}$	$9.62 \cdot 10^{-4}$	$2.75 \cdot 10^{1}$	$1.79 \cdot 10^{2}$	$-1.28 \cdot 10^{1}$	+
I.161.S8	$6.54 \cdot 10^{-3}$	$8.30 \cdot 10^{1}$	$3.50 \cdot 10^{2}$	$1.95 \cdot 10^{-3}$	$1.65 \cdot 10^{2}$	$6.96 \cdot 10^{2}$	$-8.23 \cdot 10^{1}$	+
I.143.S8	$1.21 \cdot 10^{-5}$	$3.01 \cdot 10^{-1}$	3.67	$9.70 \cdot 10^{-6}$	$2.77 \cdot 10^{-1}$	2.41	$6.92 \cdot 10^{-2}$	-
S.314.S8	$5.91 \cdot 10^{-4}$	$1.69 \cdot 10^{1}$	$1.08 \cdot 10^{2}$	$1.83 \cdot 10^{-4}$	5.21	$3.34 \cdot 10^{1}$	$1.17 \cdot 10^{1}$	-
S.116.S8	$6.01 \cdot 10^{-5}$	1.72	$1.42 \cdot 10^{1}$	$1.16 \cdot 10^{-4}$	3.32	$2.75 \cdot 10^{1}$	-1.60	+
S.134.S8	$1.30 \cdot 10^{-3}$	$3.72 \cdot 10^{1}$	$1.71 \cdot 10^{2}$	$2.01 \cdot 10^{-3}$	$5.73 \cdot 10^{1}$	$2.64 \cdot 10^{2}$	$-2.01 \cdot 10^{1}$	+
S.413.S8	$2.94 \cdot 10^{-4}$	8.59	$3.94 \cdot 10^{1}$	$6.07 \cdot 10^{-5}$	1.74	8.01	6.84	-
S.611.S8	$3.94 \cdot 10^{-3}$	$1.13 \cdot 10^{2}$	$6.05 \cdot 10^{2}$	$5.03 \cdot 10^{-3}$	$1.44 \cdot 10^{2}$	$7.73 \cdot 10^{2}$	$-3.13 \cdot 10^{1}$	+
S.431.S8	$1.86 \cdot 10^{-3}$	$5.31 \cdot 10^{1}$	$4.18 \cdot 10^{2}$	$5.03 \cdot 10^{-3}$	$1.44 \cdot 10^{2}$	$1.13 \cdot 10^{3}$	$-9.05 \cdot 10^{1}$	+
S.341.S8	$4.18 \cdot 10^{-3}$	$1.19 \cdot 10^{2}$	$4.77 \cdot 10^{2}$	$7.05 \cdot 10^{-3}$	$2.01 \cdot 10^{2}$	$8.04 \cdot 10^{2}$	$-8.20 \cdot 10^{1}$	+
S.161.S8	$3.64 \cdot 10^{-3}$	$1.14 \cdot 10^{2}$	$9.15 \cdot 10^{2}$	$3.71 \cdot 10^{-3}$	$1.06 \cdot 10^{2}$	$0.93 \cdot 10^{2}$	-2.19	+
S.143.S8	$1.28 \cdot 10^{-3}$	$3.65 \cdot 10^{1}$	$2.01 \cdot 10^{2}$	$2.48 \cdot 10^{-3}$	$7.08 \cdot 10^{1}$	$3.90 \cdot 10^{2}$	$-3.43 \cdot 10^{1}$	+

$Co_{9-x-y}Fe_xN_yS_4Se_4$ series								
P314.S4	$5.58 \cdot 10^{-5}$	$5.68 \cdot 10^{-2}$	$3.04 \cdot 10^{-1}$	$\cdot 10^{-3}$	$8.76 \cdot 10^{-2}$	$4.68 \cdot 10^{-1}$	$-3.07 \cdot 10^{-2}$	+
P.116.S4	$7.56 \cdot 10^{-5}$	$7.63 \cdot 10^{-5}$	$4.08 \cdot 10^{-1}$	$\cdot 10^{-3}$	$8.62 \cdot 10^{-2}$	$4.61 \cdot 10^{-1}$	$-9.84 \cdot 10^{-3}$	+
P.134.S4	$1.52 \cdot 10^{-5}$	$1.55 \cdot 10^{-2}$	$8.28 \cdot 10^{-2}$	$\cdot 10^{-3}$	$2.75 \cdot 10^{-2}$	$1.47 \cdot 10^{-1}$	$-1.20 \cdot 10^{-2}$	+
P.413.S4	$1.12 \cdot 10^{-4}$	$1.13 \cdot 10^{-1}$	$6.03 \cdot 10^{-1}$	$\cdot 10^{-3}$	$1.95 \cdot 10^{-1}$	$1.04 \cdot 10^{-1}$	$-8.23 \cdot 10^{-2}$	+
P.611.S4	$7.21 \cdot 10^{-5}$	$7.36 \cdot 10^{-2}$	$3.94 \cdot 10^{-1}$	$\cdot 10^{-3}$	$1.19 \cdot 10^{-1}$	$6.36 \cdot 10^{-1}$	$-4.53 \cdot 10^{-2}$	+
P.431.S4	$4.89 \cdot 10^{-5}$	$4.86 \cdot 10^{-2}$	$2.60 \cdot 10^{-1}$	$\cdot 10^{-3}$	$1.16 \cdot 10^{-1}$	$6.21 \cdot 10^{-1}$	$-6.76 \cdot 10^{-2}$	+
P.341.S4	$1.47 \cdot 10^{-5}$	$1.49 \cdot 10^{-2}$	$7.96 \cdot 10^{-2}$	$\cdot 10^{-3}$	$2.62 \cdot 10^{-2}$	$2.64 \cdot 10^{-1}$	$-1.14 \cdot 10^{-2}$	+
P.161.S4	$3.26 \cdot 10^{-5}$	$3.25 \cdot 10^{-2}$	$1.74 \cdot 10^{-1}$	$\cdot 10^{-3}$	$6.37 \cdot 10^{-2}$	$3.40 \cdot 10^{-1}$	$-3.12 \cdot 10^{-2}$	+
P.143.S4	$2.02 \cdot 10^{-5}$	$1.99 \cdot 10^{-2}$	$1.07 \cdot 10^{-1}$	$\cdot 10^{-3}$	$3.14 \cdot 10^{-2}$	$1.68 \cdot 10^{-1}$	$-1.14 \cdot 10^{-2}$	+
I.314.S4	$4.20 \cdot 10^{-4}$	$4.51 \cdot 10^{-1}$	2.30	$\cdot 10^{-3}$	$1.73 \cdot 10^{-1}$	$8.84 \cdot 10^{-1}$	$2.78 \cdot 10^{-1}$	-
I.116.S4	$8.49 \cdot 10^{-5}$	$9.52 \cdot 10^{-2}$	$4.85 \cdot 10^{-1}$	$\cdot 10^{-3}$	$1.39 \cdot 10^{-1}$	$7.09 \cdot 10^{-1}$	$-4.37 \cdot 10^{-2}$	+
I.134.S4	$2.08 \cdot 10^{-4}$	$7.56 \cdot 10^{-2}$	$3.86 \cdot 10^{-1}$	$\cdot 10^{-3}$	$8.75 \cdot 10^{-2}$	$4.47 \cdot 10^{-1}$	$-1.19 \cdot 10^{-2}$	+
I.413.S4	$9.27 \cdot 10^{-5}$	$1.76 \cdot 10^{-1}$	$8.96 \cdot 10^{-1}$	$\cdot 10^{-3}$	1.42	7.24	-1.24	+
I.611.S4	$4.69 \cdot 10^{-4}$	$3.53 \cdot 10^{-1}$	1.80	$\cdot 10^{-3}$	$2.92 \cdot 10^{-1}$	1.49	$6.15 \cdot 10^{-2}$	-
I.431.S4	$6.87 \cdot 10^{-5}$	$7.89 \cdot 10^{-2}$	$4.02 \cdot 10^{-1}$	$\cdot 10^{-3}$	$1.36 \cdot 10^{-1}$	$6.92 \cdot 10^{-1}$	$-5.68 \cdot 10^{-2}$	+
I.341.S4	$3.51 \cdot 10^{-4}$	$3.42 \cdot 10^{-1}$	1.75	$\cdot 10^{-3}$	2.95	$1.50 \cdot 10^{1}$	-2.61	+
I.161.S4	$1.48 \cdot 10^{-4}$	$1.37 \cdot 10^{-1}$	$6.98 \cdot 10^{-1}$	$\cdot 10^{-3}$	$1.15 \cdot 10^{-1}$	$5.86 \cdot 10^{-1}$	$2.19 \cdot 10^{-2}$	-
I.143.S4	$1.97 \cdot 10^{-4}$	$1.89 \cdot 10^{-1}$	$9.66 \cdot 10^{-1}$	$\cdot 10^{-3}$	$8.04 \cdot 10^{-1}$	4.10	$-615 \cdot 10^{-1}$	+
S.314.S4	$3.54 \cdot 10^{-3}$	3.50	$1.79 \cdot 10^{1}$	$\cdot 10^{-3}$	2.79	$1.42 \cdot 10^{1}$	$7.19 \cdot 10^{-1}$	-
S.116.S4	$2.61 \cdot 10^{-3}$	2.45	$1.25 \cdot 10^{1}$	$\cdot 10^{-3}$	1.40	7.15	1.05	-
S.134.S4	$3.63 \cdot 10^{-3}$	$3.11 \cdot 10^{-1}$	1.59	$\cdot 10^{-3}$	$2.42 \cdot 10^{-1}$	1.24	$6.91 \cdot 10^{-2}$	-
S.413.S4	$9.61 \cdot 10^{-3}$	$1.16 \cdot 10^{1}$	$5.91 \cdot 10^{1}$	$\cdot 10^{-3}$	8.97	$4.58 \cdot 10^{1}$	2.61	-
S.611.S4	$3.08 \cdot 10^{-3}$	3.04	$1.55 \cdot 10^{1}$	$\cdot 10^{-3}$	4.04	$2.06 \cdot 10^{1}$	$-9.94 \cdot 10^{-1}$	+
S.431.S4	$4.24 \cdot 10^{-3}$	5.58	$2.85 \cdot 10^{1}$	$\cdot 10^{-3}$	6.67	$3.40 \cdot 10^{1}$	-1.09	+
S.341.S4	$4.59 \cdot 10^{-3}$	5.05	$2.58 \cdot 10^{1}$	$\cdot 10^{-3}$	3.56	$1.82 \cdot 10^{1}$	1.49	-
S.161.S4	$6.31 \cdot 10^{-3}$	6.91	$3.52 \cdot 10^{1}$	$\cdot 10^{-3}$	$1.83 \cdot 10^{1}$	$9.35 \cdot 10^{1}$	$-1.14 \cdot 10^{1}$	+
S.143.S4	$2.80 \cdot 10^{-4}$	$2.76 \cdot 10^{-1}$	1.41	$\cdot 10^{-3}$	2.47	$1.26 \cdot 10^{1}$	$-2.20 \cdot 10^{-2}$	+

Table S4. R_{CT} and R_u determined by means of EIS.

Powders			Ingots			Pellets (sinters)		
Sample	**R_{CT} [Ω]**	**R_u [Ω]**	**Sample**	**R_{CT} [Ω]**	**R_u [Ω]**	**Sample**	**R_{CT} [Ω]**	**R_u [Ω]**
$Co_3Fe_3Ni_3S_{8-x}Se_x$ series								
P.S8	481.9	100.80	**I.S8**	23.51	5.01	**S.S8**	11.46	4.69
P.S7	4087	87.76	**I.S7**	25.78	5.65	**S.S7**	17.94	3.54
P.S6	1709	94.95	**I.S6**	19.60	4.65	**S.S6**	25.80	2.86
P.S5	857	90.74	**I.S5**	46.02	5.07	**S.S5**	66.50	4.45
P.S4	2148	88.62	**I.S4**	161.60	5.35	**S.S4**	45.04	4.61
P.S3	3451	83.53	**I.S3**	26.94	6.15	**S.S3**	16.61	2.77
$Co_{9-x-y}Fe_xNi_yS_8$ series								
P.314.S8	451.22	86.72	**I.314.S8**	100.49	3.86	**S.314.S8**	14.87	2.94
P.116.S8	5.42	75.60	**I.116.S8**	274.61	4.42	**S.116.S8**	8.01	3.50
P.134.S8	343.98	84.96	**I.134.S8**	190.12	4.03	**S.134.S8**	13.23	3.77
P.413.S8	634.40	82.25	**I.413.S8**	101.29	3.73	**S.413.S8**	27.91	3.54
P.611.S8	228.56	81.48	**I.611.S8**	109.10	4.81	**S.611.S8**	3.21	4.11
P.431.S8	733.92	81.57	**I.431.S8**	64.62	3.45	**S.431.S8**	7.79	4.59
P.341.S8	360.20	83.35	**I.341.S8**	70.28	3.34	**S.341.S8**	9.61	2.83
P.161.S8	284.12	84.05	**I.161.S8**	19.38	3.67	**S.161.S8**	18.38	2.76
P.143.S8	40.18	79.21	**I.143.S8**	56.57	2.22	**S.143.S8**	15.19	3.20

$Co_{9-x-y}Fe_xNi_yS_4Se_4$ series								
P.314.S4	1667.14	91.50	**I.314.S4**	471.19	11.35	**S.314.S4**	47.07	15.50
P.116.S4	434.56	88.72	**I.116.S4**	184.32	17.21	**S.116.S4**	76.15	22.55
P.134.S4	159.71	74.18	**I.134.S4**	469.91	16.32	**S.134.S4**	195.73	17.27
P.413.S4	691.52	88.08	**I.413.S4**	397.86	12.84	**S.413.S4**	40.81	18.25
P.611.S4	380.61	87.99	**I.611.S4**	203.25	15.63	**S.611.S4**	47.20	19.48
P.431.S4	185.20	81.83	**I.431.S4**	140.90	16.82	**S.431.S4**	42.25	12.06
P.341.S4	183.83	76.20	**I.341.S4**	108.95	43.14	**S.341.S4**	41.32	19.20
P.161.S4	270.68	81.12	**I.161.S4**	203.71	14.41	**S.161.S4**	9.74	14.06
P.143.S4	70.05	85.13	**I.143.S4**	235.70	11.73	**S.143.S4**	84.59	19.53

Table S5. Summary of overpotentials for all samples from all series for "prior" and "post" stability test normalized to ECSA and geometric area with Tafel Slope values.

Sample	η Electrochemical Active Area [mV]		Tafel slope [mV/dec]		η Geometric Area		Tafel slope [mV/dec]	
				$Co_3Fe_3Ni_3S_{8-x}Se_x$ series				
	Prior 0.2 [mA/cm²]	Post 0.2 [mA/cm²]	Prior	Post	Prior 10 [mA/cm²]	Post 10 [mA/cm²]	Prior	Post
P.S8	505	n/a	73	79	n/a	n/a	73	79
P.S7	431	481	80	93	463	505	80	93
P.S6	531	510	84	63	n/a	n/a	84	63
P.S5	467	n/a	84	90	n/a	n/a	84	112
P.S4	n/a	n/a	84	91	n/a	n/a	84	91
P.S3	n/a	n/a	88	81	n/a	n/a	88	81
I.S8	347	341	84	103	360	357	79	104
I.S7	286	318	76	98	327	377	75	154
I.S6	365	352	191	235	509	n/a	190	235
I.S5	n/a	553	149	158	n/a	n/a	148	153
I.S4	337	383	187	218	371	422	187	219
I.S3	408	410	262	278	373	387	268	277
S.S8	369	n/a	210	185	295	295	211	182
S.S7	387	n/a	160	162	322	374	152	156
S.S6	290	481	221	165	310	351	232	160
S.S5	209	466	229	217	314	371	234	217
S.S4	309	307	192	163	233	243	185	161
S.S3	357	362	179	168	348	376	164	164

$Co_{9-x-y}Fe_xN_yS_8$ series								
	Prior 0.2 [mA/cm²]	**Post 0.2 [mA/cm²]**	**Prior**	**Post**	**Prior 5 [mA/cm²]**	**Post 5 [mA/cm²]**	**Prior**	**Post**
P.314.S8	n/a	645	140	89	795	357	140	89
P.116.S8	n/a	n/a	239	144	n/a	n/a	230	140
P.134.S8	n/a	n/a	184	125	n/a	771	185	124
P.413.S8	536	465	136	120	581	477	138	125
P.611.S8	n/a	n/a	258	134	615	728	252	132
P.431.S8	n/a	n/a	191	144	n/a	n/a	194	140
P.341.S8	658	771	143	116	567	595	143	118
P.161.S8	795	n/a	116	119	773	n/a	178	180
P.143.S8	675	803	150	171	661	790	149	171
	Prior 0.2 [mA/cm²]	**Post 0.2 [mA/cm²]**	**Prior**	**Post**	**Prior 10 [mA/cm²]**	**Post 10 [mA/cm²]**	**Prior**	**Post**
I.314.S8	333	358	250	168	n/a	n/a	257	167
I.116.S8	331	380	131	129	587	n/a	131	131
I.134.S8	356	398	142	303	557	n/a	135	289
I.413.S8	338	374	133	134	547	n/a	134	142
I.611.S8	323	550	87	145	528	n/a	84	148
I.431.S8	350	397	75	153	421	514	78	151
I.341.S8	n/a	n/a	137	171	465	445	138	175

I.161.S8	n/a	n/a	156	175	377	361	159	177
I.143.S8	542	n/a	404	450	n/a	n/a	356	359
S.314.S8	575	577	277	281	452	n/a	235	322
S.116.S8	291[1]	356[1]	113	91	341	388	92	86
S.134.S8	n/a	n/a	211	274	467	423	214	263
S.413.S8	492	464	200	204	520	n/a	196	198
S.611.S8	n/a	n/a	466	406	220	288	537	423
S.431.S8	n/a	n/a	204	205	318	276	214	210
S.341.S8	n/a	n/a	291	275	380	320	297	281
S.161.S8	n/a	n/a	162	164	285	288	162	171
S.143.S8	n/a	n/a	239	258	391	385	237	258

$Co_{9-x-y}Fe_xN_yS_4Se_4$ series								
	Prior 0.2 [mA/cm²]	**Post 0.2 [mA/cm²]**	**Prior**	**Post**	**Prior 2 [mA/cm²]**	**Post 2 [mA/cm²]**	**Prior**	**Post**
P314.S4	n/a	n/a	223	159	n/a	n/a	221	158
P.116.S4	494	490	131	128	481	467	115	128
P.134.S4	307	403	103	112	399	460	102	110
P.413.S4	n/a	n/a	190	146	n/a	n/a	196	157
P.611.S4	477	n/a	172	114	462	447	170	112
P.431.S4	265	383	86	100	285	341	93	100
P.341.S4	297	423	164	126	417	481	161	125
P.161.S4	390	476	112	113	443	478	111	113
P.143.S4	282	379	104	97	340	421	102	95
	Prior 0.2 [mA/cm²]	**Post 0.2 [mA/cm²]**	**Prior**	**Post**	**Prior 10 [mA/cm²]**	**Post 10 [mA/cm²]**	**Prior**	**Post**
I.314.S4	n/a	468	202	142	n/a	533	203	143
I.116.S4	334	347	91	91	414	405	95	92
I.134.S4	346	344	90	89	423	431	94	90
I.413.S4	316	455	81	75	357	288	81	64
I.611.S4	446	425	131	133	444	441	131	128
I.431.S4	306	311	88	74	400	384	97	74
I.341.S4	501	n/a	130	141	502	314	131	150

I.161.S4	341	340	93	92	394	399	95	96
I.143.S4	311	384	91	80	348	305	91	78
S.314.S4	n/a	n/a	203	200	306	303	284	200
S.116.S4	n/a	567	209	196	354	354	226	203
S.134.S4	435	383	175	146	451	416	116	139
S.413.S4	n/a	n/a	495	248	348	302	578	260
S.611.S4	n/a	n/a	299	305	313	302	309	331
S.431.S4	n/a	n/a	253	179	283	258	250	188
S.341.S4	n/a	n/a	415	263	359	289	474	255
S.161.S4	n/a	n/a	205	401	306	303	267	432
S.143.S4	312	586	114	114	354	354	114	112

n/a – not achieved

[1] – see chapter 4.4.2